Inkjet Printing at High Resolution

A thesis Submitted to the University of Manchester
for the Degree of Doctor of Philosophy in the
Faculty of Science and Engineering

2021

Jinxin Yang

Department of Materials

School of Natural Sciences

Contents

Word count: 54,892

List of Figures

List of Tables

Abstract

Inkjet printing has been used as a manufacturing tool for a wide range of applications beyond its original use for text and graphics printing. This thesis aims to investigate the stability and electrical properties of inkjet printed line structures at high spatial resolution, using piezoelectric drop on demand (DOD) printing and electrohydrodynamic (EHD) inkjet printing.

An experimental study of the stability of lines produced by DOD printing drops of volume in the range 1 – 10 pL using an ink/substrate combination with zero receding contact angle is presented. These results are used to validate existing models of the limiting bounds for the formation of stable parallel-sided lines as a function of drop spacing and printing speed. The model for the maximum drop spacing bound shows good agreement with our results. The minimum drop spacing bound is limited by a bulging instability and our results agree with the existing model, except for the printings with large drop volumes at low temperature. It is shown that in this circumstance there is a different mechanism for bulging that occurs after printing over a period of minutes, if the liquid bead is present on the surface for a significant period of time before drying.

A study of the stability of lines printed on ink/substrate combinations with finite receding contact angles is also presented, over the same range of droplet size as the zero receding contact angle work. In this case, all the printed structures are found to be unstable, showing either individual large drops or continuous lines showing irregular periodic bulges at lower values of advancing and receding contact angles. The morphology change is shown to be due to the change of boundary conditions for the liquid bead at decreased contact angle. A dynamic model based on previous analysis methods is developed to predict the mean wavelength of the bulging morphology. It is further shown that stabilized line structures can be obtained on substrates with finite receding contact angle by pre-depositing droplets to generate small regular disturbances that initiate the formation of controlled periodic bulges, thus making the ridges relatively stable due to loss of liquid to the adjacent bugles.

Finally, a study is presented on the stability and electrical properties of lines printed at ultra high resolution using an EHD inkjet printing system. Stable DOD EHD printing using femtolitre volume droplets is achieved by controlling the flow rate and pulse width time. The stability model for the formation of parallel-sided lines is shown to agree well with the results on the low contact angle silicon substrates and also with results in the literature. However, large deviations were observed for results from high contact angle substrates. We hypothesize that this is possibly due to the deviations from the calculated ejected volume per pulse. Stable inkjet printed line electrodes with sub ten micrometre width are successfully achieved, with conductivities within an order of magnitude of bulk silver.

Declaration

No portion of the work referred to in the thesis has been submitted in support of an application for another degree or qualification of this or any other university or other institute of learning.

Some of the work in the thesis has been published in: *Yang J, Zheng F, Derby B. Stability of Lines with Zero Receding Contact Angle Produced by Inkjet Printing at Small Drop Volume. Langmuir, 2021, 37(1): 26-34*.

Copyright Statement

i. The author of this thesis (including any appendices and/or schedules to this thesis) owns certain copyright or related rights in it (the "Copyright") and he has given The University of Manchester certain rights to use such Copyright, including for administrative purposes.

ii. Copies of this thesis, either in full or in extracts and whether in hard or electronic copy, may be made only in accordance with the Copyright, Designs and Patents Act 1988 (as amended) and regulations issued under it or, where appropriate, in accordance with licensing agreements which the University has from time to time. This page must form part of any such copies made.

iii. The ownership of certain Copyright, patents, designs, trademarks and other intellectual property (the "Intellectual Property") and any reproductions of copyright works in the thesis, for example graphs and tables ("Reproductions"), which may be described in this thesis, may not be owned by the author and may be owned by third parties. Such Intellectual Property and Reproductions cannot and must not be made available for use without the prior written permission of the owner(s) of the relevant Intellectual Property and/or Reproductions.

iv. Further information on the conditions under which disclosure, publication and commercialisation of this thesis, the Copyright and any Intellectual Property and/or Reproductions described in it may take place is available in the University IP Policy (see http://www.campus.manchester.ac.uk/medialibrary/policies/intellectual-property.pdf), in any relevant Thesis restriction declarations deposited in the University Library, The University Library's regulations (see http://www.manchester.ac.uk/library/aboutus/regulations) and in The University's policy on presentation of Theses.

Acknowledgements

First of all, I would like to express my sincere gratitude to my supervisor, Professor Brian Derby, for his patient guidance and invaluable support through my whole PhD studies.

I would like to thank all the colleagues in the Derby group, particularly Michael Avery, Rachel Saunders, Andy Wallwork, Chongguang Liu, Hu Zhao, Hui Ding, Joseph Neilson, and Zixin Wang for their help and support in last four years. I would like to thank Dr. Fei Zheng and Dr. Pe He for their advice and support in my studies. I also appreciate for the funding support from China Scholarship Council (CSC) and EPSRC.

I would also like to thank all the friends I met in Manchester, including Changrun Cai, Hanxiao Wang, Kaitao Wu, Meng Lyu, Wentao Zou, Zhenfei Chai, Zhiying Xin. The full list of people is endless. Thank you all for making my life in Manchester colourful and enjoyable.

Finally, I would like to thank my parents, parents-in-law for their consistent love and care during my PhD period. Last but not least, my special thanks to my dear wife, Yinuo (Ella) Zhao. Thanks for your support and company. The beginning of our marriage brings a wonderful ending to my PhD life.

Chapter 1 Introduction

1.1 Background

In recent years, inkjet printing technology has gained considerable interest in material science areas beyond its original functions in graphic output.[1] Compared with traditional processing methods, inkjet printing can achieve direct low-cost writing at large scale with reduced chemical waste through efficient material utilization, and a variety of ink and substrate combinations and hence relatively high flexibility and reproducibility in patterning.[1, 2] Thus, owing to these advantages, inkjet printing has become an additive manufacturing tool in a wide range of areas, such as: displays,[3, 4] bio-applications,[5, 6] and electronic devices[7-9].

Many applications for inkjet printing of functional materials and devices require stability and uniformity of the printed structures. Hence, as a starting point there is a need to understand how a stable parallel line forms. The formation of a stable parallel sided line involves sequential overlap and coalescence of a series of identical liquid drops on a surface to create a liquid bead, which must remain stable until it solidifies by solvent evaporation or phase change. In the case of zero receding contact angle, a critical drop overlap is required to form the stable lines due to the need to conserve volume and maintain the equilibrium contact angle,[10, 11] resulting in the maximum drop spacing. Further reduction in drop spacing leads to a stable parallel line with the line width increasing as the drop spacing reduces, until a critical minimum drop spacing occurs, depending on the ink and substrate conditions, below which a bulging instability forms.[11-13] Various models have been developed to predict the drop spacing range for a stable parallel sided line at various printing conditions including ink rheological properties, advancing contact angle of the ink on the substrate and printing velocities,[12-14] however, the experimental work to validate these models was carried out at relatively low drop generation rates (<1 kHz) with large drop volumes (50–100 pl), due to the limitation of laboratory piezoelectric inkjet drop generators at that time. These conditions are not within the range of most conventional drop on demand (DOD) inkjet equipment, which typically have drop volumes in the range 1 – 30 pL and drop generation rates > 10 kHz. Thus, it's necessary to validate these models at smaller droplet volume to provide guidelines of line stabilities for current researches.

Although zero receding contact angle leading to contact line pinning is a common phenomenon in inkjet printing with particle suspension inks, there are still cases in which inkjet printing may be applied on a substrate with finite receding contact angles.[15, 16] The finite receding contact angle condition can influence the stability of printed lines during both the printing and drying process, and current models to predict line stabilities with zero receding contact angle may not be applicable due to the change of contact line conditions. Thus, an understanding of the stability of printed structures with finite receding contact angle is also important for applications of functional material inkjet printing.[17]

For piezoelectric DOD printing systems, the smallest droplet volume can be achieved is around 1 pL, thereby with deposited diameter around 20 μm.[1] Further reduction in droplet size by reducing the nozzle size is difficult because of the extreme pressure required to overcome the capillary forces,[18] thus limiting the use of inkjet printing method at high resolution applications. With the increasing demand of patterning on surfaces at micrometre and sub-micrometre length scales for electronic applications, electrohydrodynamic (EHD) inkjet printing was developed to achieve direct high resolution printing in arbitrary geometries. For EHD printing, electrostatic force is applied to pull the liquid out of the nozzle tip to form a conical Taylor cone,[19] with sufficient high voltage output, electrostatic stresses exceed the surface tension and droplets are ejected from the tip of the Taylor cone.[18] The new printing method makes it possible to eject droplets of femtolitre size with a wide range of inks (1–10 000 cps).[18] However, few researches have been made to achieve deposition on demand with identical droplet size by EHD printing, and also few researches to give a systematic study of the influence of printing parameters (such as drop spacing, printing velocity, droplet contact angle on the surface, etc.) on the stability of the printed lines at such small scale.

The 'resolution' in this thesis means the feature size of the inkjet printed structures, i.e. diameter of the single deposited dots or width of the printed continuous lines, and we define 'high resolution' for the printed structures with the feature size smaller than 50 μm.

1.2 Thesis Objective and Outline

The main objective of the thesis is to understand the fundamentals of inkjet printed line stability at high resolution. Thus, the work in the thesis involves inkjet printing line structures at a series of droplet sizes from 10 pL to 10 fL, and on a range of substrates.

A summary of the thesis is as follows.

Chapter 1 introduces the background and motivation for the research. The objective and outline of the thesis is also summarized.

Chapter 2 reviews the development of inkjet printing technology, current studies for the fundamentals of inkjet printing processes, and inkjet printed silver tracks.

Chapter 3 describes the experimental materials and methods used in the study, including ink and substrate materials, inkjet printers and printheads, characterization methods and related analysis techniques.

Chapter 4 describes the stability of lines produced by the commercial Dimatix inkjet printer on the substrate with zero receding contact angle. The PDMS coated glass substrate was exposed to UV-Ozone treatment for 30 min to eliminate the receding contact angle. Silver nanoparticle suspensions were printed onto the substrate at a series of printing velocity and drop spacing conditions, with substrate temperature of 28 and 60 °C, droplet size of 8.5 and 1.5 pL, respectively. The stability results were used to verify Stringer's line stability model at smaller droplet scale. The agreements and discrepancies between the results and model predictions were discussed.

Chapter 5 describes the stability of lines produced by a Dimatix inkjet printer on the substrate with finite receding contact angles. UV-Ozone treatment with various time periods was applied to the PDMS coated glass substrate to obtain different receding contact angles. Printing was carried out at a series of printing velocity and drop spacing conditions, with different drop volumes. The experimental results were discussed. A model based on Duineveld's analysis was established to predict the mean wavelength between the bulges of the printed lines. Finally, stabilized line structures were obtained on the substrate with finite receding contact angle by pre-depositing periodic single droplet dots on the substrate first and then printing line structures on them.

Chapter 6 describes the stability and electrical properties of the lines produced by an electrohydrodynamic based Super Inkjet Printer. Deposition on demand printing at ultra high resolution was developed. Printing was carried out onto different substrates with a wide range of printing conditions. The stability results compared with Stringer's line stability predictions were discussed. The electrical properties of the printed line electrodes on different substrates were studied.

Chapter 7 summarizes the conclusions of the thesis, and presents an outline for future work.

Chapter 2 Literature Review

2.1 Inkjet Printing Technology

The beginning of inkjet printing technology can be traced back to 19th century when Felix Savart showed that the breakup of liquid into a series of droplets was controlled by the laws of fluid dynamics in 1833.[20] In 1856, Plateau studied the liquid jets formation from circular nozzles and also pointed out the influence of jet diameter on drop sizes.[21] Later in 1867, Lord William Kelvin patented his Syphon Recorder, which was developed to record telegraph signals by depositing droplets on paper deflected by electrostatic forces.[1] In 1878, Rayleigh produced a model that explained the mechanism for liquid stream breaking up into a series of droplets.[22] After more than half century, inkjet technology was first commercially used by Siemens in chart recorders in 1951.[23] Subsequently, inkjet printing technology was developed for computer graphic output.[1] In more recent years, inkjet printing has gained considerable interest as a patterning tool in a large range of areas beyond its origin in graphics output including: displays,[3, 4] bio-applications,[5, 6] and electronic devices such as thin film transistors,[7-9] sensors,[24, 25] and solar cells.[26-28] Compared with traditional processing methods, inkjet printing can achieve direct writing at a large scale, with a variety of ink and substrate combinations and hence relatively high flexibility and reproducibility in patterning.[1] In addition, the reduced chemical waste through efficient material utilization and a simplified process can contribute to a relatively low cost in production.[2] Thus, inkjet printing has been used with multifarious materials from ceramic components [29-31] to organic materials,[32, 33] nano-materials,[34-36] graphene,[37-39] and biomaterials,[40] for a wide range of applications.

Inkjet printing is conventionally divided into two technologies that are distinguished by different methods for drop generation and placement control. These are known as continuous inkjet (CIJ) printing and drop-on-demand (DOD) inkjet printing.[41] Both techniques can produce droplets with volume size in the range 1 – 500 picolitres (pL).[1] To achieve droplets of smaller volume, electrohydrodynamic (EHD) inkjet printing was developed to produce droplets with volumes < 1 pL. These three printing technologies will be reviewed in this section.

2.1.1 Continuous Inkjet Printing

The first inkjet printer was developed by Sweet in 1965.[42] Subsequently, IBM commercialised the CIJ system in product IBM 4640 printer in 1976.[43] These devices generate a stream of liquid droplets by forcing a liquid under high pressure through a nozzle.[44] The droplets form through the Plateau-Rayleigh instability,[22] and are charged at the nozzle by an electric device (Figure 2-1). The charged droplets can be further deflected by electrostatic deflector plates to achieve controlled deposition on the substrate. The deflected droplets are collected by a gutter and can be recycled for further use. This droplet generation technique is continuous with unwanted droplets discarded, hence the terminology of continuous inkjet printing (CIJ). The high drop velocity of CIJ printing makes its use practical in industrial manufacturing such as for marking and coding. However, the conductivity required for the ink and contamination that may occur during recycling limit the use of CIJ printing in material science researches.[1] CIJ printing generates drops that are similar in diameter to the nozzle. Commercial CIJ printers typically generate drops around 100 μm in diameter (a volume of approximately 400 pL).

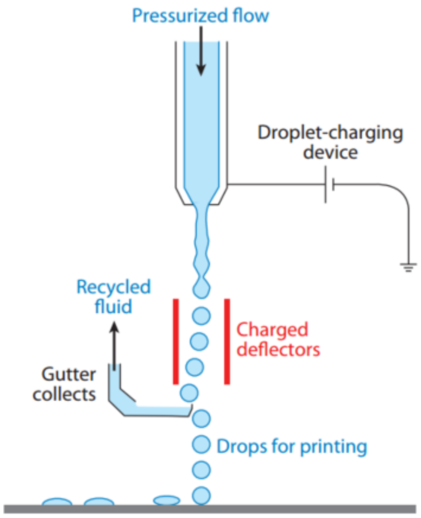

Figure 2-1 Schematic illustration of continuous inkjet printing process. Adapted from Derby.[1]

2.1.2 Drop on Demand Inkjet Printing

Drop on Demand (DOD) inkjet printing was developed at a later date than CIJ. DOD printing generates droplets only when required for printing, hence reducing ink waste and minimising the possibility of contamination. Drops are generated by a pressure pulse only when required, and the accurate deposition of droplets is achieved by precise mechanical movement of either the nozzle or the platform stage. As an electrically conductive ink is no longer required for DOD printing, a wide range of liquids can be applied using this printing technique. In addition, the direct deposition on demand and absence of recycling droplets make DOD system more efficient in ink usage. Based on the mechanism of pressure pulse generation, DOD inkjet printing can be mainly divided into two systems: thermal inkjet printing and piezoelectric inkjet printing.

2.1.2.1 Thermal DOD Inkjet Printing

One of the first thermal DOD inkjet printers was developed by Mark Naiman from the Sperry Rand Corporation in 1965.[45] In thermal DOD printing, a thin film resistive heater is located in the chamber near the nozzle. As current passes through the heater the adjacent ink will be heated up to its boiling point to form a vapour pocket or bubble (shown in Figure 2-2 a). Once heating is removed, the bubble will collapse rapidly. The expansion and collapse of the bubble introduce volume changes and thus the required pressure pulse to generate droplets at the nozzle. The droplet generation process occurs in approximate 10 μs,[45] and the maximum jetting frequency is influenced by the ink properties, with a higher maximum jetting frequency possible as the boiling point of the ink decreases.[46] The low production cost of thermal DOD printheads makes it widely used in desktop printing systems, such as the printers from Canon (FINE Cartridge system) and Hewlett-Packard. Thermal DOD inkjet printing has also been used as a deposition tool in material science research.[47-49] However, the generation of vapour bubbles for droplet ejection limits thermal DOD printing to only use high vapour pressure liquids.[50] The high temperature near the heater within the printhead also limits its applications in printing functional materials, such as heat sensitive polymers.[45]

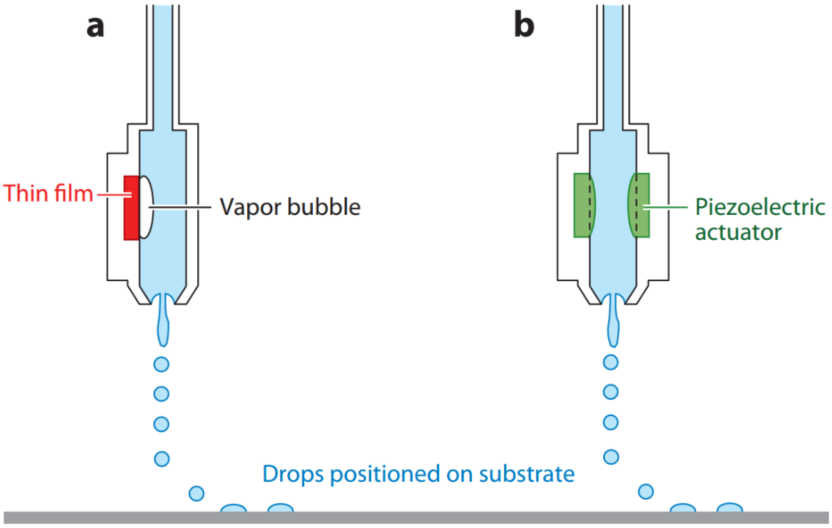

Figure 2-2 Schematic illustrations of operation principles for different DOD printing systems: a) thermal DOD printing and b) piezoelectric inkjet printing. Adapted from Derby.[1]

2.1.2.2 Piezoelectric DOD Inkjet Printing

The first piezoelectric DOD printing system can be traced back to the late 1940s when the Radio Corporation of America developed a fax machine by using mechanical deformation of a piezoelectric disc to generate transient pressure waves.[51] Different from thermal DOD inkjet printing, which uses the generation and collapse of vapour bubble to produce pressure pulses, piezoelectric DOD inkjet printing systems use the mechanical deformation of a piezoelectric actuator in contact with the ink to generate pressure pulses (Figure 2-2 b). This pressure pulse acts to overcome the surface tension of the ink, which typically holds the liquid ink at the orifice of the nozzle. Once the applied pressure exceeds a critical value, the liquid meniscus at the nozzle orifice will deform and ultimately pinch-off into a droplet.[52, 53] According to the different piezoelectric actuation modes, piezoelectric DOD printheads can be divided into squeeze mode, bend mode, push mode and shear mode, as shown in Figure 2-3.

(a) Squeeze mode **(b) Bend mode**

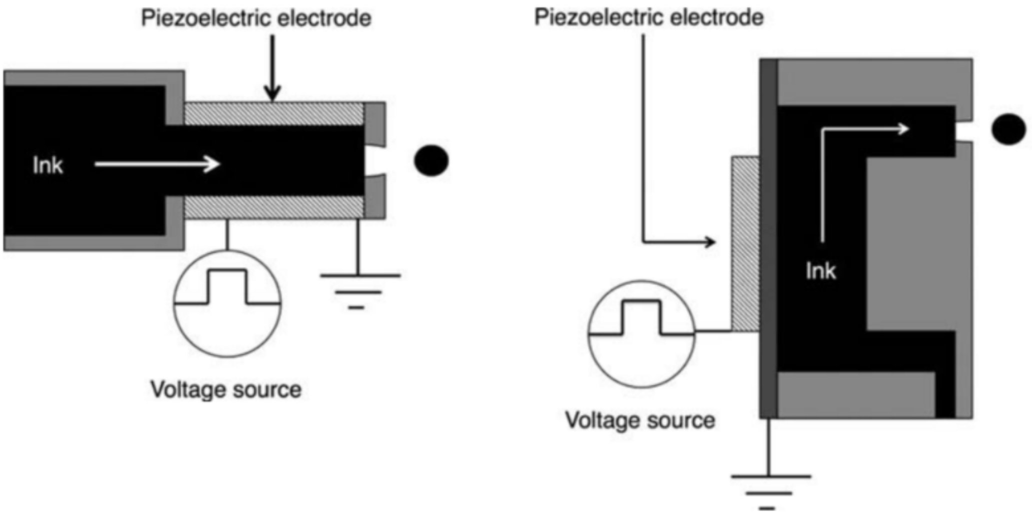

(c) Push mode **(d) Shear mode**

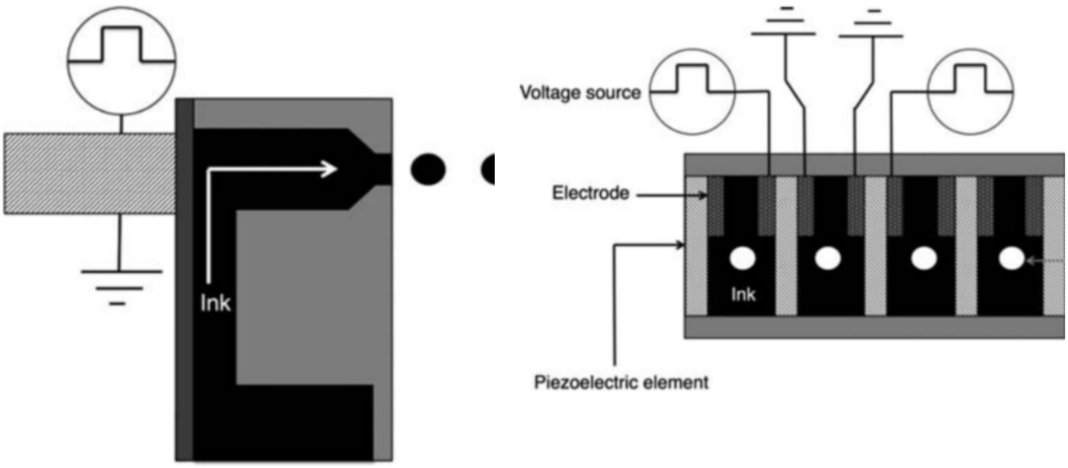

Figure 2-3 Schematics of different modes of piezoelectric DOD printheads: (a) squeeze mode, (b) bend mode, (c) push mode and (d) shear mode. Adapted from Cummins and Desmullie.[45]

During squeeze mode printing, a short rise-time voltage pulse is applied to the piezoelectric tube electrode, as shown in Figure 2-3 a. The contracted electrode will squeeze the ink chamber and eject a droplet out of the nozzle.[54] Squeeze-mode MicroFab printheads have been widely used in the literature for functional material depositions.[55-57] A bend-mode piezoelectric printhead consists of a small ink chamber with an ink supply tube and an opposite nozzle for droplet ejections (Figure 2-3 b). With applied voltage, the actuated piezoelectric electrode causes the chamber wall to bend inwardly, and the reduction of the volume in the chamber generates the pressure pulse for droplet ejection.[58] Bend-mode piezoelectric DOD printing has been used in commercial inkjet printers produced by Epson, Kyocera, Tektronix and Xerox.[45] In the push-mode printing, the expansion of piezoelectric rod electrode by applied voltage pushes the liquid out of the orifice to generate droplets (Figure 2-3 c). Push-mode printheads have been developed by Brother, Epson, Trident and Hitachi.[45] For a shear-mode printhead, the shear deformation of the piezoelectric electrode by the driving voltage signals deforms the upper half of the channels. The lower half of the channels follows the motion of the upper half and the deformation is mirrored.[59] This makes the channel into a chevron shape and droplets are ejected by flexing of the channel (Figure 2-3 d). Shear mode printheads are supplied by Fujifilm Dimatix and Xaar.[45]

Piezoelectric DOD printing has advantages over other printing techniques. The deposition is on demand, with no need for ink recycling, which increase the efficiency of ink usage. It is also a non-contact process, which limits any contamination during fabrication. As no conductivity or volatility requirements for liquids are needed compared with CIJ printing and thermal DOD printing, respectively, piezoelectric DOD printing allows the usage of a wider range of inks. The design of piezoelectric DOD printheads allows precise deposition of picolitre quantities of liquid materials, which can significantly increase the product quality.[60]

Piezoelectric DOD printing is the main printing technology used for materials fabrication in the majority of published work.[61] However, with the increasing demand of patterning on surfaces at micrometre and nanometre length scales for electronic applications, developing new techniques for fabrications at ultra high resolution has become important. For piezoelectric DOD printing systems, the smallest droplet volume that can be achieved is around 1 pL with a consequent deposited diameter around 20 μm.[1] It is difficult to produce smaller droplet sizes by reducing the nozzle size because of the extreme pressure required to overcome the capillary forces.[18] The alternative method for piezoelectric DOD printing to achieve high resolution features is by carefully patterning the substrate in some limited conditions by adjusting surface wettability or using lithography,[62-64] which are more complex and expensive. Thus, an alternative printing technique, electrohydrodynamic inkjet printing, has been developed to achieve direct high resolution printing in arbitrary geometries.

2.1.2.3 Electrohydrodynamic Inkjet Printing

The observation of the electrohydrodynamic process can be traced back to the late 16th century when William Gilbert discovered that a water drop would form into a cone shape and eject droplets at the tip when an electrically charged piece of amber was brought near it.[65] In 1914 John Zeleny studied the behaviour of fluid droplets at the end of metal capillaries.[66] His effort started the researches to mathematically model the behaviour of fluids under electrostatic forces.[67] In the 1960s Taylor studied the droplet ejection behaviour from a liquid nozzle under electrostatic force and mathematically modelled the shape of the resulting (Taylor) cone.[19] The use of electrostatic force on liquids in material fabrication can be divided into three categories: the electrospray process to generate films or designed patterns,[68-70] the electrospinning process to generate polymer fibres,[71-73] and electrohydrodynamic (EHD) drop ejection, exploited as an inkjet printing process, to achieve precise deposition of functional materials.[74-76]

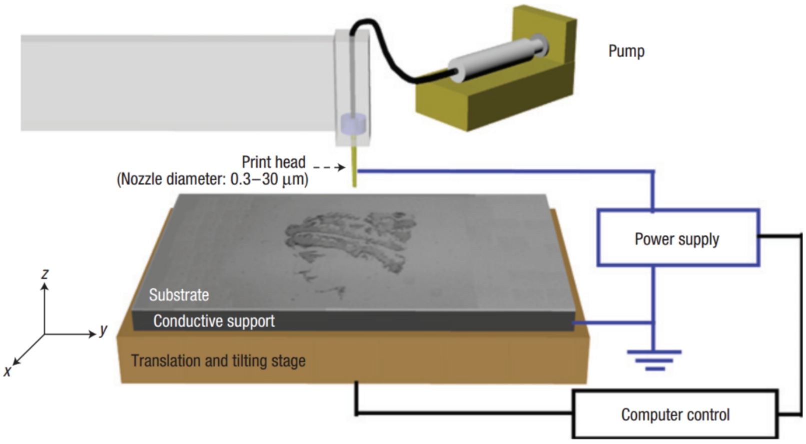

Figure 2-4 Schematic illustration of an EHD printing system. Adapted from Park.[74]

For electrohydrodynamic (EHD) inkjet printing, a voltage supply is applied between the nozzle and the conductive substrate support to generate an electrostatic force for droplet ejection, as shown in Figure 2-4. The nozzle is typically fabricated by pulling glass capillaries, with inner diameter typically from < 1 μm to 10 μm and coating them with a thin conductive layer of metal.[18, 74] A syringe pump is connected to the nozzle to deliver the ink to the nozzle tips at a fixed rate. Under electric field, the mobile ions in the ink are accumulated to the regions near the liquid/air interface. The meniscus will deform due to columbic repulsion between these ions and finally form into a conical shape known as a Taylor cone [19] (Figure 2-5). With sufficiently high voltage output, electrostatic stresses exceed the surface tension and droplets are ejected from the tip of the Taylor cone.[18] The liquid does not need to be very conductive, even very small ion concentrations are sufficient for droplet generation.[74] For example, Jayasinghe showed that droplet ejection is still possible for liquids with conductivity of 10^{-13} Sm^{-1}.[77]

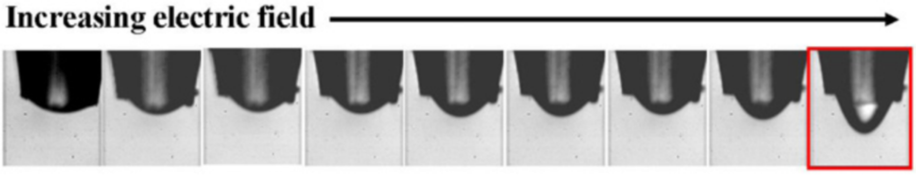

Figure 2-5 The meniscus changes of the fluid at the nozzle tip with increasing voltage potential between the nozzle tip and the substrate. Adapted from Mishra et al.[78]

For both CIJ and DOD inkjet printing, the nozzle size plays an important role in determining the ejected droplet volume. With a much smaller scale of nozzle diameter, EHD printing would be expected to generate smaller droplets than thermal/piezoelectric DOD printing. In addition, as droplets are ejected from the tip of the Taylor cone, the droplet volume is smaller still and femtolitre size droplets are produced. Thus, EHD printing can achieve direct patterning at ultra-high resolution in arbitrary geometries.[74]

In practice, the physics of drop ejection during EHD inkjet printing is far more complex than this brief summary, with numbers of factors influencing the jetting behaviour such as ink rheological properties, substrate conductivity, pressure from the syringe pump, and applied voltage, etc.[79] Thus, careful ink and process developments are required to achieve controllable DOD deposition by EHD inkjet printing. The objective of this project is to investigate the stability and resolution control of inkjet printed silver tracks produced both by piezoelectric DOD printing and EHD printing.

2.2 Inkjet Printing Droplet Generation

DOD inkjet printing process can be divided into five stages: drop ejection, drop flight, drop impact, drop spreading and drop solidification.[80] As the mechanisms of droplet generation for piezoelectric DOD printing and EHD printing are different, the droplet generation process (drop ejection and flight) will be reviewed separately for both printing techniques in this section.

2.2.1 Piezoelectric DOD Printing Droplet Generation

Figure 2-6 illustrates a typical droplet formation process from a piezoelectric DOD printhead. When a voltage is applied to the actuator it displaces fluid and generates a pressure wave that ejects a column of liquid out of the nozzle. The initial liquid column then deforms under capillary forces into a shape of a leading droplet followed by an elongated tail or ligament that detaches from the remaining liquid column. The ligament shrinks and will either retract back into the leading drop or rupture to form small satellite droplets behind the leading drop. The satellite drops may catch up and merge with the front drop in flight to form a stable droplet, such as the one shown in Figure 2-6. However, if the satellite drops still exist when the leading drop impacts on the substrate, they will lead to noncircular deposition, influencing the printing precision, resolution, and accuracy.[1] Thus, the presence of satellite drops are deleterious and should be avoided in most applications. The stable droplet formation is influenced by a variety of factors, including: fluid properties, waveform design, and nozzle geometry.[81-83]

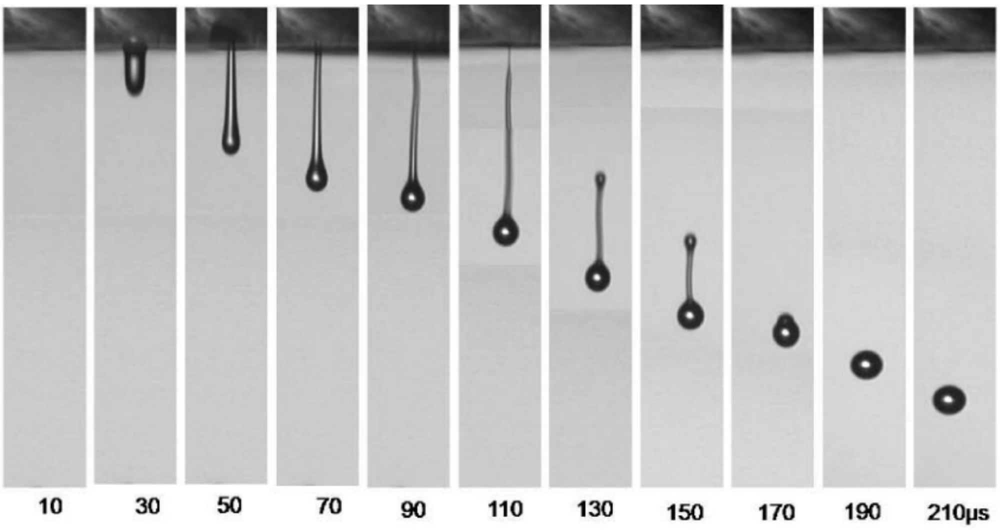

Figure 2-6 Drop formation process for fluid (66% glycerol and 33% water) with a dimensionless Z value of 3.57. Reproduced from Jang et al.[81]

2.2.1.1 Printable Fluid Properties

The most important parameters that determine ink printability are the fluid rheology properties such as viscosity, surface tension and density.[81] These parameters are crucial for jettability as well as the presence or absence of satellite drops and deposited droplet spreading behaviour on the substrate.[45] A high viscosity will lead to energy dissipation and hinder the propagation of the applied pressure wave within the nozzle, and thus a reduced pressure pulse at the nozzle to overcome the meniscus forces to form a droplet, while a low viscosity usually results in satellite formation and residual pressure wave interaction between droplets.[82] Generally, for Newtonian inks with constant viscosity, the recommended viscosities for printable fluids should be within the range of 1 – 25 mPa·s.[45] For non-Newtonian inks with shear rate dependent viscosities, the viscosities at high shear rate (> 1000 s^{-1}) should be considered because the working frequency for DOD printing is typically in the range of 1 – 20 kHz.[1] Similarly, if the surface tension of the fluid is high, the strength of pressure pulse needed to overcome meniscus forces and form a drop is large. At low values, the liquid cannot be held at the nozzle by surface tension when printing is not needed and unwanted dripping can occur.[45] Thus the surface tension values suitable for inkjet printing are recommended in the range of 25 – 50 mNm^{-1}.[45]

The influence of fluid rheology properties and nozzle diameter on droplet ejection behaviour can be characterized by three main dimensionless physical parameters, which are the Reynolds (*Re*), Weber (*We*) and Ohnesorge (*Oh*) numbers.[1] The Reynolds number is the ratio between the inertial forces and the viscous forces and can be expressed as:

$$Re = \frac{v\rho a}{\eta} \qquad (2-1)$$

where v, ρ, a, and η are the drop velocity, fluid density, characteristic length (generally the nozzle diameter [1, 84]), and fluid dynamic viscosity, respectively. The Weber number is defined as the ratio of the inertial forces to the surface tension forces:

$$We = \frac{v^2 \rho a}{\gamma} \qquad (2-2)$$

where γ is the surface tension of the fluid. The Ohnesorge number is a combination of the viscous forces, surface tension and inertial forces, and describes droplet formation:[85]

$$Oh = \frac{\sqrt{We}}{Re} = \frac{\eta}{(\gamma \rho a)^{1/2}} \qquad (2-3)$$

The Ohnesorge number is independent of fluid velocity and is often used in the literature concerning drop formation by a number of mechanisms. Fromm established the earliest significant study on droplet generation using these dimensionless constants.[86] He used a dimensionless number Z, which is the reciprocal of the Ohnesorge number, to characterize droplet formation and proposed $Z > 2$ for stable droplet generation. Reis and Derby [87] further refined this analysis by numerical simulations and proposed that the range of fluid properties, $1 < Z < 10$, described the conditions for stable droplet generation. This hypothesis has been supported by a number of experimental studies of drop formation in DOD inkjet printing, albeit with slightly different limiting bounds in each publication.[31, 81]

Apart from Z number, another factor that influences the drop formation process is the energy required to overcome the fluid/air surface tension for droplet ejection at the nozzle.[1] This leads to a minimum velocity required for droplet ejection:[84]

$$v_{\min} = (\frac{4\gamma}{\rho a})^{1/2} \qquad (2-4)$$

By substituting v with v_{min} in Equation 2 – 2, a minimum Weber number can be derived for droplet generation:

$$We = \frac{v^2 \rho a}{\gamma} > \frac{v_{\min}^2 \rho a}{\gamma} = 4 \qquad (2-5)$$

In addition, the impact of the ejected drop on a substrate should also be considered for the ink printability. If the drop velocity exceeds a critical value, the onset of splashing would occur. Stow and Hadfield [88] first presented an experimental threshold for the onset of splashing using the above dimensionless constants:

$$We^{1/2} Re^{1/2} > f(R) \qquad (2-6)$$

where $f(R)$ is a function of surface roughness, and further research proposed $f(R) \approx 50$ for flat, smooth surfaces.[89] With the thresholds defined from Equation 2-4 to 2-6 and the range of Z number, Derby constructed a map with Weber and Reynolds number as coordinates to define the suitability of fluid properties for DOD inkjet printing,[1] as shown in Figure 2-7. Typically for Newtonian fluids, with $Z < 1$ drop ejection is hindered by the large critical threshold energy required, while with $Z > 10$ satellite drops together with the leading drop are formed. The map gives a useful guild for ink properties selection for Newtonian fluids.[2, 81]

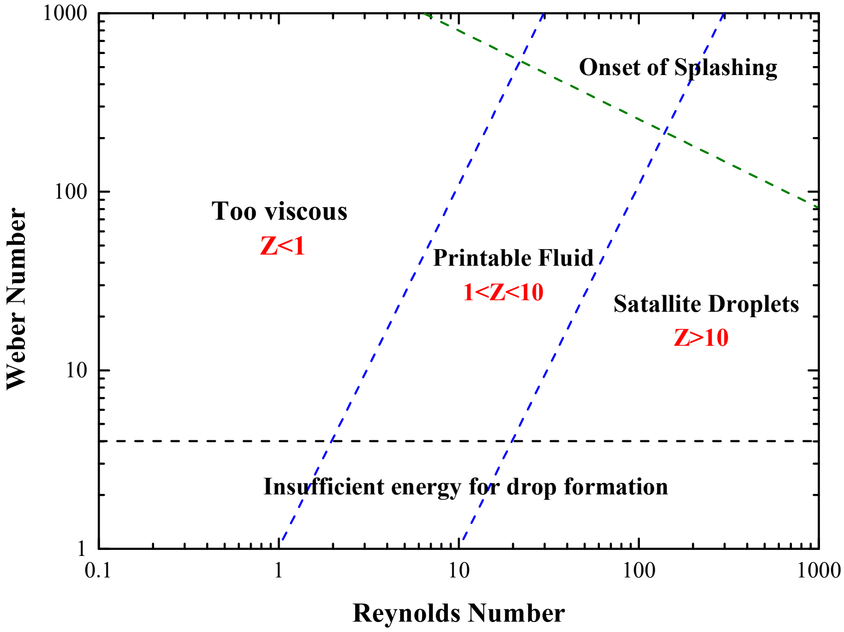

Figure 2-7 A map illustrating the influence of fluid properties on the printability for DOD inkjet printing with Weber and Reynolds number as coordinates. Adapted and corrected from Derby.[1]

Various studies have been made to investigate the influence of Z number on the fluid printability. Jang et al. [81] experimentally studied the printing behaviour of various mixture solvents by a squeeze mode Microfab printhead, and defined the printable range of Z as $4 \leq Z \leq 14$ considering single droplet formability, positional accuracy, and maximum allowable jetting frequency. Liu and Derby [31] investigated the drop formation dynamics of Newtonian fluids using a shear mode Dimatix printhead and suggested that the practical range of Z and We for ink printability are $2 < Z < 20$ and $2 < We < 25$, respectively.

The above studies are carried out with Newtonian fluids. However, for printing fluids with non-Newtonian behaviours such as polymer solutions and concentrated particle suspensions, of which the dynamic viscosity is non-linear and shear rate dependent, the printability of fluid rheological properties shown in Figure 2-7 may be further modified.[1] Reports have shown that for the inks with a low concentration of polymer, the ejected fluid ligament can be stabilized and will retract into the leading drop during flight rather than break up into a train of satellite droplets,[90] which allows the printability of inks with Z larger than 10. With increasing polymer molecular weight and concentration, the tails are found to be longer and more stable, and above a critical value the tail will not rupture to form an individual droplet.[91]

2.2.1.2 Waveform Influence

Besides the ink rheological properties, the applied waveform is another important factor that determines the jetting behaviour of piezoelectric DOD inkjet printing. The waveform shape, driving voltage, and pulse width can each significantly influence the droplet generation process.[82] Many researchers have studied the relationship between droplet formation and the behaviour of piezoelectric actuator.[92-94] Bogy and Talke [92] proposed that, for a squeeze mode printhead and single trapezoidal waveform, the pressure at the nozzle is related to the propagation and reflection of the acoustic waves in the printhead, which is caused by the expansion and contraction of the piezoelectric actuator, as shown in Figure 2-8. The dwell time of applied voltage influences the interference conditions between the acoustic waves. With dwell time of L/C, where L is the length of the chamber and C is the speed of sound in the fluid, the positive wave generated by the contraction of the actuator can superimpose with the previous waves at the middle of the chamber to cancel the wave opposite to nozzle and amplify the wave towards the nozzle.[92] Thus any changes in dwell time from the efficient dwell time (L/C) will lead to the acoustic waves out of phase, influencing the jetting behaviour. Kwon [95] suggested that a 20 – 30% longer dwell time compared with the efficient dwell time could reduce the ligament length and suppress satellite formation. For fluids with higher Z numbers, longer dwell time will also increase the speed of satellite drops and reduce the distance between the satellite and the main drop, leading to stable droplet formation. The influence of jetting frequency on drop formation is similar to that of the pulse dwell time. With fixed waveform shape, the adaption of jetting frequency will change the parameters of T_{rise}, T_{dwell} and T_{fall}, altering the drop velocity and jetting behaviour. Thus, there is an upper limit on the jetting frequency for the acoustic wave interference to exist, which is determined by the time required for droplet separation.[92]

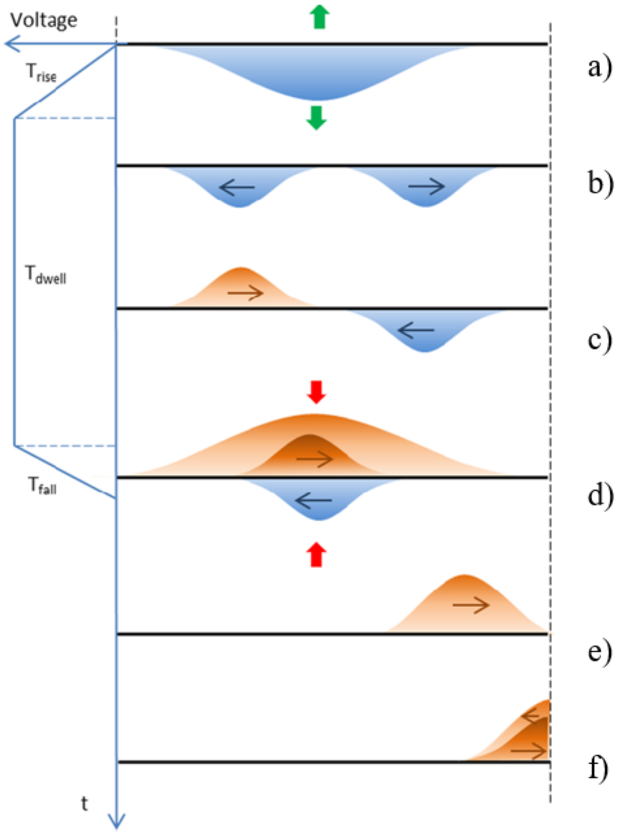

Figure 2-8 Pressure wave propagation and reflections in a squeeze mode printhead: a) negative pressure wave generated by the expansion of PZT, b) pressure wave propagates during voltage dwell time, c) Reflection of acoustic wave from nozzle and reservoir during dwell time, d) positive acoustic wave superimposes with the previous waves to reinforce wave to nozzle and cancel the wave to reservoir due to PZT contraction, e) and f) positive acoustic wave travels to the nozzle to generate a droplet. Adapted from Liu.[93]

The applied dwell voltage (or pulse amplitude) also affects the formation of the droplet as well as its volume and velocity.[96] A higher dwell voltage will increase the amplitude of the acoustic waves in the chamber, leading to a larger pressure pulse at the nozzle and thus an increase in droplet volume. This can also introduce satellite drops as the pulse amplitude exceeds critical values. On the contrary, a lower dwell voltage will lead to a smaller ejected droplet volume. With the applied voltage below the threshold voltage, droplet formation will be prevented due to insufficient energy to overcome the capillary effect of the meniscus.[31]

Various studies have been undertaken to study the effect of waveform shapes on the droplet formation. Chen and Basaran used a waveform with three square pulses to suppress satellite droplets by the second negative voltage.[97] Shin et al. [98] applied a double waveform with two square pulses to eliminate satellite drops for low viscosity fluids. Gan et al. [99] studied the influence of waveforms, including unipolar, bipolar, *W* shaped, and *M* shaped waveforms, in droplet volume reduction. He suggested the use of a bipolar waveform for Newtonian or near Newtonian fluids due to the waveform simplicity and printing quality, and M- or W- shaped waveforms with suitable parameters for non-Newtonian fluids to significantly reduce droplet volume.

In summary, the printability of the ink for piezoelectric DOD system is influenced by a combination of fluid rheological properties, nozzle geometry and waveform design including waveform shape, applied voltage, pulse time and frequency.

2.2.2 EHD Printing Droplet Generation

Different from piezoelectric DOD inkjet printing, that uses actuation pulses for droplet generation, electrohydrodynamic (EHD) inkjet printing applies an electric field between the nozzle tip and the substrate to generate an electrostatic force for droplet ejection. The fluid meniscus at the nozzle tip deforms under the electric field, and is balanced by three main forces for a static Taylor cone, which are the hydrodynamic force (F_h) to supply fluid to the meniscus, the capillary force (F_γ) to hold the droplets on the capillary tip, and the electrostatic force (F_E) for droplet ejection,[100] as shown in Figure 2-9. Charges are accumulated at the apex of the deformed cone under electric field, and lead to the electric normal stress ($F_{e,n}$) and electric tangential stress ($F_{e,t}$).[100, 101] Both stresses have significant influences on the jetting behaviour of the cone.

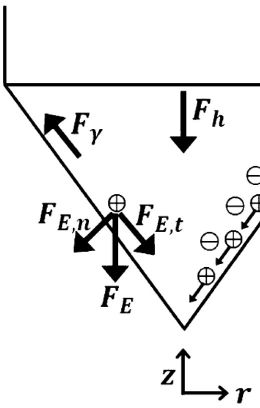

Figure 2-9 Forces on the deformed fluid meniscus. S, L, and G represents the solid, liquid and gas phase, respectively. Adapted from Lee.[100]

The jetting behaviour of EHD inkjet printing is affected by a variety of parameters, the most important of which are fluid properties such as density, surface tension, viscosity, conductivity and permittivity, nozzle diameter, distance between nozzle and substrate electrode, supplied flow rate and applied voltage.[100] Thus, droplet generation for EHD inkjet printing is a complex process and an understanding of it is a starting point to achieve uniform, controllable high resolution printing.

2.2.2.1 Modes of Jetting

The strength of the local electric field and flow rate leads to different modes of jetting. As shown in Figure 2-10, at low electric field and flow rate, dripping mode can be achieved with large droplets generated from the end of the nozzle associated with gravitational forces.[102] An increase in electric field or flow rate will lead to pulsed jets of liquid droplets by repeated Taylor cone formation and relaxation. The pulsating mode can be achieved either by applying flow rates smaller than the minimum flow rate (Q_m) required for the steady Taylor cone-jet, or by applying an electric field smaller than the critical value when the flow rate is larger than Q_m.[103] With further increased electric field, the cone jet mode can be realized with a continuous stream of liquid jetting from the apex of the consistent Taylor cone. A much higher electric field will result in complex jetting behaviours such as tilted jet mode or multi-jet mode.[100]

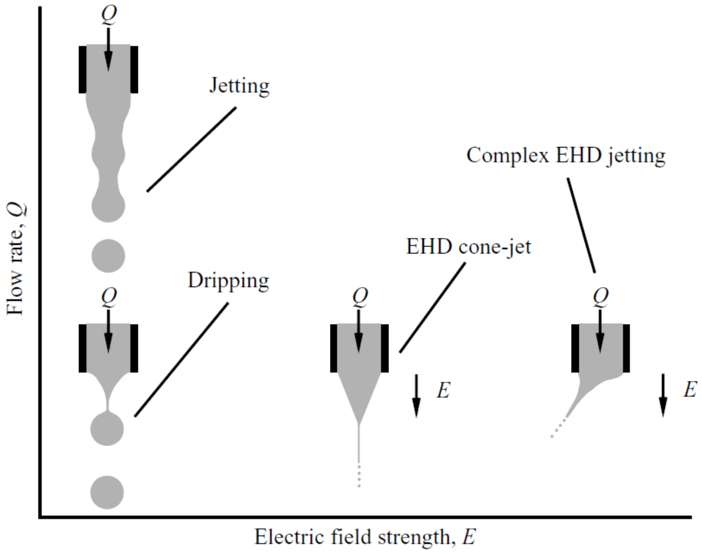

Figure 2-10 Modes of jetting for EHD printing system with electric field and flow rate variations. Adapted from Collins et al.[102]

Pulsating mode and cone jet mode are two main jetting modes used to achieve stable, high-resolution EHD printing. Thus, an understanding of parameter influences on determining different modes of jetting is critical to achieve optimum printing.[18] Various studies have been undertaken to investigate the jetting performance of different modes and the onset Taylor cone behaviour experimentally and mathematically.[71, 100, 104-106] Lee et al. [100] systematically studied the jetting behaviour of ethanol and terpineol mixtures by applying six dimensionless parameters, among which the dimensionless flow rate α and voltage β are used to distinguish the jetting behaviours, as shown in Figure 2-11. The dimensionless flow rate α is defined as the ratio of supplied flow rate (Q_s) and critical flow rate (Q_c), and the dimensionless voltage β is defined as the ratio between applied voltage (V_a) and critical voltage (V_c). Q_c is the minimum flow rate required for cone-jet formation, and V_c is the minimum voltage that supports the meniscus on the nozzle of diameter d. The Q_c and V_c can be expressed as:

$$Q_c = \frac{\gamma \varepsilon_0 \varepsilon'}{\rho K} \qquad (2-7)$$

$$V_c = \sqrt{\frac{\gamma d}{\varepsilon_0}} \qquad (2-8)$$

where γ is the fluid surface tension, ρ is the fluid density, ε_0 is the permittivity of free space, ε' is the permittivity of the fluid, K is the conductivity, and d is the nozzle diameter.

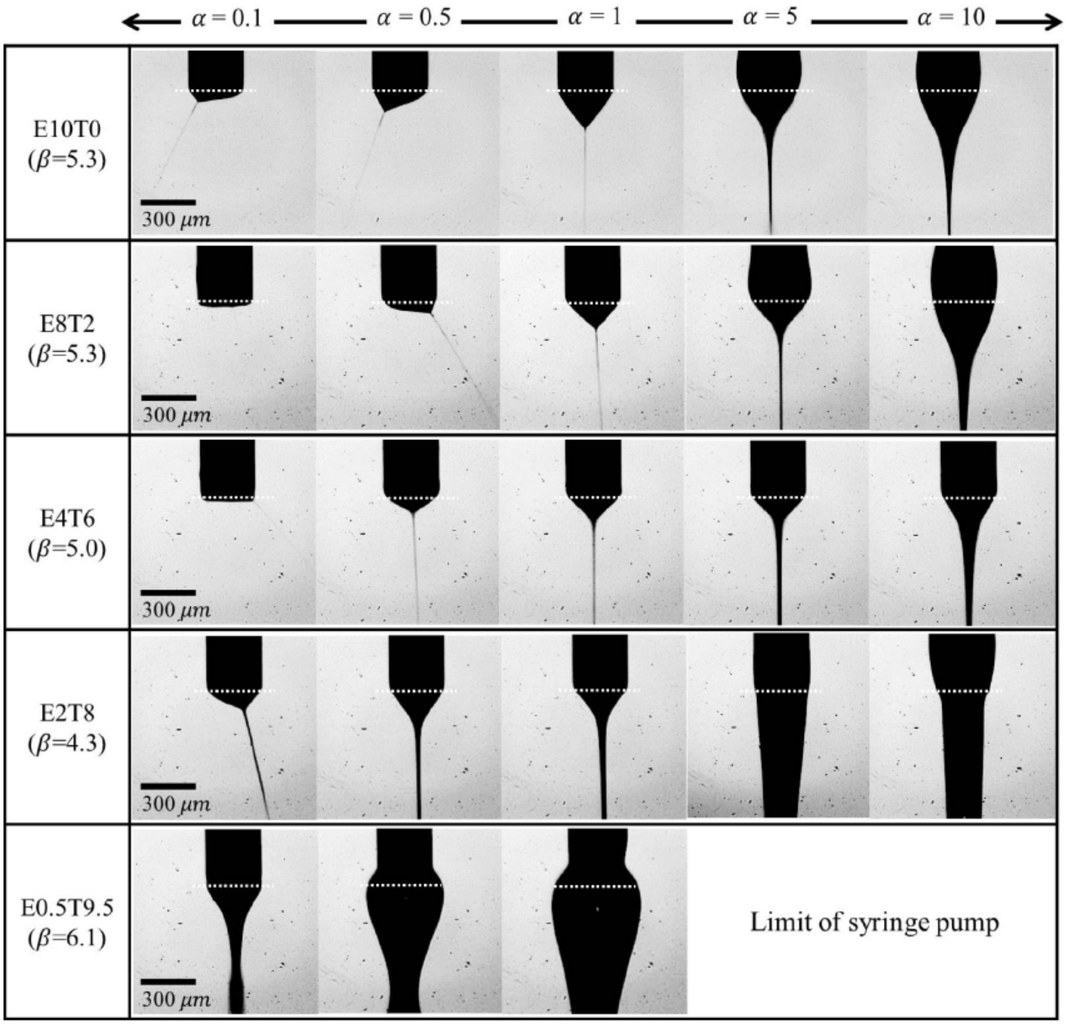

Figure 2-11 Jetting behaviours of ethanol and terpineol mixtures as a function of dimensionless flow rate (α) and voltage (β). For example, E8T2 represents the mixture of 80% ethanol and 20% terpineol in volume. Adapted from Lee et al.[100]

The images shown above can be used to construct a map determining the regimes of jetting modes with dimensionless flow rate and voltage as coordinates, as shown in Figure 2-12. This approach was an effective way to evaluate jetting stabilities and thus choose optimum parameters for printing. Yu et al. [107] applied similar method to investigate the influence of viscoelasticity on jetting behaviours of Taylor cone.

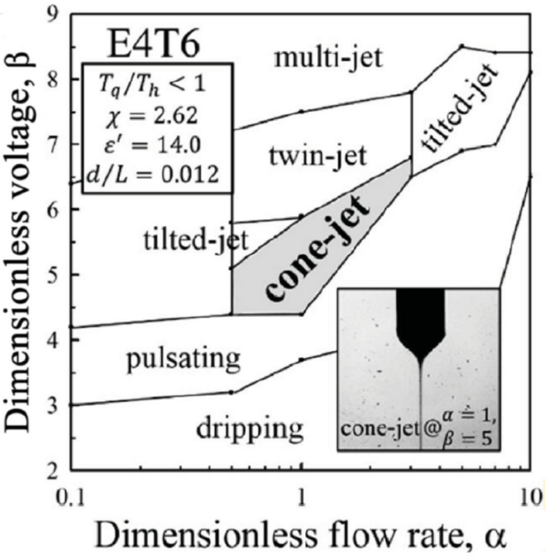

Figure 2-12 A map showing modes of jetting for the mixture of 40% ethanol and 60% terpineol in volume with dimensionless flow rate and voltage as coordinates. Adapted from Lee et al.[100]

2.2.2.2 EHD Printing on Demand

Using EHD printing to deposit droplets on demand has received considerable interest, as it can achieve uniform, stable and precise deposition of individual droplets. Pulsating mode and pulsed cone jet mode are typically applied to achieve DOD printing.

a) Pulsating Mode

Pulsating mode relates the use of the intrinsic natural frequency of the jetting to generate droplets. Pulsating jets occur due to the imbalance between the supply and loss of fluid, and the natural frequency strongly depends on flow rate and electric field.[108] Thus, an understanding of the scaling laws for the pulsating mode is important to characterize the intrinsic frequency and control deposited droplet size. The jetting flow rate is critical in determining the deposited droplet size for both printing modes. It relates the balance between electric stress, applied pressure and capillary pressure, and can be estimated using a Poiseuille-type relation:[79]

$$Q \approx \frac{\pi d_N^4}{128\mu L}\left(\frac{1}{2}\varepsilon_0 E^2 + \Delta P - \frac{2\gamma}{d_N}\right) \qquad (2-9)$$

where d_N and L are the inner diameter and length of the nozzle, μ is the fluid viscosity, ε_0 is the vacuum permittivity, E is the strength of applied electric field, ΔP is the applied hydrostatic pressure, and γ is the surface tension of the fluid. The electric field strength at the nozzle tip can be estimated by using a model of a semi-infinite wire perpendicular to an infinite planar counter electrode:[109, 110]

$$E = \frac{4V_0}{d_N \ln(\frac{8H}{d_N})} \qquad (2-10)$$

where V_0 is the applied voltage and H is the nozzle to substrate distance.

Chen et al. [79] derived a scale analysis for the jetting flow rate and intrinsic pulsating frequency corresponding to a high-frequency mode, and found that the intrinsic pulsating frequency f scales with E^2. The analysis was further investigated by experimentally studying the jetting behaviour of water using a Teflon nozzle with inner diameter of 50 μm and length 30 mm, as shown in Figure 2-13. Choi et al. [110] presented scaling laws showing the intrinsic pulsation frequency to be proportional to the electric field strength to the power of 1.5, and validated the analysis with experiment results using a nozzle with an inner diameter of 30 μm along with the data from literature.

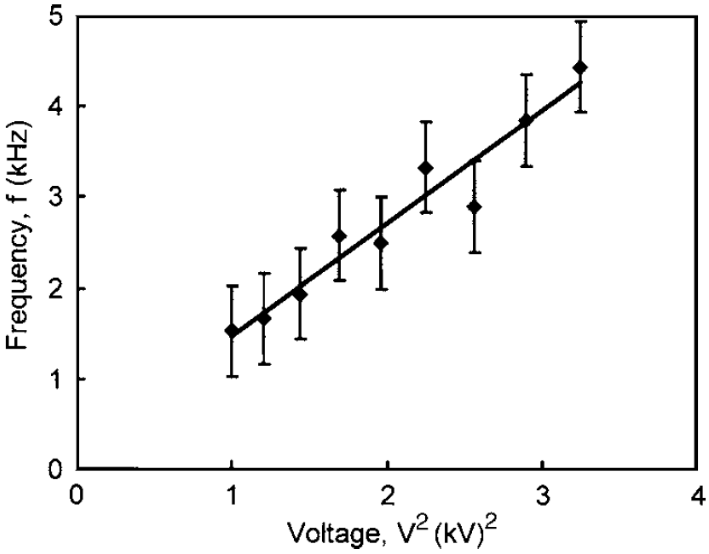

Figure 2-13 The relationship between intrinsic pulsation frequency and applied voltage with d_N of 50 μm, L of 30 mm, and H of 110 μm. Reproduced from Chen et al.[79]

By obtaining the jetting flow rate and the intrinsic pulsating frequency, the scale of deposited features on the substrate can be estimated, which is important for choosing parameters to achieve optimum printing on demand. However, the limitation of using intrinsic pulsating frequency to achieve drop on demand EHD printing is also obvious. The ejected droplet diameter and jetting frequency are both influenced by the electric field, thus it is impossible to change one parameter and maintain the other by adjusting the applied voltage, which limits the control of sizes of deposited droplets. In addition, for pulsating mode with a constant voltage difference between the nozzle and the substrate, the jetting performance is quite sensitive to the nozzle to substrate distance *H*, and any small deviations of *H* would lead to significant changes in the deposited structures.[78]

b) Pulsed Cone Jet Mode

Pulsed cone jet EHD printing is developed to achieve DOD deposition with controllable jetting frequency and droplet size by the use of a pulsed electric field.[111-114] The design of the pulse voltage and time is important to achieve stable printing on demand beyond intrinsic jetting.[18] An electrical setup with a pulsed high voltage superimposed with a low bias voltage is suitable to achieve such printing requirements, as shown in Figure 2-14. The pulse width determines the deposited droplet volume per pulse, while the duration between two successive pulses controls the deposition frequency, and drop spacing for a constant print velocity.[78] The bias voltage, or baseline voltage should be large enough to maintain the formation of a Taylor cone at the tip of the nozzle during printing, and should also be low enough to avoid jetting at this voltage.[78] When the pulse peak voltage exceeds the threshold voltage, ejection of droplets on demand can be achieved.

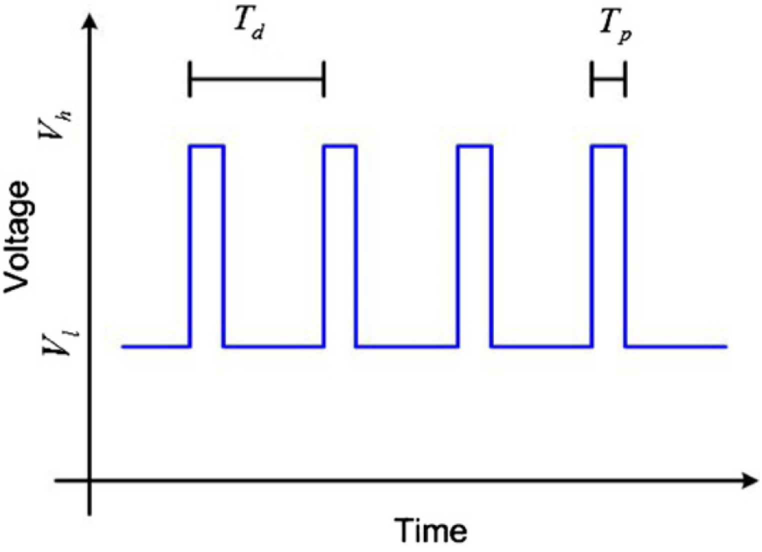

Figure 2-14 Schematic of voltage profile with time for pulsed EHD printing. T_d denotes the time between two adjacent pulses, and T_p denotes the pulse width. V_h and V_l are the high and low voltages, respectively. Adapted from Mishra et al.[78]

The applied voltage V_h and V_l and pulse width time T_p determine the stability of the pulsed cone jet. The pulse width time should be sufficiently long enough to allow meniscus deformation and droplet ejection, a small pulse width time below a critical value could lead to no jetting or other modes of jetting. Such phenomenon was observed by Li [106] when he studied the influence of pulse voltage on the deformation of a meniscus using ethanol as the jetting liquid. He pointed out that the formation of pulsating mode or cone jet mode requires sufficient time for the meniscus to develop, and a short pulse width time leads to a dripping mode regardless of applied peak voltage. With increased pulse width time, both bias voltage and pulse peak voltage influence the tangential electrical stress on the cone surface, which contributes to the deformation of the Taylor cone and the onset of jetting. Pulsed cone jet behaviour can be achieved by applying a high bias voltage and a high pulse peak voltage.[106]

The frequency for pulsed cone jet mode can be varied by adjusting the time, T_d, between successive pulses. With fixed ratio between T_p and T_d, which is also called the duty ratio, the pulse width time T_p decreases with increasing frequency. Thus, there is an upper frequency limit for printing determined by the minimum pulse width time. Higher pulsed voltage frequency might lead to a reduction in drop generation frequency due to insufficient fluid relaxation time, causing uncontrolled drop on demand printing,[112, 115] as shown in Figure 2-15. Hence a small minimum pulse width time, to ensure a stable pulsed cone jet, is important to achieve high frequency printing.

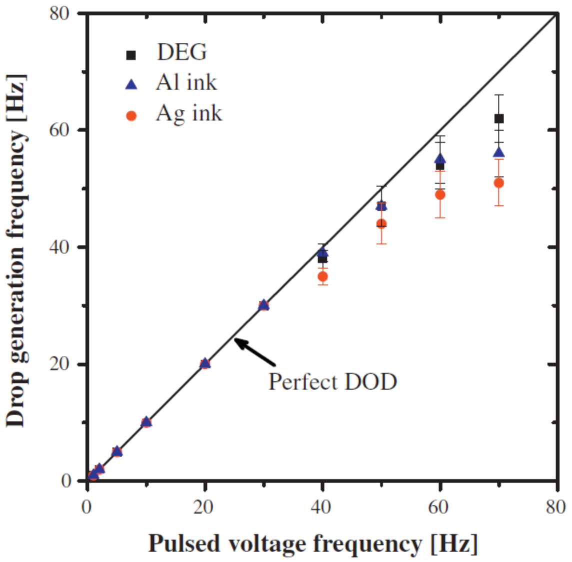

Figure 2-15 Relationship between pulsed voltage frequency and drop generation frequency. DEG relates the ink of Al particles dispersed in diethylene glycol (DEG). Adapted from Lee et al.[102]

By carefully design the parameters of voltage and pulse time, stable drop on demand printing can be achieved by a pulsed cone jet mode. The ejected droplet volume per pulse can be estimated using the jetting flow rate, Q, multiplied by the pulse width time, T_p. Thus, the scale of deposited droplets and lines can also be modelled by the ejected droplet volume, jetting frequency, print velocity and contact angle. The droplet deposition behaviour of piezoelectric DOD printing and EHD pulsed cone jet DOD printing will be reviewed in the next section.

2.3 Inkjet Printing Droplet Deposition and Solidification

After droplet generation from the nozzle, the next processes for DOD inkjet printing are droplet deposition and solidification. The droplet deposition process involves drop impact and spreading on the substrate, and droplet solidification is the final step to achieve desired structures. As the mechanisms of droplet generation for piezoelectric DOD printing and EHD DOD printing are different, the droplet deposition process for both systems also has significant differences.

2.3.1 Piezoelectric DOD Printing Droplet Deposition

The impact behaviour of a liquid droplet on the solid surface is influenced by three main forces: inertial forces, capillary forces, and gravitational forces.[1] The Bond number is used to determine the relative influence of gravitational and capillary forces on droplets,

$$B_0 = \frac{\rho g a^2}{\gamma} \qquad (2-11)$$

where g is the acceleration of gravity. For DOD printing process the Bond number is approximately 10^{-2} to 10^{-3},[11] hence gravitational forces can be neglected.

With piezoelectric DOD printing the initial impact of a droplet on the substrate is driven by the kinetic energy with a duration of less than 1 μs.[45] The droplet spreads and recoils, and the oscillation is dissipated by viscous forces within a small timescale. At a longer timescale capillary forces become dominant, and at a time range of 0.1 – 1 ms capillarity starts to fully control the spreading behaviour of the droplet.[1, 116] Spreading continues till the droplet reaches an equilibrium diameter determined by the surface energy between the ink and the substrate within tens of milliseconds.[1, 116]

The dimensionless group of parameters such as the Reynolds, Weber, and Ohnesorge numbers can be used to determine whether "Impact Driven" or "Capillarity Driven" is dominant in the drop deposition process.[45] Schiaffino & Sonin proposed that at high Weber numbers the droplet is pushed radially outwards by the impact due to inertial forces, while at low Weber numbers spreading due to capillarity is dominant.[117] The Ohnesorge number can be used to characterise the resistance to spreading of the droplet, with high numbers the resistive force dominated by viscosity while low numbers dominated by inertial forces.[117] For the droplet generated from DOD system with a diameter less than 100 μm, spreading due to capillarity is dominant. With negligible influence of gravitational forces, the equilibrium shape of the deposited droplet on the substrate appears as a spherical cap, and the wetting of the droplet can be characterised by the contact angle between the droplet and the substrate, which can be calculated using Young's equation,[118]

$$\cos\theta = \frac{\gamma_{SA} - \gamma_{SL}}{\gamma_{LA}} \qquad (2-12)$$

where θ is the contact angle, γ_{SA} is the solid surface energy, γ_{SL} is the solid/liquid interfacial energy, and γ_{LA} is the liquid surface tension. Assuming volume conservation between the ejected droplet and the spherical cap, the diameter of the final spread drop d_{eqm} is determined by the ejected droplet size and the equilibrium contact angle:[11]

$$d_{eqm} = d_0 \sqrt[3]{\frac{8}{\tan\frac{\theta}{2}(3+\tan^2\frac{\theta}{2})}} \qquad (2-13)$$

where d_0 is the diameter of the initial ejected droplet in flight. Thus, the resolution of piezoelectric DOD printing is controlled by the diameter of the impacting droplet in flight and the contact angle, with a smaller spread drop diameter (increased resolution) as the contact angle increases.[1]

2.3.2 EHD DOD Printing Droplet Deposition

For pulsed cone jet EHD printing system, a stream of liquid from the apex of the Taylor cone is ejected onto the substrate within the applied pulse period to form the desired droplet on demand.[78] Thus, a uniform deposited droplet on demand requires both the liquid ejection from the cone and coalescence of fluid on the substrate to be stable. This relates the choose of appropriate parameters such as applied voltage, nozzle to substrate distance and ink conductivity etc. With unsuitable parameters the droplet deposition would lead to atomization problems, which could influence the stability and uniformity of the deposited features, as shown in Figure 2-16.

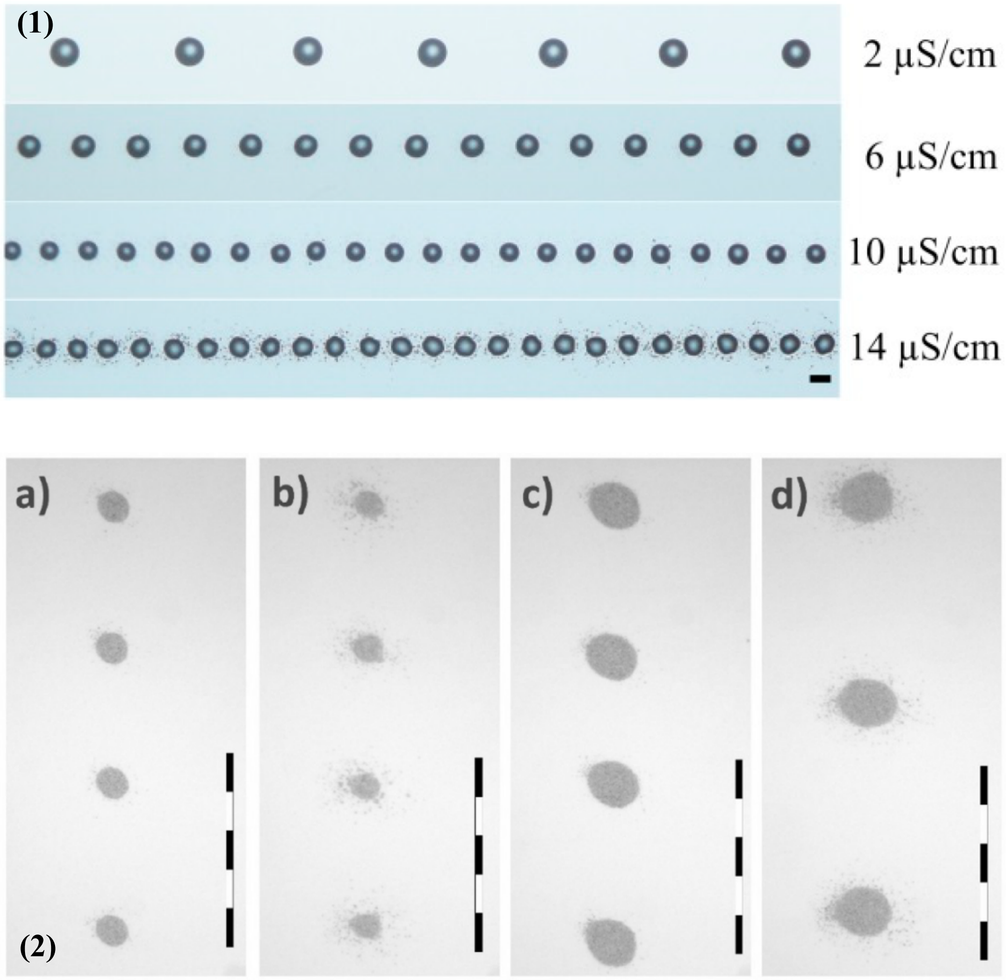

Figure 2-16 Images showing the atomization behaviour of deposited droplets: (1) Atomization happens with increased conductivity of the ink. The scale bar is 100 µm. Adapted from Guo et al;[119] (2) Deposited droplets with diameter of 7.5 µm ((a) and (b)) and 12.5 µm ((c) and (d)). The nozzle to substrate distance in (a) and (c) is 50 µm and in (b) and (d) 70 µm. Higher nozzle to substrate distance will lead to atomized deposition. The scale bar is 50 µm. Adapted from Laurila et al.[120]

A stable deposited droplet delivered by pulsed EHD printing also has a spherical cap geometry. The deposited droplet diameter is influenced by the contact angle and the deposited liquid volume per pulse, which is determined by the ejected flow rate from the cone and the pulse width time. The drop spacing between adjacent droplets depends on applied print velocity and frequency. The total ejected drop volume per pulse can be calculated as:

$$V_{drop} = Q \cdot T_p = Q \frac{x_p}{f} \qquad (2-14)$$

where V_{drop} is the total ejected drop volume per pulse, Q is the jetting flow rate that is determined by Equation 2 – 9, x_p is the duty ratio of the pulse, which is the ratio between pulse width time T_p and time period T_d (T_p and T_d are shown in Figure 2-14), and f is the applied pulse frequency. Assuming volume conservation between the total ejected liquid per pulse and the deposited droplet, the deposited droplet diameter can be calculated by the total ejected volume per pulse together with the contact angle between the droplet and the substrate:

$$d_{eqm} = \left\{ \frac{48Qx_p}{\pi f \tan\frac{\theta}{2}(3+\tan^2\frac{\theta}{2})} \right\}^{\frac{1}{3}} \qquad (2-15)$$

From Equation 2 – 15, the single deposited droplet diameter is not only dependent on the jetting flow rate and the contact angle, but also influenced by the applied pulse frequency and duty ratio. As shown in Figure 2-17, with increased pulse frequency and fixed duty ratio, the deposited droplet diameter decreases due to a reduced pulse width time. Meanwhile, the drop spacing between two adjacent droplets also decreases due to the decrease of time period T_d. Thus, in order to achieve repeatable droplets with the same deposited diameter, the pulse width time should be maintained the same for all the conditions. This requires either a fixed applied pulse frequency with fixed duty ratio, or an adjusted frequency and duty ratio to ensure the same pulse width time.

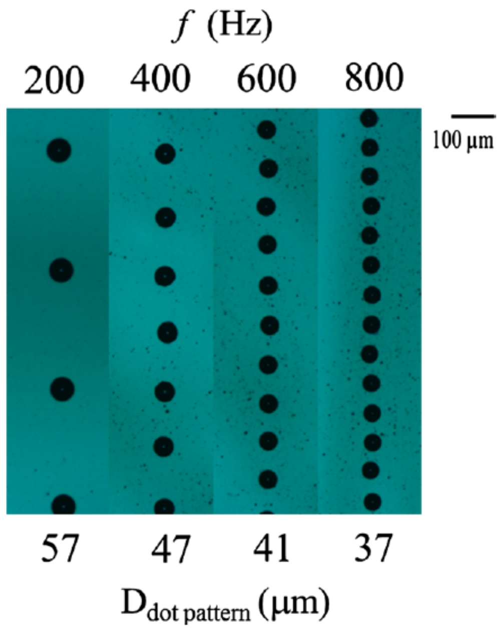

Figure 2-17 Printed droplets at different pulse frequencies with fixed applied voltage, duty ratio and print velocity. Adapted from Park et al.[121]

2.3.3 Inkjet Printing Droplet Solidification

After droplet deposition on the substrate, drop solidification to the desired features is the final process in inkjet printing. The solidification process involves different mechanisms, such as polymerization or evaporation.[45] For many inkjet printing inks such as nanoparticle suspensions or dilute polymer solutions, solidification due to evaporation is dominant. Thus, a good understanding of the evaporation mechanisms is important to achieve uniform, stable solid patterns.

Picknett and Bexon [122] proposed two modes of evaporation for the sessile drops: the constant contact radius mode with diminished contact angle, and the constant contact angle mode with diminished contact radius, during evaporation. The constant contact radius mode is the dominant mode for the water droplets with initial contact angle smaller than 90°, while the constant contact angle mode can be observed for the evaporation of a pure liquid on a substrate with initial contact angle larger than 90°.[123] However, in practice, the evaporation of a sessile drop often contains both modes, with one mode switching to the other in different stages, and a mix of the two modes can occur at the final stages of evaporation, with the decreasing of both contact angle and contact radius.[124, 125]

The contact angle plays an important role in droplet deposition and solidification process. The equilibrium contact angle from Young's equation (Equation 2 – 12) assumes a static state and the solid surface is homogeneous, smooth and rigid. However, the contact angle on a substrate can range between the advancing and receding values, apart from the equilibrium value, depending on the previous history of the triple line.[123] The advancing contact angle θ_a is found at the advancing edge of the liquid drop, and the receding contact angle θ_r is found at the receding edge.[126] The difference between the advancing contact angle and receding contact angle (θ_a - θ_r) is defined as the contact angle hysteresis, θ_{hyst}. The contact angle hysteresis phenomenon is quite common and generally all solid surfaces exhibit hysteresis behaviour when in contact with a liquid. The reason for this hysteresis is complex, however, it is believed to be mainly due to surface roughness, heterogeneity, and metastable surface energetic states.[126-130] Meanwhile, the properties of the deposited liquid such as solute size and mobility can also influence the hysteresis behaviour.[126, 131] Thus, the use of equilibrium state contact angle θ_{eqm} in all the states is not appropriate. For the droplet deposition process, as the droplet impacts and spreads over the dry surface, the use of static advancing contact angle in Equation 2 – 15 would be more appropriate instead of the equilibrium value.[1] For the droplet solidification process due to solvent evaporation, the existence of a receding contact angle would lead to the decrease of the deposited droplet diameter as the droplet volume reduces due to evaporation.[1]

The deposition of droplets of liquid solution usually exhibits a contact line pinning effect due to contact angle hysteresis during drying period. The evaporation of droplets with pinned contact lines will initially lead to a reduced contact angle with fixed footprint area. Once the contact angle is reduced to the receding contact angle, the contact line is no longer pinned (i.e. depinned) and the contact area will retract at the receding contact angle during fluid evaporation.[122] Thus, the extent of receding contact angle influences the contact line pinning behaviour. With zero or approaching zero receding contact angle the contact line of the droplets will be pinned through the whole evaporation period with constant contact radius, while at large receding contact angles both pinning and depinning process will occur. Contact line pinning is quite common for the drying of solution based inks used in the inkjet printing process, and only systems with the cleanest and purest solvents do not show this effect.[14, 132]

Solute transport and distribution during evaporation are the dominant factors in determining the final shape of the dried solid material. With a pinned contact line, solute is seen to segregate at the contact line of the initial drop edge during evaporation and form a ring like geometry, with no or little solute elsewhere. This phenomenon is known as the coffee ring or coffee stain effect,[133] as shown in Figure 2-18, and is commonly observed in the inkjet printed dried patterns with inks containing particle suspensions or polymer solutions.[1] Deegan proposed that the coffee ring effect is caused by an outward flow within the drop that brings the solutes to the edge during evaporation. This capillary outward flow is driven by the loss of solvent due to evaporation and the geometrical constraint of the drop edge or contact line due to contact line pinning.[134] The coffee stain phenomenon can significantly influence the final shape of the deposited droplet or line features from overlapping drops formed by inkjet printing. For most applications the presence of a coffee stain is an unwanted defect and should be avoided in most cases to achieve better properties.

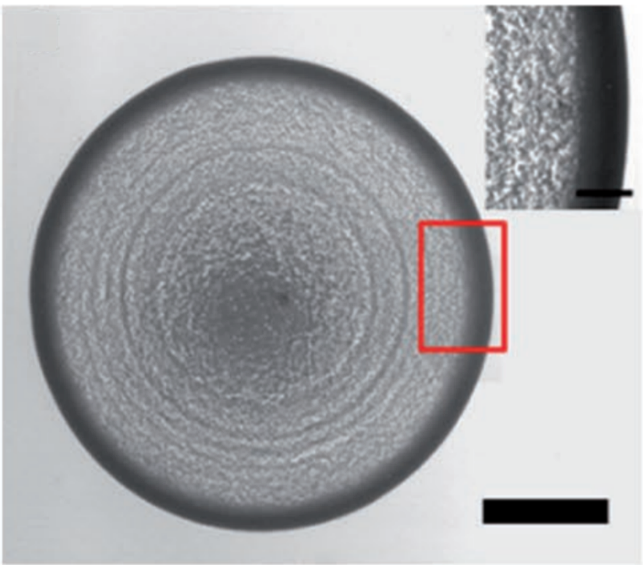

Figure 2-18 SEM images showing the coffee ring effect of the printed GO ink droplets on Si/SiO2 substrates after drying at 30 °C. Adapted from Pei & Derby.[135]

Several methods have been developed to reduce or eliminate the coffee stain effect, and the typical approaches involve modifying the driving force of the outward flow or introducing an opposite flow by the Marangoni effect during evaporation.[1, 136] As the outward flow is driven by the loss of solvent due to evaporation, the use of high boiling point, non-volatile solvent could significantly increase the evaporation time and reduce the outward flow due to evaporation, thus suppressing the coffee ring effect.

Kim et al. [137] developed a silver nanoparticle ink formulation with a high boiling point and low surface tension solvent, ethylene glycol. This diminished the coffee stains associated with printed conductive tracks by reducing the outward flow during evaporation. Yunker et al. [138] studied the influence of the shape of suspended particles on coffee ring formation and proposed that elongated ellipsoidal shaped particles can produce strong interparticle capillary interactions and restrain the outward flow and hence reduce the coffee staining effect during evaporation.

The Marangoni effect is another flow within the deposited drop induced by a surface tension gradient caused either by a solute concentration or a temperature gradient at the liquid – air interface during evaporation.[136] These gradients lead to an associated gradient in interfacial tension that can induce a surface flow in opposition to the radial flow that generates the coffee ring. The use of Marangoni flow is an effective method to reduce the coffee staining effect, and typically involves the use of appropriate mixtures of solvents with different surface tension and vapor pressure.[139] Park and Moon [139] achieved uniform deposition of silica particles beyond coffee staining by applying a mixed solvent of water and a minor component of drying control agents, diethylene glycol or formamide with high boiling point and low surface tension. During the drying process, the evaporation of water at the contact line decreases the surface tension of the droplet edge and leads to an inward Marangoni flow from the contact line to the drop center due to the surface tension gradient. The Marangoni flow counterbalances the outward flow by evaporation and drives the particles back to the center of the droplet to reduce coffee staining. Similar approaches have been developed to suppress the coffee ring effect of deposited droplets in other studies.[30, 140-142]

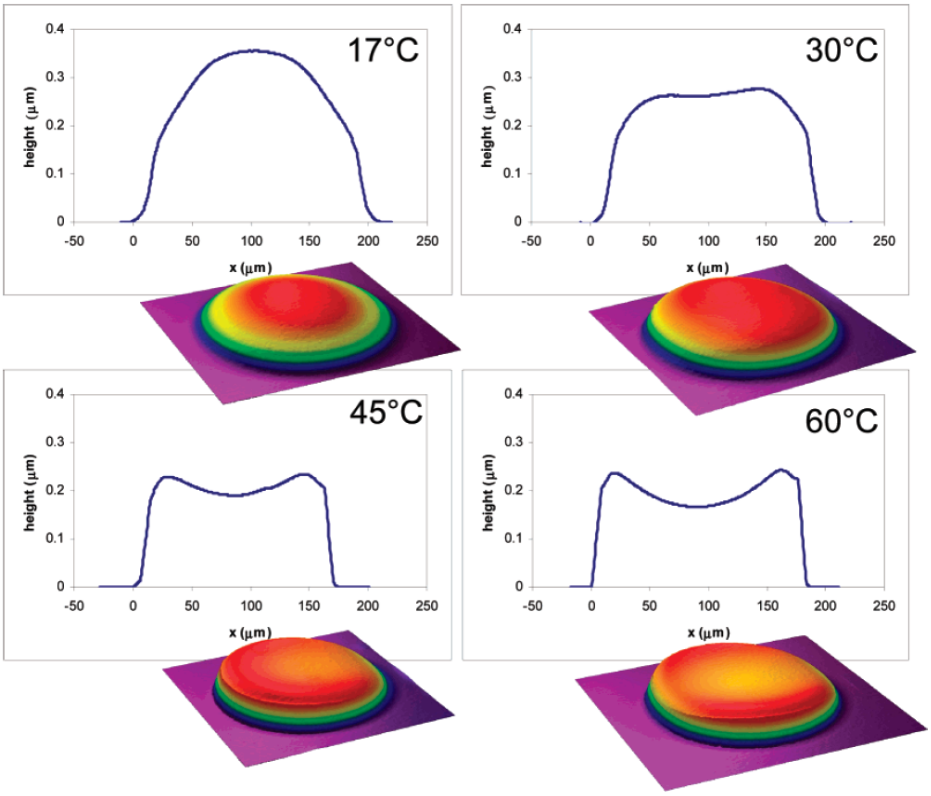

Figure 2-19 Cross section and 3D profile from an optical profilometer of single drops printed at the noted temperatures. Adapted from Soltman and Subramanian.[13]

The substrate temperature can also influence the onset of coffee staining. Soltman and Subramanian [13] studied the influence of temperature on the shape of the deposited PEDOT/PSS droplets. They proposed that the elevated substrate temperature could lead to greater evaporation at the contact line compared with the droplet centre, hence further increase the outward flow to the droplet edge and exacerbate the coffee staining effect. On the contrary, the use of a lower substrate temperature could suppress the evaporation at the contact line and thus reduce or eliminate the coffee ring effect at the drop edge, as shown in Figure 2-19. However, their analysis was carried out using a single solvent system with absence of the Marangoni flow. Rui et al. [30] suggested that the influence of temperature on the Marangoni flow is complex. On the one hand, elevated temperature could increase the diffusion within the liquid droplet, which decreases the concentration gradient and hence leads to a reduction in the Marangoni flow. On the other hand, increased substrate temperature would reduce the liquid viscosity, which could enhance the Marangoni flow. Thus, the concentration of solvents to apply Marangoni flow to reduce coffee staining at room temperature might not be applicable for elevated temperature conditions.

2.4 Inkjet Printing Droplet coalescence

Unlike graphic printing that uses isolated droplets to produce images, most applications in inkjet printing functional materials, e.g. printed electronics, displays and photovoltaics, require droplet coalescence to achieve continuous features.[1] The overlap of a series of droplets will form line structures, and the overlap of lines will lead to film structures. Thus, an understanding of the coalescence and spreading of droplets to form stable line structures is important for the printing of desired 2-D patterns.

2.4.1 Lines with Zero Receding Angle

A line produced by inkjet printing is formed by the sequential overlap and coalescence of a series of identical liquid drops on a surface, creating a liquid line or bead that must remain stable until it solidifies by solvent evaporation or phase change. Davis [143] considered the stability of a static liquid bead by using linearized stability theory for three cases: (a) the contact line is fixed while the contact angle is free to change; (b) the contact line is free to move with a fixed contact angle; (c) the contact line is free to move and the contact angle is a smooth function of contact line speed. Davis showed that for the liquid bead in cases (b) and (c) there are always possible axial wavenumbers that make the bead unstable, while a parallel sided liquid bead in case (a) can be stable against shape change when the contact line is fixed and the contact angle is $< \pi/2$. These observations were confirmed experimentally by Schiaffino and Sonin.[144] However, there was no consideration of the case when the liquid bead shows contact angle hysteresis, since the boundary conditions are nonlinear in this case.

The drop spacing, which is the spacing between two adjacent deposited droplets, plays an important role in determining the final morphology of printed lines. As shown in Figure 2-20, when the drop spacing is larger than the single deposited droplet diameter d_{eqm}, no overlap will occur and individual deposited droplets can be obtained (Figure 2-20 a). By decreasing the drop spacing the individual drops begin to overlap and coalesce to form a scalloped (wavy) line structure (Figure 2-20 b). As the drop spacing continues decreasing to a critical value, a stable parallel sided line can be obtained (Figure 2-20 c). However, further reduction in drop spacing below a critical minimum value leads to a bulging instability (Figure 2-20 d). In addition, if the single deposited droplet dries before another droplet deposits and overlaps with it due to increased substrate temperature and reduced evaporation time scale, a "stacked coins" structure can be obtained (Figure 2-20 e).

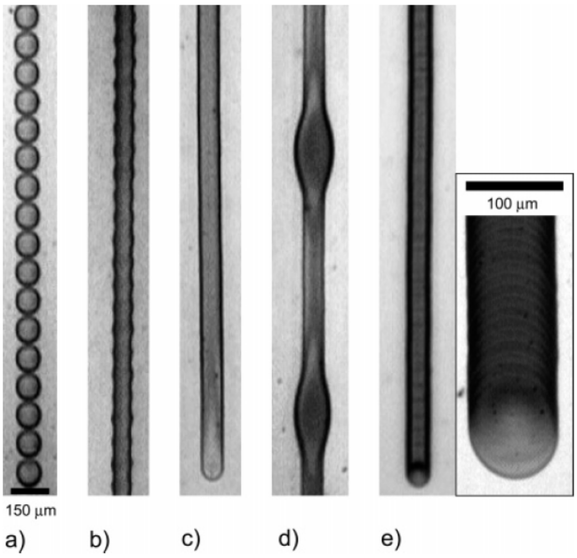

Figure 2-20 Examples of principal printed line morphologies: (a) individual drops, (b) scalloped, (c) uniform, (d) bulging, and (e) stacked coins lines. Drop spacing decreases from left to right. Adapted from Soltman and Subramanian.[13]

Thus, if the evaporation time scale is long enough compared with the printing process and the contact line of the printed structure is pinned due to zero receding contact angle, the formation of a stable inkjet printed line is limited by two bounds. The lower bound line width for line stability is determined by contact line pinning and the liquid bead surface tension,[10, 11] and this also defines the maximum drop overlapping spacing. The upper bound width is limited by the bulging instability, this is a dynamic instability and together with the rate of drop arrival, a minimum drop spacing for stable line formation could be obtained.[12, 14]

Various studies have been undertaken to investigate the phenomenon of drop spreading and coalescence to predict the dimensions of a printed line. Smith et al. [10] developed a model for the line width of a stable parallel sided liquid bead through droplet overlap. As the Bond number is significantly lower than 1, the shape of the liquid bead is controlled by capillarity and can be assumed to have a uniform circular segment cross section that is determined by the contact angle. As shown in Figure 2-

21, through volume conservation between the total deposited droplets and the coalesced liquid bead, the liquid bead width can be calculated as:

$$w = \sqrt{\frac{2\pi d_0^3}{3p\left(\frac{\theta}{\sin^2\theta} - \frac{\cos\theta}{\sin\theta}\right)}} \qquad (2-16)$$

where d_0 is the ejected droplet diameter in flight, p is the drop spacing and θ is the equilibrium contact angle.

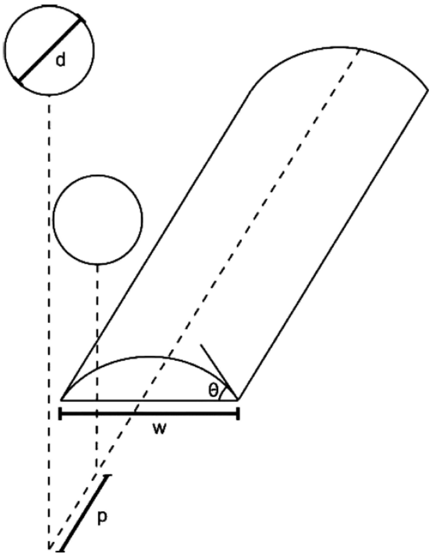

Figure 2-21 Schematic diagram showing the theoretical assumptions made in modelling the relationship between final track width and contact angle. Adapted from Smith et al.[10]

Thus, the deposited liquid bead width is influenced by the single droplet volume, contact angle and drop spacing. Further studies found that the prediction of line width from Equation 2 – 16 is more accurate by using the advancing contact angle rather than the equilibrium value.[14]

Stringer and Derby [11] proposed that for a stable parallel sided liquid bead with pinned contact lines (i.e. a zero receding contact angle), the minimum width of the bead will be equal to the single deposited droplet diameter, d_{eqm}. Thus, based on the calculation of the bead width from equation 2 – 16, the maximum drop spacing for a stable parallel sided liquid bead can be defined:

$$p_{\max} = \frac{2\pi d_0}{3\beta_{eqm}^2 \left(\frac{\theta_a}{\sin^2\theta_a} - \frac{\cos\theta_a}{\sin\theta_a} \right)} \qquad (2-17)$$

where β_{eqm} is the ratio between the diameter of the spherical cap on the substrate, d_{eqm}, and the droplet diameter in flight, d_0, and θ_a is the advancing contact angle.

Duineveld [12] studied the behaviour of inkjet printed lines formed from drops showing a zero receding contact angle, and showed that stable parallel sided line structures can be obtained with a range of printing parameters. However, under certain conditions, the printed lines become unstable with a structure of periodical bulges connected by ridges, similar to those observed by Soltman and Subramanian.[13] The onset of bulges was dependent on the advancing contact angle, drop spacing and printing velocity conditions. Duineveld [12] proposed that the onset of the bulging instability represented a dynamic process considering the competition between the spreading of the liquid bead due to sequential deposition of droplets and the axial transported flow of liquid through the existing liquid bead on the surface driven by the Laplace pressure difference between the stable liquid bead and a disturbance to the bead behind the deposition front. The formation of bulges can be divided into two conditions determined by the advancing contact angle. At high advancing contact angle, capillary spreading is relatively slow, and the axial transported flow back along the bead generated by the Laplace pressure difference is, in comparison, large. Thus, newly deposited liquid will flow towards the low pressure region to enhance a bulging instability, if the contact angle in the bead is larger than the advancing contact angle. At low advancing contact angle, however, the flow rate in the bead is significantly reduced due to a reduced pressure difference. In this case bead spreading due to capillarity is dominant. Hence the stability of the printed line structure is a dynamic process that is controlled by the fluid/substrate contact angles and the rate at which drops arrive at the surface.

Stringer developed Duineveld's model [12] by proposing that the condition for the onset of the bulging instability requires the fluid flow rate, Q, along the bead, which is driven by the pressure difference between the bulge and the leading tip of the growing liquid bead, to be much larger than the flow rate, Q_A, of new liquid arriving at the growing tip.[14] After considerable manipulation the threshold, or minimum drop spacing for the formation of stable lines, is defined by the following inequality:

$$\frac{\eta U_T}{\sigma_{LV}} > \frac{4\pi S \sin\theta_a}{3\beta_{eqm}^3 K_1 (p^*)^2} \left\{ \frac{\sqrt{\frac{2\pi}{3p^* f(\theta_a)}} - 1}{\sqrt{\frac{2\pi}{3p^* f(\theta_a)}}} \right\} \qquad (2-18\text{ a})$$

or

$$\frac{\eta U_T}{\sigma_{LV}} > g(p^*, \theta_a) \qquad (2-18\text{ b})$$

with

$$U_T^* = \frac{\eta U_T}{\sigma_{LV}} \qquad (2-18\text{ c})$$

and

$$g(p^*, \theta_a) = \frac{4\pi S \sin\theta_a}{3\beta_{eqm}^3 K_1 (p^*)^2} \left\{ \frac{\sqrt{\frac{2\pi}{3p^* f(\theta_a)}} - 1}{\sqrt{\frac{2\pi}{3p^* f(\theta_a)}}} \right\} \qquad (2-18\text{ d})$$

where p^* is the dimensionless drop spacing, $p^* = p/d_{eqm}$, K_1 is a constant > 1, θ_a is the advancing contact angle, S is a shape factor, and $f(\theta_a)$ is a function of β_{eqm} and θ_a. The left side of inequality 2 – 18 is a dimensionless function of printing velocity, U_T, and the right side is a function $g(p^*, \theta_a)$ of θ_a, the advancing contact angle, and p^*, the dimensionless drop spacing. By determining the two drop spacing limits for stable line deposition from Equation 2 – 17 and 2 – 18, a stability map can be established with U_T^* and $g(p^*, \theta_a)$ as coordinates, as shown in Figure 2-22. The solid diagonal line indicates the onset of the bulging instability, the horizontal dashed line indicates the maximum printing speed for a particular printing system, and the vertical dotted lines indicate the maximum drop spacing limit for a range of contact angles. The triangle area formed by these three lines is the region of stability for printed parallel sided line structures. The stability model has been validated experimentally with droplet size around 100 pL,[14, 30] and can give instructive guidance in printing parameter selections.

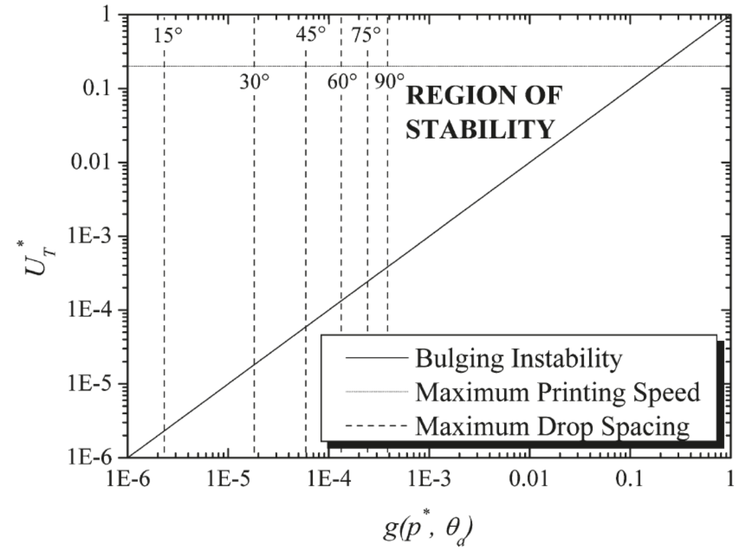

Figure 2-22 Stability map defined by a dimensionless velocity and a function of p^* and θ_a. Adapted from Stringer & Derby.[14]

The formation of bulges in a linear sequential printed line with zero receding contact angle relates to the pressure imbalance within the liquid bead. Normally, there is an additional bulge at the printing start of a line, which is possibly due to a geometric change from spherical to cylindrical symmetry of the printed droplets.[12] Abunahla et al.[145] investigated a novel segmented and symmetric printing methodology to suppress the formation of bulges at both the beginning and middle of the printed lines, which involves first printing three-drop segments with the central drop deposited last (Figure 2-23 a), and connecting the three-drop segments with an individual droplet to form a line (Figure 2-23 b). This segmented and symmetric printing method rather than the linear sequential printing reduces the pressure imbalance within the bead during printing, and with appropriate drop spacing parameters, stable lines could be obtained in the absence of bulges across the whole line (Figure 2-23 c to e). This method can also be used to print X-, T-, and L-shaped structures, which show better stabilities compared with those by linear sequential printing.

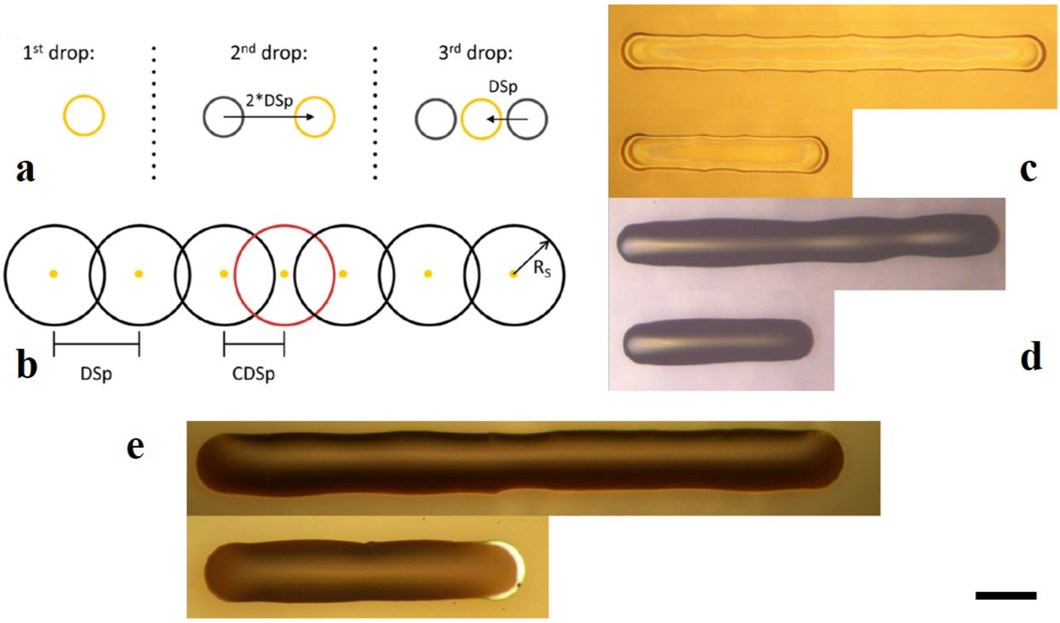

Figure 2-23 Illustration of the segmented and symmetric inkjet printing method (a and b): (a) printed three drop segments with central drop deposited last, (b) the three-drop segments are connected by an individual drop to form a line. DSp is the drop spacing within the segment, and CDSp is the connected spacing between segments. (c) to (e): Symmetrically printed stable lines with four (up) and two (down) segments with CDSp the single deposited droplet diameter. (c) Poly-4-vinylphenol (PVP) on glass, (d) silver on polymer, and (e) silver on glass. The scale bar is 200 μm. Adapted from Abunahla et al.[145]

The above researches were carried out to investigate printed structures on a homogenous substrate. Inkjet printing on pre-defined topographical features is also important to achieve high resolution patterning or other special defined patterns.[146-148] Nguyen et al. [149] investigated inkjet printed PEDOT/PSS conductive tracks on patterned PET surfaces with controllable wettability for flexible electronic applications. Through a two-step hydrophilic−hydrophobic coating followed by a selective hydrophilic treatment, printed fine features up to 35 μm, which is much smaller than the droplet diameter in flight (around 55 μm), could be obtained on the high wettability contrast surface. Kant et al. [150] studied the spreading behaviours of sequential inkjet printed droplets on the patterned shallow recessed regions (pixels), motivated by the organic light emitting-diode display manufacture. From experimental studies and numerical modelling, they proposed that the presence of sloped side walls promotes the spreading of liquid through the local increase in contact angle. Associated with wettability patterning, robust and uniform containment of the fluid within the pixel can be achieved.

2.4.2 Lines with Finite Receding Angle

Although inkjet printing with zero (or approaching zero) receding contact angle is a common phenomenon for particle suspension inks, there are still cases in which inkjet printing may be applied on a substrate under conditions with a moving contact line and finite receding contact angles.[15, 16] The finite receding contact angle condition can influence the stability of printed lines during both the printing and drying process.

Stable parallel sided lines can be obtained through inkjet printing within a range of droplet overlap on the substrate with zero receding contact angle. For the structures printed on the substrate with high receding contact angle, however, the deposited liquid bead breaks up into individual droplets rather than forming a stable line, as observed by Duineveld [12] (Figure 2-24). He proposed that this instability can be characterised by a constant contact angle boundary condition, as reported by Davis [143] and further studied by Schiaffino and Sonin [144]. Lee and Son [151] studied the influence of receding contact angle on the coalescence behaviour of two printed droplets. Through numerical simulations they proposed that at low receding contact angle (θ_r = 30°) the two deposited droplets would merge and spread into a micro line with a neck in the middle, while at high receding contact angle (θ_r = 120°) droplet spreading is highly limited and the two droplets would coalesce to form a larger droplet.

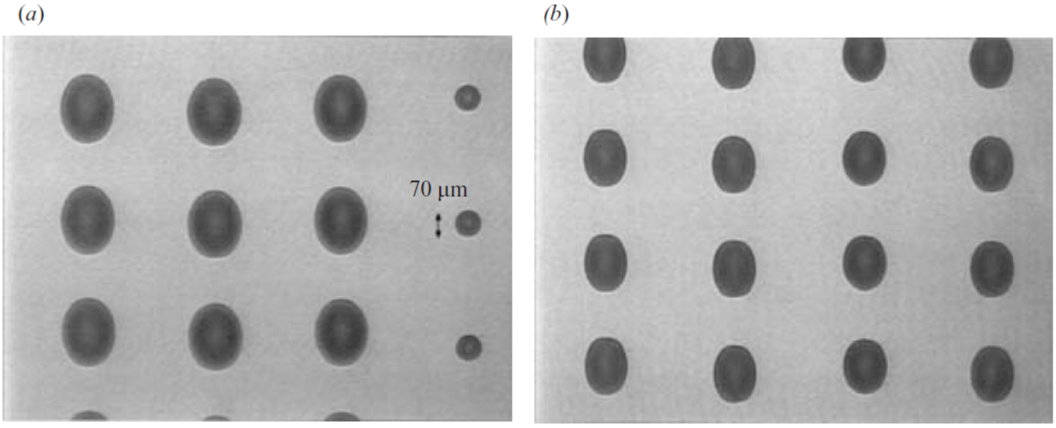

Figure 2-24 Results of inkjet printed unstable lines on CF4-treated resist substrates with receding contact angle of 32° at printing velocity of 5mms^{-1} and different drop spacing: (a) 30 μm drop spacing (note the individually printed liquid drops with a diameter of 70 μm); (b) 50 μm drop spacing. Adapted from Duineveld.[12]

Fukai et al. [152] studied the influence of droplet size on the contact line behaviour of droplets deposited on a homogenous substrate with finite receding contact angle, and proposed that the receding behaviours for droplets with macro and micro sizes are different. For macro droplets with initial diameter in flight > 1mm, the contact angle at which the contact line starts to recede decreases with increasing initial solute concentration. In contrast, for the micro droplets produced by inkjet printing with droplet diameter in flight around 60 μm, the contact line starts to recede at an angle higher than the measured receding contact angle, till the contact line is pinned and the contact angle then decreases due to evaporation, and the initial solute concentration has little effect on the receding process. Hsiao et al. [17] studied the coalescence of printed droplets on a surface with finite receding contact angle using high-speed imaging, and proposed that the drop spacing plays an important role in determining the printed liquid bead stability. He showed that at small drop spacing the printed liquid tracks were potentially continuous liquid beads, but were destabilized by contact line retraction during and after printing, while at larger drop spacing, stable continuous tracks can be formed without destabilizing effect, which is due to converged track radii at increased drop spacing. Thompson et al. [153] investigated inkjet printed line morphologies on the substrate with a small finite receding contact angle ($\theta_r < 4°$) by numerical modelling. The redistribution of the first few droplets to form a bulge at the beginning of the line was captured by a simple model only considering the surface tension force, while the latter line morphologies were well predicted by a model considering a balance between surface tension and viscosity. They also proposed that the presence of viscous effects causes the subsequent periodic bulging instabilities.

Du et al. [154] investigated the coalescence of inkjet printed dots on the substrate with very small receding contact angle ($\theta_r \approx 3°$) by controlling the printed drop spacing and ink surface tension/viscosity ratio (Figure 2-25). He found that at small receding contact angle, continuous printed lines can be achieved without a destabilizing effect. By adjusting the ink surface tension/viscosity ratio to reduce the spreading speed of deposited droplets on the substrate, stable symmetrical and regular beads can be achieved in a certain range of drop spacing. Soltman et al. [155] developed a methodology for optimized printing of partially wetting films by adjusting the line to line spacing, and achieved uniform square patterning with sharp bead corners by utilizing contact angle hysteresis.[16]

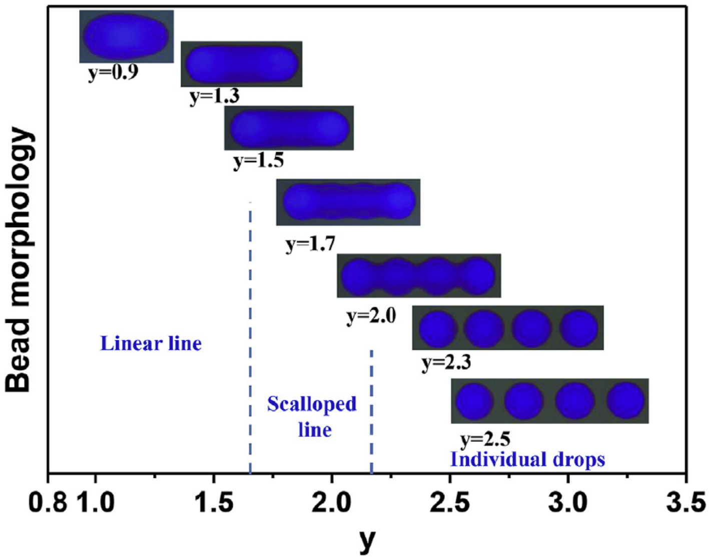

Figure 2-25 Ink droplet coalescence results at various drop distances (y equals drop spacing divided by the single deposited droplet radius). Adapted from Du et al.[154]

From the above literature, structures printed on substrates with finite receding contact angle can be unstable, due to retraction of the contact line during printing or drying period. The receding effect of the deposited structures is dependent on both the receding contact angle value and the feature size.

2.4.3 Inkjet Printed Silver Tracks

In the past two decades, narrow conductive tracks produced by inkjet printing has gained extensive interest for electronics applications, due to its ability to achieve direct, precise deposition on a wide range of substrates at low cost.[1, 156] To achieve printed electronics with high conductivity and resolution, various researches have been investigated on improving the conductive materials, ink formulations, and printing procedures.[157] Conductive polymers, such as PEDOT-PSS and polyanilines, could be an option to achieve direct printed tracks.[84, 158] However, these polymers have low conductivity (~10^2 S.cm^{-1}) and chemical instability.[159] Thus, to achieve printed tracks with high conductivity, metallic inks containing gold, silver, or copper, are commonly applied. Of these, silver inks are most commonly used due to their high intrinsic conductivity and low oxidation rate.[157] Silver nanoparticles are most widely used in inkjet-printed ink formulations to achieve stable conductive tracks.[18, 157] The metallic nanoparticles are typically dispersed in an organic solvent with stabilizers to prevent particle aggregation or nozzle clogging,[160, 161] and the deposited inks require a further thermal sintering process to remove the organic compounds in the ink and allow the particles to coalesce into a dense structure.[18]

Lee et al. [156] investigated printed silver tracks with a water-based ink of well dispersed silver nanoparticles. By using an ordinary commercial inkjet printer, continuous lines with width from 400 to 130 μm were successfully printed onto glass substrates. The resistivity of the lines decreases with increased sintering temperature and time, due to melting of the nanoparticles into bulk material, as shown in Figure 2-26. The optimum sintering option was heating up the substrate at 260 °C for 3 min, and the resistivity was 1.6×10^{-7} Ω·m, which is ten times of that of bulk silver (1.6×10^{-8} Ω·m). Van Osch et al. [34] studied the printed silver tracks on polymer substrates with high glass transition temperature by using a commercial silver nanoparticle suspension, and proposed that the resistance of the printed lines increases with increasing drop spacing, due to less material deposited per unit length. The high glass transition temperature of the polymer substrate allows the printed structures to be sintered at a high temperature of 200 °C, and the conductivity was 23% compared with the bulk silver (6.3×10^{7} Sm^{-1}) for the tracks printed at a drop spacing of 5 μm with line width of 80 μm, and 13% for the lines printed at the drop spacing of 25 μm with line width of 40 μm. Similarly, Jeong et al. [159] printed narrow silver tracks with low resistivity (4×10^{-8} Ω·m) on the polyimide substrate with line width of 60 μm after annealing at a temperature of 250 °C.

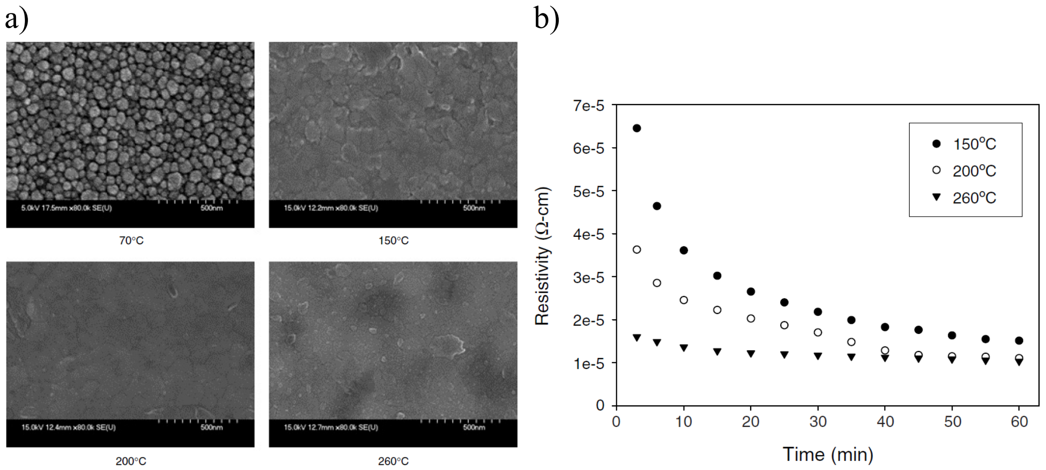

Figure 2-26 a) SEM images of surface morphology after different temperature sintering for 45 min; b) Electrical resistivity after heating as a function of sintering time for different temperatures (actual line width = 130 μm for these data). Adapted from Lee et al.[156]

The high sintering temperature required to form narrow silver tracks with high conductivity from printed silver nanoparticle suspensions limits its usage on flexible (polymeric) substrates, which typically have a low glass transition temperature.[34] Thus, the ink formulation and post treatment need to be adjusted for the printed structures on flexible substrates. By applying argon plasma sintering, Reinhold et al. [162] achieved solidification of printed silver nanoparticles on polymer substrates with low temperature post treatment. The use of inert gas in plasma treatment can protect the polymer substrates from surface degradation, and the solidified silver tracks showed resistivity values of less than one order of magnitude larger compared with the resistivity of bulk silver. Other low temperature sintering processes such as microwave flash sintering,[163] infra-red assisted sintering,[164] and UV-sintering [165] are also investigated to achieve solidification of silver tracks on the flexible substrates with low glass transition temperature.

Besides the above post treatments, the adaption of ink formula to allow low temperature thermal sintering of the printed structures has also been investigated. Huang et al. [166] developed a low temperature curing silver nanoparticle ink by dispersing the synthesized silver nanoparticles into a mixture of ethylene glycol and water. They showed that the conductivity of the printed silver tracks on the photo paper sintered at 150 °C reached 2.1×10^{7} $\mathrm{Sm^{-1}}$, which was approximately one third that of bulk silver. Apart from silver nanoparticle suspensions, organometallic silver ink is an alternative for printing on flexible substrates. Organometallic silver compounds are silver salts dissolved in organic solvents or aqueous solutions with high concentration.[157] The silver salts are typically organic silver complex, which can be decomposed easily at low curing temperature.[167] Thus, the printed silver patterns can be sintered at a low temperature around 90 – 150 °C with conductivities competitive with bulk silver.[168, 169] Smith et al. [10] investigated the inkjet-printed silver tracks on a wide range of substrates with an organometallic silver ink. By applying a low sintering temperature of 150 °C for 60 min, the resistivity of the sintered silver tracks was in the range $2 – 3\times10^{-8}$ $\Omega\cdot\mathrm{m}$, which is 1.3 to 2 times that of bulk silver. Perelaer et al. [170] developed a one-step process to fabricate conductive silver tracks on flexible polymer substrates by direct printing organometallic silver ink onto a substrate that is pre-heated to 130 °C. With a sintering time of 5 min, the printed silver tracks on the polyethylene terephthalate (PET) substrate generated a resistivity of 1.3×10^{-7} Ω·m with a line width of 197 μm.

The above researches were carried out using typical piezoelectric printheads, which can generate direct printed microstructures with feature size in the range between tens of micrometre to hundreds of micrometre. While further increasing resolution for direct piezoelectric printing is difficult due to the limitation of nozzle size, electrohydrodynamic (EHD) inkjet printing has been dedicated to achieve direct deposition at ultra-high resolution with a wide range of inks.[171-173] Through EHD printing, printed patterns with feature size ranged from tens of micrometre to sub-micrometre can be achieved by adjusting the printing parameters such as applied voltage and pressure. Wang et al. [174] investigated EHD printed silver micro tracks by using a commercial organometallic silver ink. Silver tracks with line width of 70 μm were successfully printed on the silicon substrate (Figure 2-27), and a low resistivity of 3.9×10^{-8} Ω·m were achieved after sintering at a temperature of 220 °C for 20 min. Lei et al. [173] developed an Ag-PEO (polyethylene oxide) reactive ink for microscale electrohydrodynamic printing, and showed that full reaction of Ag–PEO inks to form silver particles occurred at a substrate temperature of 90 °C. The printed silver tracks at such low curing temperature showed a conductivity of 3.3×10^{6} Sm^{-1} with a line width of 27.6 μm. Rahman et al. [175] investigated EHD printed silver line electrodes on substrates with non-flat surfaces. By using a high viscosity silver paste and near-field electrospinning (NFES) technique, continuous lines with total length of 1.2 mm and width around 30 μm were successfully printed on the 'п' shaped glass surfaces, with an average resistance of 0.84 Ω.

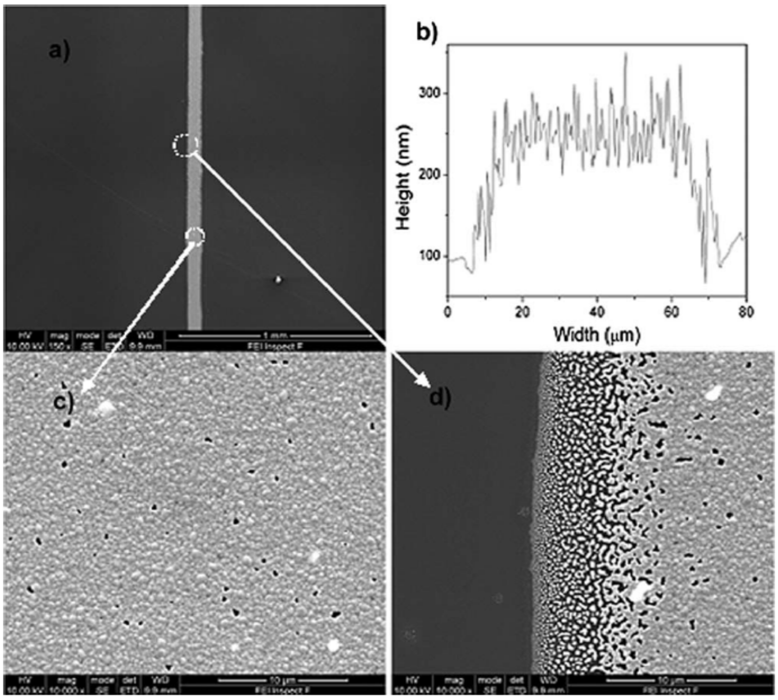

Figure 2-27 SEM images and AFM profile of silver tracks printed on the silicon substrate: a) silver track with total length of several mm and line width of 70 μm, b) cross sectional profile of the track from an AFM measurement, showing ~150 nm in height, c) and d) the surface morphology of the centre and the edge of the track, respectively. Adapted from Wang et al.[174]

For the EHD printed fine features on insulating substrates, one critical challenge is to solve the charging effect caused by the charge accumulation on the printed features.[176] Qin et al. [177] developed a new EHD printing method to achieve direct patterning stable structures onto insulating substrates by using an alternating current (AC) modulated waveform. By applying a modulated ac-pulse, the residual positive and negative charges in the adjacent deposited droplets could be neutralized to achieve stable deposition. They showed that increasing the number of printing layers can significantly increase the height to width ratio of the tracks, and that printed silver tracks with 20 layers showed an average line width of 13.1 μm and reached a resistivity of 5.1×10^{-8} Ω·m after annealing at 200 °C for 30 min. Wang et al. [178] successfully printed transparent silver grids with line width of 3.5 μm and low sheet resistance of $1.3429\ \Omega\ \mathrm{sq}^{-1}$ by mounting a copper foil on the insulating glass nozzle to serve as an extraction electrode to reduce the charging effect. Son et al. [176] achieved stable EHD deposition onto insulated substrate by optimizing the printing parameters. With printing layers of 40 and laser sintering, stable silver tracks with line width of 3.0 μm and resistivity of 1.7×10^{-7} Ω·m were achieved on the nonconductive glass substrate

(Figure 2-28). The high resolution and high conductivity of the printed features show its potential prospect in electronic applications such as forming or repairing fine patterns for flat panel displays. For summary, the post treatment conditions, line width, and resistivity of the printed silver tracks on various substrates by piezoelectric inkjet printing and EHD inkjet printing from the literature are listed in Table 2-1.

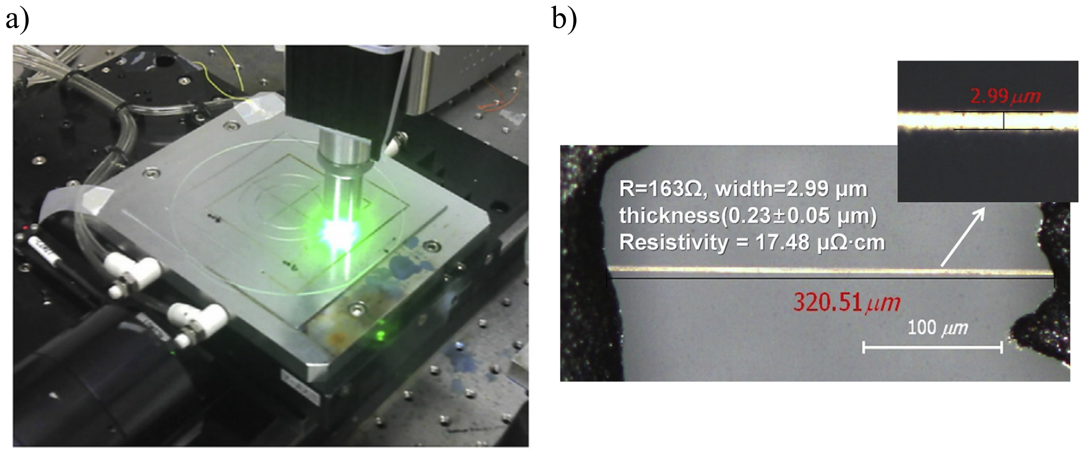

Figure 2-28 a) Photograph of the laser sintering system, b) EHD printed high resolution silver line printing result. Adapted from Son et al.[176]

Table 2-1 Summary of printed silver tracks from literature.

Ink Type	Substrate	Post Treatment	Line Width (μm)	Resistivity (Ω·m)	Author
Ag NPs	Glass	Sintering at 260 °C for 3 min	130	1.6×10^{-7}	Lee et al. [156]
Ag NPs	Polyarylate	Sintering at 200 °C for 1 h	40	1.2×10^{-7}	Van Osch et al. [34]
Ag NPs	Polyimide	Sintering at 250 °C for 1 h	60	4.0×10^{-8}	Jeong et al. [159]
Ag NPs	Polyethylene terephthalate	Argon plasma sintering	218	1.0×10^{-7}	Reinhold et al. [162]
Ag NPs	Photo paper	Sintering at 150 °C for 10 min		4.7×10^{-8}	Huang et al. [166]
Organo-metallic silver	Polyimide	Sintering at 150 °C for 60 min	204	3.0×10^{-8}	Smith et al. [10]
Organo-metallic silver	Polyethylene terephthalate	Sintering at 130 °C for 5 min	197	1.3×10^{-7}	Perelaer et al. [170]
Organo-metallic silver	Polyarylate	Sintering at 130 °C for 5 min	163	1.9×10^{-7}	Perelaer et al. [170]

Organo-metallic silver	Silicon	Sintering at 220 °C for 20 min	70	3.9×10^{-8}	Wang et al. [174]
Reactive Ag Ink	Insulated substrate	Curing at substrate temperature 90 °C	27.6	3.0×10^{-7}	Lei et al. [173]
Ag NPs	Polyethylene terephthalate	Sintering at 200 °C for 30 min	13.1	5.1×10^{-8}	Qin et al. [177]
Ag NPs	Silicon	Curing at substrate temperature 200 °C	50	6.5×10^{-8}	Wang et al. [179]
Ag NPs	Pyrex glass	Laser sintering	3.0	1.7×10^{-7}	Son et al. [176]

Apart from EHD printing to achieve direct patterning at ultra high resolution, it is also possible to achieve ultra small features by piezoelectric inkjet printing through the modification of ink and the substrate. As discussed in section 2.3.3, coffee ring effect leads to segregation of the solute at the contact line and is usually detrimental in inkjet printing. However, high resolution printing can be achieved by utilizing the coffee ring effect. This involves modification of the ink and the substrate wettability to induce an outward capillary flow carrying the solute to the contact line during evaporation, resulting in two parallel lines. The challenge of this strategy is careful control of the particle migration within the evaporating droplets to ensure no particles remaining in the middle of the contact lines. Zhang et al. [180] achieved inkjet printed silver lines with an average width of 5–10 μm on the hydrophilic glass substrates by utilizing the coffee ring effect (Figure 2-29). Bridonneau et al. [181] applied similar method to investigate line morphological control of inkjet printed silica nanoparticles, and achieved three lines with two thin lines of 1 μm width at the contact lines and a wider central line with width of around 20 μm.

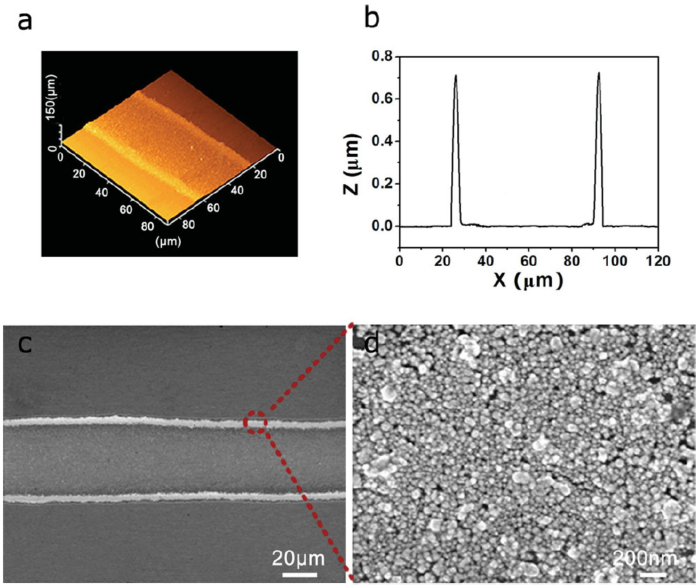

Figure 2-29 Structural characterization of inkjet printed silver line by utilizing the coffee ring effect. a) AFM image showing the printed coffee line. b) The height profile of the printed coffee line. c) SEM image of the printed coffee line. d) Magnified SEM image of the printed coffee line. Adapted from Zhang et al. [180]

Another strategy to obtain printed line features with ultra high resolution by conventional piezoelectric inkjet printing is to deposit conductive ink into a cross linkable viscous liquid substrate. The encapsulation of the ink by the viscous substrate inhibits the spreading of the ink, hence resulting in the embedded conductive lines with high resolution and aspect ratio.[182] The embedded structure protects the conductive patterns away from the influence of ambient environment, and the cross lined flexible polymer matrix allows the patterns to be bendable and stretchable. Jiang et al. [182] fabricated transparent multilayer circuits with line width of 1.6 μm and aspect ratio of 1.7 by inkjet printing silver nanoparticle inks into the spin coated poly(dimethylsiloxane) (PDMS) film (Figure 2-30). The resistance of the embedded microcables remained nearly unchanged after 3000 times of bending, showing excellent electric stability due to the special embedded structure. Zhang et al. [183] achieved a similar embedded structure by inkjet printing reduced graphene oxide (rGO) lines into the PDMS film. The rGO lines with width of 10 μm could be stretched to 180% of its original length with no shedding or breaking.

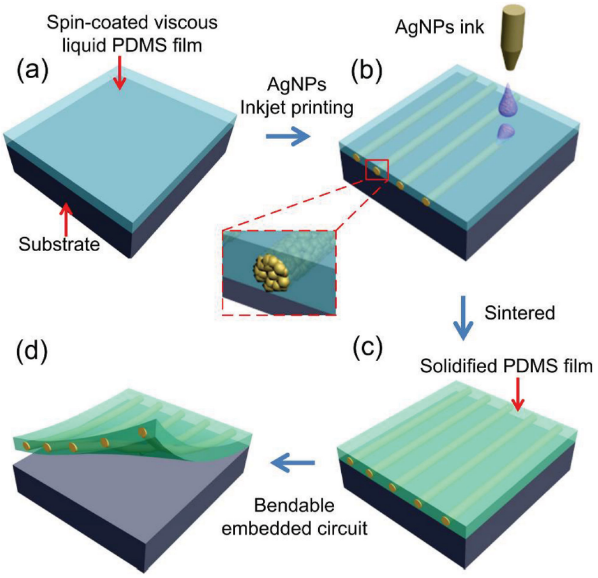

Figure 2-30 Schematic illustration of inkjet printed embedded silver lines. a) PDMS precursor was spin-coated on a PET substrate. b) Silver nanoparticle ink was inkjet printed onto the liquid substrate to form microcables. c) The structures were sintered after the printing process. d) The PDMS film with embedded silver cables were peeled off from the PET substrate. Adapted from Jiang et al. [182]

2.5 Summary

In recent years, inkjet printing technology has been applied as a manufacturing tool beyond its original development as a graphics printing tool. A key difference between these new applications and the original purpose, is the need to print stable linear and 2D features from patterns of overlapping drops. In this chapter, the droplet generation, deposition, coalescence and solidification for both piezoelectric inkjet printing and electrohydrodynamic inkjet printing have been reviewed, as well as the stability of printed structures before drop drying.

The objective of the thesis is to further investigate the stability and electrical properties of inkjet printed lines at high resolution by using piezoelectric inkjet printing and electrohydrodynamic inkjet printing. The literature review has provided useful guidance for our research, including materials selection, model development, and experiment setup. It is clear that, the stability of the printed lines with reduced droplet size needs further investigation, which requires a systematic study of the influence of printing parameters on the final line morphology. This is carried out in Chapter 4, where Stringer's model for the stability of inkjet printed lines is tested for small drop volumes.

Most prior work on the stability of inkjet printed structures has assumed that the ink dries with zero receding contact angle. This is extended in Chapter 5, where the condition of small but finite receding contact angle is explored. This chapter studies the wavelength of bulges on substrates with a finite receding contact angle, using a model based on Duineveld's analysis, with the formation of a new bulge when the ridge contact angle exceeds the advancing contact angle.[12]

Chapter 6 uses prior work on EHD printing to achieve direct DOD printing with identical droplet size,[78, 121, 184] as well as a waveform designed to minimise charging effects on isolated substrates.[177] This has allowed a demonstration that Stringer's model also applies to droplets of femtolitre volume. Finally, we explore electrical properties of EHD inkjet printed lines, on a range of substrates.

Chapter 3 Experimental Materials and Methods

3.1 Ink Parameters Measurements

All experiments were carried out using a commercial silver nanoparticle ink (Silver dispersion, 736465, Sigma Aldrich, Gillingham, UK). The viscosity of the ink was measured by a rheometer (Discovery HR-3 hybrid rheometer, TA Instruments, New Castle, DE, USA) at a shear rate of 1000 s^{-1}. The surface tension of the ink was measured using a drop shape analyser (DSA 100, Krüss, Hamburg, Germany). The ink density was determined by measuring the weight of 5 ml ink on a laboratory balance (ATX Series Analytical Laboratory Balance, Marsden Weighing Machine Group Ltd., Rotherham, UK). The thermogravimetric analysis of the silver nanoparticle ink was performed by a TGA equipment (STA 449 F5 Jupiter, NETZSCH-Gerätebau GmbH, Wolverhampton, UK).

3.2 Substrate Preparation

The substrates used in the experiments are polydimethylsiloxane (PDMS) (101697, Onecall, Leeds, UK) coated glass slide (13192131, Fisher Scientific, Loughborough, UK), silicon (N-type, 647799, Sigma Aldrich, Gillingham, UK), PDMS coated silicon, and polyimide (Kapton HN, DuPont, US) substrates. The PDMS liquid was premixed with the cross linker with a ratio of 10:1 in weight in a glass specimen vial (15394779, Fisher Scientific, Loughborough, UK), and was then put into a vacuum oven (Fistreem, Cambridge, UK) at room temperature with -500 mbar pressure (compared with the atmospheric pressure) for 20 min to degas the bubbles inside the mixture. As PDMS liquid is too viscous, we first deposited the mixed PDMS liquid (approximate 2 ml) onto the glass slides or silicon wafers, and then applied spin coating at 2000 rpm for 1 min using a spin coater (Ossila, Solpro Business Park, Sheffield) to form a uniform PDMS layer. The substrates were then cured at 70°C for 2 hours in an oven (Genlab, MINO/30/F/PDIG, Widnes, UK). Before printing experiments, the substrates were first put into the glass beaker containing acetone for 30 min ultra-sonic bath (Ultrasonic water bath Grant XUBA3, Cambridgeshire, UK), and the substrates were then cleaned by 30 min ultra-sonic bath in ethanol and DI-water, respectively. The cleaned substrates were then dried by a gas gun with air gas.

In order to modify the surface properties of the substrates, the PDMS coated glass substrates were exposed to UV-Ozone surface treatment (ProCleaner™, Bioforce Nanosciences, USA) for 10, 20 and 30 minutes, separately. 10 min and 40 min UV-Ozone treatments were applied to the silicon substrate and the PDMS coated silicon substrate, respectively.

3.3 Inkjet Printing Method

Two inkjet printing systems were used in our experiments, which are Dimatix Inkjet Printer (DMP 2800, Fujifilm Dimatix, Santa Clara, USA), and Super Inkjet Printer (SLTS0505-KBD, SIJ Technology, Tsukuba, Japan).

3.3.1 Dimatix Inkjet Printing

Two types of printheads, DMC 11610 and DMC 11601 (Fujifilm Dimatix) that deposited drops of nominal volume 10 pL and 1 pL, were equipped to the Dimatix inkjet printer. Both have 16 individually nozzles with a nozzle to nozzle spacing of 254 μm, and all printing experiments were carried out with single nozzle printing. A schematic diagram showing the main parts of cartridge and nozzle is shown in Figure 3-1.

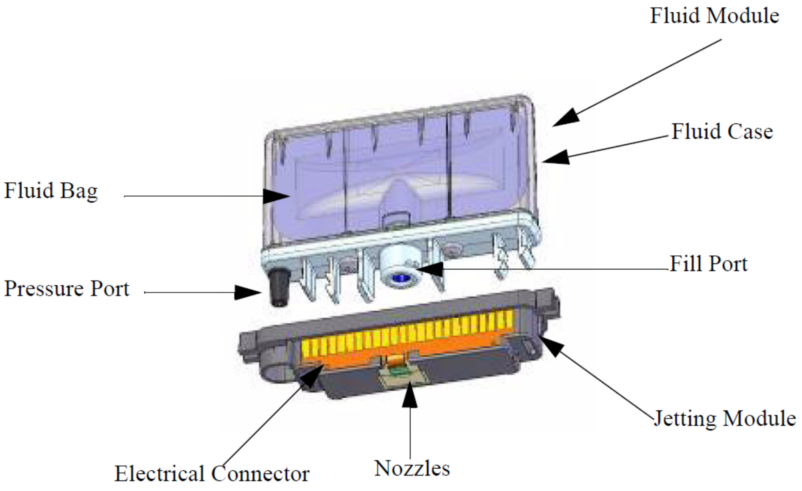

Figure 3-1 Schematic diagram showing the major parts of the cartridge. Adapted from the “Dimatix Materials Printer DMP-2800 Series User Manual”.[185]

The actuation waveform used is the ANP – Dimatix Model Fluid waveform, as shown in Figure 3-2. The total jetting period is 11.52 μs, and the applied voltage is the peak voltage shown in the plot. The jetting waveform can be divided into four stages, as shown in Figure 3-3:[185]

1) Start, or standby stage: The PZT/Si bimorph is slightly deflected prior to the initiation of the driving pulse.

2) Phase 1: A decrease of voltage to zero moves the bimorph upward and draws the ink fluid into the chamber from the reservoir.

3) Phase 2: Increased voltage deflects the PZT/Si bimorph and causes the droplet formation at the nozzle.

4) Phase 3: The droplet is ejected from the nozzle, and the voltage decreases to the bias level for the PZT/Si bimorph to move to the standby position for next droplet ejection.

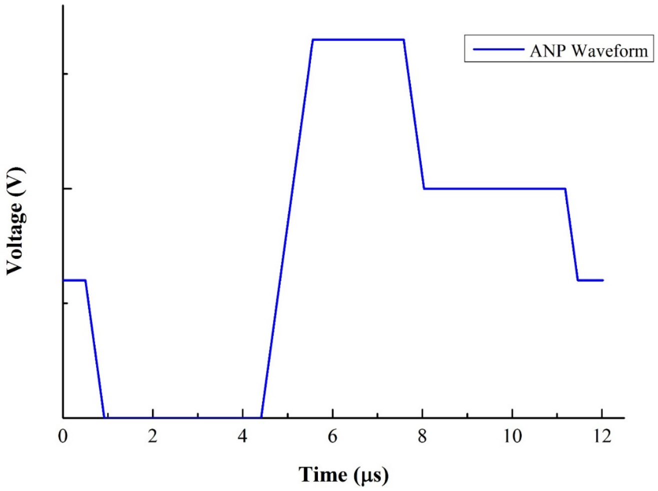

Figure 3-2 ANP Waveform setting used in the experiments.

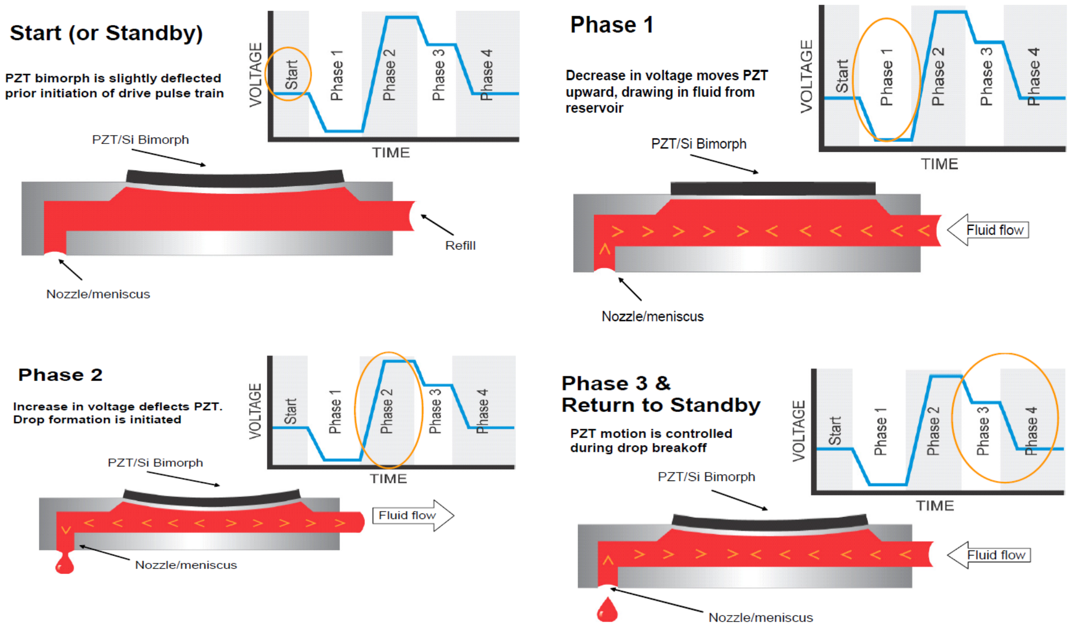

Figure 3-3 Schematic illustration of printhead during jetting period. Adapted from the “Dimatix Materials Printer DMP-2800 Series User Manual”.[185]

During printing, the cartridge temperature was set to 35 °C, and the printhead to substrate distance was set to 1 mm. The substrate temperature can be adjusted by changing the platform temperature. The actual drop volumes generated under the experimental conditions were determined by printing a fixed number of drops onto a piece of tin foil at room temperature and measuring their mass.

3.3.2 Super Inkjet Printing

The super inkjet printing system is composed of three main parts: the printer, voltage control and computer control, as shown in Figure 3-4 a. The chamber view of the printer is shown in Figure 3-4 b.

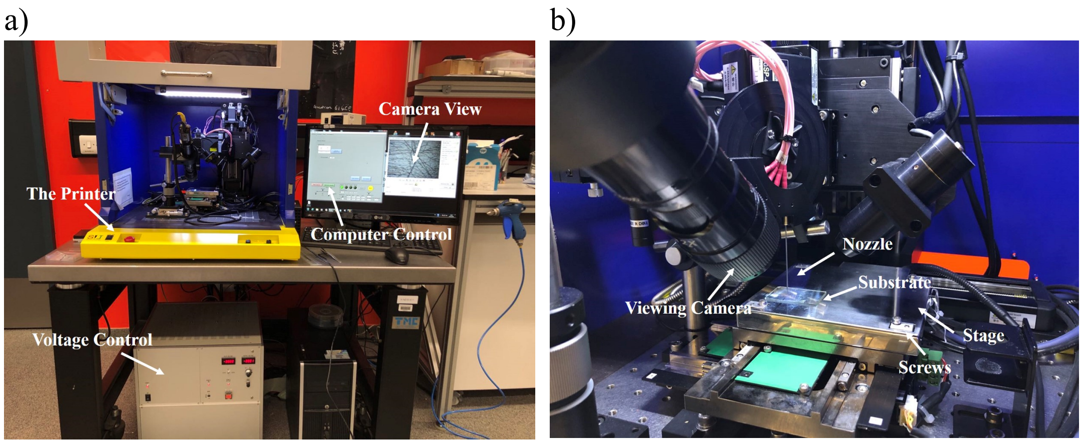

Figure 3-4 Images showing the Super inkjet printing system: a) the outlook of the system, and b) the printing chamber.

The printhead used in the experiments is the Super Fine glass nozzle with the tip diameter around 2 μm (Figure 3-5 a). The silver nanoparticle ink was filled into the glass nozzle with a 10 μl pipette (Eppendorf UK Limited, Stevenage, UK), and the nozzle filling process requires the tip of the nozzle to be fully occupied by the ink without any bubbles. The flatness of the substrate influences the nozzle to substrate distance during printing, thus the substrate requires to be horizontally flattened before printing. This is done by adjusting the screws shown in Figure 3-4 b and observing the nozzle to reflection distance with blank run of the nozzle at zero applied voltage. The nozzle and substrate conditions can be viewed by the camera in the chamber, as shown in Figure 3-5 b.

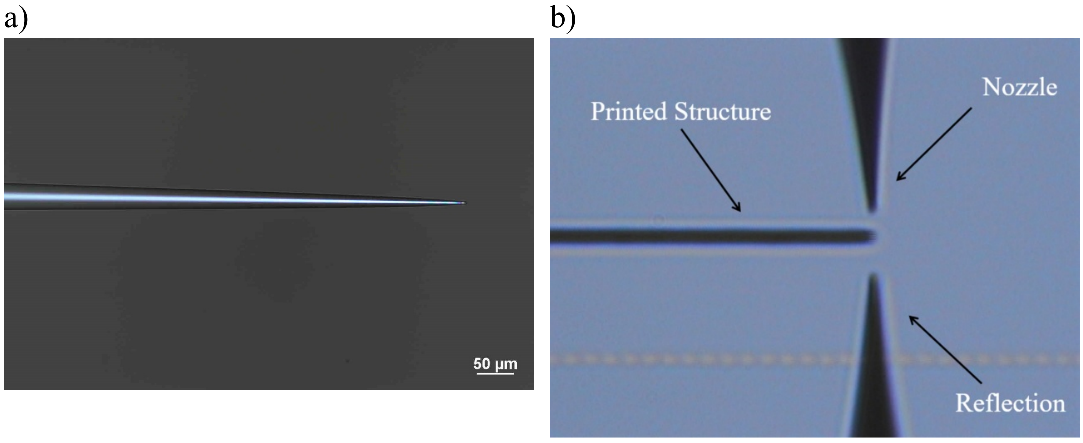

Figure 3-5 a) Image of the Super Fine nozzle used in the experiments, and b) camera view during printing.

Three types of substrates were applied to the super inkjet printing experiments, which are silicon wafer, PDMS coated silicon, and polyimide. The waveform used for printing on the silicon substrate is a periodic single pulse waveform with specific pulse width time (T_p), bias voltage (V_{bias}), and amplitude voltage (V_{amp}), as shown in Figure 3-6 a. As the PDMS and polyimide surfaces are nonconductive and might lead to droplet atomization due to the charging effect, a bipolar waveform was applied to the substrates with the purpose of neutralizing the charging effect, as shown in Figure 3-6 b. The time period between two adjacent bipolar pulse was set the same to achieve stable deposition with identical drop spacing.

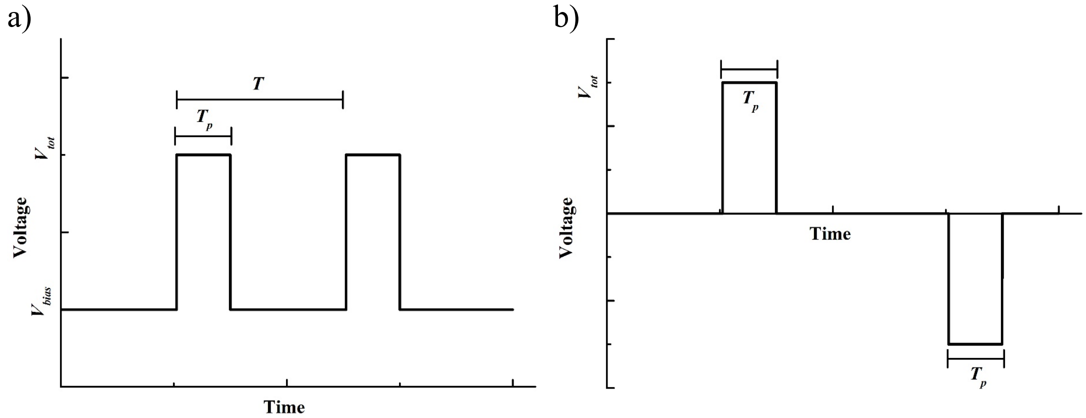

Figure 3-6 Waveform used in the super inkjet printing experiments: a) single pulse waveform, and b) bipolar waveform.

As the pulse width time T_p is dependent on the applied jetting frequency f, to remain the same pulse width time during printing, the duty ratio of pulse x_p was adjusted for specific frequency. The duty ratio and frequency in our experiments at various printing velocity and drop spacing conditions are listed in Appendix A and B.

3.4 Characterization and Analysis Methods

The contact angles of the ink deposited on the substrates were measured using a drop shape analyser (DSA 100, Krüss, Hamburg, Germany). For the advancing contact angle measurement, ink was pumped into a deposited droplet through the needle continuously to grow the droplet, and this process was recorded into a video. From the video the advancing contact angle was measured from the frame in which the contact line started to advance. Similarly, for the receding contact angle measurement liquid was shrunk from the deposited droplet by the needle and the receding contact angle was measured from the frame in which the contact line started to recede. An example of the advancing and receding contact angle measurements on the 10 min UV-Ozone treated PDMS coated glass (F10 substrate) is shown in Figure 3-7. The contact angle data on various substrates are summarised in Table 3-1.

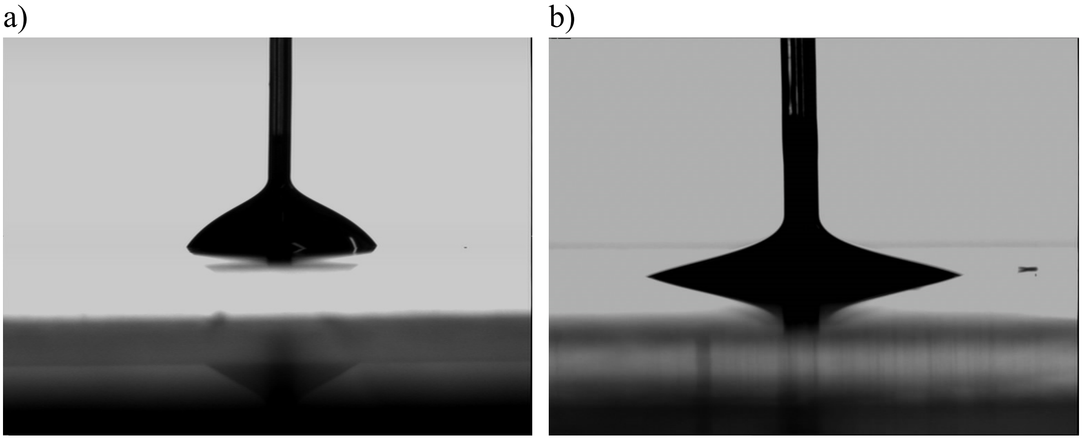

Figure 3-7 Images showing the measurements of contact angles of silver ink deposited onto 10 min UV-Ozone treated PDMS coated glass: a) advancing contact angle, and b) receding contact angle.

Table 3-1 The advancing and receding contact angle of the ink on various substrates.

Substrate	**Substrate Type**	**UV-Ozone treatment time (minutes)**	**Advancing Contact angle**	**Receding Contact angle**
F0	PDMS coated glass	0	59.2° ± 2.1°	21.6° ± 1.9°
F10	PDMS coated glass	10	54.1° ± 1.5°	16.0° ± 1.7°
F20	PDMS coated glass	20	50.3° ± 1.7°	9.3° ± 0.5°
Z10	Silicon	10	10.9° ± 1.2°	0°
Z30	PDMS coated glass (28 °C)	30	45.5° ± 1.4°	0°
Z30	PDMS coated glass (60 °C)	30	53.8° ± 1.1°	0°
Z40	PDMS coated silicon	40	34.7° ± 1.5°	0°
PI	Polyimide	0	19.1° ± 1.2°	0°

The dimensions and morphologies of the printed structures were measured using an optical microscopy (Nikon Eclipse LV100ND, Japan), and the profile of the structures was characterized by a white light interferometry (Bruker ContourGT, USA). ImageJ was used to analyse the area of the deposited droplets on the nonconductive substrates in Chapter 6. The image was first converted to an 8-bit image, and the area of the deposited droplets were analysed by adjusting the threshold of the image. The integral calculations in Chapter 5 were processed by using Mathematica.

To test the electrical properties of the lines printed at ultra high resolution, a series of line electrodes with various printing layers was printed onto silicon, PDMS coated silicon and polyimide substrates by the Super Inkjet printer. The electrodes were composed of a 2 mm line in the middle and two 100 μm × 100 μm squares on both sides for electrical testing. The printed line electrodes were annealed in an oven (Genlab, MINO/30/F/PDIG, Widnes, UK) at 150 °C for 1 h. The conductance of the electrodes was then measured by using a two-point probe (Keithley 2400 Source Meter, UK).

Chapter 4 Stability of Line Structures with Zero Receding Contact Angle Produced by Inkjet Printing at Small Drop Volume

4.1 Introduction

In recent years, inkjet printing technology has gained considerable interest as a patterning tool in a large range of areas beyond its origin in graphics output. Many applications for inkjet printing of functional materials and devices require stability and uniformity of the printed structures. Hence, an understanding of how a stable parallel line structure forms is taken as a starting point. Davis studied the stability of a static liquid bead by using linearized stability theory and proposed that [143] a parallel sided liquid bead can be stable against shape change when the contact line is fixed and the contact angle is $< \pi/2$. These observations were confirmed experimentally by Schiaffino and Sonin.[144] However, there was no consideration of the case when the liquid bead shows contact angle hysteresis, since the boundary conditions are nonlinear in this case.

In order to achieve stable printed lines, the printed liquid drops must clearly be positioned sufficiently close together to allow overlap; i.e. the drop spacing must be smaller than the equilibrium diameter of a single printed droplet. However, simple overlap is not sufficient to ensure the formation of a parallel line. It has been shown that, in the case of contact line pinning, where liquid on the substrate can only spread but cannot retract due to a zero receding contact angle, a critical overlap is required to ensure a parallel sided liquid drop because of the need to conserve volume and maintain the equilibrium contact angle, this can be thought of as a limiting maximum drop spacing.[11, 186] Further reduction in drop spacing leads to a stable parallel line with the line width increasing as the drop spacing reduces, until a critical minimum drop spacing occurs, depending on the ink and substrate conditions, below which a bulging instability forms.[11-13] Thus the formation of a stable inkjet printed parallel line is limited by two bounds. The lower bound line width for line stability is determined by the liquid bead surface tension and contact line pinning,[11, 186] this defines the maximum drop centre spacing that allows sufficient drop overlap such that a stable line forms without the need for the contact line to recede. The upper bound width is limited by the bulging instability that occurs when drop spacing is smaller than a minimum critical value, this is a dynamic instability and also depends on the rate of drop arrival.[11-13]

The lower bound for line width (maximum drop spacing) is easily calculated assuming an equilibrium contact angle and conservation of volume.[11, 13, 186] However, the upper bound for line width or minimum drop spacing is less obvious. Duineveld [12] analysed the conditions for the onset of the bulging instability assuming a zero receding contact angle ink on the substrate. The onset of the instability was considered in terms of the dynamic process for the growth of a liquid line through the sequential deposition of overlapping liquid drops considering the competition between the spreading of the new liquid onto unwetted substrate and the flow of liquid through the existing liquid bead on the surface driven by the lower Laplace pressure of the stable liquid bead. The fluid regime leading to a bulging instability can be divided into two conditions, distinguished by the magnitude of the advancing contact angle of the newly deposited liquid. At high advancing contact angle, the flow back along the bead, generated by the Laplace pressure difference, is relatively large, resulting in the newly deposited liquid flowing towards the low pressure region to form periodic regular bulging instability rather than extending the bead. At low advancing contact angle, however, the pressure difference is significantly reduced, leading to a relatively low flow rate in the bead. Hence the stability of the printed line structure is a dynamic process that is controlled by the fluid/substrate contact angles and the rate at which drops arrive at the surface.

Stringer and Derby [14] developed a model for inkjet printed line stability, which combined the volume conservation approach valid for the minimum line width (maximum droplet spacing) limiting bound with a modification of Duineveld's model for the dynamic instability at maximum stable line width (minimum drop spacing), to predict printed line stability as a function of drop spacing and printed line speed (droplet deposition rate) with the principal controlling variable being the drop volume and its contact angle on the surface.

Stringer reported experimental work to validate these models with fluids showing zero, or close to zero, receding contact angle at relatively low drop generation rates (<1 kHz) with drop volumes in the range (50–100 pl). These conditions are not within the range of most commercial DOD inkjet equipment, which typically have drop volumes in the range 1 – 30 pL and drop generation rates > 10 kHz. The results reported in this chapter investigate the applicability of Stringer's model for line stability in this smaller droplet size regime using droplet 10 pL and 1 pL.

4.2 Stringer's Line Stability Model

For convenience, a summary of the line stability model proposed by Stringer is presented here. For a full derivation the reader is referred to the original publication.[14]

The Bond number, $Bo = \rho g d_o^2 / \sigma_{LV}$, where ρ is the density of the fluid, σ_{LV} is the liquid/vapour surface energy of the fluid, g is the gravitational acceleration, and d_0 is the length scale, is used to determine whether gravitational or capillarity forces are dominant in fluid processes. In the case of inkjet printing, where the length scale of a droplet is typically in the range 10 – 100 μm, Bo is significantly lower than 1 for typical ink fluid properties. Hence gravitational forces can be neglected and the shape of the drop will be controlled by capillarity. In this case the equilibrium shape of an isolated deposited drop can be modelled as a spherical cap. The parameter β_{eqm} is defined as the ratio between the equilibrium base diameter of the spherical cap, d_{eqm}, and, d_o, the diameter of the original spherical drop before contact with the surface:

$$\beta_{eqm} = \frac{d_{eqm}}{d_o} = \left(\frac{8}{\tan(\theta/2)\left(3 + \tan^2(\theta/2)\right)} \right)^{\frac{1}{3}} \qquad (4-1)$$

where θ is the equilibrium contact angle as defined by Young's equation. As the droplet spreads and advances on the solid surface after impact, the use of static advancing contact angle (θ_a) instead of equilibrium contact angle in Equation 4 – 1 is more appropriate.[1, 14]

If a line of evenly spaced intersecting drops of spacing, p, coalesce to form a stable liquid bead of circular cross-section and base width, w, volume conservation leads to the following relation between these parameters and the initial drop diameter:[10]

$$w = \sqrt{\frac{2\pi d_0^3}{3p\left(\frac{\theta_a}{\sin^2\theta_a} - \frac{\cos\theta_a}{\sin\theta_a}\right)}} \tag{4 – 2a}$$

Or in dimensionless form with $w^* = w/d_0$ and $p^* = p/d_0$

$$w^* = \sqrt{\frac{2\pi}{3p^*\left(\frac{\theta_a}{\sin^2\theta_a} - \frac{\cos\theta_a}{\sin\theta_a}\right)}} \tag{4 – 2b}$$

Stringer showed that for the case of a liquid bead made from the coalescence of a line of evenly spaced sessile drops that have pinned contact lines (i.e. a zero receding contact angle), the minimum width of the a parallel sided liquid bead will be equal to the diameter of a single equilibrium drop, d_{eqm}, on the substrate,[14] or $w^*_{min} = \beta_{eqm}$. This defines, p^*_{max}, the maximum drop spacing that can form a stable parallel sided liquid bead, with

$$p^*_{\max} = \frac{2\pi}{3\beta_{eqm}^2\left(\frac{\theta_a}{\sin^2\theta_a} - \frac{\cos\theta_a}{\sin\theta_a}\right)} = \frac{2\pi}{f(\theta_a)} \tag{4 – 3a}$$

where

$$f(\theta_a) = 3\beta_{eqm}^2\left(\frac{\theta_a}{\sin^2\theta_a} - \frac{\cos\theta_a}{\sin\theta_a}\right) \tag{4 – 3b}$$

and the maximum drop spacing, p_{max}, is

$$p_{\max} = \frac{2\pi d_o}{f(\theta_a)} \tag{4 – 3c}$$

The threshold or minimum drop spacing for the bulging instability is based on the prior work of Duineveld.[12] When the drop spacing is below the minimum value, the liquid bead forms a series of bulges connected by narrow beads of constant width. The condition for the onset of the bulging instability requires the fluid flow along the bead,

Q, which is driven by the pressure difference between the bulge and the leading tip of the growing liquid bead to be much larger than the flow rate, Q_A, of new liquid arriving at the growing tip. Duineveld defined Q as

$$Q = \frac{4S\Delta PA^2}{\eta l} \qquad (4-4)$$

where ΔP is the pressure difference between the tip of the bead and an incipient bulge, A is the cross-sectional area of the liquid bead, η is the fluid dynamic viscosity, l is the length from the bead tip to the bulge and S is a shape factor with:

$$S = \frac{\theta_c - \sin\theta_c \cos\theta_c}{8\left(\sin\theta_c + \theta_c\right)^2} \qquad (4-5)$$

where θ_c is the dynamic contact angle on drop impact. Stringer [14] defined Q_A as the rate of arrival of fluid from the printed droplets, which is defined as the volume of a single droplet, V_D, multiplied by the drop generation frequency, f:

$$Q_A = V_D f = \frac{V_D U_T}{p} = \frac{\pi d_o^3 U_T}{6p} \qquad (4-6)$$

where U_T is the printing velocity defined as the rate at which the drop generator moves along the printed line parallel to the liquid bead.

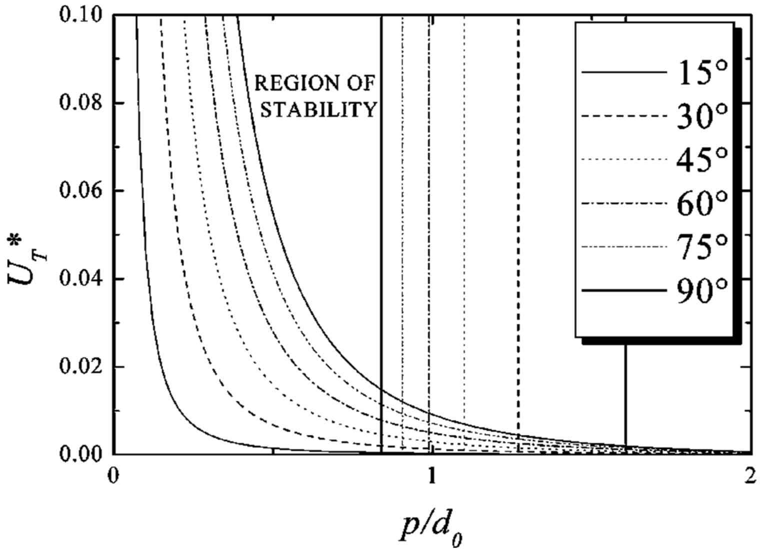

Figure 4-1 The region of stable, parallel sided liquid lines formed by overlapping trains of identical liquid drops is defined by a parameter space described by the dimensionless drop spacing, $p^* = p/d_o$, and the dimensionless traverse velocity of the drop generator, U^*_T. The curved line rising to the left represents the onset of the bulging instability at small drop spacing and the vertical line to the right represents the maximum drop spacing for a parallel line. Both limits are a function of the contact angle of the liquid drop on the substrate. Reproduced from Stringer and Derby.[14]

After considerable manipulation the threshold for the formation of stable lines is defined by the following inequality:

$$\frac{\eta U_T}{\sigma_{LV}} > \frac{4\pi S \sin\theta_a}{3\beta_{eqm} K_1 (p^*)^2} \left\{ 1 - \left(\frac{p^* f(\theta_a)}{2\pi} \right)^{1/2} \right\} \qquad (4-7a)$$

or

$$U_T^* > g(p^*, \theta_a) \qquad (4-7b)$$

with

$$U_T^* = \frac{\eta U_T}{\sigma_{LV}} \qquad (4-7c)$$

and

$$g(p^*, \theta_a) = \frac{4\pi S \sin\theta_a}{3\beta_{eqm} K_1 (p^*)^2} \left\{ 1 - \left(\frac{p^* f(\theta_a)}{2\pi} \right)^{1/2} \right\} \qquad (4-7d)$$

where p^* is the dimensionless drop spacing, $p^* = p/d_o$, K_1 is a constant > 1 and θ_a is the advancing contact angle. Stringer assumed that at the onset of the bulging instability $\theta_a = \theta_c$. The left side of inequality 4 – 7 is a dimensionless function of printing velocity, U_T, that has a similar form to the Capillary number but should not be confused with it. The right side is a function $g(p^*, \theta_a)$ of θ_a, the advancing contact angle, and p^*, the dimensionless drop spacing. Notice that the drop spacing in our analysis is normalized by d_0 for simplicity rather than d_{eqm} as Stringer presented, there is a slight change in the g function for the β_{eqm} compared with the original equation in the paper. Figure 4-1 shows a graphical representation of inequality 4 – 7 plotted as a series of curved lines, each representing a different value of the advancing contact angle, in a parameter space defined by U_T^* and p^*, the region above and to the right of the line defines the conditions for the formation of stable lines. The dashed vertical lines represent the maximum drop spacing, p_{max}, or minimum line width condition (Equation 4 – 3), also for a number of representative values of the contact angle. This plot clearly shows that the limiting p_{max} determined by force equilibrium is independent of the rate at which a liquid bead is deposited, while p_{min}, represented by $g(p^*_{min}, \theta_a)$, shows a dynamic dependence on both drop spacing and printing rate. Finally, Stringer proposed that there could be a further limit to stable drop printing (the horizontal line towards the top of the figure), perhaps indicating the mechanical limitations of the printing equipment. Derby has shown that this could also be represented by the known limits for drop generation mechanisms.[2]

4.3 Results and Discussion

4.3.1 Inkjet Printing Droplet Generation and Deposition

In order to investigate the stability of printed structures on the substrate with zero receding contact angle, silver nanoparticle ink was deposited onto the PDMS coated glass substrate. The physical properties of the silver ink are shown in Table 4-1. The waveform used was the ANP Waveform with a print voltage of 16.5V for the 10 pL head and 10.5V for the 1 pL head. 30 min UV-Ozone treatment was applied to the PDMS substrate to eliminate the receding contact angle, and for simplicity the substrate was named as Z30 substrate, with the contact angle information listed in Table 4-2. The actual drop volumes generated under the experimental conditions were determined by printing a fixed number of drops and measuring their mass, this indicated that the drop volume with the 10 pL head was 8.5 pL and with the 1 pL head 1.5 pL.

Table 4-1 Physical properties of the silver nanoparticle ink.

Temperature (°C)	**Surface Tension (mNm^{-1})**	**Viscosity (mPa·s)**	**Density (kgm^{-3})**
28	28	6.6	1450
60	24.3	3.4	1450

Table 4-2 Contact angle of silver ink on PDMS coated glass at different substrate temperatures.

Substrate	**Temperature (°C)**	**UV-Ozone treatment time (minutes)**	**Advancing Contact angle**	**Receding Contact angle**
Z30	28	30	45.5° ± 1.4°	0°
Z30	60	30	53.8° ± 1.1°	0°

Figure 4-2 shows images illustrating the droplet formation process from a 10 pL Dimatix printhead at print voltage 16.5 V. At first it appears that a sphere appears in the nozzle. However, as more liquid emerges this is seen to form a leading droplet followed by a long tail. After 29 µs the long ligament ruptures close to the nozzle and starts to coalesce into the leading droplet before rupturing again and retracting into a satellite drop, shown in the image at 50 µs. The satellite drop then catches up with the leading drop and merges to form the final stable spherical droplet.

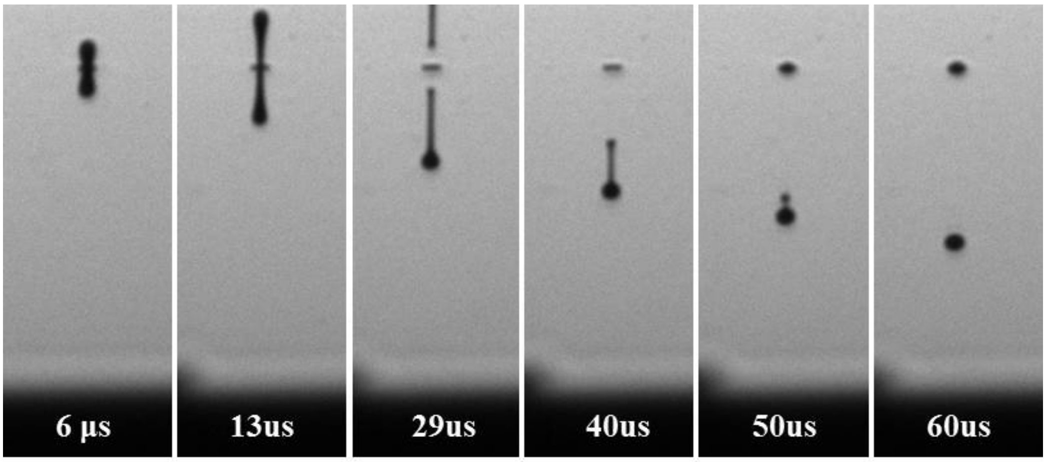

Figure 4-2 Droplet generation process with time by a 10 pL printhead at voltage 16.5 V.

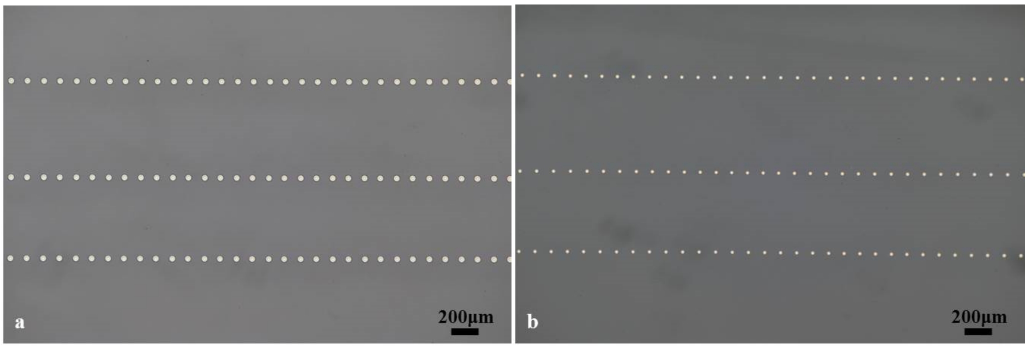

Figure 4-3 Printed dot structures on Z30 substrate at 28 °C, drop spacing 120 µm and print speed 300 mms^{-1} (a) 10 pL printhead, and (b) 1 pL printhead.

Figure 4-3 shows an array of discrete printed dots on a Z30 substrate printed at 28 °C using printheads of nominal drop size 10 pL and 1 pL, respectively. The print speed was set to 300 mms^{-1} and drop spacing to 120 µm. As expected, large dots were obtained with 10 pL drops and smaller dots are seen with 1 pL drops. Both printheads produce regularly spaced drops and no subsidiary drops, indicative of satellite drops, are seen. The nominal 10 pL head produces drops of volume 8.5 pL and the 1 pL head 1.5 pL. The single deposited diameter d_{eqm} on Z30 substrate with different printhead and substrate temperature conditions are shown in Table 4-3.

Table 4-3 Single deposited droplet diameter on Z30 substrate.

Temperature (°C)	**Printhead (pL)**	**Droplet Volume (pL)**	**d_{eqm} (μm)**	**Contact Angle**
28	1	1.5	27.0 ± 0.3	45.5° ± 1.4°
60	1	1.5	24.8 ± 0.3	53.8° ± 1.1°
28	10	8.5	46.3 ± 0.6	45.5° ± 1.4°
60	10	8.5	42.1 ± 0.5	53.8° ± 1.1°

4.3.2 Lines printed on Z30 substrates with 1 pL printhead

To investigate the stability of printed line morphologies with zero receding contact angle, silver nanoparticle ink was deposited onto the Z30 substrate, see Table 4-2 for substrate treatment and contact angles. Printing was carried out with substrate temperature of 28 °C and 60 °C using 1 pL and 10 pL printheads, respectively. Three lines were printed consecutively onto the substrate from left to right for each printing setup, and the printing direction was along the deposited lines. Drop spacing can be easily adjusted through the printer's built-in function, and the printing velocity was adjusted by changing the jetting frequency at specific drop spacing. The printing speed ranged from 300 to 30 mms^{-1} and drop spacing was in the range 5 – 30 μm. The dried morphologies of the printed lines were imaged and shown below.

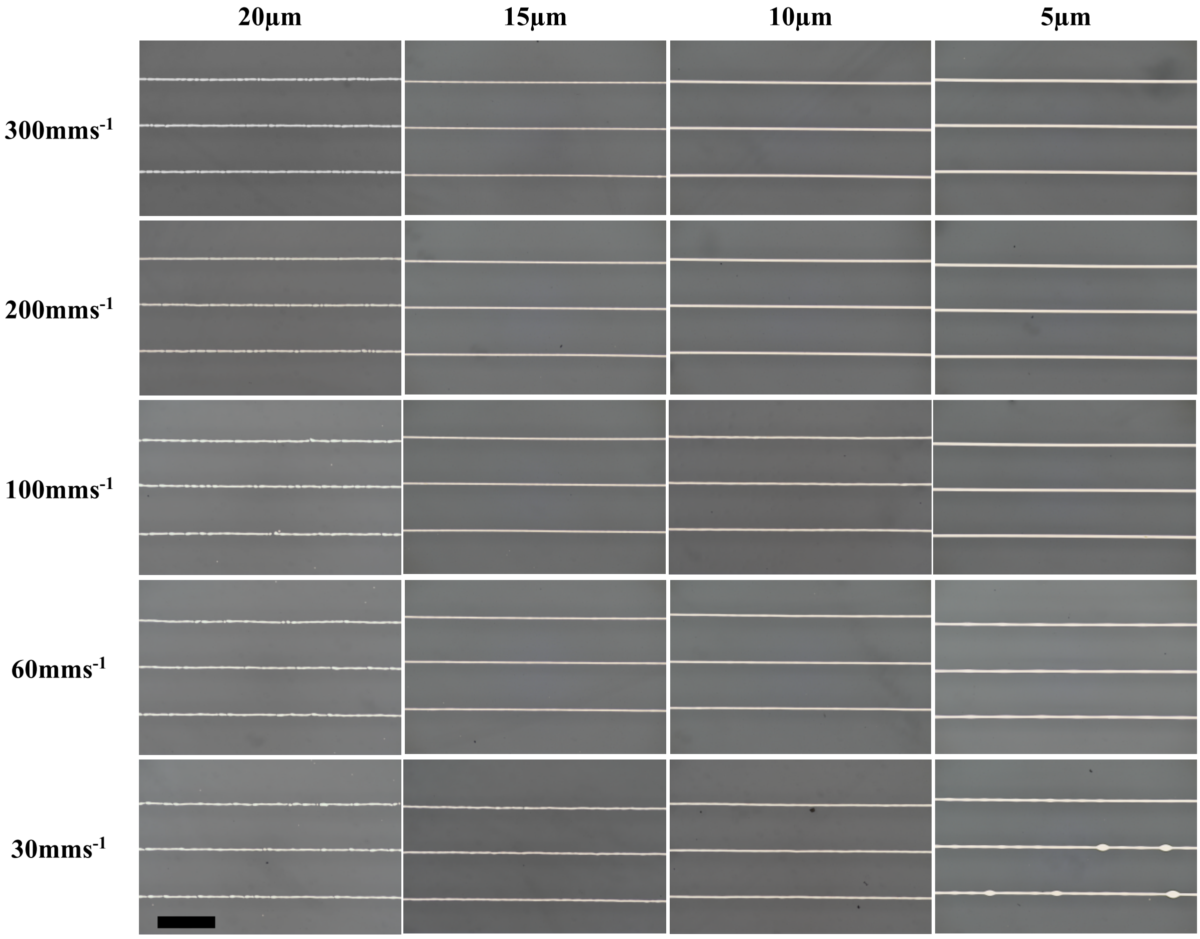

Figure 4-4 Printed structures on Z30 substrate with temperature 28 °C at various print speeds and drop spacing with 1 pL printhead. The scale bar is 500 μm.

Figure 4-4 shows the resulting printed structures as printed with 1 pL drops at 28 °C, with advancing contact angle 45.5° and receding contact angle 0°. Stable line structures can be obtained from a range of drop spacings. For all print speeds, discrete line segments were obtained at drop spacing 20 μm, and stable lines were formed at drop spacing < 15 μm. Stable parallel sided line structures were achieved at all values of drop spacing < 15 μm for print velocity in the range 100 – 300 mms^{-1}, however at the lowest print velocity of 30 mms^{-1}, bulges are observed at a drop spacing of 5 μm and at 60 mms^{-1} printing at a drop spacing of 5 μm shows line width irregularity but no discrete bulges. For a better viewing, magnified pictures of discrete line segments at large drop spacing and bulging lines at small drop spacing are shown in Figure 4-5.

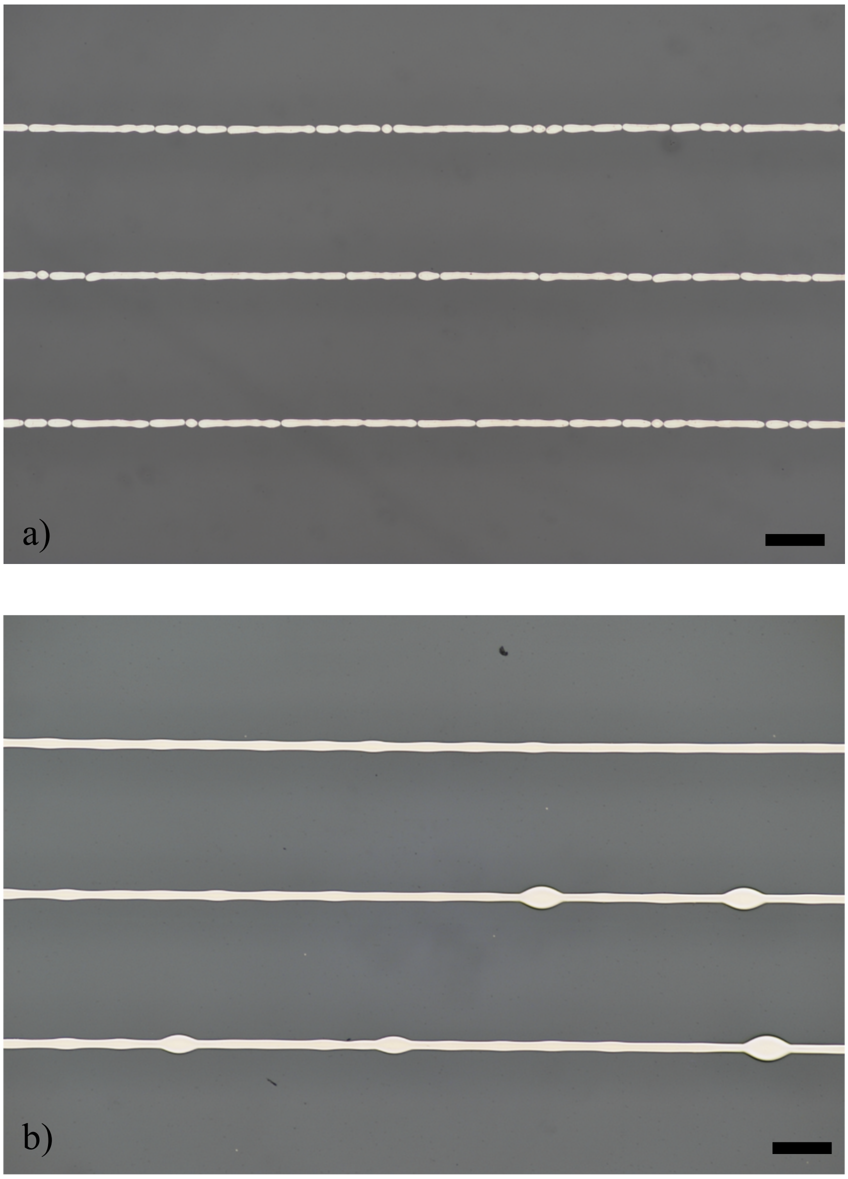

Figure 4-5 Magnified printed structures with 1 pL printhead on Z30 substrate with temperature 28 °C: (a) discrete segments at drop spacing of 20 µm and print velocity of 300 mms^{-1}, (b) bulging lines at drop spacing of 5 µm and print velocity of 30 mms^{-1}. The scale bar is 200 µm.

A similar series of printed lines at different drop spacings and print speeds obtained using the 1 pL printhead at 60 °C with advancing contact angle 53.8° and receding contact angle 0° is shown in Figure 4-6. For all the print speeds, stable parallel sided lines were firstly observed at drop spacing 15 µm, above which line segments were obtained. For the structures printed in the print velocity range 100 – 300 mms^{-1}, all the structures from drop spacing 15 µm to 5 µm were shown to be stable parallel sided lines. At the print velocity of 60 and 30 mms^{-1}, stable lines were formed from drop spacing 15 to 10 µm, and unstable bulging structures were observed at a drop spacing of 5 µm.

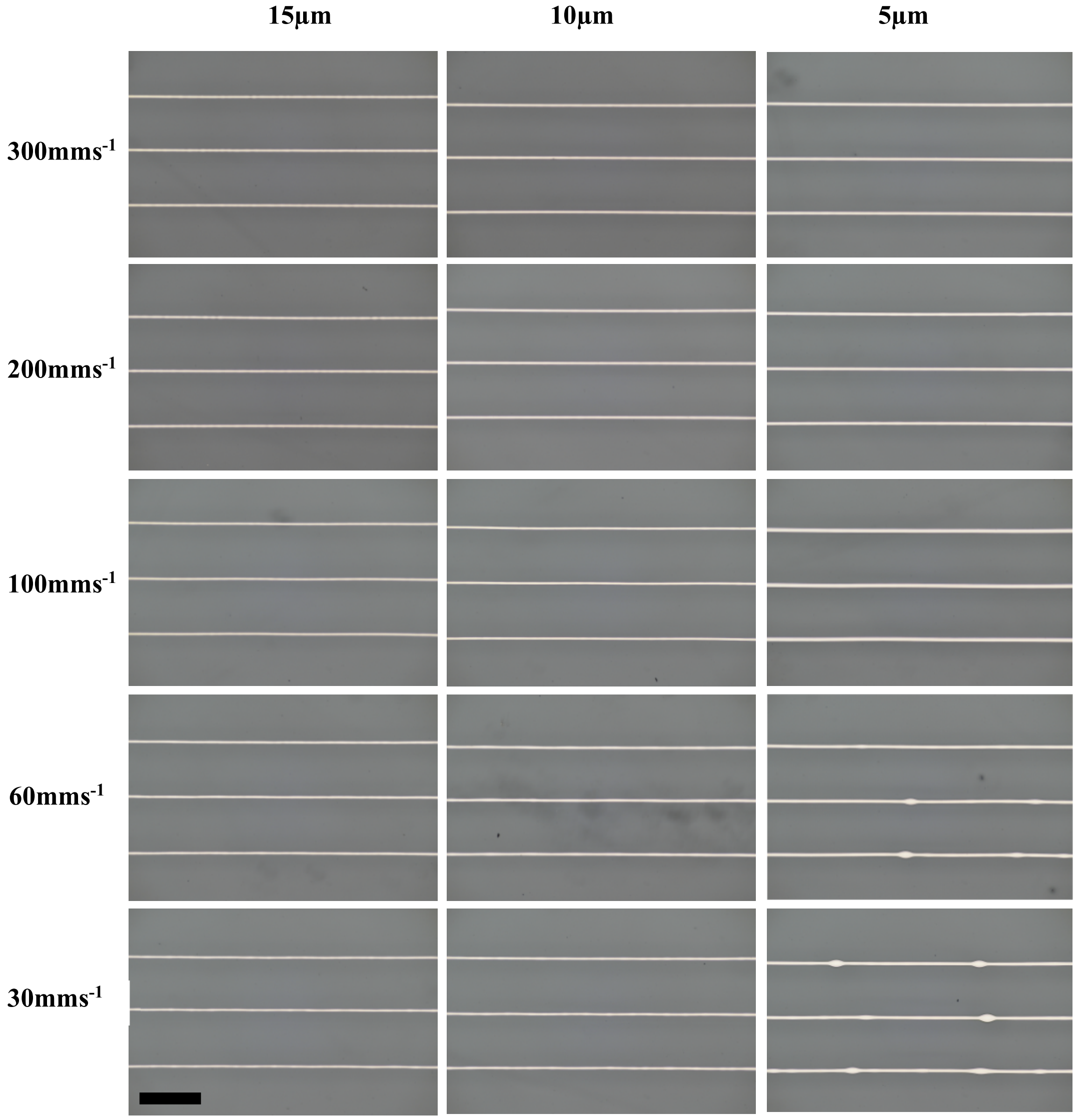

Figure 4-6 Printed structures Z30 substrate with temperature 60 °C at various print speeds and drop spacing with 1 pL printhead. The scale bar is 500 µm.

Figure 4-7 shows our experimental results compared with the predictions of Stringer's model. The maximum drop spacing results generally agree quite well for printing at both substrate temperatures, with a predicted maximum drop spacing of 15.5 and 14.7 µm for 1.5 pL drops (nominally 1 pL printhead) on substrates with temperature 28 and 60 °C, respectively, although for the temperature 60 °C the prediction for p_{max} is slightly smaller than the observed stability limit. The onset of the bulging instability using the inequality in Equation 4 – 7 is shown as the curved line in Figure 4-7. Agreement between the observed printed line stability limit and Stringer's model is excellent for both the maximum and minimum drop spacing bounds. Note that it was not possible to print lines with $p^* < 0.35$ because of the physical limitations of the printer used in this study.

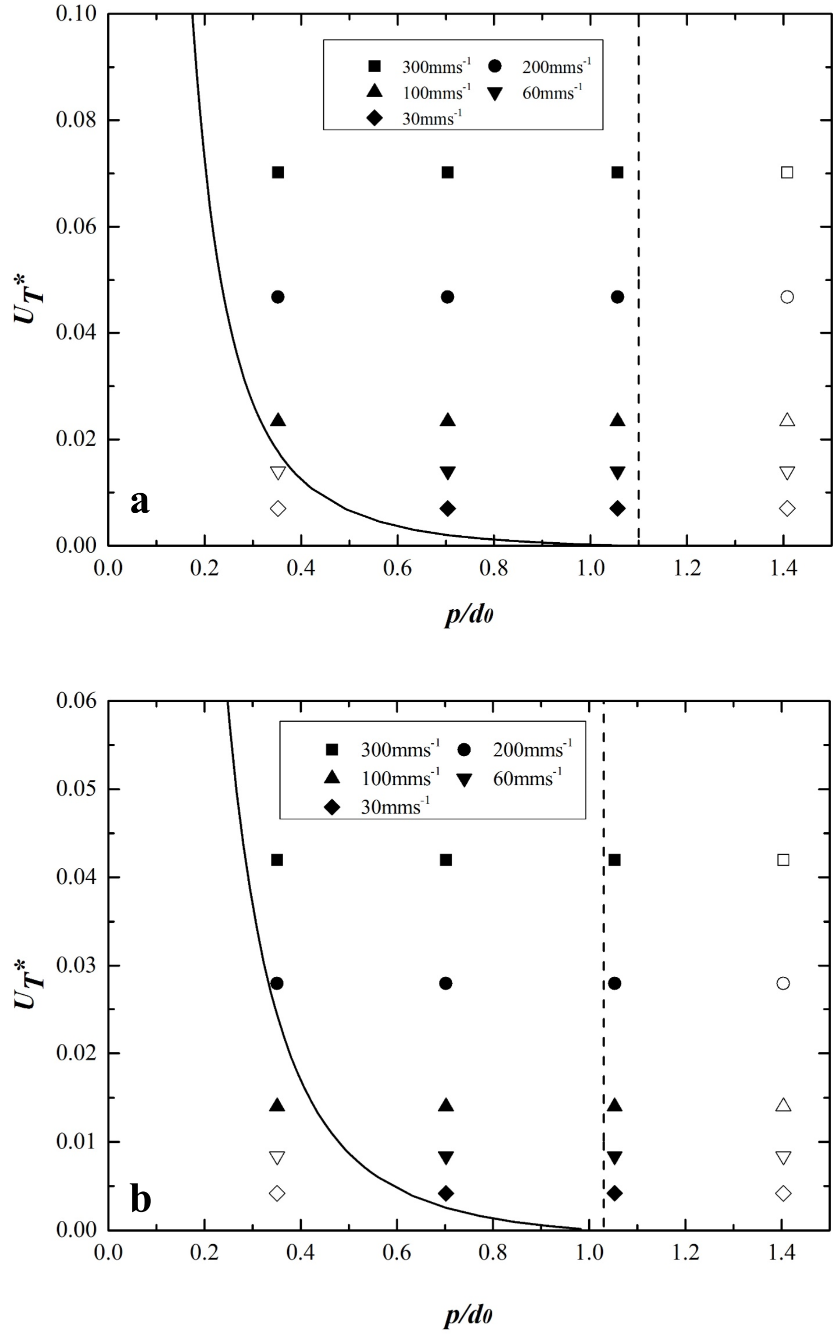

Figure 4-7 Stability map showing the condition for the onset of the bulging instability with data for the nanoparticle ink experiments with 1 pL head at (a) substrate temperature 28 °C, and (b) substrate temperature 60 °C, respectively. Open symbols indicate unstable morphology and filled symbols indicate stable morphology. The dashed line shows the maximum drop spacing bound, and the solid line is the bulging instability bound.

Figure 4-8 compares our experimental results for the line width with Stringer's prediction (Equation 4 – 2a). For structures which displayed bulges, the width of the parallel sided connecting ridge is used. There is good agreement between the model and experimental results at drop spacings of 10 and 15 µm, with no clear systematic variation as a function of printing velocity for either printing temperature. However, with a drop spacing of 5 µm the agreement is much less good for lines at 28 °C that show bulges and those that display parallel sides, although the greatest deviation occurs at the lowest printing speed when the number of bulges is greatest.

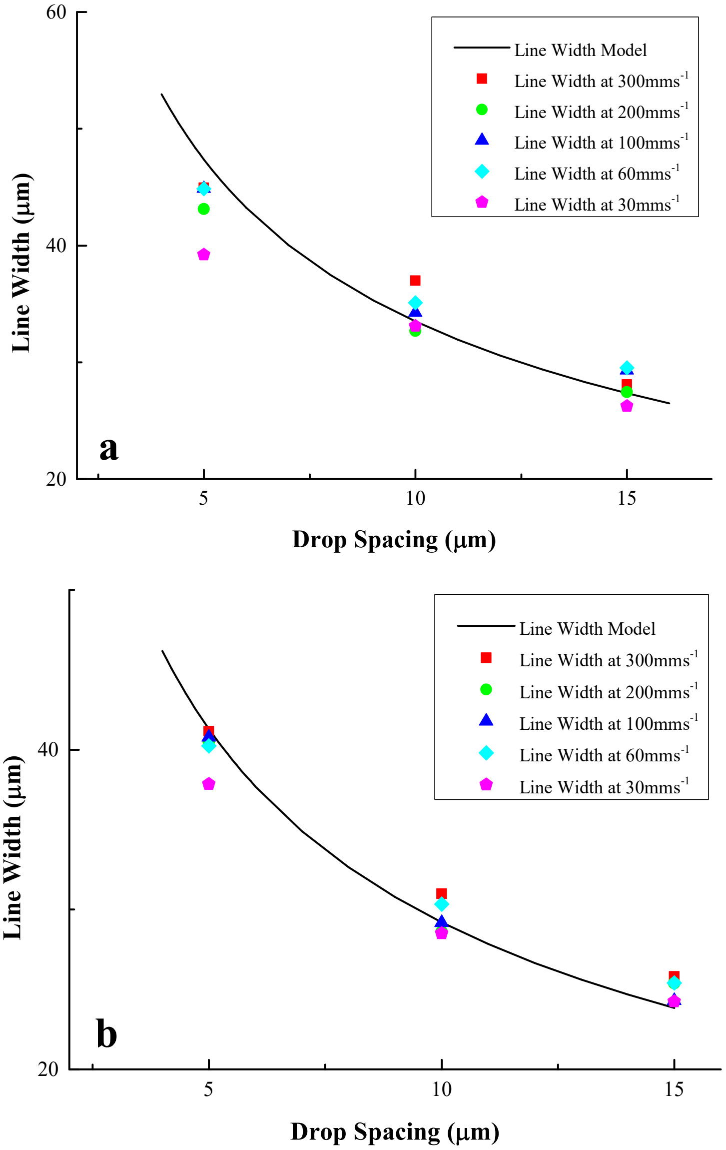

Figure 4-8 Measured line width results on Z30 substrate using 1 pL printhead at (a) substrate temperature 28 °C, and (b) substrate temperature 60 °C, along with line width model prediction. The standard deviations of the line widths are all below 1 µm for stable lines.

4.3.3 Lines printed on Z30 substrates with 10 pL printhead

The printed structures on Z30 substrates at 28 °C with 10 pL drops and advancing contact angle 45.5° are shown in Figure 4-9. For all print speeds, line segments were obtained at drop spacing of 30 μm. Stable parallel line structures were obtained for drop spacing in the range 15 – 25 μm, with the bulging instability observed at a smaller drop spacing of 10 μm and 5 μm. There is a difference in the morphology of the bulges that depends on the print velocity. At a print velocity of 300 mms^{-1} the bulging instability at small drop spacing leads to a single large bulge. However, at the lowest print velocities of 60 and 30 mms^{-1}, the instability leads to multiple bulged regions of varying size and spacing. At intermediate velocity of 100 or 200 mms^{-1}, behaviour showed a hybrid of the two extremes. The conditions for the onset of bulging show qualitative agreement with the 1 pL data and with Stringer's work with stable lines observed at larger drop spacing and print velocities. The magnified pictures of discrete line segments at large drop spacing and bulging lines at small drop spacing are shown in Figure 4-10 as an example for a better view.

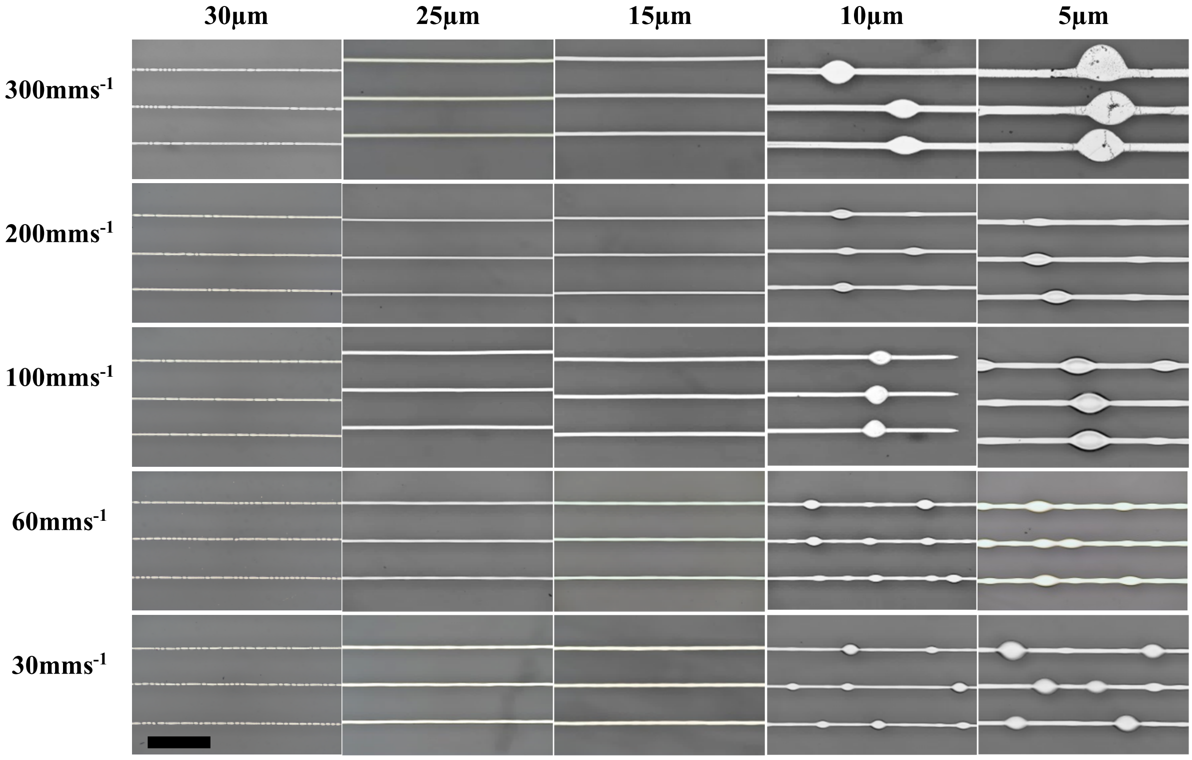

Figure 4-9 Printed structures on Z30 substrate with temperature 28 °C at various print speeds and drop spacing with 10 pL printhead. The scale bar is 500 μm.

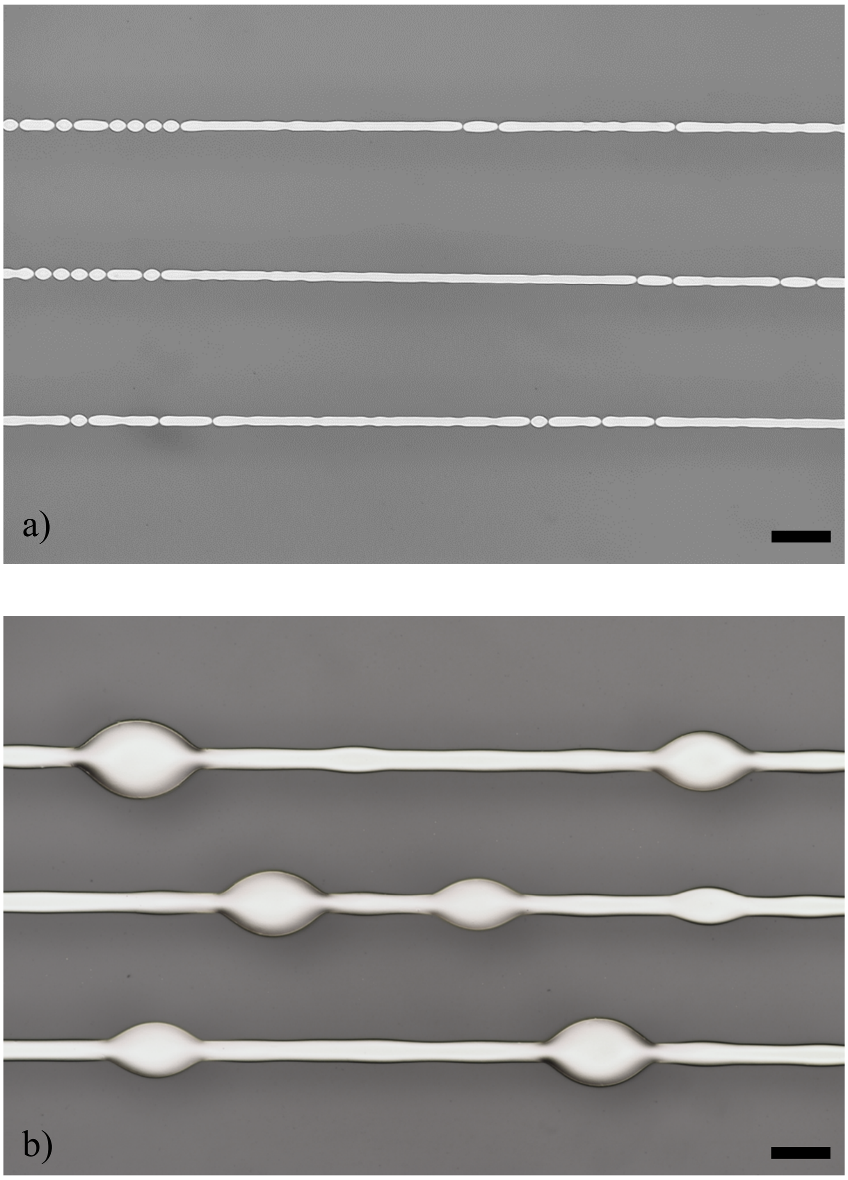

Figure 4-10 Magnified printed structures with 10 pL printhead on Z30 substrate with temperature 28 °C: (a) discrete segments at drop spacing of 30 µm and print velocity of 300 mms^{-1}, (b) bulging lines at drop spacing of 5 µm and print velocity of 30 mms^{-1}. The scale bar is 200 µm.

Figure 4-11 exhibits the resulting printed structures with 10 pL drops at 60 °C with advancing contact angle 53.8°. For all print speeds, stable lines were firstly achieved at drop spacing of 25 µm, above which discrete line segments were obtained. For the structures printed in the print velocity range 100 – 300 mms^{-1}, stable parallel sided lines were obtained in the drop spacing range 10 – 25 µm, and bulging instabilities were observed at a smaller drop spacing of 5 µm. Meanwhile, a significant difference in bulge morphology with print speed was observed, with ungrown small bulges obtained at print velocity of 300 mms^{-1}, and big bulges obtained at print velocity of

100 mms^{-1}. For the structures printed at the print velocity of 60 mms^{-1}, stable lines were achieved at drop spacing of 25 and 20 µm. A small line width irregularity was observed at drop spacing of 15 µm, and the line width deviation became more severe at drop spacing of 10 µm. Unstable bulging structures were obtained at drop spacing of 5 µm. For the structures printed at the lowest print velocity of 30 mms^{-1}, stable lines were formed at drop spacing of 25 and 20 µm, and small line width deviation was observed at drop spacing of 15 µm. Bulging instabilities were observed at drop spacing of 10 and 5 µm.

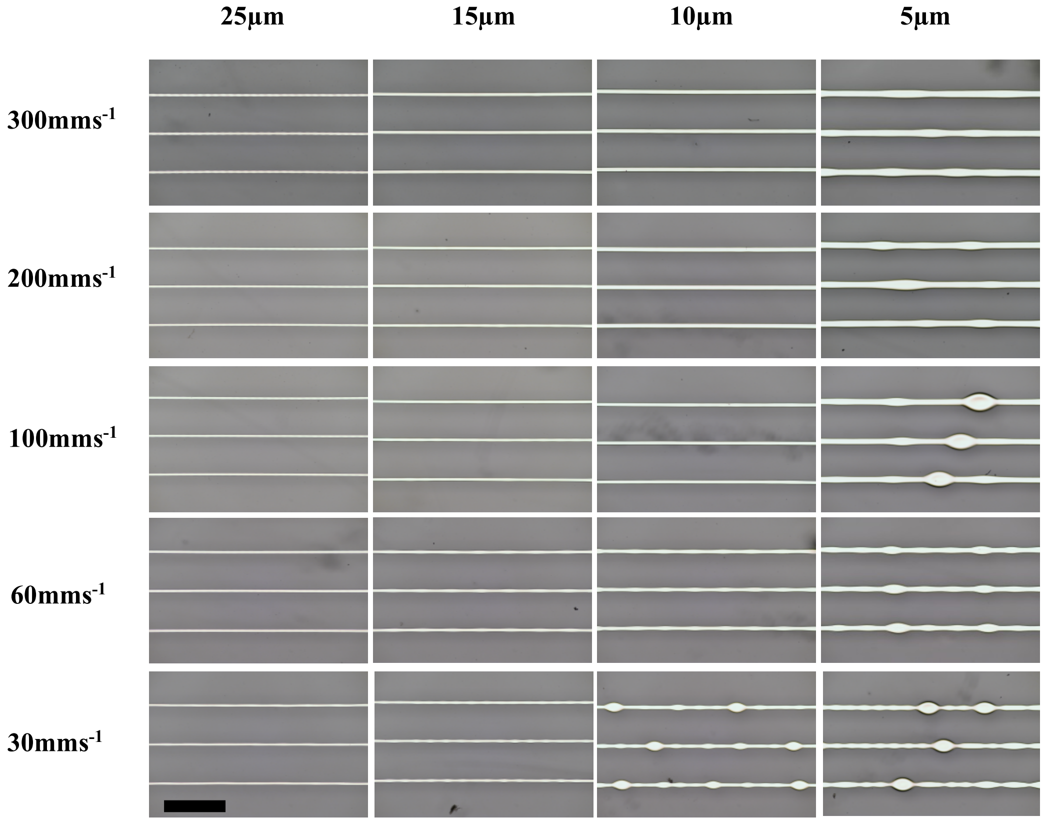

Figure 4-11 Printed structures on Z30 substrate with temperature 60 °C at various print speeds and drop spacing with 10 pL printhead. The scale bar is 500 µm.

The predicted maximum drop spacing by the Stringer's line stability model for 8.5 pL drops (nominally 10 pL printhead) on substrates with temperature 28 °C is 27.8 µm. A slight smaller drop spacing value of 26.1 µm is predicted for the drops on substrates with temperature 60 °C due to increased advancing contact angle. With stable lines achieved at drop spacing 25 µm, the maximum drop spacing results agree quite well with the Stringer's line stability model for both print conditions, as shown in Figure 4-12. However, the agreement between Stringer's model and the minimum drop spacing bound is poor when printing at 28 °C, with unstable bulged lines observed at all drop velocities at a normalised drop spacing < 0.6 (Figure 4-12 a). When printing at the higher substrate temperature of 60 °C (Figure 4-12 b), agreement with Stringer's model is much better.

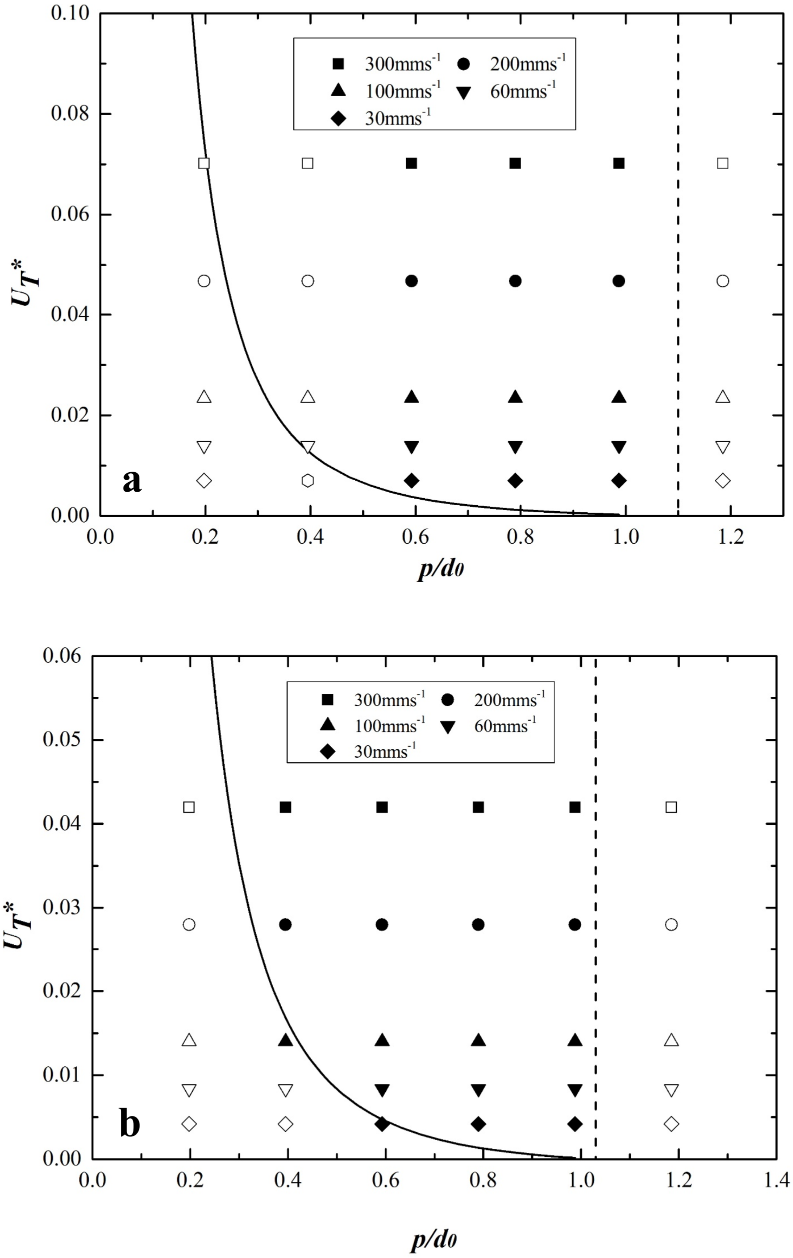

Figure 4-12 Stability map showing the condition for the onset of the bulging instability with data for the nanoparticle ink experiments with 10 pL head at (a) substrate temperature 28 °C, and (b) substrate temperature 60 °C, respectively. Open symbols indicate unstable morphology and filled symbols indicate stable morphology. The dashed line shows the maximum drop spacing bound, and the solid line is the bulging instability bound.

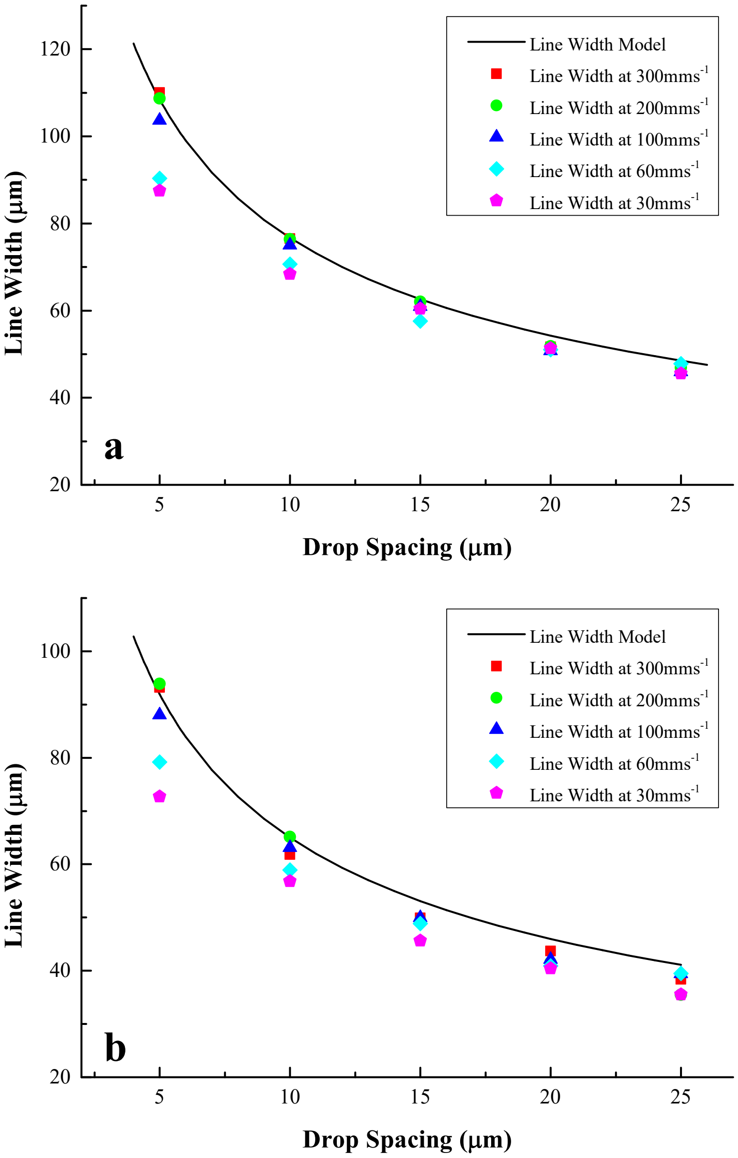

Figure 4-13 Measured line width results on Z30 substrate using 10 pL printhead at (a) substrate temperature 28 °C, and (b) substrate temperature 60 °C, along with line width model prediction. The standard deviations of the line widths are all below 2.5 μm for stable lines.

The relationships between the measured line width results at various printing conditions and the line width model predictions at 28 °C and 60 °C are plotted in Figure 4-13. As with the 10 pL data, agreement with the line width model is good at larger drop spacing and the greatest deviations are seen at the smallest drop spacings when bulges form on the lines.

The relationship between line width and drop spacing can also be expressed by their dimensionless forms, with the dimensionless line width being linearly related to the square root of the inverse of the drop spacing (Equation 4 – 2b), with the constant of proportionality a simple function of the contact angle. This prediction is explored in Figure 4-14. It can be seen that with the 1 pL printhead there is quite good agreement between experiment and prediction for the larger drop spacing of 10 and 15 µm, whereas at 5 µm the measured drop spacing is smaller because of the presence of fluid in the bulges. The data from the 10 pL printhead shows the same trend of a linear relation at larger drop spacing and a deviation towards narrower lines between the bulges at 5 µm spacing. However, there is poorer quantitative agreement with Equation 4 – 2b with the predicted behaviour (dashed lines in the figure) being consistently above the measured line width. Note that there appears to be an effect of printing speed with the lower speed printed lines being consistently narrower. This effect is not captured or considered in the model.

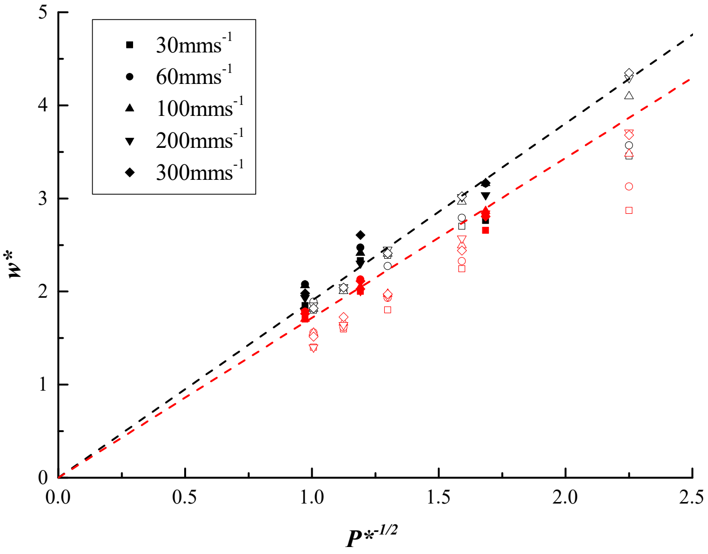

Figure 4-14 The relation between normalised drop spacing and line width (Equation 4 – 2b) is shown as a dashed line. 1 pL printhead solid symbols, 10 pL printhead open symbols, substrate/printing temperature: black is 28 °C with $\theta_a = 45.5°$, red is 60 °C with $\theta_a = 53.8°$

In summary, Stringer's line stability model works quite well in predicting line stabilities in some of our experimental cases (1 pL drops with substrate temperature 28 °C and 60 °C and 10 pL drops with substrate temperature 60 °C), however, there is still one case where the model is not valid (10 pL drops with substrate temperature 28 °C). If we plot the inequality in Equation 4 – 7 as a direct comparison between $g(p^*, \theta a)$ and U_T^* (Figure 4-15), it is possible to study the overall discrepancy between Stringer's model and our experimental results. Using this representation of the data, the linear relation between the dimensionless velocity and the stability criterion is clearly evident as is the anomalous behaviour of the lines printed with the 10 pL printhead at 28 °C. Hence, it's important to further consider the model and the experimental results presented here to explain these discrepancies and inconsistencies.

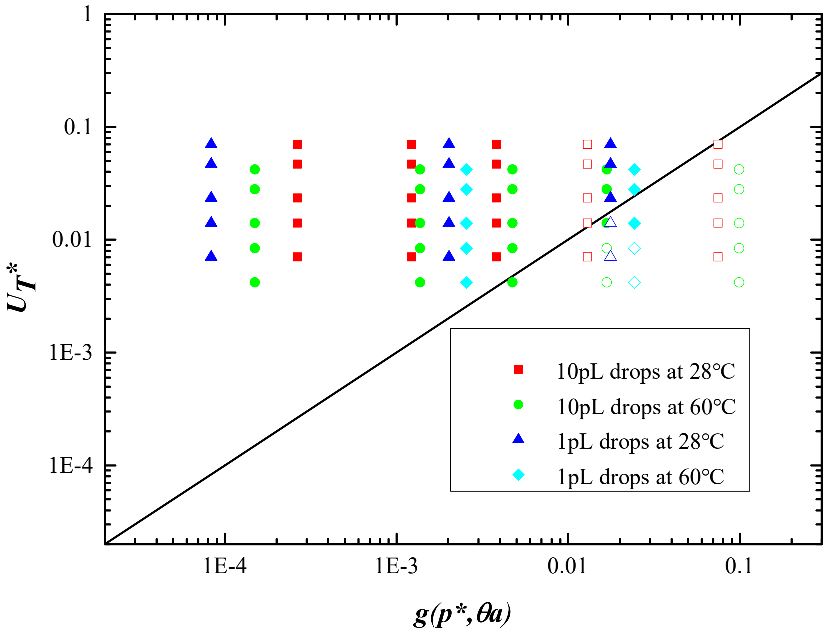

Figure 4-15 The upper bound line instability is represented in the form of inequality in Equation 4 – 7, with the data from the four printing conditions plotted. Filled symbols indicate stable lines and open symbols bulging lines.

4.3.4 Discussion

In our analysis, the liquid bead emphasizes the deposited liquid structures prior to drying, and the ridge indicates the stable parallel parts between adjacent bulges, while the terminology 'line' is a general description of the printed structures. From previous studies, the bulging instability appeared at small drop spacing is driven by the axial transported flow rate Q generated by the Laplace pressure difference due to width change in the liquid bead.[12, 14] The pressure in a stable line bead can be calculated by

$$P = \frac{2\sigma_{LV} \sin\theta_a}{w} \qquad (4-8)$$

where σ_{LV} is the surface tension of the ink, θ_a is the advancing contact angle, and w is the liquid bead width. From this equation, any disturbance that results in an increase in the bead width will reduce the pressure within that region. Driven by this pressure difference, liquid from the adjacent bead will flow into the disturbed region. The new flow will increase the bead width in the disturbance region, further decreasing the pressure of that area. Thereby a growing bulge forms at the disturbance due to the continuing decrease in the local pressure. Stringer found that using the pressure difference between the initial deposited bead width d_{eqm} and the bead width w at the advancing contact angle was more appropriate to describe the driving force for bulging instability, which can be expressed as:[14]

$$\Delta P = P_{\beta_{eqm} d_0} - P_w = \frac{2\sigma_{LV} \sin\theta_a (w - \beta_{eqm} d_0)}{w \beta_{eqm} d_0} \qquad (4-9)$$

Thus, the axial transported flow rate Q along the bead can be calculated by combining Equation 4 – 4 and Equation 4 – 9 using the aforementioned pressure difference. Figure 4-16 shows the axial transported flow rate change at various drop spacing for both the 10 pL and 1 pL printheads. The flow rate is relatively small at large drop spacing, and increases exponentially with decreasing drop spacing for both printheads. However, the increase in Q for the 1 pL head is much smaller than that for the 10 pL head due to the smaller deposited droplet volume. At a drop spacing of 5 μm, the flow rate for the 1 pL head becomes an order magnitude smaller than that for the 10 pL printhead.

Duineveld pointed out that the bulge formation due to the axial transported flow rate, and the bead spreading to its equilibrium line width due to capillarity, are two competing processes during inkjet printing when the initial contact angle θ_1 is larger than the advancing contact angle. From his results, when the fluid has a large advancing contact angle, the growth of small disturbances into bulges due to the large axial transported flow rate is dominant and capillary spreading is negligible. This can be reflected in the ridge width of the bulging structures, which equals that of the single deposited drop diameter, d_{eqm}. While with low advancing contact angle, the transvers flow rate is decreased massively and liquid bead spreading due to capillarity is dominant. In this case the line width of the printed line structures increases with decreasing drop spacing, and the structures were also shown to be stable. Stringer also pointed out that if a bulging instability occurs, the capillary spreading of ridge will be suppressed dramatically.

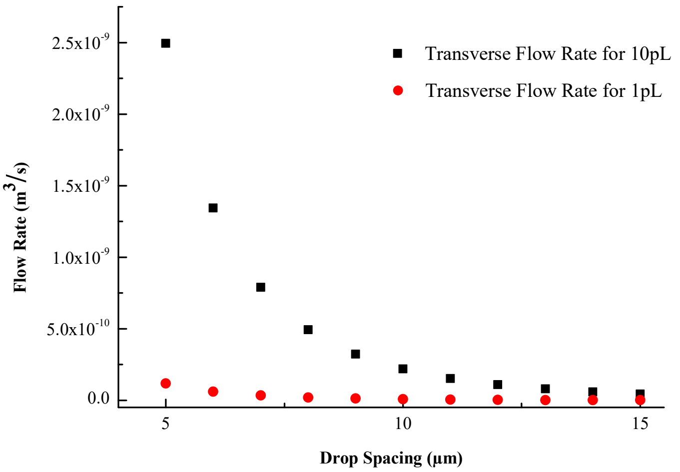

Figure 4-16 Axial transported flow rate at various drop spacing for 10 pL and 1 pL printheads.

In our experiment, the solvent of the silver nanoparticle ink is triethylene glycol monomethyl ether (90450, Sigma Aldrich, Gillingham, UK) with a high boiling point of around 245 °C (1013 hPa), thus the evaporation rate of this non-volatile ink is extremely low at room temperature. The low evaporation of the ink can be evaluated from the TGA results, with only 5% of mass loss after 10 min's heating to 100 °C (Figure 4-17). The use of a high boiling point ink is to avoid rapid evaporation of the deposited structures during printing, thus influencing validation of the model. It is proposed that this relatively low ink volatility and a longer drying time when printing at 28 °C rather than 60 °C can be used to explain the different behaviour of the printing experiments when compared with the predictions of Stringer's model with the 10 pL printhead at 60 °C. With Stringer's model, the condition for line stability is that the mean flow rate caused by droplet deposition at the advancing front of the liquid bead, Q_A, should be larger than the axial transported flow rate Q. It is implicitly assumed that the bulging instability is driven solely by processes at the tip of the growing bead and that fluid flow in the stable bead after printing can be ignored. With small drops and volatile inks this condition is true because evaporation of the solvent in the bead leads to a rapid increase in viscosity and solidification. In the case of low volatility inks, large axial transported flows within the liquid bead after printing can still occur due to the relatively long drying time. Thus, once small disturbances are generated in the liquid bead, the relatively large axial transported flow rate can still drive the liquid in the bead to move to these low pressure regions after printing. The small disturbances will continually grow into big bulges by enhanced pressure difference until the bead is dried.

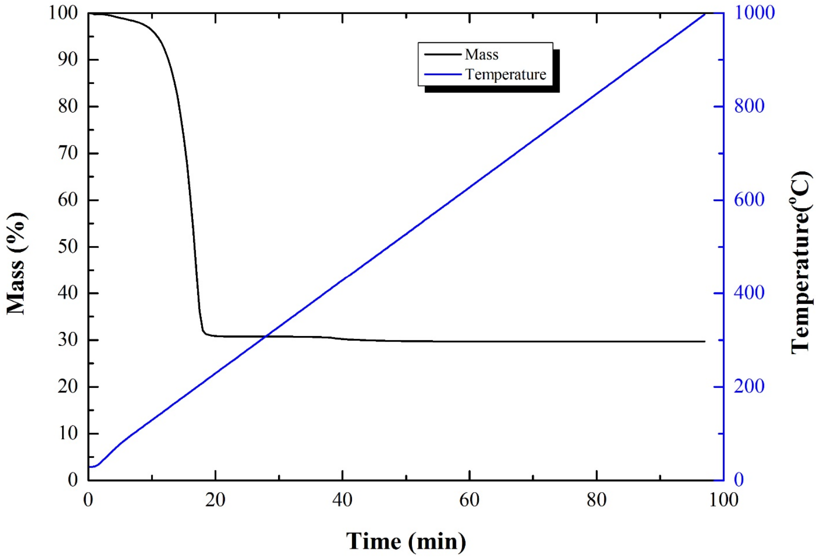

Figure 4-17 TGA test of the silver nanoparticle ink.

This assumption can be tested by observing the growth of a bulge from a small disturbance after printing on the Z30 substrate at a substrate temperature 28 °C, with drop spacing 5 μm and print speed 300 mms^{-1}, shown in Figure 4-18. The images were consecutively captured from the fiducial camera of the printer, showing the growth of a local disturbance. With increased time it is clear that the small bulge grows by absorbing the liquid from the adjacent bead till the bulge reaches its equilibrium state after 5 min, possibly limited by the evaporation of solvent.

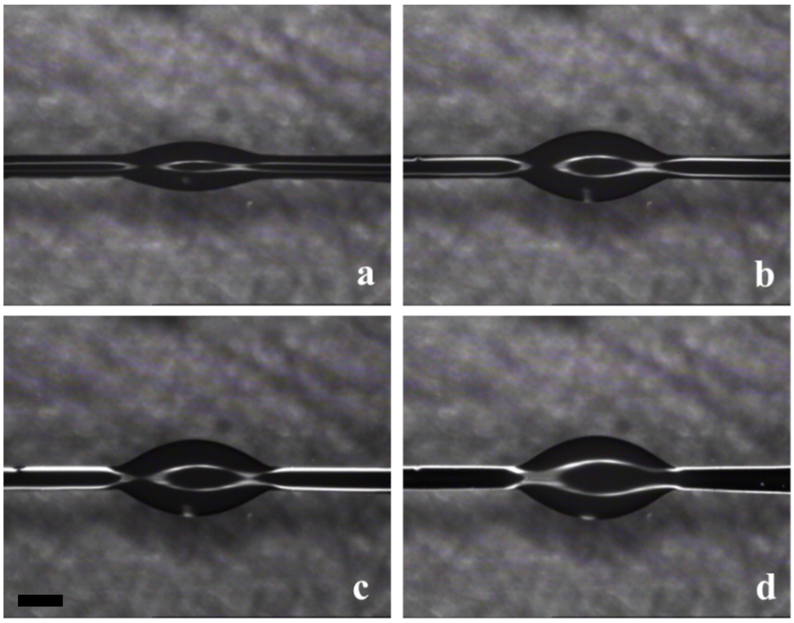

Figure 4-18 Bulge instability with 10 pL head for printing on Z30 substrate at drop spacing of 5 µm, print speed of 300 mms^{-1} and substrate temperature 28 °C: a. after printing; b. 1 min; c. 2 min; and d. 5 min. The scale bar is 200 µm.

The bulging morphology difference between the single large bulge obtained after printing a line at 300 mms^{-1} and the multiple bulges seen when printing at 60 and 30 mms^{-1} (Figure 4-9) also indicates that the mechanisms of bulge formation at high and low speeds are different. If the bulging instability occurs during the printing process, capillary spreading of the ridge bead to its equilibrium state will be suppressed. This is confirmed by the reduction in ridge width compared with the line width predicted by volume conservation in the equilibrium state (Figure 4-13). For the structures printed with 10 pL drops at high print velocity, small drop spacing and substrate temperature 28 °C, the good agreement between the line width results and the predictions from the model shown in Figure 4-13 indicates that capillary spreading of the bead to its equilibrium state is complete. In contrast, for the multiple bulging structures obtained at lower print speeds, there is a significant decrease in the measured ridge width when compared with the model, indicating that capillary spreading has been limited. Thus, the observed single large bulge structures are more likely formed during drying in the static liquid ridges and the model, which considers the dynamics of fluid flow at the advancing liquid ridge, is not applicable. Thus, we conclude that the relatively long drying time scale of the ink and large axial transported flow rate might be the possible reasons that lead to the discrepancy between the stability prediction and our experimental results with 10 pL drops at substrate temperature of 28 °C.

A similar observation that increasing printing temperature leads to improved line stability has been reported in the previous literature. Kang and Oh [187] studied the influence of substrate temperature on the behaviour of printed droplets and lines using a nanoparticle silver ink on a polyimide substrate. By heating up the substrate, continuous stable lines on a relatively hydrophobic substrate were obtained by enhanced evaporation rate of the solvent. However, beyond suggesting that the suppression of bulge formation could be a result of enhanced evaporation from the ink after printing, no mechanism for the observation of improved stability was proposed.

To summarise: The anomalous behaviour seen with the 10 pL drop experiments at room temperature is explained by the long drying time of the ink allowing an instability to form in the static liquid bead. The elevated temperature condition in our experiments still follow the assumptions applied for the line stability model, with pinned contact line and low evaporation rate during printing. The good agreement between the stability of our experimental results and the predictions from the line stability model shown in Figure 4-12 b indicates that the bulge formation process during drying period is possibly inhibited, and the flow rate theory resulting in bulging instability during printing can be applied. For the printed structures with 1 pL printhead at both temperatures, the axial transported flow rate at small drop spacing is over one order magnitude smaller compared with that for 10 pL printhead. Meanwhile, the drying time is reduced with decreased bead volume. Thus, after printing the relatively small axial transported flow rate and short drying time make it difficult for a small disturbance to grow into a big bulge. The good agreement between the stability of our results and the predictions from the model shows that Stringer's line stability model can still be used as the droplet volume decreases to 1 pL, subject to the condition that the ink dries rapidly after deposition.

The predicted line width as a function of drop spacing is in reasonable agreement with experimental results (Figure 4-14), although there is an effect of printing speed not predicted by the model, which results in the lines printed with 10 pL printheads at the largest printing speeds of 300 mms^{-1} being approximately 10% wider than those printed at 30 mms^{-1}. A possible explanation for this discrepancy is our assumption that the printed drop volume is constant under all printing conditions. In order to adjust the drop spacing at different printing axial transported velocities, it is necessary to adjust the frequency of drop ejection, with $p = U_T/f$. It is well-known that the ejected drop volume can be influenced by both the actuating pulse shape and frequency during inkjet printing because of acoustic resonances within the drop generator.[53] This can be confirmed by calculating the single droplet volume from the width results of stable lines at various printing velocities using Equation 4 – 2 a, as shown in Figure 4-19. The calculated single droplet volumes from the width results with 1 pL printhead at both substrate temperatures are independent with the printing velocity, while an approximate 5% to 10% decrease of drop volume from 300 mms^{-1} to 30 mms^{-1} is seen with 10 pL printhead at both temperatures. Thus, we hypothesize that the lower drop generation frequencies required to produce a constant drop spacing as the printing velocity decreases, also results in a slightly smaller drop volume with 10 pL printhead.

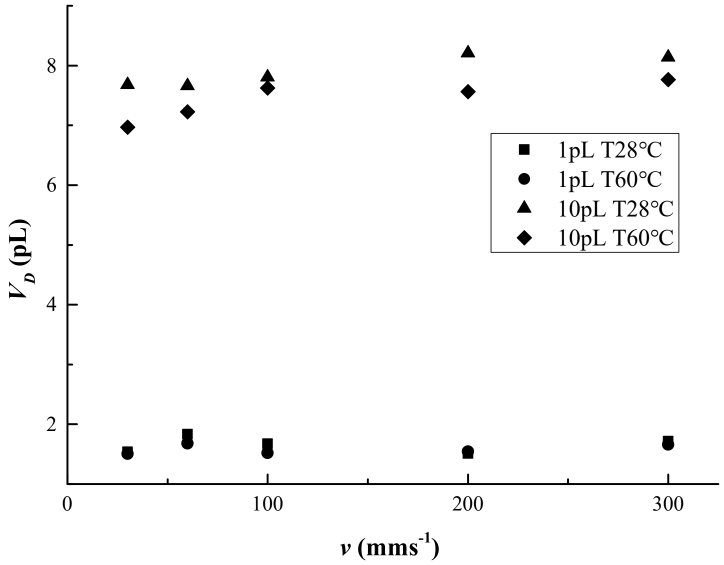

Figure 4-19 Mean calculated single droplet volume at various printing velocities from the width results of stable lines using Equation 4 – 2 a.

From the line width diagrams shown in Figure 4-8 and Figure 4-13, it's obvious to notice the much smaller ridge width connecting the bulges once the instability forms compared with the prediction for the equilibrium ridge width, indicating that capillary spreading is suppressed when the axial transported flow rate is sufficiently large to form bulges. However, unlike the report from Duineveld, where the ridge width between the bulges approached diameter of a single deposited drop, d_{eqm},[12] in our experiments the ridge width in the bulging lines were found to be larger than d_{eqm}. This is possibly due to the smaller advancing contact angle in our experiments, where the maximum advancing contact angle is 53.8°, while the advancing contact angle on type II substrate in Duineveld's work was around 66°; the influence of axial transported flow rate reduces with decreased advancing contact angle.

4.4 Conclusions

1) The stability of printed structures with 1 pL printhead at both 28 °C and 60 °C and lines with 10 pL printhead at 60 °C all exhibit good agreement with the predictions from the line stability model.

2) The stability of printed structures with 10 pL printhead at 28 °C shows discrepancies with the predictions from the model at high print velocities. This is possibly due to the influence of axial transported flow rate Q during long drying process, hence the bulging instability at high print velocity is not a dynamic process during printing.

3) Stringer's line stability model is still valid to predict line stability as the droplet size decreases to 10 and 1 pL, subject to the conditions that the assumptions for the model are applied and the ink dries rapidly after printing.

Chapter 5 Stability of Line Structures with Finite Receding Contact Angle Produced by Inkjet Printing at Small Drop Volume

5.1 Introduction

A stable parallel sided line can be obtained by inkjet printing a high boiling point ink with zero receding contact angle that results in contact line pinning.[10-12, 14] Although contact line pinning is a common phenomenon in inkjet printing with particle suspension inks, there are still cases in which inkjet printing may be used on a substrate under conditions which lead to a moving contact line and finite receding contact angles.[15, 16] The finite receding contact angle condition can influence the stability of printed lines during both the printing and drying process. Duineveld [12] showed that lines printed with high receding contact angle inks will break up into individual droplets rather than form a stable liquid bead. This instability can be characterised by a constant contact angle boundary condition as reported by Davis [143] and further studied by Schiaffino and Sonin [144]. Duineveld demonstrated that, for the case of inks with zero receding contact angle and a high advancing contact angle, a bulging instability occurs during drop deposition, with periodic bulges separated by a narrow parallel sided liquid ridge. Furthermore, it was shown that the instability occurred if the contact angle in the ridge is larger than the advancing contact angle.

Fukai et al.[152] studied the behaviour of droplets deposited on a homogenous substrate with finite receding contact angle and proposed that the characteristic features of the receding contact line during drying are strongly dependent on the droplet size. For droplets with initial diameter in flight > 1 mm, the contact angle at which the contact line starts to recede decreases with increasing initial solute concentration. In contrast, if the droplet size is typical of that produced by inkjet printing, with droplet diameter in flight around 60 μm, the contact line starts to recede at an angle higher than the measured receding contact angle, until the contact line is pinned. After this, the contact angle then decreases due to evaporation and the initial solute concentration has little effect on the receding process. Hsiao et al.[17] used high speed imaging to study the coalescence of printed droplets on a surface with a non-zero receding contact angle. They showed that printed liquid tracks formed at small drop spacing were potentially continuous liquid beads, but were destabilized by contact line retraction during and after printing. The uniform direction of retraction also indicates that there is a preferential liquid flow from the deposition front to the rear of the liquid bead, similar to the axial transported flow considered by Duineveld [12]. Soltman et al.[155] developed a methodology for optimized printing of partially wetting films by adjusting the line to line spacing, and achieved uniform square patterning with sharp bead corners by utilizing contact angle hysteresis.[16] Thus, an understanding of the stability of printed structures with finite receding contact angle is also important for applications of functional material inkjet printing.[17]

In this chapter we consider the stability of inkjet printed lines, with a range of receding contact angles. A model based on Duineveld's analysis is proposed to interpret the wavelength of the bulging instability. Finally, it is shown that a stabilized line structure, with a constant periodicity, can be achieved by applying defined periodic disturbances to the line, controlling the axial transported flow.

5.2 Lines Printed on Substrates with Finite Receding Angle

5.2.1 Line stability as a function of contact angle

This study used a model system of an Ag nanoparticle ink printed onto PDMS substrates with a range of receding contact angles. This was achieved by using a range of UV ozone surface treatments on PDMS coated glass slides. Table 5-1 shows the parameters of advancing contact angle, receding contact angle, single printed drop volume and deposited equilibrium drop diameter after various substrate treatment conditions. The surface tension, dynamic viscosity, and density of the silver nanoparticle ink, measured at 28 °C, are 28 $mN.m^{-1}$, 6.55 mPa·s, and 1450 kgm^{-3}, respectively. The waveform used is the ANP waveform (Figure 3-2 in Chapter 3) and printing was carried out at substrate temperature 28 °C.

Table 5-1 Single deposited droplet properties on UV treated substrates.

	UV Time (min)	Printhead (pL)	Applied Voltage (V)	θa (degree)	θr (degree)	Drop Volume (pL)	Deposited Diameter (µm)
F0	0	10	16.5	59.2° ± 2.1°	21.6° ± 1.9°	7.4	38.0 ± 0.3
F10	10	10	16.5	54.1° ± 1.5°	16.0° ± 1.7°	7.4	40.3 ± 0.4
F20	20	10	14.5	50.3° ± 1.7°	9.3° ± 0.5°	5.5	37.3 ± 0.3
F20	20	1	10.5	50.3° ± 1.7°	9.3° ± 0.5°	1.2	22.5 ± 0.2

Figure 5-1 shows printed structures formed with 10 pL drops at a print velocity of 300 mms^{-1} with various drop spacings on the F0 substrate (θ_a = 59.2° and θ_r = 21.6°). Figure 5-1 a shows that when the drop spacing was larger than the droplet equilibrium diameter on the surface, an array of discrete printed dots results, with no subsidiary drops, indicative of satellites, was observed. Figure 5-1 b – f show the printed results when the drop spacing is considerably smaller than the equilibrium drop diameter (Table 5-1), which results in drop overlap during printing. In this case the printed liquid bead retracts into large liquid dots, with generally increased liquid dot size with decreased drop spacing, instead of forming a continuous line. This is due to the relatively large receding contact angle leading to contact line retraction during or after printing. This is similar to the structures reported by Duineveld [12] for polymer solutions printed on substrates with a similar large receding contact angle.

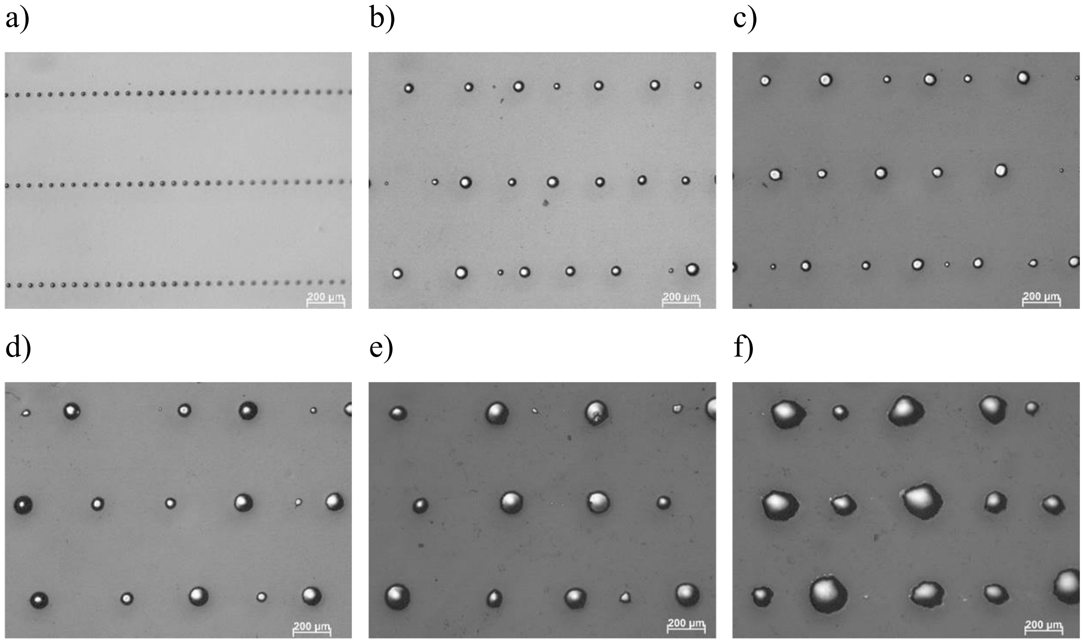

Figure 5-1 Printed structures with 10 pL printhead on F0 substrate with print velocity of 300 mms^{-1} and temperature 28 °C: (a) individual drops at drop spacing of 60 µm, (b) to (f) unstable structures at drop spacing of 30, 25, 15, 10, and 5 µm, respectively.

The instability of the structures on F0 substrates can be predicted using a constant contact angle boundary condition, as reported by Davis [143] and further studied by Schiaffino and Sonin [144]. The instability wavelength of the printed structures, which is the distance between adjacent liquid dots, can be estimated by an equation derived from Duineveld,[12] based on Schiaffino's one-dimensional stability theory:[144]

$$\lambda = \frac{1}{A}\sqrt{\frac{2V_d}{\pi p}} \qquad (5-1)$$

where V_d is the single droplet volume in flight, p is the drop spacing, and A is the h/λ value as a function of contact angle in Schiaffino's analysis, with h the height of the printed structure. With an advancing contact angle of 59.2°, the h/λ value is approximately 0.06 in the stability map proposed by Schiaffino [144]. By substituting the h/λ value into Equation 5 – 1, the predicted wavelength as a function of drop spacing can be established, as shown in Figure 5-2. The predictions are in reasonable agreement with our experimental results at a drop spacing > 10 µm, with both the predicted and observed wavelength decreasing with increasing initial drop spacing. However, at 5 µm drop spacing there is considerable divergence with the observed wavelength being significantly smaller than the predicted value.

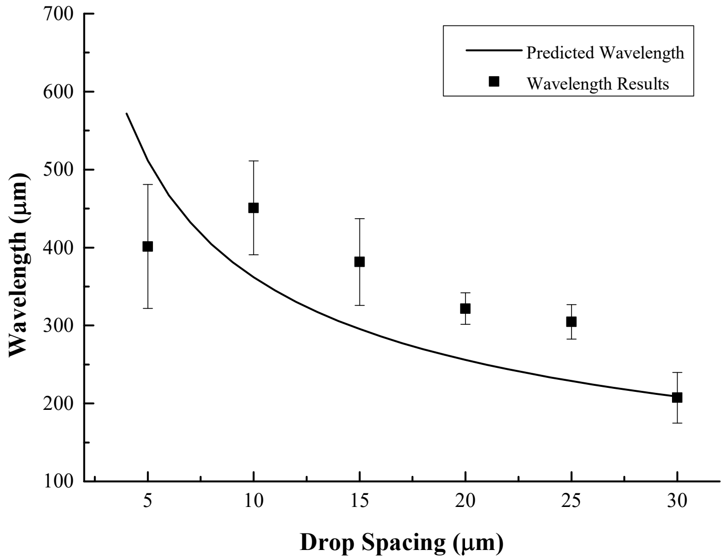

Figure 5-2 Wavelength of liquid dot structures on F0 substrates along with the prediction from Equation 5 – 1.

With increasing ozone treatment of the substrate, the advancing and receding contact angles both decrease (Table 5-1). Figure 5-3 shows the printed structures formed with the 10 pL printhead on the F10 substrate (θ_a = 54.1° and θ_r = 16.0°) with printing speed in the range 30 – 300 mms^{-1} and drop spacing in the range 5 – 20 μm. Under all printing conditions, continuous liquid ridges of constant width were formed between irregular bulges. At all print velocities the bulges become larger with decreasing drop spacing, while at a fixed drop spacing the bulges become smaller with decreasing print velocity. In addition, at the lowest print velocity of 30 mms^{-1} and at drop spacings of 10 and 5 μm, the ridges connecting the adjacent bulges appear to show a secondary instability, showing small incipient bulges or width deviations. The formation of the secondary instability initiates during printing and grows during the long drying period.

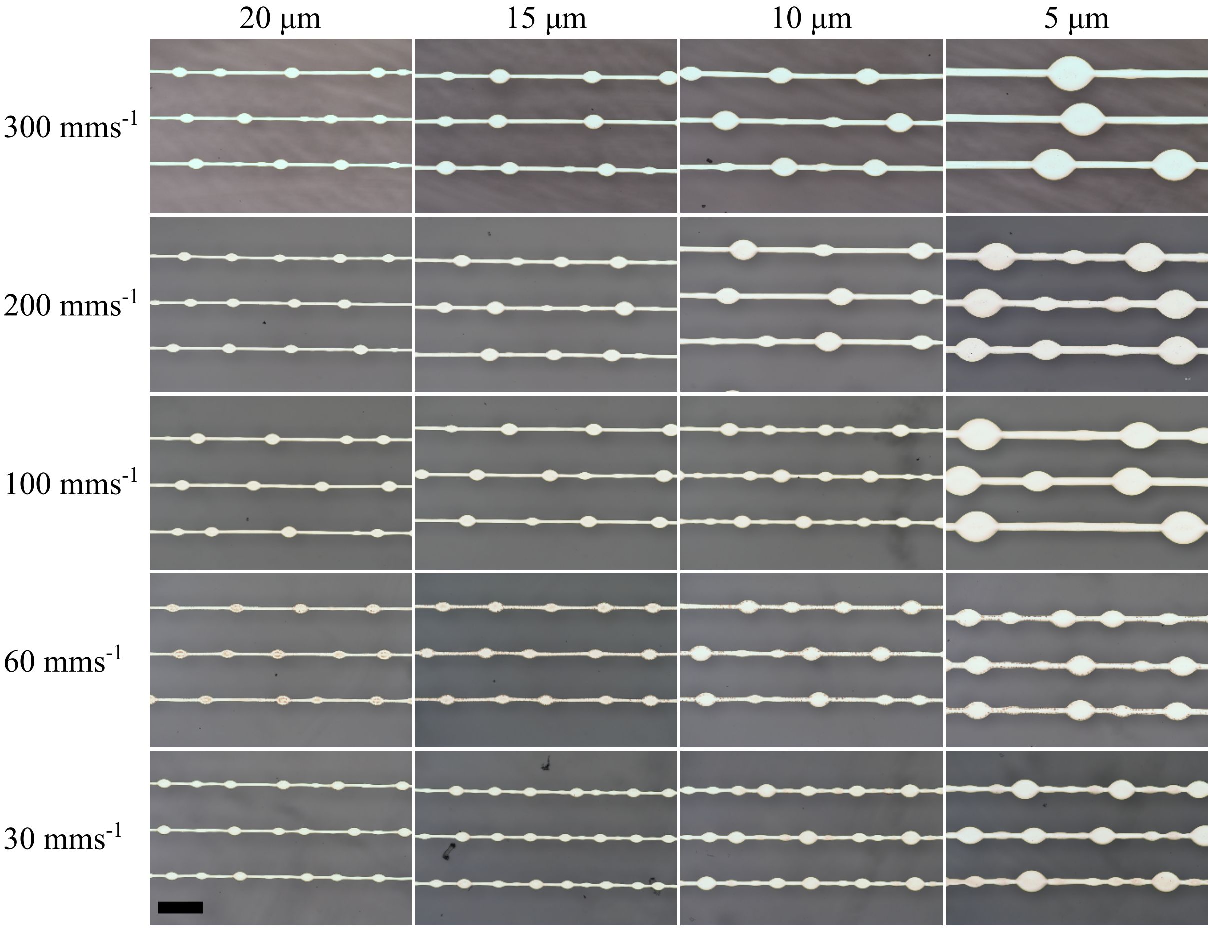

Figure 5-3 Printed structures on F10 substrates with temperature 28 °C at various printing conditions with 10 pL printhead. The scale bar is 500 μm.

The bulge wavelength is defined as the mean distance between the centres of two adjacent bulges. As there are width deviations and poorly defined incipient bulges in the ridges, we defined a mature bulge used in the wavelength measurements as having a centre bulge width larger than 1.2 w, where w is the mean width of the connecting line between the bulges. Seven successive measurements of bulge wavelengths were established for each line, resulting in 21 results for each printing setup to obtain the mean bulge wavelength. Figure 5-4 shows the mean bulge wavelength results as a function of drop spacing at various printing velocities, along with the predictions from Equation 5 – 1, on the F10 substrate with 10 pL printhead. Clearly the predictions from the model show poor agreement with the experimental results, and the influence of printing velocity on the wavelength is not captured in the equation. Similarly, the predictions from the equation also agrees poorly with the results on the F20 substrate, indicating that the model cannot be applied to these substrates due to the change of boundary conditions, and a new model should be developed for the bulge wavelength prediction, considering the influence of the printing velocity.

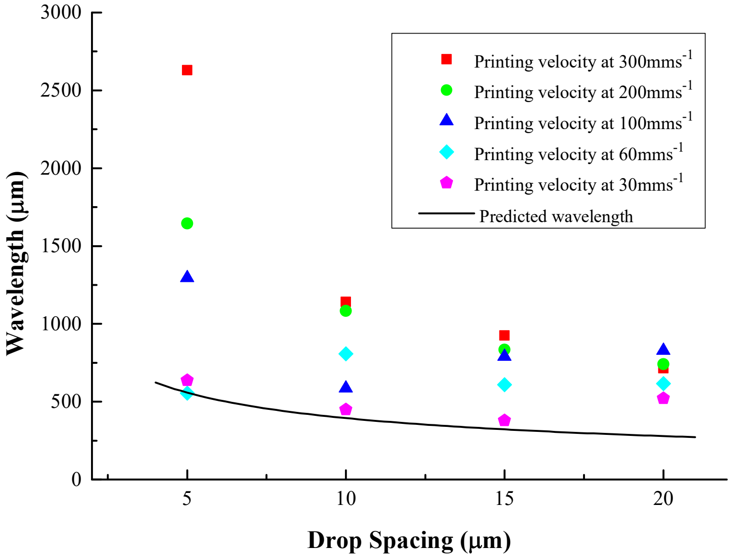

Figure 5-4 Mean bulge wavelength as a function of drop spacing, *p*, on F10 substrate at 28 °C, along with the predictions from Equation 5 – 1, using 10 pL printhead.

Figure 5-5 shows the results obtained when similar structures were printed on the F10 substrate using the 1 pL printhead. In this case no continuous lines were obtained, although some lengths of bulges connected with parallel sided ridges can be seen.

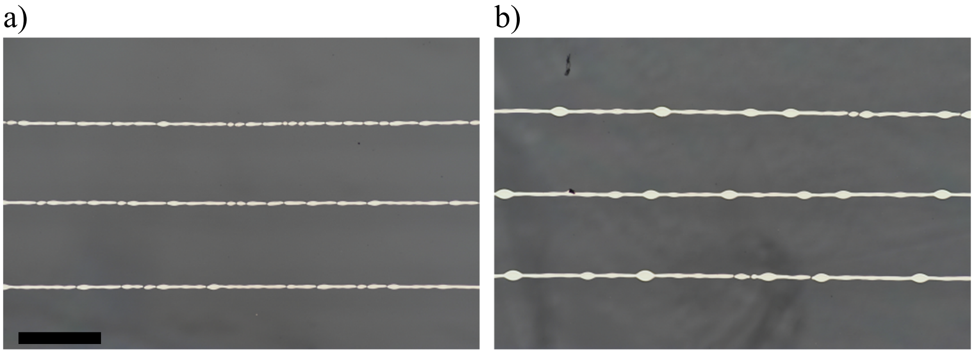

Figure 5-5 Discrete line segments on F10 substrates with 1 pL printhead at the drop spacing of (a) 15 µm and (b) 10 µm, at the print velocity of 300 mms^{-1}. The scale bar is 500 µm.

Figure 5-6 shows the structures printed on F20 substrates (θ_a = 50.3° and θ_r = 9.3°) with 10 pL drops at 28 °C. Unstable bulging structures, similar to those seen on the F10 substrate, were observed for all printing conditions. The change in bulge shape, under different printing conditions, showed a similar trend to that obtained on F10 substrates, with bulge volume increasing with decreasing drop spacing at a fixed print velocity, and decreasing bulge volume when the print velocity decreases at fixed drop spacing. In addition, ridge width deviations were also observed at a print velocity of 60 mms^{-1} and drop spacing of 5 µm as well as with the structures formed at a print velocity of 30 mms^{-1}.

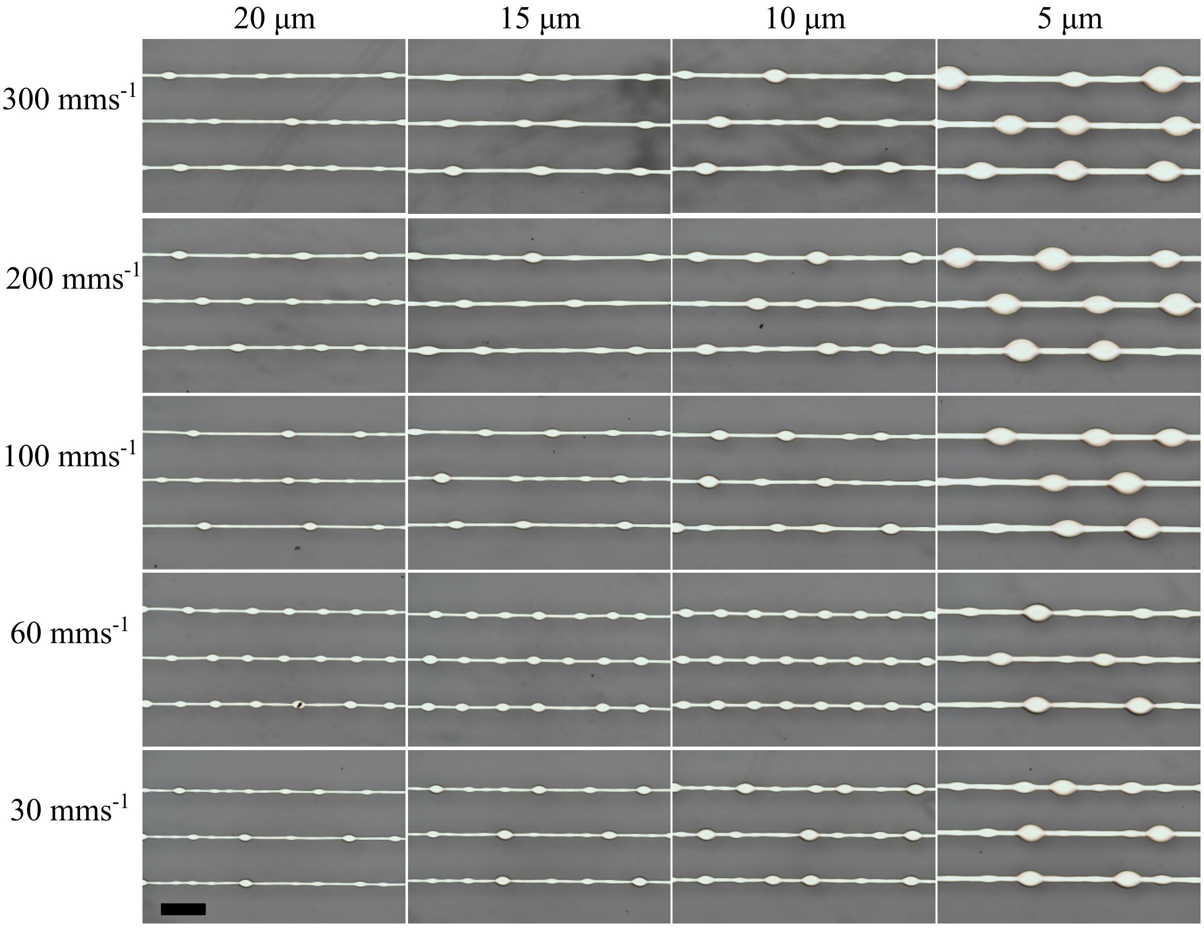

Figure 5-6 Printed structures on F20 substrates with temperature 28 °C at various printing conditions with 10 pL printhead. The scale bar is 500 µm.

Figure 5-7 shows the structures printed on F20 substrates at 28 °C with the 1 pL printhead. With these smaller droplets, continuous lines form at a drop spacing of 10 µm. For all print velocities, discrete line segments were obtained at a drop spacing of 15 µm. All the printed structures display unstable bulging structures. In this case the ridge widths were not parallel sided but showed small bulges or deviations in width, with the deviations more severe than those found on both the F10 and F20 substrates with lines printed using the 10 pL printhead.

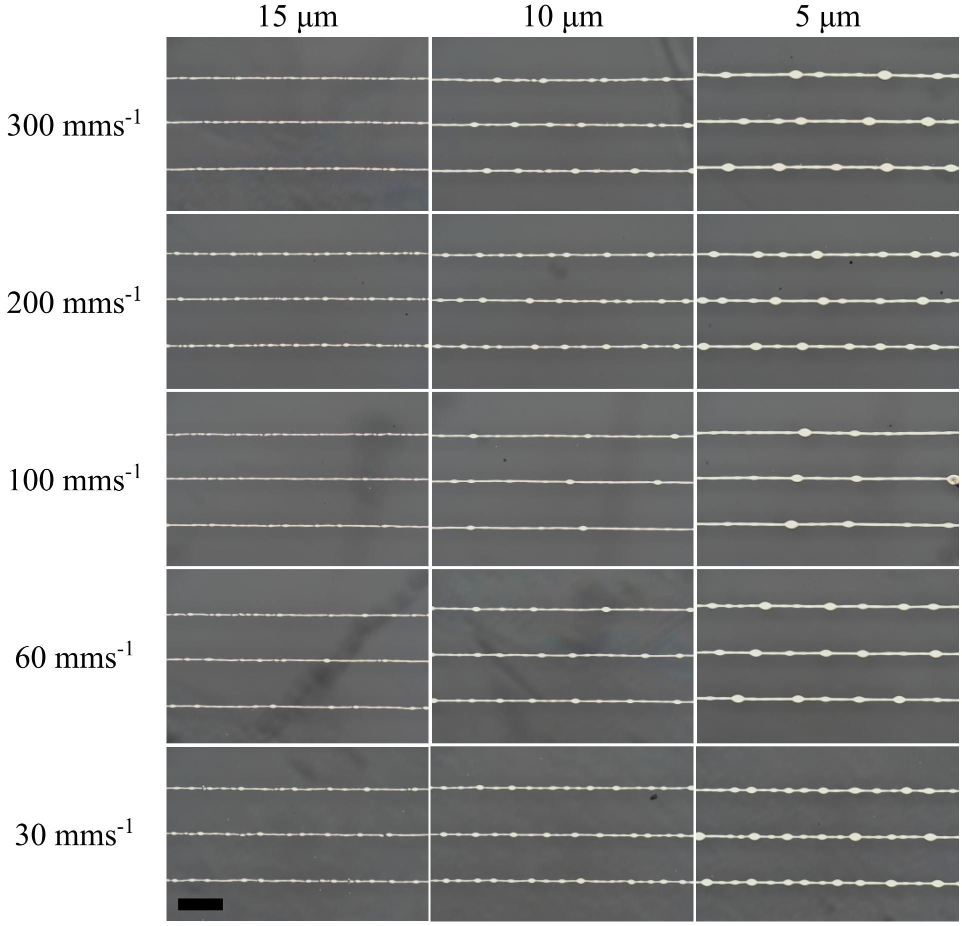

Figure 5-7 Printed structures on F20 substrates with temperature 28 °C at various print speeds and drop spacing with 1 pL printhead. The scale bar is 500 µm.

The ridges that link the bulges are of approximately constant width, and are similar to the features reported in Chapter 4 that formed during the printing of lines from inks with zero receding contact angle. In this case, it was shown that the width of a line, *w,* formed by the coalescence of drops of diameter, d_o, and spacing, *p*, is a function of the advancing contact angle, with:[10]

$$w = \sqrt{\frac{2\pi d_0^3}{3p\left(\frac{\theta_a}{\sin^2\theta_a} - \frac{\cos\theta_a}{\sin\theta_a}\right)}} \qquad (5-2a)$$

Or in dimensionless form with $w^* = w/d_0$ and $p^* = p/d_0$

$$w^* = \sqrt{\frac{2\pi}{3p^*\left(\frac{\theta_a}{\sin^2\theta_a} - \frac{\cos\theta_a}{\sin\theta_a}\right)}} \qquad (5-2b)$$

Hence, the dimensionless line width is linearly related to the square root of the inverse of the dimensionless drop spacing (Equation 5 – 2 b), with the constant of proportionality a simple function of the advancing contact angle.

The relationships between w^* and $p^{*-1/2}$ for the ridges connecting the bulges along with the results of Equation 5-2 are plotted in Figure 5-8. Note that the normalised width of the ridge follows a close to linear relation with $p^{*-1/2}$, as predicted by volume conservation (dashed lines in Figure 5-8) but with a slightly lower gradient, which is consistent with the extra volume that flows into the bulges. A very similar relationship between the width of the ridge and drop spacing was reported in Chapter 4 for the case of the bulging instability that occurs with zero receding contact angle fluids at small drop spacing and low print speeds. Another similarity seen with both fluid cases is that the line width is a function of print velocity, with lines formed at lower velocity showing a smaller width.

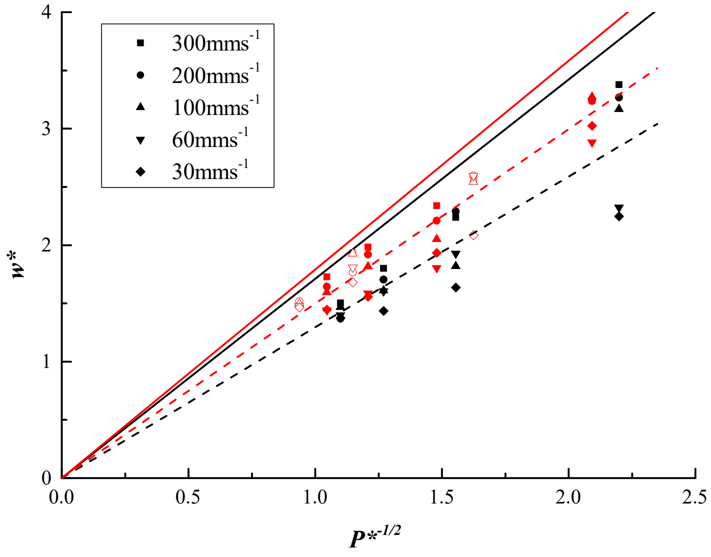

Figure 5-8 The relations between normalised drop spacing and line width (Equation 5 – 2b) are shown as the solid lines, and the fitting of the results using linear regression are shown as the dashed lines. 10 pL printhead solid symbols, 1 pL printhead open symbols, substrate: black is F10 substrate with $\theta_a = 54.1°$, red is F20 substrate with $\theta_a = 50.3°$.

5.2.2 Discussion

Under all conditions of drop spacing and printing velocity, the structures exhibit unstable bulges connected with stable parallel sided liquid ridges. The morphology and volume of the bulges and the width of the connecting ridges appear to be controlled by the printing conditions. We note that these structures are inconsistent with conventional models for static liquid bead instability, which would expect structures similar to those found on the F0 substrate of isolated, unconnected, liquid drops as a result of line instability and the driving force for surface energy minimisation.[143, 144]

Images of the dried structures after printing provide valuable information, which can be interpreted to probe the behaviour of the liquid structures prior to drying. Figure 5-9 shows white light interferometry 3D reconstructions of the shape of the dried deposits from lines printed on the F20 substrate at two printing speeds. In both cases the images of the dried ridges between the bulges show raised regions towards the contact line and a depressed region in the interior. This morphology after drying shows the effect of solute transport towards the contact line during drying, otherwise known as the coffee stain or coffee ring effect,[133] which indicates that the contact line was pinned during drying. Thus, although the ink has a finite receding contact angle, the drying process and possible solid deposition at the contact line can lead to contact line pinning in the printed ridges. Conversely, the images of the bulges show a more uniform domed profile and no raised edges at the contact line, suggesting that in the bulges the drops retracted during drying preventing coffee ring formation. Finally, further study of the ridges between the bulges show that they are not uniform in height and are lower towards the centre between the bulges and higher at the point where they join the bulges. We interpret this as evidence for fluid flow from within the ridges to the bulges during drying.

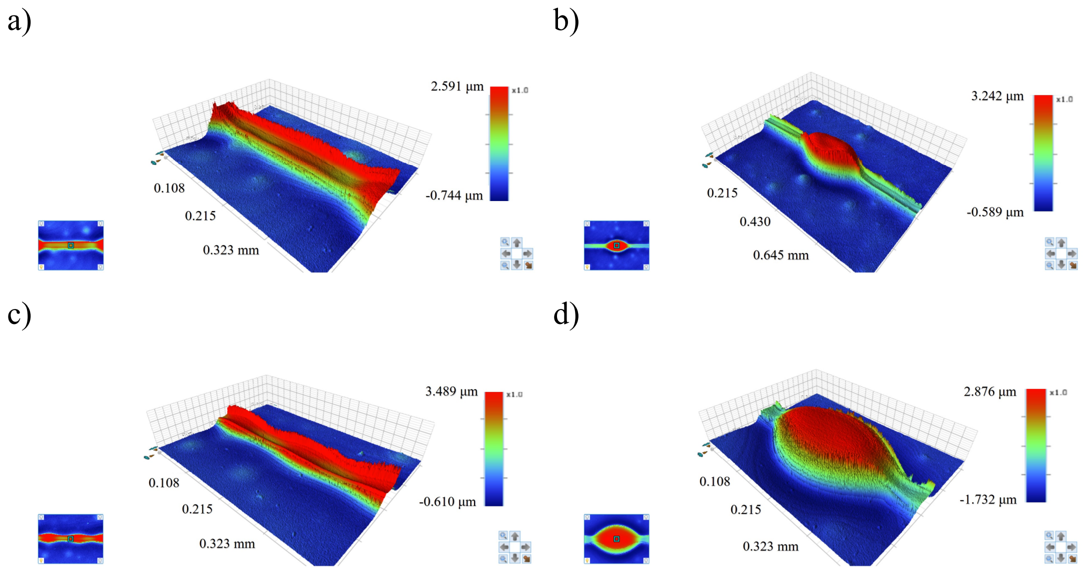

Figure 5-9 White light interferometry reconstructed profiles of line structures printed on the F20 substrate at 28 °C with a 10 pL printhead: (a) ridge profile at print velocity 300 mms^{-1} and drop spacing 10 µm, (b) bulge profile at print velocity 300 mms^{-1} and drop spacing 10 µm, (c) ridge profile at print velocity 30 mms^{-1} and drop spacing 10 µm, and (d) bulge profile at print velocity 30 mms^{-1} and drop spacing 5 µm.

In Chapter 4, the mechanism for the formation of bulges in the case of substrates with zero receding contact angle was discussed in detail (Z30 Substrate). For comparison, profiles of bulge and ridge connecting structures printed on the zero receding contact angle substrate are shown in Figure 5-10. On both types of substrate, the ridges show raised edge profiles indicating contact line pinning behaviour. However, on the Z30 substrate, the pinned ridge height at the contact line is shown to be more uniform (Figure 5-10 a). Note that the bulge shows a significant depression in its centre in Figure 5-10 b, indicating coffee stain behaviour during drying of both the ridge and bulge.

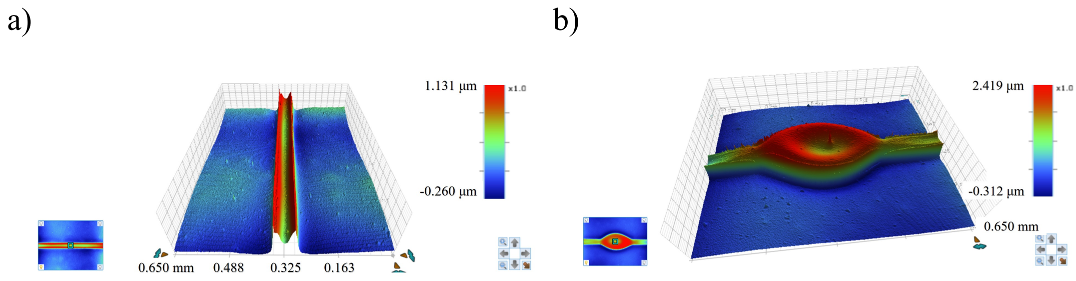

Figure 5-10 Profiles of printed line structures on Z30 substrate (zero receding contact angle) at 28 °C with 10 pL printhead from white light interferometry: (a) ridge profile at print velocity 300 mms^{-1} and drop spacing 10 µm, (b) bulge profile at print velocity 300 mms^{-1} and drop spacing 10 µm.

To summarise, the bulge profiles on the F20 substrate exhibited unpinned contact lines compared with the adjacent ridge structures, where contact line pinning is inferred, while the bulge profile on the Z30 substrate indicates that both the ridge and the bulge structures are pinned on substrates with zero receding contact angle. Thus, we conclude that the printed line structures seen on the substrates with finite receding contact angles (F10 and F20) result from a combination of conditions, in which the contact line of the ridge is pinned while the contact line of the bulge structure is free to move with a constant contact angle. The bulging behaviour can be analysed using the flow theory produced by Duineveld, and our printed structures are similar to the structures produced by Duineveld on the Type II substrate with high advancing and zero receding contact angle.[12]

The printed structures on the F10 and F20 substrates, with a finite receding contact angle, show differences when compared with those on Z30 substrates with zero receding contact angle. At larger drop spacing the finite receding contact angle (F10 and F20) enables the liquid beads to break into shorter sections, which recede to form isolated sessile drops in order to minimise surface energy. At smaller drop spacing there is the possibility of a different instability that occurs at any value of the receding contact angle, which is caused by a competition between the capillary spreading of drops onto the unwetted substrate and the axial transported flow along the existing liquid bead driven by a difference in Laplace pressure with a disturbed (bulged) region behind the tip of the bead. For the structures printed on Z30 substrates (as discussed in Chapter 4), capillary spreading of the bead is only limited when bulging instabilities occur at low drop spacing. Above a critical drop spacing, the liquid bead will spread to its equilibrium state to form stable lines. However, for the structures printed on F20 substrates, with a finite receding contact angle, the spreading of the bead due to capillarity is suppressed under all the printing conditions. With larger axial transported flow rates, any disturbances in the bead will create a low pressure region and grow into bulges, leading to the bulging structures seen with all the printing conditions on the F10 and F20 substrates. Comparing the bulging instabilities on F10 and F20 substrates in Figure 5-3 and Figure 5-6 respectively, shows that bigger bulges and smaller ridges were formed on the F10 substrate with the same printing conditions. On both substrates, larger bulges were formed as the printed drop spacing decreases and the printing speed (drop deposition rate) increases.

The formation of stable liquid ridges between the bulges on the F10 and F20 substrates appears to contradict our normal understanding of the behaviour of liquid structures on flat surfaces. If there is a finite receding contact angle, we would normally expect the bulges to continue growing, depleting the liquid in the ridges, which would eventually pinch-off to form isolated sessile drops, as seen with large drop spacing in Figure 5-1, and expected by analogy to the Rayleigh instability of liquid columns. The presence of a stable ridge of liquid between the bulges (Figure 5-3 and Figure 5-6) suggests that the contact line in the ridge has been pinned. This hypothesis is consistent with the elevated regions seen in the dried structures close to the original contact line (Figure 5-9). For a droplet deposited on the substrate with a pinned contact line, the contact angle between the liquid and the surface will reduce first due to evaporation, with the contact area remaining constant. Once the contact angle reduces to the receding contact angle, the contact line will retract and is no longer pinned.[188] In our experiments, the capillary spreading of the ridge is strongly limited, thus, we hypothesise that the contact angle in the ridge is always larger than the receding contact angle during printing and the subsequent drying process. The contact line in the ridge is pinned during the whole process, therefore resulting in the observed continuous liquid ridges.

The ridges of the printed line structures with finite receding contact angles can also be unstable. The large axial transported flow rate allows any small disturbances in the ridge to grow bigger, if there is sufficient time before the liquid bead dries.

Table 5-2 Nominal ridge contact angle values for the structures on F10 substrates.

P (μm)	300mms^{-1}	200 mms^{-1}	100 mms^{-1}	60 mms^{-1}	30 mms^{-1}
20	72.4°	81.2°	74.6°	79.2°	80.8°
15	69°	74.2°	79.4°	79.8°	90°
10	67.6°	65.6°	86.8°	81.4°	96.2°
5	61.8°	64.8°	67.6°	96°	98.8°

The criteria for bulging instability in our results appear to be different from those obtained by Schiaffino and Sonin [144]. They showed experimentally that with a constant contact line condition, stable parallel sided liquid lines can be obtained when the ridge contact angle is smaller than $\pi/2$, while a bulging instability will occur if the ridge contact angle exceeds $\pi/2$. The contact angle values in their results are the nominal values calculated from a uniform bead with the same base width and same average mass per unit length (i.e. same V_0/p value, where V_0 is the single droplet volume in flight, and p is the drop spacing) as the actual bead. The nominal ridge contact angle values on F10 substrates, using the same approach, are shown in Table 5-2. Most of the values are smaller than π/2 (90°) and thus should be stable following Schiaffino and Sonin's prediction. However, our results show that all the printed structures are unstable and form bulging lines. This divergence is possibly due to the boundary condition differences. Schiaffino and Sonin used a boundary condition in which the contact lines are arrested in a parallel state while the contact angle is free to change, which is consistent with their experiments using molten wax, where the contact line is fixed by solidification. In our experiments, however, the contact lines are arrested by a drying process and thus are able to move during and after printing for a finite period of time. Thus, even if the ridges show contact line pinning, significant differences between the initial contact line conditions might explain the discrepancies between our results and the predictions of Schiaffino and Sonin.

5.3 Bulge Wavelength Model

5.3.1 Wavelength Results on F10 Substrates

Figure 5-4 shows the mean bulge wavelength measured from the printing experiments with 10 pL printheads on the F10 substrate at 28 °C. At a given drop spacing, the bulge wavelength obtained at high print velocities is generally larger than that obtained at low print velocities, and this variation becomes larger with decreasing drop spacing. This could be explained by the flow rate competition used in Duineveld's analysis.[12] As the applied flow rate becomes small at low print velocities, the growth of a disturbance to a bulge under relatively large axial transported flow rate would be much easier, hence leading to the formation of more bulges on the printed structures and thus leading to a shorter bulge wavelength.

5.3.2 Wavelength Model

Here we develop a model for the bulge wavelength based on Duineveld's mechanism. Duineveld [12] considered whether the contact angle in the printed liquid bead changes with time. In the case of bulging structures printed with high advancing contact angle and contact line pinning (zero receding contact angle), the contact angle θ_2 in the ridge decreases to a value lower than the advancing contact angle immediately after liquid deposition due to quick pumping of liquid to the lower pressure bulges behind the advancing tip of the line. As the printing time increases, the contact angle θ_2 increases due to the decreased pressure gradient as the line extends. If this leads to the contact angle in the bead exceeding the advancing contact angle, a new bulge can form. Here we investigate the evolution of contact angles in the ridge growing ahead of a bulge assuming volume conservation and considering the effect of contact line pinning.

In setting up the problem we define the following characteristic constants and variables. Consider the centre point of a bulge as the local origin and defining the printing velocity U, taken as constant for each particular iteration of the model, we can define the wavelength, L, with:

$$L = Ut_c \qquad (5-3)$$

where t_c is the characteristic time period for bulge formation. The ridge length, L_r, between two adjacent bulges can be expressed as:

$$L_r = Ut_c - 2x_0 \qquad (5-4)$$

where x_0 is the half bulge length. The bulge wavelength and ridge length are illustrated in Figure 5-11.

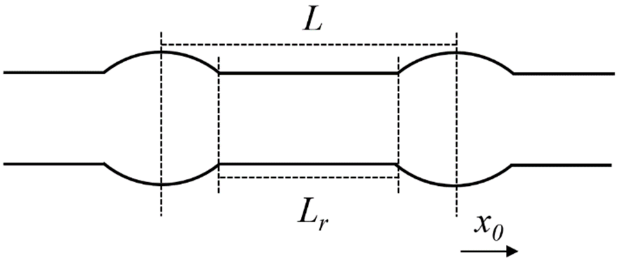

Figure 5-11 Schematic diagram of the top view of adjacent bulges showing the bulge wavelength and ridge length.

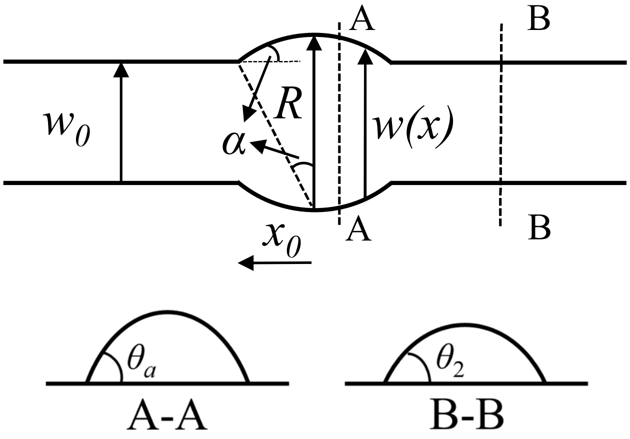

Figure 5-12 Schematic diagram of the top view of a bulge and the adjacent ridge structure. The contact angles in the bulge and ridge are the advancing contact angle θ_a and dynamic contact angle θ_2, respectively.

Figure 5-12 illustrates the top view of a bulge and the adjacent structures along with the parameters used with the model. Following the approach of Duineveld,[12] the perimeter of the bulge on the substrate is described as a circular segment with radius R, where R is also taken to be equal to the maximum width of the bulge. We assume that the bulges are identical and the ridges are uniform at the same printing conditions in the model. The bulge centre is taken as the origin, and the bulge width, $w(x)$, can be expressed as:

$$w(x) = w_0 + 2\left(\sqrt{R^2 - x^2} - R\cos\alpha\right) \qquad -x_0 \le x \le x_0 \qquad (5-5)$$

where w_0 is the ridge width, R is the centre bulge width, and α is the bulge angle where the perimeter intersects the ridge, as shown in Figure 5-12. Again following Duineveld,[12] we assume that the cross section of the bulge is a circular segment with constant advancing contact angle, the cross sectional area of the bulge, $A(x)$ can be approximated using:

$$A(x) = \frac{\left(w(x)\right)^2 \left(\theta_a - \sin\theta_a \cos\theta_a\right)}{4\sin^2\theta_a} \qquad (5-6)$$

The single bulge volume, V_b, can then be calculated by integrating the cross section area of the bulge $A(x)$ from 0 to x_0:

$$V_b = 2\int_0^{x_0} A(x)\,dx \qquad (5-7)$$

The total volume of the bead, V_t, including the front ridge and the rear bulge, i.e., a complete wavelength, is the total volume of printed drops, with:

$$V_t = \frac{V_d}{p} L \qquad (5-8)$$

where V_d is the volume of a single droplet in flight. The ridge volume, V_r, can be calculated by either subtracting the bulge volume from the total volume, or using the ridge cross section multiplied by the ridge length, assuming the ridge bead has a constant circular segment cross section:

$$V_r = V_t - V_b = \frac{w_0^2\left(\theta_2 - \sin\theta_2\cos\theta_2\right)}{4\sin^2\theta_2} L_r \qquad (5-9)$$

where θ_2 is the dynamic ridge contact angle. The ridge width, w_0, centre bulge width, R, bulge angle, α, and half bulge length, x_0, can all be determined by experiment or calculation. Thus, by substituting Equations 5 – 7 and 5 – 8 into Equation 5 – 9, the relationship between dynamic ridge contact angle, θ_2, and printing time can be obtained. Once θ_2 exceeds the advancing contact angle, a new bulge will form. The bulge wavelength can then be obtained by multiplying the print velocity and the characteristic printing time.

The big difference between Duineveld's analysis and our model is the calculation of the bulge volume. In Duineveld's analysis the bulge volume was obtained by integrating the growth rate of the bulge, and after considerable derivations the bulge volume was calculated by integrating a complicated ordinary differential equation as a function of maximum bulge width R (Equation 31 in the paper [12]). The dynamic change of bulge volume, ridge volume and total volume during printing are all a function of printing time, thus linking the relationship between dynamic ridge angle and printing time. In our model, the bulge volume was calculated from the final morphologies for simplicity, and printing time was introduced into the model through the dynamic change of ridge volume and total volume during printing.

For our experimental results with finite receding contact angles, the unpinned bulges indicate that the contact angle in the bulges on both the F10 and F20 substrates is the advancing contact angle during printing to allow the advance of the contact line. Along with the pinned ridges, our results with finite receding contact angles coincide with the conditions from Duineveld's wavelength analysis. Thus, the above wavelength model, which is based on Duineveld's analysis, can be applied to our experimental results to predict the bulge wavelength.

Four sets of measurements are required to establish the model. These are: the ridge width, w_0, bulge angle, α, bulge centre width, R, and half bulge length, x_0. The ridge width, w_0, and bulge angle, α, were measured from the dried line profiles. The bulge centre width, R, and half bulge length, x_0, were calculated through the assumed bulge geometry using w_0 and α.

In order to present a prediction of the bulge wavelength curve as a function of drop spacing, an appropriate relation between the connecting bead width, w_0, and drop spacing, p, is required. From the assumption of volume conservation, w_0 is proportional to $p^{-\frac{1}{2}}$ for a stable parallel sided bead at the equilibrium state. Hence, the relation between w_0 and p in the bulging structures on the F10 substrate was described using the relation $w_0 \propto p^n$, where n is set close to -0.5 to fit the experimental results. Figure 5-13 shows the measured ridge width results, with standard deviations, as a function of drop spacing at various print velocities along with the fitted curves. The exponents of the fitted curves along with the coefficient of determination R^2 are shown in Table 5-3. At large print velocities the exponent is close to -0.5, which would be the case for volume conservation but at lower velocities the exponent is significantly different and the pre-exponent over a factor of two smaller, indicating mass flow away from the ridge.

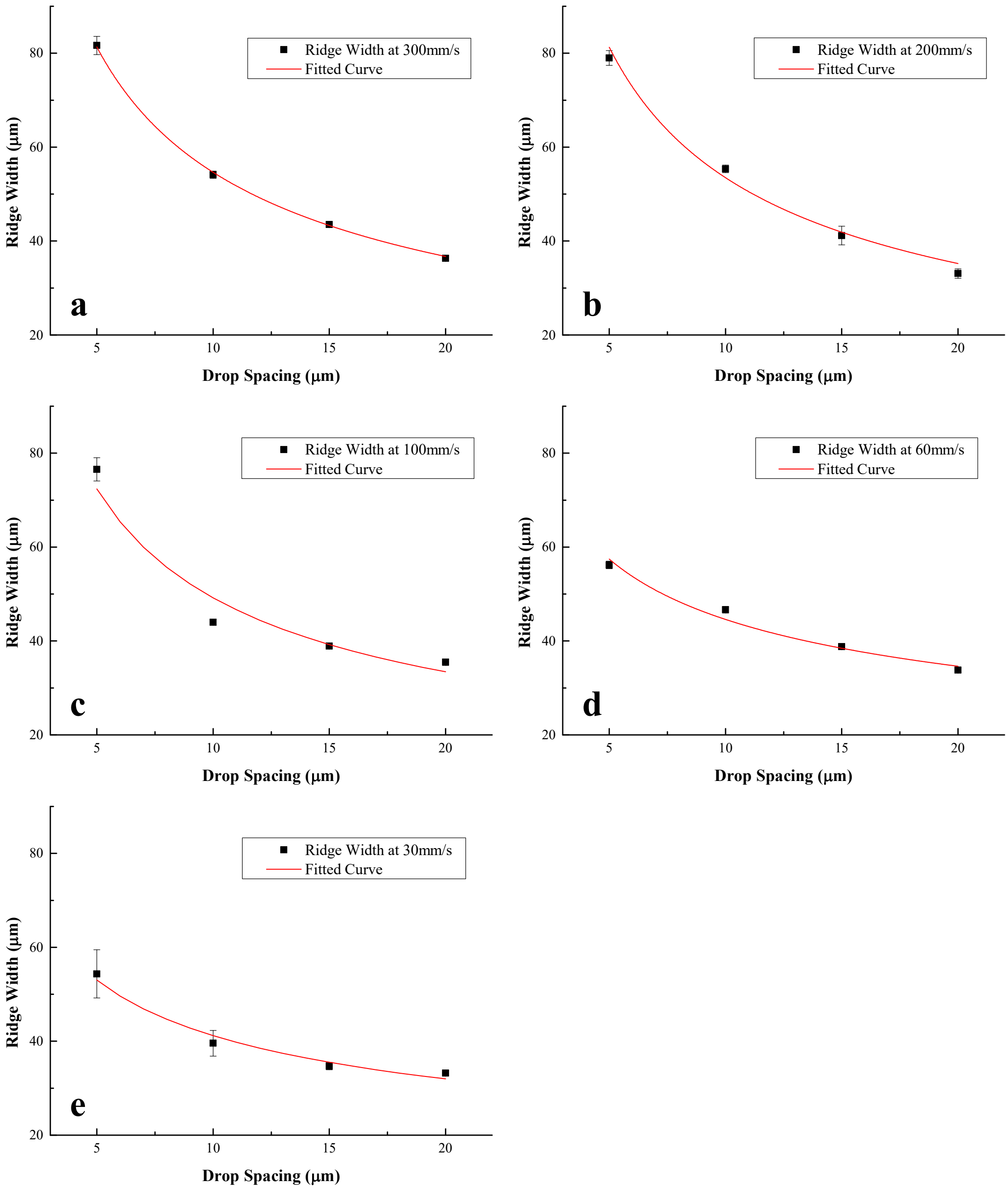

Figure 5-13 Measured ridge width results as a function of drop spacing at various print velocities on F10 substrates along with the fitted curves.

Table 5-3 Fitted equations for ridge width at various print velocities.

Print velocity (mms^{-1})	Fitted Equation	R^2
300	$w(x) = 207.39p^{-0.58}$	0.9995
200	$w(x) = 221.73p^{-0.625}$	0.9898
100	$w(x) = 177.37p^{-0.557}$	0.9457
60	$w(x) = 103.22p^{-0.364}$	0.9786

30	$w(x) = 95.44p^{-0.365}$	0.9723

Figure 5-14 shows the bulge angle, α, measured on F10 substrates with standard deviations as a function of drop spacing at various print velocities. All the measured results at various printing conditions exhibit similar values, but with deviations ranged from ± 1° to ± 3°. Considering the similar bulge shapes at various printing conditions on F10 substrates shown in Figure 5-3, an average value of bulge angles for all conditions was introduced with standard deviation, by which a maximum and minimum value of bulge angle can also be obtained from the mean value plus or minus one standard deviation, respectively. To investigate the influence of bulge angle deviations on the final wavelength predictions as well as present a better fitting of the model, all the three bulge angle values were used in the model to produce a band of wavelength with maximum and minimum bounds as a function of drop spacing. The mean bulge angle is 34.9° with standard deviation ± 3.2°. An assumption of constant angle between the bulge and the ridge is reasonable because this is likely to be driven by ink surface energy minimization and thus independent of printing conditions.

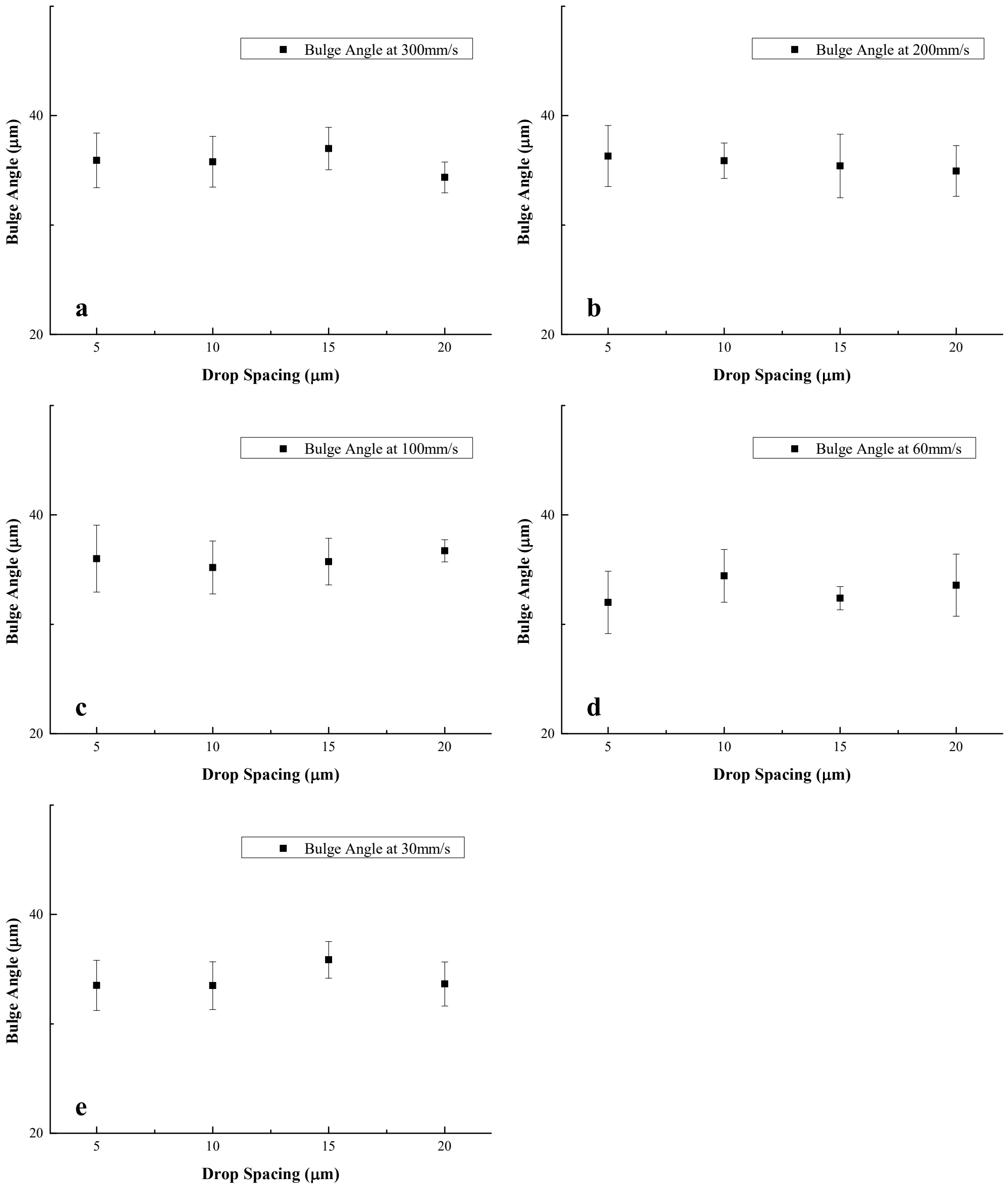

Figure 5-14 Measured bulge angle results as a function of drop spacing at various print velocities on F10 substrates.

The bulge centre width *R*, and half bulge length x_0 can be derived from their geometrical relationship with w_0 and α, as follows. From the assumed bulge geometry with bulge perimeter described as a circular segment with radius equal to the maximum width of the bulge, the following relationship can be obtained:

$$\frac{w_0}{R} = 2\cos\alpha - 1 \qquad (5-10)$$

The value of w_0/R also characterizes the bulge morphology and, following our earlier assumption that the angle, α, is constant, is also expected to be independent of printing conditions. The results of w_0/R determined from measurement are shown in Table 5-4. For all sets of printing conditions, the w_0/R generates an average value of 0.30 with standard deviation of 0.03, which is smaller than standard deviation of the bulge angle α measurements.

However, despite both our characteristic measures of bulge shape remaining invariant over the range of printing conditions, they are not mutually compatible with Equation 5 – 10. Substituting the average value of α (34.9°) into Equation 5 – 10 results in a predicted channel bulge ratio of $w_0/R = 0.64$. Conversely, using the mean ratio of $w_0/R = 0.30$ generates a bulge angle of $\alpha = 49.5°$. Thus, in order to better predict the R and x_0 values and optimise the calculated bulge volume, a shape factor constant, K, is introduced, with the following modification to our geometrical relations:

$$R = \frac{w_0}{K(2\cos\alpha - 1)} \qquad (5-11\text{ a})$$

$$x_0 = R\sin\alpha \qquad (5-11\text{ b})$$

and

$$K = {\left(\tfrac{w_0}{R}\right)_{mea}} \Big/ {\left(\tfrac{w_0}{R}\right)_{cal}} \qquad (5-11\text{ c})$$

Table 5-4 The w_0/R values from measured w_0 and R results at various printing conditions.

P (μm)	300 mms^{-1}	200 mms^{-1}	100 mms^{-1}	60 mms^{-1}	30 mms^{-1}
20	0.33	0.31	0.31	0.32	0.32
15	0.29	0.30	0.31	0.34	0.35
10	0.29	0.30	0.34	0.32	0.31
5	0.23	0.26	0.31	0.28	0.27

5.3.3 Bulge Wavelength Prediction and Discussion

By using the above parameters to investigate the dynamic change of ridge volume and total volume as a function of printing time due to the formation of bulges, the relationship between the dynamic bead contact angle and the printing time can be established for various drop spacing and print velocity conditions. Figure 5-15 shows an example relationship between contact angle in the connecting liquid bead and the printing time for the structures printed on F10 substrates with a bulge angle of 34.9° at various drop spacing and at a printing velocity of 300 mms^{-1}. The calculated contact angle θ_2 in the bead increases dramatically with the printing time, and once θ_2 exceeds the advancing contact angle a new bulge can start to form and the bulge wavelength can be obtained from Equation 5 – 3. The characteristic time is shown in the figure. Note that for times when θ_2 is larger than θ_a the curve is no longer relevant due to the formation of a new bulge and consequently, time resets to zero.

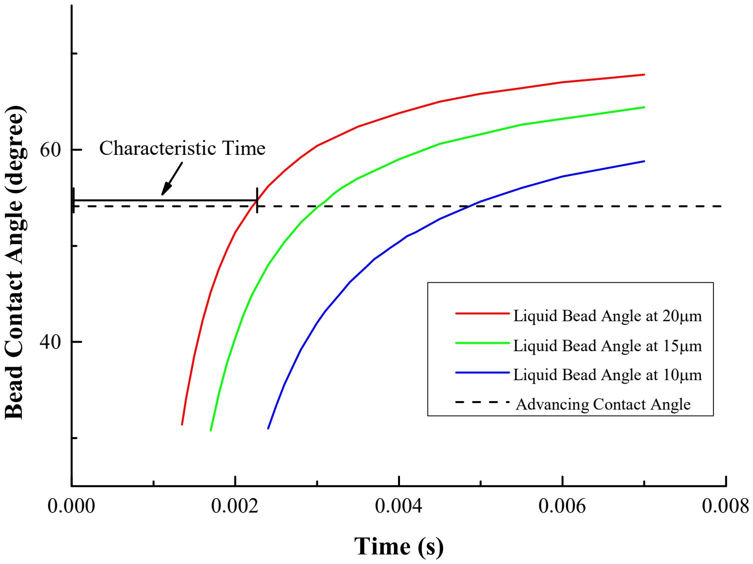

Figure 5-15 Calculated dynamic bead contact angle with time for the structures printed on F10 substrates at 300 mms^{-1} with various drop spacing. Assuming the printing time starts at the centre of the previous bulge.

The overall mean wavelength results along with the wavelength predictions at various printing conditions are shown in Figure 5-16. The predicted wavelength values generally agree well with the experimental results. The trend of wavelength change with drop spacing at various printing velocities is captured, although at lower velocities the model indicates a wavelength slightly lower than observed and at higher velocities the model predicts a larger wavelength at low drop spacing.

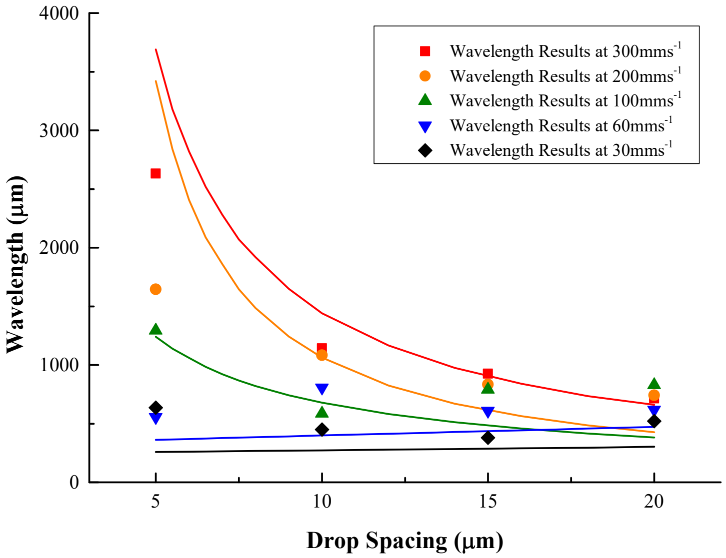

Figure 5-16 Mean wavelength results at various printing velocities along with the mean wavelength predictions in the same colour.

Exploration of the solution to Equations 5 – 5 to 5 – 9 show that the result is highly sensitive to the value of the bulge angle, α. This is illustrated in Figure 5-17, where the experimental measurements of the mean wavelength are compared with the wavelength model at various print velocities using the average value of α, and minimum and maximum values from the standard deviation (34.9° ± 3.2°), respectively. The predicted wavelength values generally agree well with the experimental results, within the bounds of uncertainty for α, indicating that the model based on the dynamic change of the ridge contact angle can be applied to our experimental printing conditions. At the largest printing velocity of 300 mms^{-1} (Figure 5-17 a), the wavelength increases with decreasing drop spacing and this is captured by the model. At 200 mms^{-1} (Figure 5-17 b) the agreement is less good at the smallest drop spacing but the general trend is captured. At the smallest printing velocities of 30 and 60 mms^{-1} (Figure 5-17 d and e), the model predicts little variation in wavelength with drop spacing, which is similar to the observed behaviour but the bulge spacing is more irregular and accurate validation is not possible.

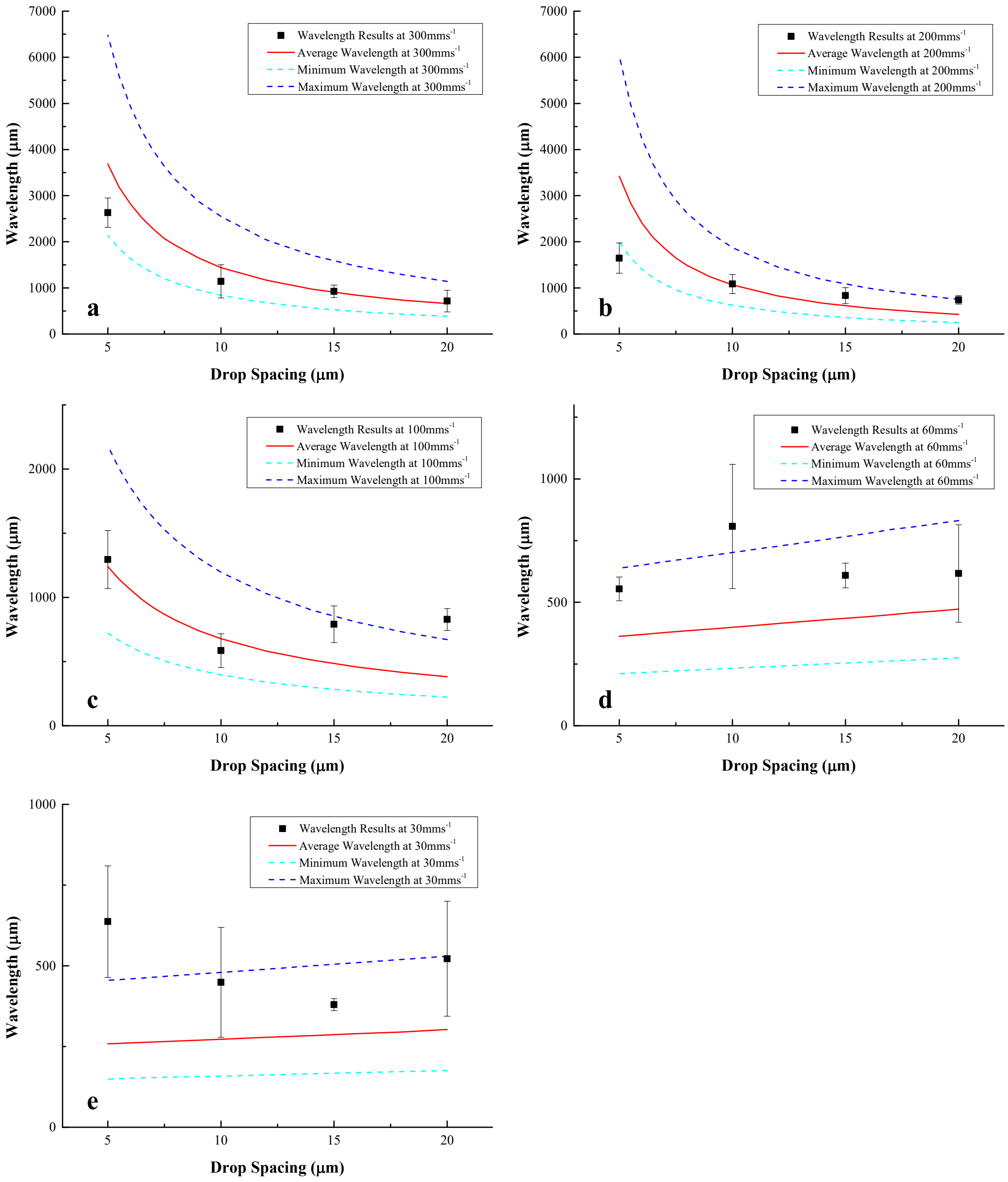

Figure 5-17 Images showing the mean wavelength results with standard deviations along with the fitted wavelength curves at various print velocities using average, minimum and maximum bulge angle, respectively. The maximum and minimum values of bulge angle were obtained from the mean value plus or minus one standard deviation, respectively.

A weakness of the model is its approximation for the bulge volume, and any big deviation in the bulge volume analysis could have a significant influence on the final wavelength prediction. In the wavelength analysis, the four sets of variables used to establish the model were either measured from the printed morphology or obtained from geometrical calculations, all with values similar to the measured results in the drying state. The wavelength model describes a dynamic process during printing, thus ideally the four sets of variables should be obtained in the printing state. In our experiments, however, the solvent is triethylene glycol monomethyl ether with a high boiling point of around 245 °C (1013 hPa), and the evaporation rate of this non-volatile ink is extremely low at room temperature. Thus, the liquid ridge and bulge structures can still grow during the long drying time, leading to changes to the measured results of the variables. This variation is most significant for the structures printed at the drop spacing of 5 μm and high printing velocities, as the bulges will continuously grow after printing due to the relatively large liquid bead volume and axial transported flow rate, which can be seen from the lower w_0/R values at a drop spacing of 5 μm and printing velocity of 300 and 200 mms^{-1} (Table 5-4). Thus, the bulge volume in the dried state is significantly larger than that during printing, this leads to the final wavelength prediction being larger than observed. For the structures printed at larger drop spacing, as the liquid bead volume and axial transported flow rate are relatively small, the growth of the structures during drying is small, hence resulting in limited change of the final shape of the structures. Thus, the wavelength predictions at larger drop spacing show better agreement with the experimental results.

For establishing the model, we assume that the ejected single droplet volume from the printhead maintains the same for all the printing conditions. However, in Chapter 4, a 5% to 10% decrease of single droplet volume was inferred as the printing velocity decreased from 300 to 30 mms^{-1}, which is possibly due to the decreased printing frequency when adjusting the drop spacing at decreased printing velocities. Thus, we hypothesize that the use of larger droplet volume of 7.4 pL, rather than the decreased value, leads to the lower wavelength predictions from the model at lower printing velocities. This can be confirmed by recalculating the wavelength from the model using a droplet volume of 6.7 pL, assuming a 10% loss from the original volume of 7.4 pL. As shown in Figure 5-18, the wavelength predictions with droplet volume of 6.7 pL at the printing velocities of 60 and 30 mms^{-1} both exhibit higher values than those with droplet volume of 7.4 pL (Figure 5-17 d and e), and agree better with the experimental results. On the other hand, the irregularities of the bulges, which are reflected in the measured wavelength results with relatively big deviations, can also influence the calculation of bulge volume, thus leading to the discrepancies of the wavelength predictions.

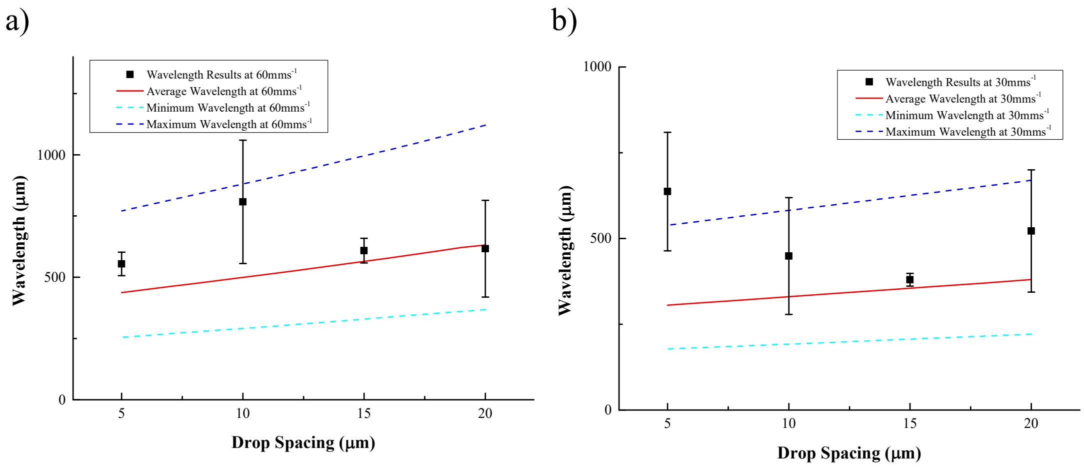

Figure 5-18 The wavelength predictions at the printing velocity of 60 and 30 mms^{-1} with single droplet volume of 6.7 pL, along with the mean wavelength results.

In Duineveld's analysis, the use of bulge growth rate to calculate the bulge volume makes it possible to predict the dynamic bead contact angle from the beginning. From Figure 18 in the original paper, the dynamic bead contact angle θ_2 rapidly decreases from its initial value θ_1 to a value below θ_a in milliseconds, indicating that spreading of the ridge is strongly limited in the presence of bulge, as it can only occur when the ridge contact angle is larger than the advancing contact angle [12]. As the bulge volume in our model was calculated from the final morphologies for simplicity, the prediction of the initial decrease of the bead contact angle was out of the limit of our model and hence not captured (Figure 5-15). Meanwhile, the absence of bulge growth with the printing time could also lead to deviations to the final wavelength predictions. Nonetheless, the good agreement between the model predictions and our wavelength results suggests that our model provides a simpler way to predict the bulge wavelength on the substrates with a finite receding contact angle.

5.4 Stabilized Line Structures

5.4.1 Stabilized Lines on F20 Substrates

From the above results and discussion, the structures printed on the substrates with finite receding contact angle will always be unstable, and bulges form in response to the growth of small disturbances in the bead width. By fully understanding the flow driven mechanism for bulge formation, it is possible to develop a strategy allowing the printing of stabilized lines on substrates with finite receding contact angle. This involves pre-depositing periodic arrays of single droplet dots on the substrate and then printing line structures on top. These pre-deposited droplets behave as small disturbances and, once superimposed line structures are printed, these dots create regularly spaced low pressure regions in the liquid bead. Thus, under axial transported flow, these small disturbances grow into a periodic array of bulges fed by flow of liquid from the higher pressure liquid bead. This stabilises the liquid ridges because the formation of a new bulge requires the contact angle in the ridge to be larger than the advancing contact angle, while the loss of liquid in the ridge to the adjacent bulges reduces the ridge contact angle. Thus, pre-depositing droplets could possibly make the rest of the bead structures stable. However, as the distance between the stabilising pre-deposited drops increase, their influence will diminish and it is possible that above some critical spacing, irregular random bulges will reappear.

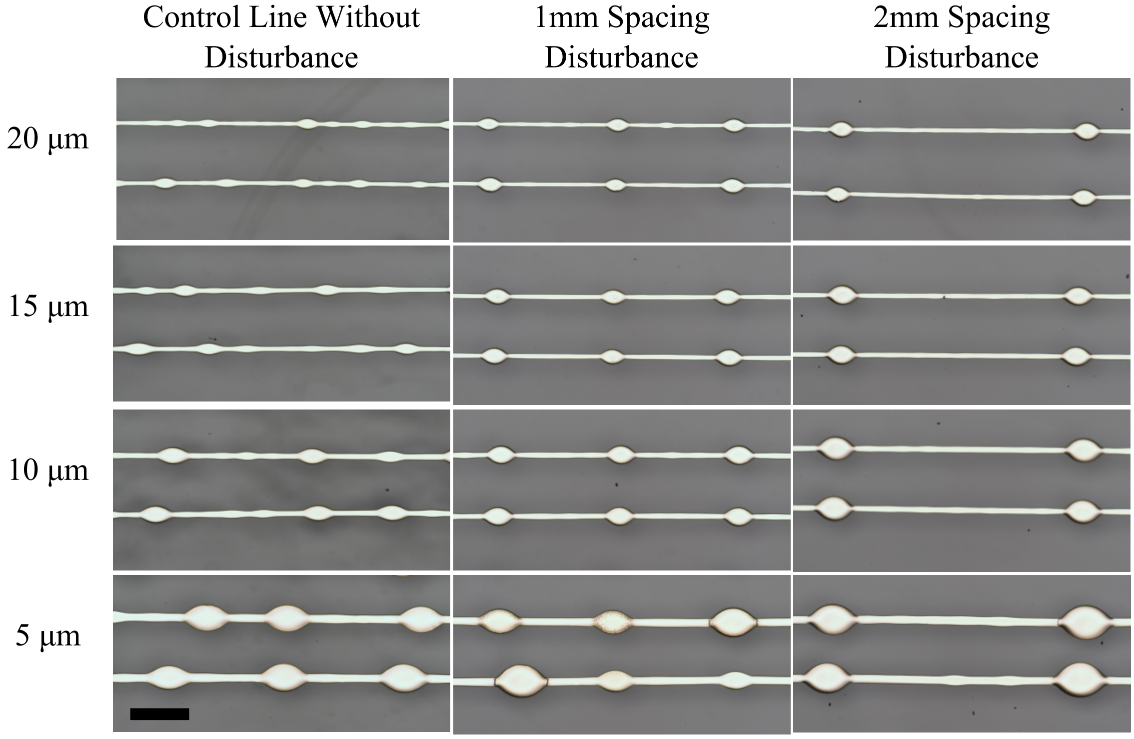

Figure 5-19 Printed structures with pre-deposited disturbances on F20 substrates using 10 pL printheads at print speed of 300 mms^{-1} and substrate temperature 28 °C, along with the direct printed structures as a comparison. The scale bar is 500 µm.

The disturbance stabilising hypothesis has been tested experimentally. Figure 5-19 shows printed line structures deposited using a 10 pL printhead on F20 substrates at a print speed of 300 mms^{-1}, with pre-deposited disturbances of different separation distances, with a standard line without disturbances, printed as a control. For the lines printed with these disturbances at drop spacing > 5 µm, large periodic bulges were formed only on the pre-deposited dots, and the ridge structures between the bulges maintained a relatively stable parallel sided ridge showing only small deviations in width. However, the lines directly printed on the unpatterned substrates formed irregular bulges. This indicates that pre-depositing disturbances can stabilise inkjet printed lines and eliminate irregular bulging instabilities. The maximum droplet spacing distance to achieve stabilized lines for all the drop spacing conditions was found to be 2 mm, and on exceeding this distance the growth of unexpected bulges in the ridges would occur, which is possibly due to insufficient liquid pumped into the adjacent bulges to reduce the ridge contact angle. The poor agreement with our hypothesis seen with some lines printed at 5 µm drop spacing may be a result of the long surface residence time with the high boiling point ink, allowing the growth of new disturbances in the ridge.

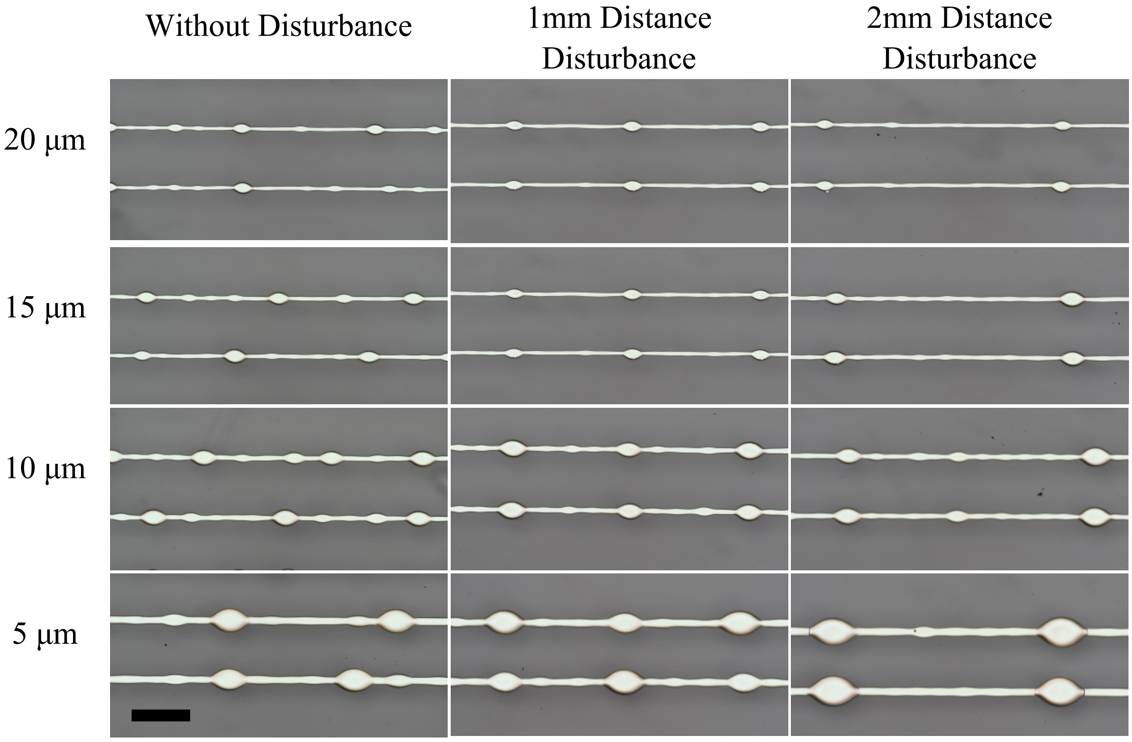

Figure 5-20 Printed structures with pre-deposited disturbances on F20 substrates using 10 pL printheads at print speed 30 mms^{-1} and substrate temperature 28 °C, along with the direct printed structures as a comparison. The scale bar is 500 µm.

The printed structures on F20 substrates at the print velocity of 30 mms^{-1} with different distances of pre-deposited disturbances along with the direct printed structures are shown in Figure 5-20. Compared with the direct printed structures, the lines printed on the pre-deposited disturbances also show periodic bulging structures. However, the ridge structures obtained at 30 mms^{-1} are shown to be unstable compared with those printed at the higher velocity. The unstable ridge structures are similar to those obtained by direct printing on F10 and F20 substrates at low print velocities due to the relatively low applied flow rate at low print speeds, as mentioned above.

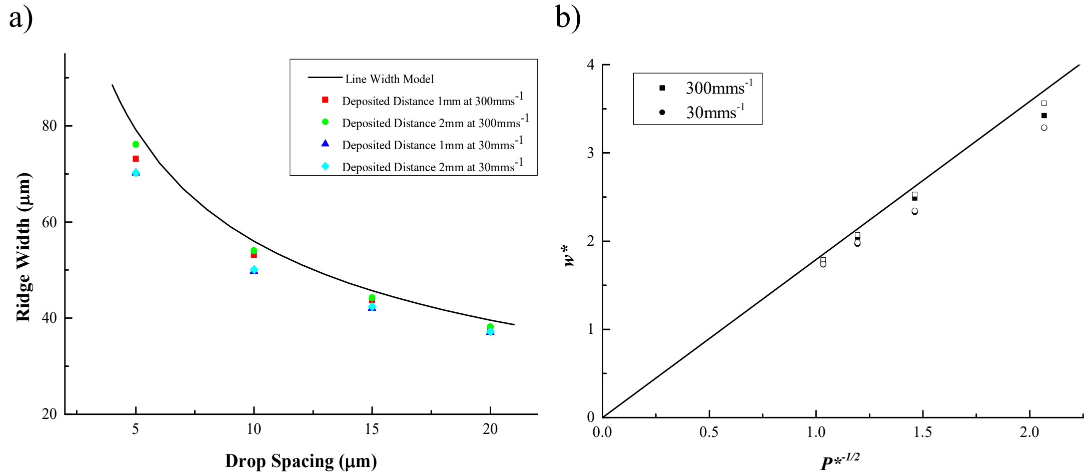

Figure 5-21 a) Measured ridge width results on F20 substrates with pre-deposited droplets using 10 pL printheads along with the curve showing the bead width of a stable line with the same printing conditions by the line width model, and b) the relations between normalised line width and drop spacing of the results along with the linear predictions from Equation 5 – 2b, filled symbols show results with deposited distance of 1 mm, and open symbols 2 mm.

The mean ridge width results of the printed structures on pre-deposited droplets on F20 substrates at various printing conditions are shown in Figure 5-21 a. Comparing with Figure 5-8, the dried liquid ridges are wider when printed on the pre-deposited disturbances than on the original substrates, especially for the structures obtained at low print velocities. This indicates that by distributing the bulges periodically and uniformly the spreading of the ridge due to capillarity is increased compared with that obtained by direct printing and is closer to the value predicted by volume conservation. This can also be seen from the normalised relations, with the normalised width of the ridge following a close to linear relation with $p^{*-1/2}$, but with a slightly lower gradient (Figure 5-21 b). As the ridges obtained at the print velocity of 30 mms^{-1} are unstable compared with those printed at 300 mms^{-1}, the respective ridge width data at 30 mms^{-1} is also smaller. In addition, the ridge widths of the structures printed at 300 mms^{-1} with pre-deposited disturbance distance of 2 mm are shown to be larger than those obtained with disturbance distance of 1 mm at small drop spacing, which is due to the smaller number of bulges obtained with disturbance of 2 mm and thus less liquid is absorbed into the bulges from the ridges.

5.4.2 Stabilized Lines on Z30 Substrates

At small drop spacing, the mechanism for bulge formation on Z30 substrates (with zero receding contact angle) is similar to that on F20 substrates, it may also be possible to achieve stabilized lines on Z30 substrates through the same pre-depositing-disturbance mechanism. Figure 5-22 shows structures printed with 10 pL printheads and with pre-deposited disturbances on the Z30 substrate at small drop spacing and two different print velocities. In the presence of pre-deposited dots, periodic bulges were formed on these sites and the ridge structures are shown to be relatively stable for both disturbance distances and print velocities. The ridge structures obtained at the print velocity of 30 mms^{-1} still show small width deviations due to limited capillary spreading at low print velocity, but are more stable than those printed on F20 substrates at 30 mms^{-1} as the receding contact angle is eliminated.

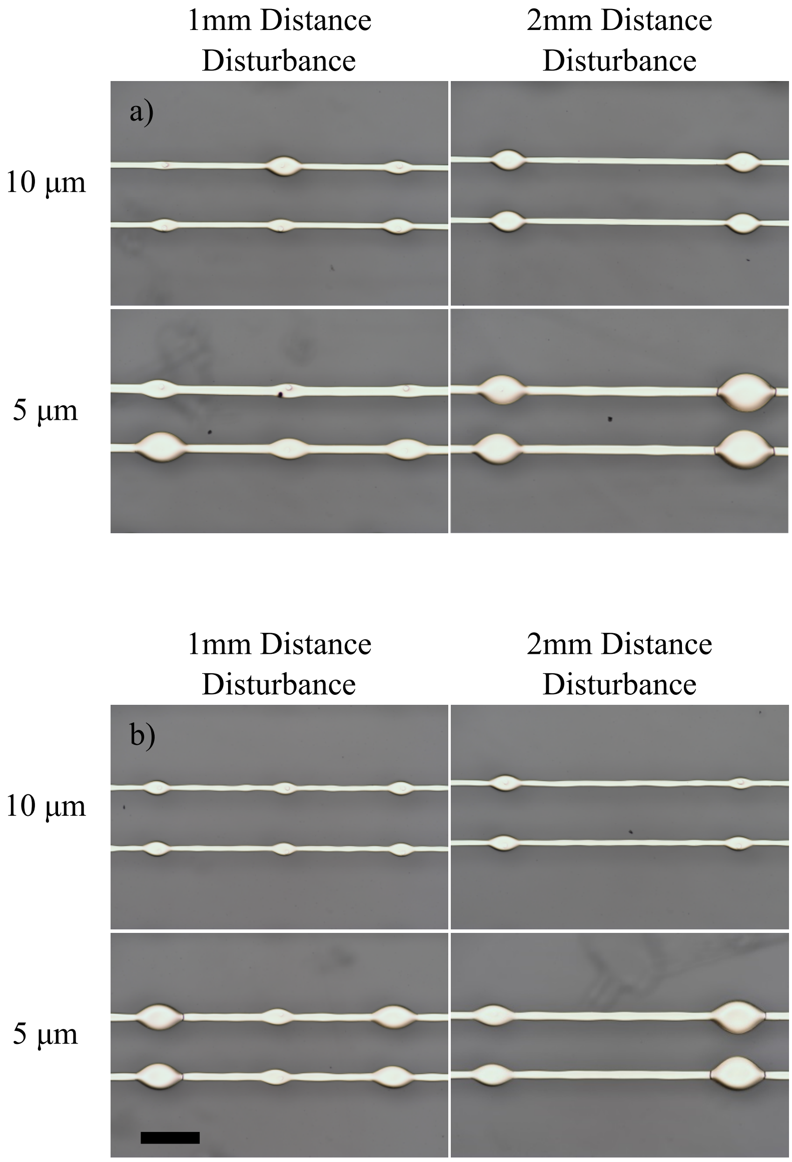

Figure 5-22 Printed structures with pre-deposited disturbances on Z30 substrates using 10 pL printheads at substrate temperature 28 °C and (a) print speed 300 mms^{-1} and (b) print speed 30 mms^{-1}, respectively. The scale bar is 500 µm.

Figure 5-23 shows the average ridge width for the structures printed on pre-deposited droplets using the Z30 substrates. The ridge widths obtained at 300 mms^{-1} are shown to be close to the values of the stable equilibrium state, while the ridge widths obtained at 30 mms^{-1} show smaller values due to limited capillary spreading and width deviations at low print velocity.

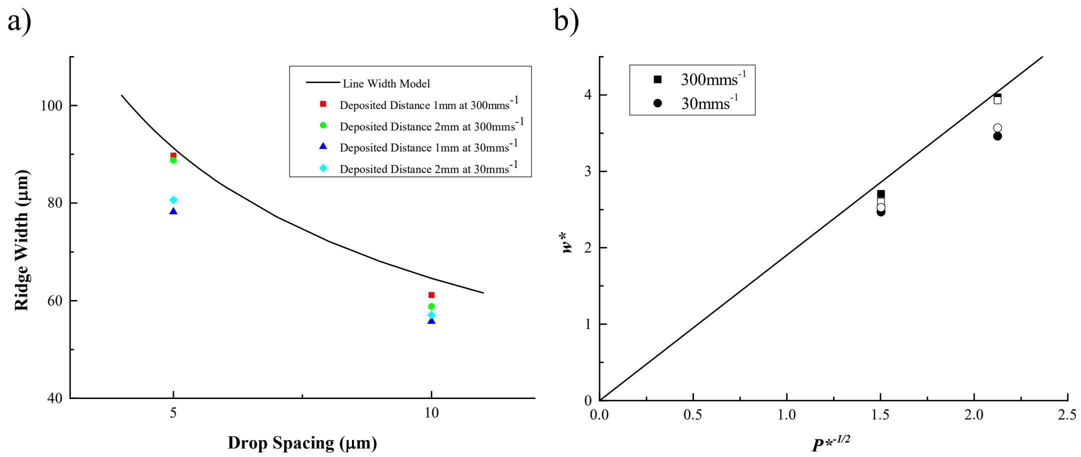

Figure 5-23 a) Measured ridge width results on Z30 substrates with pre-deposited droplets using 10 pL printheads along with the curve showing the bead width of a stable line with the same printing conditions by the line width model, and b) the relations between normalised line width and drop spacing of the results along with the linear predictions from Equation 5 – 2b, filled symbols show results with deposited distance of 1 mm, and open symbols 2 mm.

Our inkjet printed stabilized line strategy involves the formation of periodic bulges to control the pressure balance and reduce the axial transported flow within the adjacent ridges. Thus, controlling the pressure difference and suppressing the axial transported flow within the printed structures during both printing and drying period are important to achieve line stabilizing, and similar methodologies have been reported in the previous literature. Du et al. [154] achieved stable continuous printed lines on substrates with a small finite receding contact angle by adjusting the ink surface tension/viscosity ratio and drop spacing to reduce the spreading speed of deposited droplets on the substrate and control the pressure balance within the printed lines. Abunahla et al.[145] achieved stable lines without bulges at both the beginning and middle of the printed lines by applying a novel segmented and symmetric printing methodology to control the pressure balance within the printed structures.

5.5 Conclusions

1) Printed lines on the substrates with finite receding contact angles are all shown to be unstable, with isolated liquid dots at large receding contact angle and irregular bulging lines at finite receding contact angle. The unstable bulging instabilities result from both the large axial transported flow rate and the influence of the finite receding contact angle on the ridge spreading.

2) A model to predict the bulge wavelength was developed based on our experimental results and Duineveld's bulge wavelength analysis for the case of zero receding contact angle. The predicted wavelength from the model generally agrees with the experiment results. The discrepancies occurred at high printing velocities and small drop spacing are possibly due to the growth of the printed liquid bead during long drying time leading to an overestimation of the bulge volume, while droplet volume changes at low printing velocities might possibly lead to the lower prediction of the wavelength.

3) Stabilized line structures were obtained on the substrates with finite receding contact angle by pre-depositing droplets to generate small disturbances for the formation of periodic bulges, thus making the ridges relatively stable due to loss of liquid to the adjacent bugles. This method can also be used to redistribute the bulges printed at small drop spacing on the substrates with zero receding contact angle.

Chapter 6 Stability and Electrical Properties of Line Structures Produced by Inkjet Printing at Ultra High Resolution

6.1 Introduction

Inkjet printing has been used as a manufacturing tool for a wide range of applications beyond its original use for text and graphics printing. However, the physical limitations of conventional commercial inkjet printers make it difficult to achieve droplets with size smaller than 1 pL, thereby limiting its use in high resolution applications.[1] With the increasing demand of patterning on surfaces at micrometre and sub-micrometre length scales for electronic applications, electrohydrodynamic (EHD) inkjet printing was developed to achieve direct high resolution printing by droplet deposition.

Unlike conventional inkjet printers, which use thermal droplet generation and collapse, or piezoelectric actuation to eject a droplet out of the nozzle, EHD inkjet printing applies electrostatic force to pull the liquid out of the nozzle tip.[18] Under an electric field, the meniscus at the nozzle tip will deform due to coulombic repulsion and finally into a conical shape known as a Taylor cone.[19] With sufficient high voltage output, electrostatic stresses exceed the surface tension and droplets are ejected from the tip of the Taylor cone.[18] The droplet generation from the Taylor cone and the small scale of nozzle diameter allow EHD inkjet printing to eject droplets with femtolitre volume, thus achieving direct ultra-high resolution patterning in arbitrary geometries.[74] With the advantages of high resolution printing and the compatibility with a wide range of inks (1–10 000 cps),[18] EHD inkjet printing has been applied to deposit a variety of inks, including metal nanoparticle suspensions,[189, 190] nanowires,[191, 192] polymers,[76, 193] and biomaterials.[194, 195]

As the liquid is ejected from the nozzle under an electric field, the droplet size in EHD printing is influenced by the jetting flow rate and the electrical pulse time. Chen et al. [79] proposed that the jetting flow rate for pulsed EHD printing relates the balance between electric stress, applied pressure and capillary pressure. Park et al. [121] achieved drop-on-demand patterning by using pulsed EHD printing, and developed a model to predict the deposited droplet size and line width by combining the scaling law in EHD printing and the volume conservation method used to estimate droplet size in conventional DOD printing systems. A similar model to predict feature size for both pulsed and continuous EHD printing was developed by Qian et al.[184] However, there has been little systematic study of the stability of deposited features under EHD inkjet printing.

The objective of our experiment work in this chapter is to develop a drop-on-demand patterning system through EHD inkjet printing and investigate the stability and electrical properties of the printed line structures at ultra-high resolution.

6.2 Stability of Printed Structures

To investigate EHD printing, Ag nanoparticle ink was deposited onto silicon, cured polydimethylsiloxane (PDMS) coated silicon and polyimide substrates by using a commercial EHD printing system (Super Inkjet printer). UV-Ozone treatments were applied to the silicon and PDMS substrates to eliminate the receding contact angle.

A periodic pulsed waveform with pulse width time (T_p), bias voltage (V_{bias}), and amplitude voltage (V_{amp}), as shown in Figure 6-1, was used for printing on the silicon substrate. Printing was achieved by superimposing a pulsed voltage on a bias voltage, to achieve a stable meniscus at the nozzle tip, before generating deposition on demand.[106] The bias voltage was set to a value lower than the threshold voltage for jetting, and once the total applied voltage exceeds the threshold voltage, droplet ejection occurs in the pulse period.

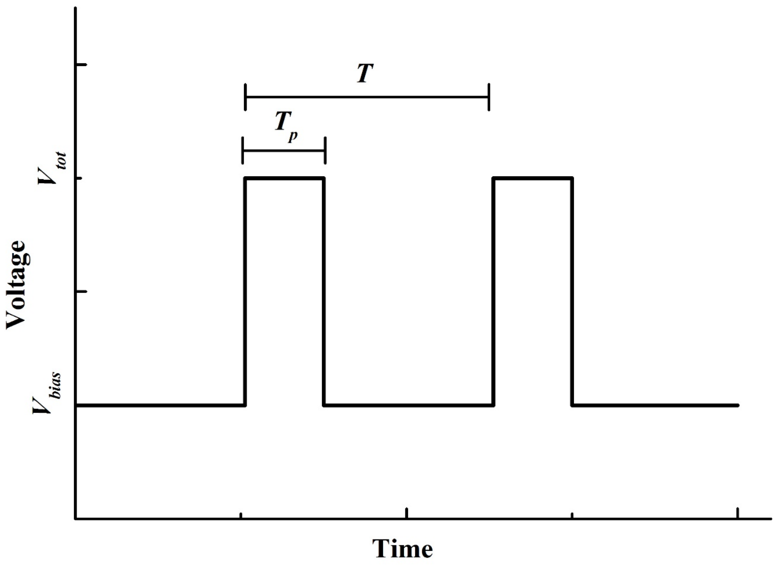

Figure 6-1 Pulsed waveform used in the experiments. V_{bias} is the bias voltage, V_{tot} is the total applied voltage, T_p is the pulse width time.

6.2.1 Single Droplet Deposition

To study the relationship between threshold voltage (V_{thr}) and nozzle to substrate distance (H) to optimize printing parameters, the V_{thr} for specific H was obtained by increasing the amplitude voltage from bias voltage, 100 V, to the voltage at which droplet ejection occurs, by using a Super-Fine printhead on the 10 min UV-Ozone treated silicon substrate. As shown in Figure 6-2 a, the threshold voltage for droplet ejection increases with increased nozzle to substrate distance. The electric field strength at the nozzle tip can be estimated by using a model of a semi-infinite wire perpendicular to an infinite planar counter electrode:[109, 110]

$$E = \frac{4V_0}{d_N \ln(\frac{8H}{d_N})} \qquad (6-1)$$

where d_N is the inner diameter of the nozzle, which is around 1.8 μm, and V_0 is the applied voltage.

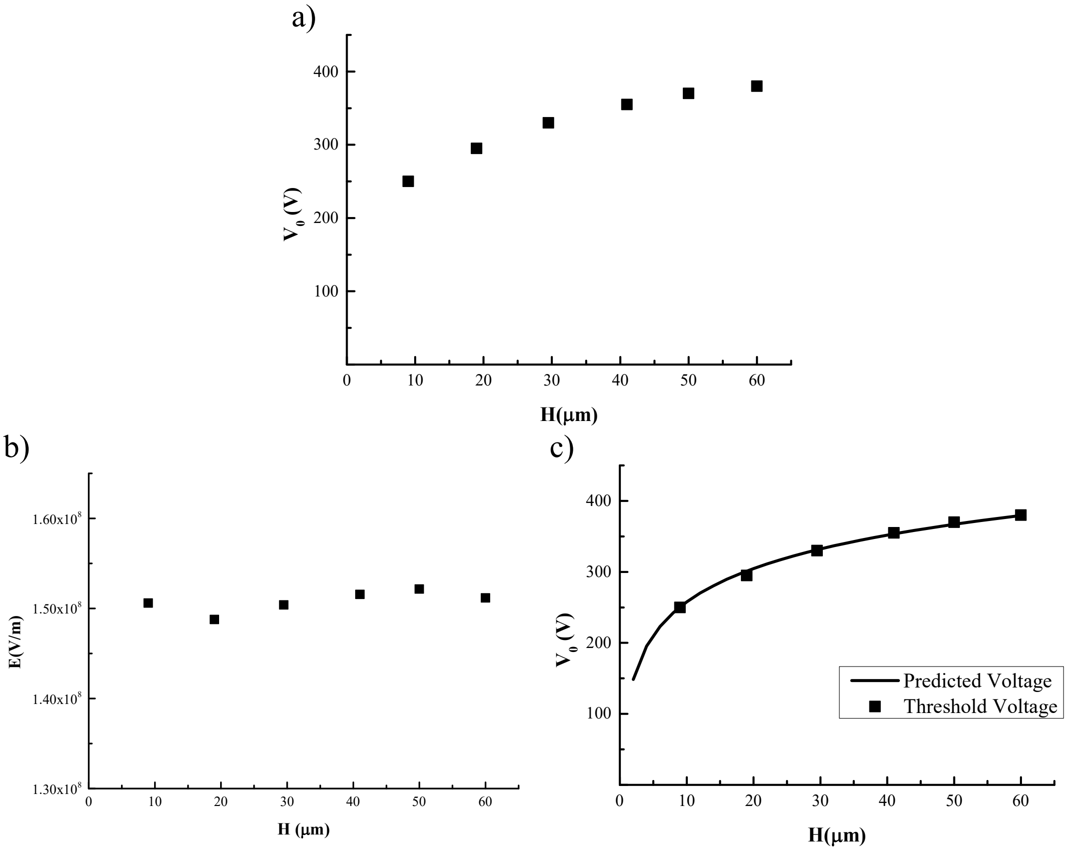

Figure 6-2 Threshold voltage (*V_{thr}*) for ejection and nozzle tip electric field (*E*) as a function of nozzle to substrate distance (*H*) on the UV-Ozone treated silicon: a) the relationship between V_{thr} and *H*; b) the relationship between *E* and *H*; c) predicted V_{thr} as a function of *H* by using average *E* and Equation 6 – 1.

The electric field strength, calculated using Equation 6-1, for the threshold jetting voltage at different nozzle to substrate distance is plotted in Figure 6-2 b. The threshold electric field strength for jetting is approximately constant over all nozzle to substance distances studied. This is consistent with the predictions of the relationship between fluid flow rate, *Q*, and EHD jetting parameters proposed by Chen et al:[79]

$$Q \approx \frac{\pi d_N^4}{128\mu L}\left(\frac{1}{2}\varepsilon_0 E^2 + \Delta P - \frac{2\gamma}{d_N}\right) \qquad (6-2)$$

where *L* is the length of the nozzle, *μ* is the fluid viscosity, ε_0 is the vacuum permittivity, *E* is the strength of applied electric field, *ΔP* is the applied hydrostatic pressure, and *γ* is the surface tension of the fluid. The threshold for jetting requires the sum of the electric pressure $\varepsilon_0 E^2/2$ and hydrostatic pressure *ΔP* to exceed the capillary pressure, $2\gamma/d_N$, at the nozzle. At the threshold for jetting, the flow rate *Q* should be constant. Given that the hydrostatic pressure and capillary pressure remain constant at the threshold for jetting, independent of nozzle to substrate distance conditions, the electric pressure also remains the same, thus explaining the constant electric field strength at the threshold for droplet ejection. This agreement between the predicted electric field strength and observation, indicates that our printing conditions can be described by EHD principles and meniscus behaviour, although it is difficult to observe the meniscus deformation during printing in our system due to the relatively small nozzle size.

By using the average electric field strength from the calculated results, the predicted threshold voltage for jetting can be obtained as a function of nozzle to substrate distance by using Equation 6 – 1. This is shown in Figure 6-2 c, with the predicted curve agreeing well with our measured results. After a series of experiments, we chose an applied voltage pulse of 310 V with bias voltage 100 V, with a nozzle to substrate distance of 20 μm, for optimum printing conditions. The pulse voltage is chosen to be just above the threshold voltage for jetting (295V) to achieve stable minimised feature size, and the nozzle to substrate distance is chosen with an intermediate value to minimise the deviation in the printed feature size at small values and unstable spraying at large distances.

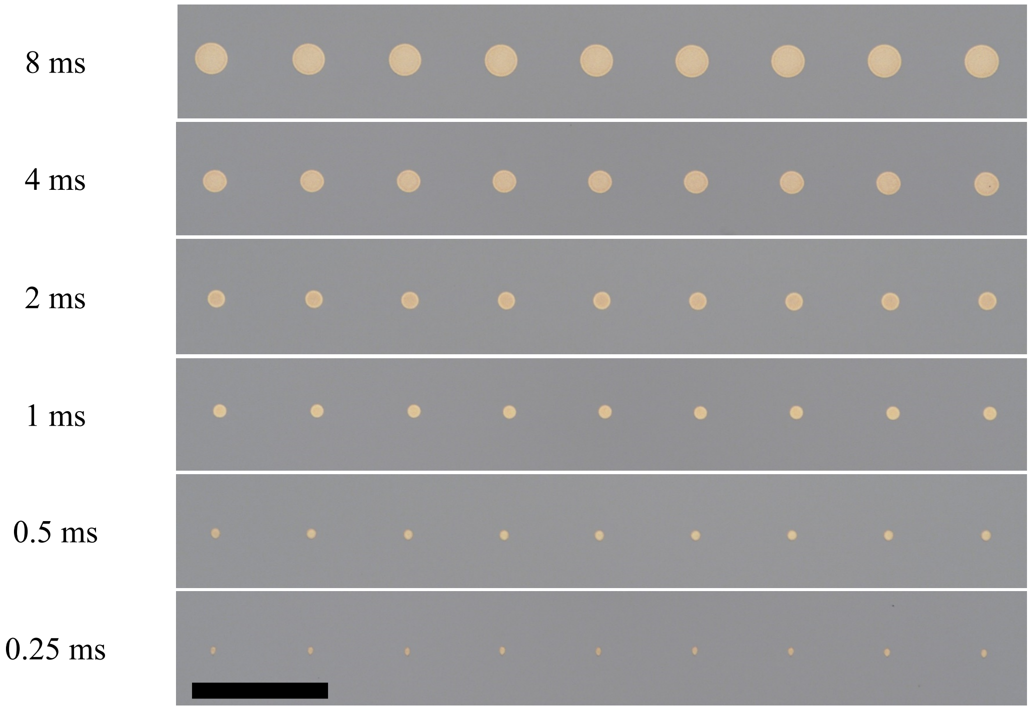

Figure 6-3 Single dots deposited on 10 min UV-Ozone treated silicon as a function of pulse width time at an applied voltage of 310 V. The nozzle to substrate distance is 20 μm. The scale bar is 100 μm.

For pulsed EHD inkjet printing, the total ejected volume per pulse is determined by the ejected flow rate from the cone and the pulse width time. This can be calculated as:

$$V = Q \cdot T_p = Q \frac{x_p}{f} \qquad (6-3)$$

where V is the total ejected drop volume per pulse, Q is the jetting flow rate, T_p is the pulse width time, x_p is the duty ratio of the pulse, and f is the applied pulse frequency. To investigate the relationship between deposited droplet diameter and pulse width time, a series of individual dots were printed onto 10 min UV-Ozone treated silicon at different pulse width times, as shown in Figure 6-3. It can be seen that stable, uniform dots were obtained over a range of pulse width times, with the dot diameter increasing dramatically at elevated pulse width time. Assuming the jetting flow rate remains constant during printing, as the electric pressure, hydrostatic pressure, and capillary pressure remain the same in our experiment set up, the deposited droplet diameter should be proportional to the cube root of the pulse width time:

$$d_{eqm} = \beta_{eqm} \sqrt[3]{\frac{6Q}{\pi} T_p} \qquad (6-4)$$

where β_{eqm} is a factor only determined by the contact angle between the deposited droplet and the surface, which is given in Equation 4 – 1 (Chapter 4). The flow rate, Q, in Equation 6 – 4 was obtained by using the mean deposited dot diameter at pulse width time 0.5 ms, and the calculated value is 2.39×10^{-14} m^3s^{-1}. By using the calculated flow rate and the above equation, the dot diameter as a function of pulse width time is predicted, as shown in Figure 6-4. These predictions agree well with the experimental results, indicating that the flow rate maintains constant in the printing equipment.

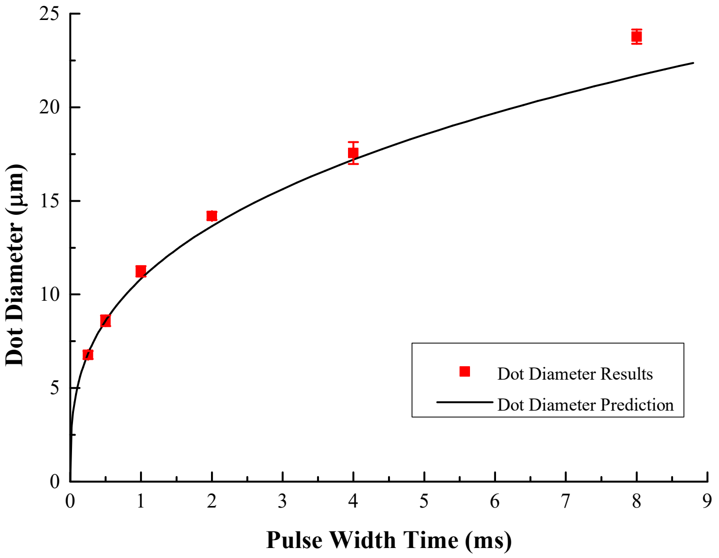

Figure 6-4 The deposited dot diameter on the UV-Ozone treated silicon substrate as a function of pulse width time, along with the dot diameter prediction curve.

In order to test the models for line stability used in the previous chapters, it is necessary to provide constant drop volume at a range of drop spacings and printing velocities. However, the drop generation frequency is a function of drop spacing and velocity. Thus, to achieve a constant ejected volume per pulse, the pulse width time T_p should remain constant as the frequency is changed, requiring the applied duty ratio of pulse x_p to also change with frequency, in accordance with Equation 6 – 3. The appropriate duty ratio and frequency for the printing velocity and drop spacing conditions used in the study are listed in Appendix A for the single pulse waveform.

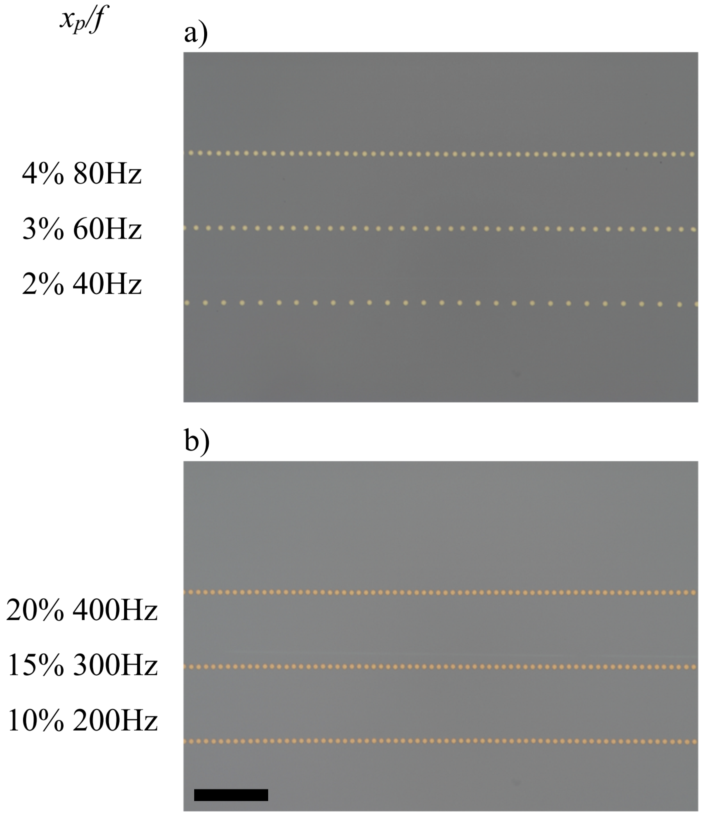

Figure 6-5 Printed dots at applied voltage 310 V, nozzle to substrate distance 20 µm, and pulse width time 0.5 ms, with different jetting frequency and duty ratio: a) at low frequency and fixed print velocity of 1 mms^{-1}, b) at high frequency and fixed drop spacing of 10 µm. The scale bar is 100 µm.

To confirm the deposited droplet size at various printing frequencies, printing was carried out onto 10 min UV-Ozone treated silicon at a drop spacing significantly larger than the deposited droplet diameter, and with a fixed pulse width time, 0.5 ms. As shown in Figure 6-5, a series of stable circular dots were obtained at various printing frequency conditions. The average deposited droplet diameter is 8.4 µm with a standard deviation of 0.3 µm, indicating that droplets with identical size can be obtained at various jetting frequencies. The ejected volume per pulse can be calculated from the deposited droplet diameter and the contact angle on the substrate by using volume conservation, assuming a spherical cap geometry:

$$V_0 = \frac{\pi \tan\frac{\theta}{2}\left(3 + \tan^2\frac{\theta}{2}\right)}{48} d_{eqm}^3 \qquad (6-5)$$

where θ is the contact angle of the deposited droplet on the substrate, and d_{eqm} is the deposited droplet diameter. Here we used the advancing contact angle (θ_a) instead of the equilibrium contact angle (θ_{eqm}), as the droplet spreads and advances on the solid surface after impact. By substituting the average deposited droplet diameter of 8.4 μm and the advancing contact angle of 10.9° into Equation 6 – 5, the estimated drop volume per pulse from our printing setup is around 11 fL, which is 2 to 3 orders of magnitude smaller than that generated from a conventional piezoelectric inkjet printer.

6.2.2 Lines Printed on Silicon

In order to investigate the stability of printed line structures formed with femtolitre drops, a series of prints were carried out onto 10 min UV-Ozone treated silicon substrates (Z10 substrate) using a Super-Fine printhead at 25 °C. Two lines were printed consecutively onto the substrate from left to right for each printing setup, and the printing direction was along the deposited lines. The printing velocity can be easily adjusted through the printer's built-in function, and the drop spacing was adjusted by changing the printing velocity at specific jetting frequency. The printing speed ranged from 0.1 to 2 mms^{-1} and the drop spacing from 1 – 7 μm. The applied voltage and nozzle to substrate distance were 310 V and 20 μm, respectively, the same values as used to generate individual droplets previously. The pulse width was set to 0.5 ms for all the prints to ensure same deposited droplet size. The corresponding frequency and duty ratio combinations are listed in Appendix A. As only natural numbers are allowed for duty ratio in the printing system (e.g. 1%, 2%, 5%, etc.), some printing velocity and drop spacing combinations cannot be achieved, an approximate printing velocity was applied in this case, as listed in Appendix A.

Figure 6-6 shows the resulting printed structures with nominal drop volume of 11 fL, with advancing contact angle 10.9° and receding contact angle 0°. For all print speeds, stable parallel sided lines started to be formed at a drop spacing of 5 μm. At printing velocities of 2 and 1 mms^{-1}, stable lines were achieved at all values of drop spacing < 5 μm, while bulges were observed at drop spacings of 2 and 1 μm at a printing velocity of 0.4 mms^{-1}. As the maximum jetting frequency of the machine is 1 kHz, it is impossible to print at a printing velocity of 2 mms^{-1} and drop spacing of 1 μm. At printing velocities of 0.2 and 0.1 mms^{-1}, relatively stable lines were obtained at the drop spacing of 5 and 4 μm, while a periodic bulge connected by ridge instability was observed as the drop spacing ranged from 3.3 to 1 μm, and the instability appeared to be more severe with decreased drop spacing. The transition in behaviour is identical to that seen with picolitre drop volumes produced by conventional inkjet printers and discussed earlier in Chapter 4.

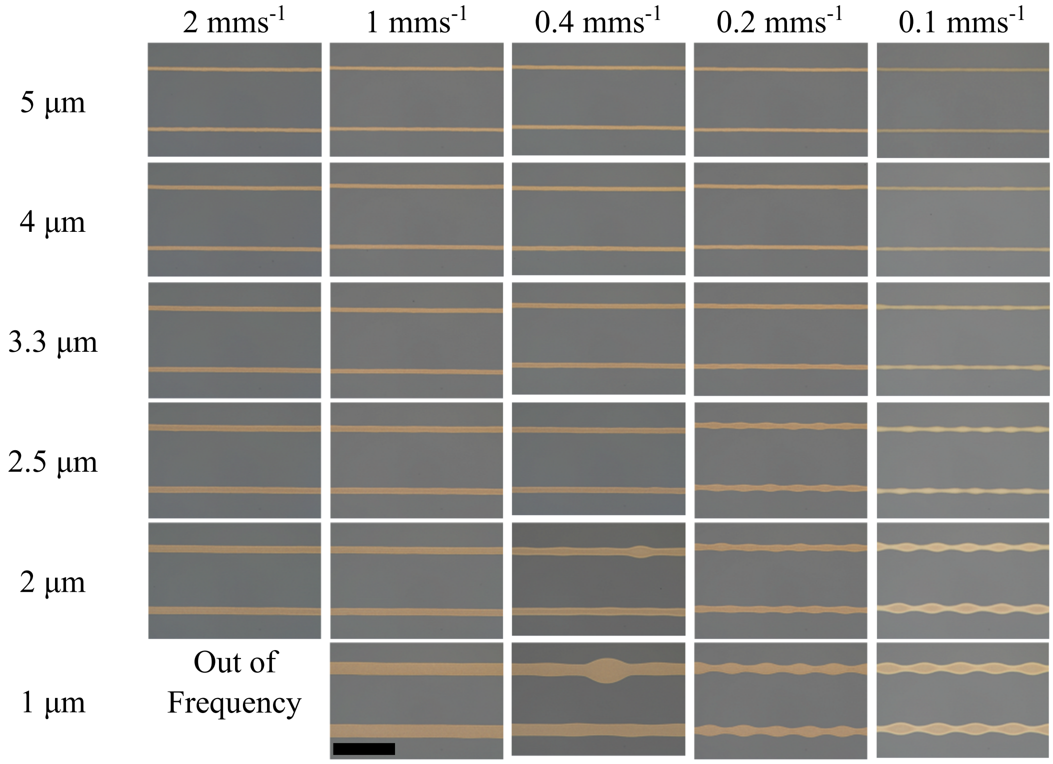

Figure 6-6 Lines printed on the Z10 substrate with printing speed in the range 0.1 – 2 mms^{-1} and drop spacing 1 – 5 µm, with 11 fL drops. The scale bar is 100 µm.

Figure 6-7 shows printed structures obtained at larger drop spacings of 6 and 7 µm and both high and low printing speeds. At 6 µm drop spacing, continuous line structures were obtained at both high and low print speeds, however, the printed lines show ridge width deviations. At a drop spacing of 7 µm, discrete line segments were obtained.

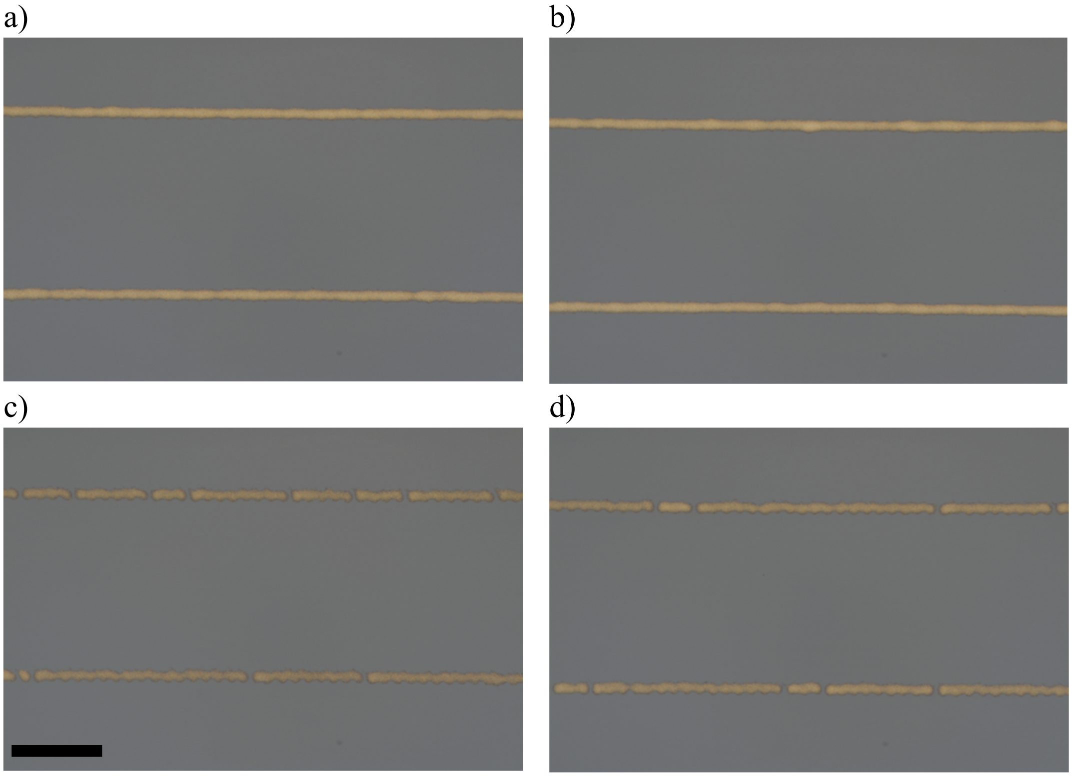

Figure 6-7 Printed lines on the Z10 substrate with: a) printing speed 0.12 mms^{-1}, drop spacing 6 µm; b) printing speed 1.92 mms^{-1}, drop spacing 6 µm; c) printing speed 0.14 mms^{-1}, drop spacing 7 µm; and d) printing speed 1.96 mms^{-1}, drop spacing 7 µm. The scale bar is 50 µm.

Given the similarity in behaviour with lines produced by conventional inkjet printing, the validity of Stringer's model for use with these ultra-small EHD printed droplets was explored. Stringer's model, in dimensionless form, predicts a region for stable parallel line formation at a given printing velocity above a critical minimum value. This is limited by an upper bound of drop spacing, above which there is insufficient droplet overlap to form a uniform width line if the liquid has a zero receding contact angle, and a lower bound below which bulges form because of an imbalance between the spreading flow of a new drop and flow backwards through the growing liquid bead.[14] This is shown in Figure 6-8 along with our experimental results displayed using the normalisation as presented in Chapter 4. The boundary conditions for maximum and minimum drop spacing predictions were obtained by Equation 4 – 3 and 4 – 7 in Chapter 4, respectively. The dashed line shows the maximum drop spacing bound, above which unstable wavy structures or line segments would occur, and the solid line is the bulging instability bound, below which bulging structures would be obtained. From the diagram, the maximum drop spacing prediction generally agrees well with our experimental results, although the predicted value is slightly smaller than the observed stability limit, with a predicted maximum drop spacing of 4.9 μm while stable lines obtained at 5 μm. The minimum drop spacing prediction also agrees well with our experimental results.

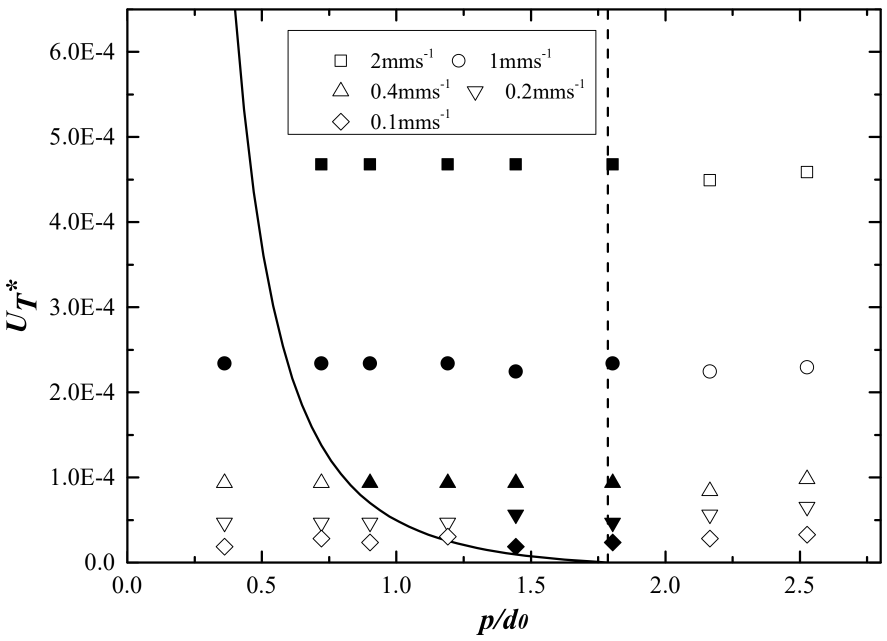

Figure 6-8 Stability map showing the condition for the maximum and minimum drop spacing limits for stable lines with data from the super inkjet printing experiments on the Z10 substrate. Open symbols indicate unstable morphology and filled symbols indicate stable morphology. The dashed line shows the maximum drop spacing bound, and the solid line is the bulging instability bound.

The relationships between the measured line width results at various printing conditions along with the line width model predictions from Equation 4 – 2a in Chapter 4 for a stable, parallel sided bead with zero receding contact angle are plotted in Figure 6-9. For structures which displayed bulges, the width of the parallel sided connecting ridge was used. At the drop spacing ranged from 3.3 μm to 5 μm, the width predictions agree well with our experimental results, with no clear systematic variation as a function of printing velocity. At the drop spacing < 2.5 μm, however, this good agreement only occurs for the lines printed with printing velocity larger than 0.4 mms^{-1}, while big deviations are seen for the lines printed at the printing velocity of 0.2 and 0.1 mms^{-1}, when bulges were formed on the lines.

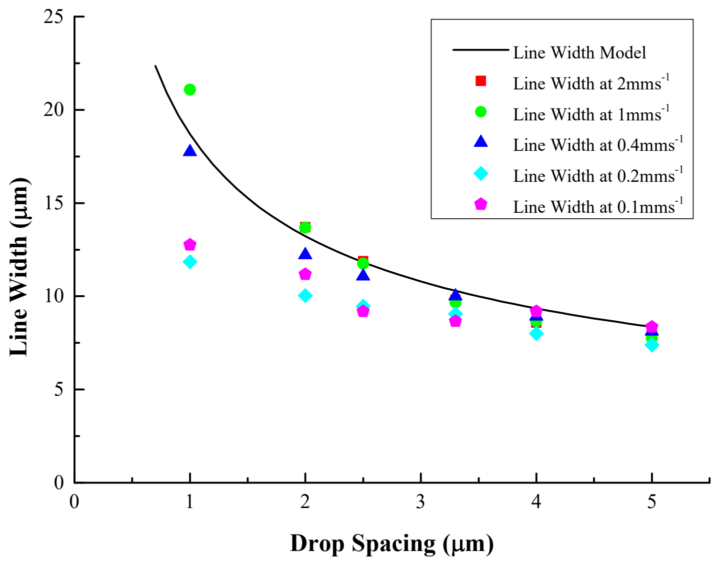

Figure 6-9 Measured line width results on the Z10 substrate as a function of drop spacing along with the line width model prediction.

To further extend the application of the printed stable line structures using EHD printing, narrow line width 2D grids were deposited on the Z10 substrate, as shown in Figure 6-10. The voltage and nozzle to substrate distance parameters remained the same as that used previously, while two pulse width times, 0.5 and 0.25 ms were applied to investigate the ejected volume influence on the printed feature size. The horizontal lines were printed first by printing along each line consecutively from left to right, and the vertical lines were then printed along the line direction from bottom to up. Figure 6-10 a and b show the printed silver grids at the printing velocity of 2 mms^{-1} and drop spacing of 5 µm with pulse width time of 0.5 ms, and Figure 6-10 c and d show the printed grids at the printing velocity of 3 mms^{-1} and drop spacing of 3.75 µm with pulse width time of 0.25 ms. It can be seen that, for the structures printed at both pulse width times, relatively stable grids with straight lines crossing each other can be obtained. The mean line width of the grids printed with pulse width time of 0.5 ms is 8.2 µm, while a smaller width of 5.7 µm was obtained for the grids printed with pulse width time of 0.25 ms. This indicates that by decreasing the pulse width time to reduce the ejected volume per pulse, in this case to approximately 4 fL, the printed features could be further minimized. In addition, where the printed lines intersect there is a clear broadening of the cross-over region for both printing conditions. We interpret this as the consequence of the difference in pressure within the intersecting liquid beads, resulting from the smaller mean surface curvature at the intersection, which leads to a pumping flow of ink to the intersection before drying occurs.

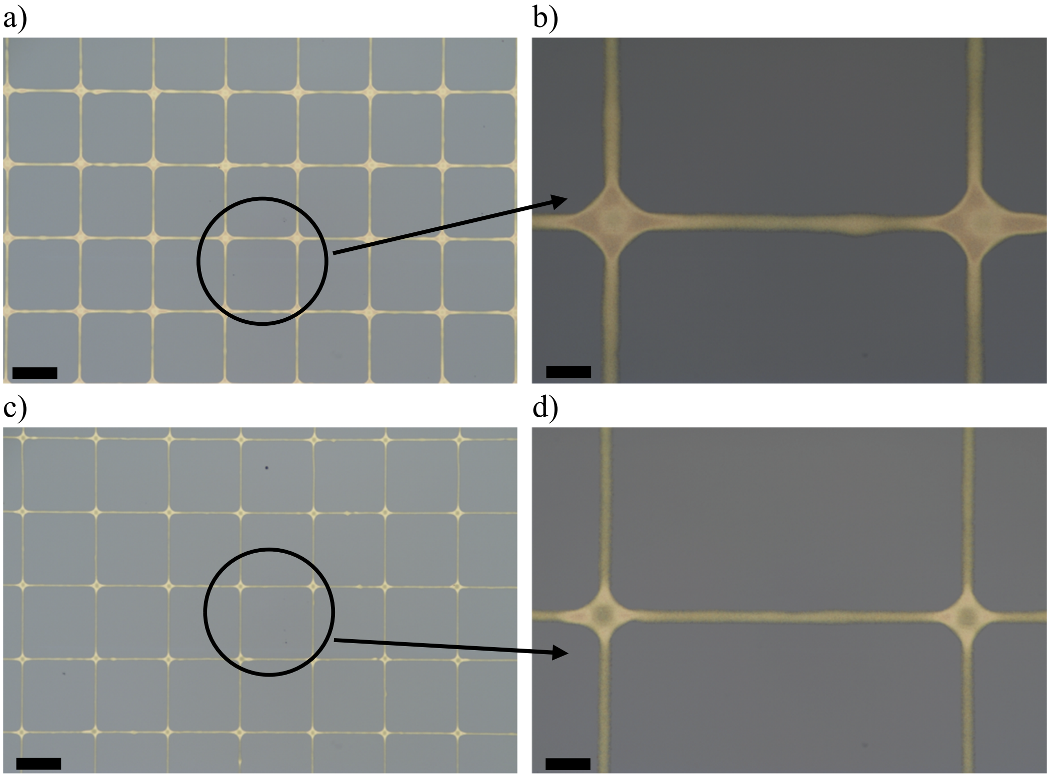

Figure 6-10 Printed silver grids on the Z10 substrate: a) and b) printed grids at the printing velocity of 2 mms^{-1} and drop spacing of 5 μm with pulse width time 0.5 ms; c) and d) printed grids at the printing velocity of 3 mms^{-1} and drop spacing of 3.75 μm with pulse width time 0.25 ms. The scale bar in a) and c) is 100 μm, b) and d) 20 μm.

6.2.3 Lines Printed on PDMS

From previous experiments, continuous stable lines were printed on the silicon substrate with high resolution. However, the contact angle on the silicon substrate is small (10.9°), and for a fixed single droplet volume the deposited feature size could be further reduced with increasing contact angle.[14] Thus, to investigate the stability of high-resolution inkjet printed line structures on substrates with a high contact angle, silver nanoparticle suspensions were printed on a PDMS coated silicon substrate. UV-Ozone treatment of a time period of 40 min was applied to the PDMS surface to eliminate the receding contact angle and reduce the advancing contact angle to 34.7°. This is henceforth called a Z40 substrate. As the PDMS coated silicon substrate is an electrical insulator, the charges from the deposited droplets cannot be earthed. This leads to a well-known charging effect,[176] which can distort or deflect subsequent printed drops leading to atomisation and unwanted droplet spray. Hence, to minimise the charging effect, a bipolar waveform was applied during printing, as shown in Figure 6-11. Each positive or negative pulse can generate one droplet, with each adjacent drop now of opposed charge to reduce long range charging effects. The time period between adjacent positive and negative pulses was set to be the same to ensure deposition with identical drop spacing. In this case the deposition frequency is twice the applied pulse frequency. The nozzle to substrate distance was set to 20 μm, the total applied voltage was set to 500 V, and the pulse width time for each positive and negative pulse was maintained at 0.5 ms by adjusting the printing frequency and duty ratio.

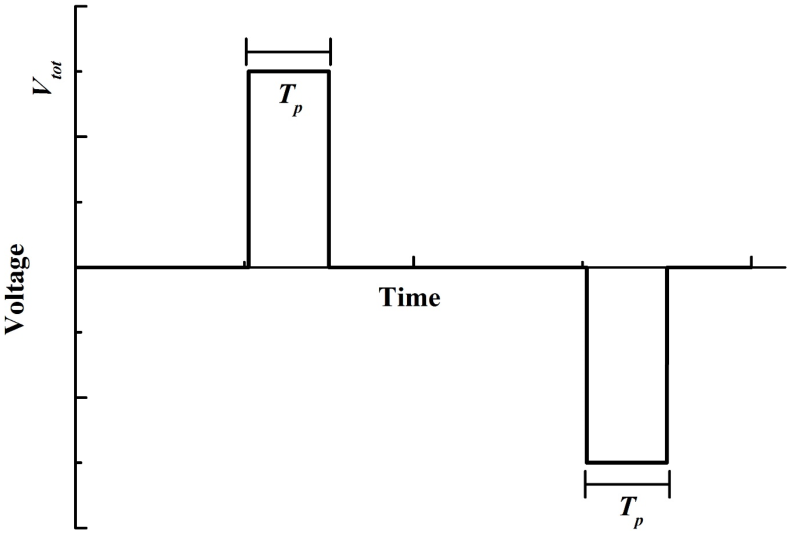

Figure 6-11 Bipolar waveform used in the experiments. V_{tot} is the total applied voltage, T_p is the pulse width time.

Figure 6-12 a shows the printed individual dots on the Z40 substrate at the drop spacing of 15 μm. It can be seen that the individual dots show irregular shapes with unwanted spraying of nanoparticles on other areas of the substrate, indicating that there is a severe charging effect during printing on the nonconductive substrate. The single ejected volume in this printing setup could be roughly estimated by using the mean deposited droplet area and the advancing contact angle between the droplet and the substrate (34.7°). The mean area of the deposited droplets was obtained by analysing the total area of 38 deposited dots by ImageJ, as shown in Figure 6-12 b. Assuming a stable deposition of the droplets on the substrate with the spherical cap shape, the mean deposited droplet diameter can be estimated from the mean area

($d_{eqm} = 2\sqrt{\frac{A_{area}}{\pi}}$), which is 6.4 µm. The ejected volume per pulse can be then estimated from Equation 6 – 5, giving approximately 16 fL.

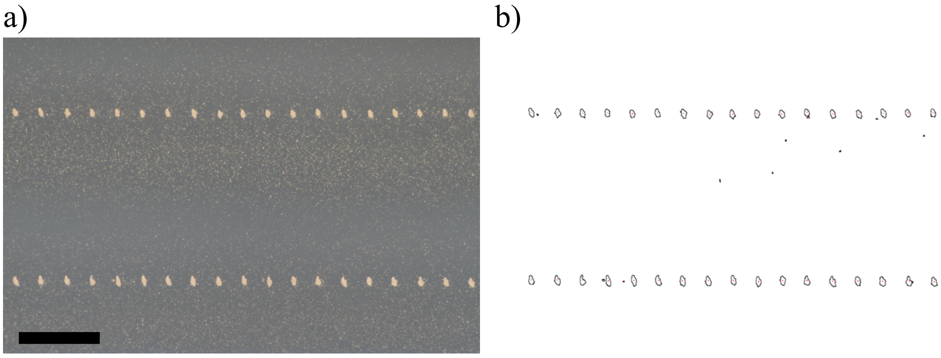

Figure 6-12 Printed individual dots on the Z40 substrate at the printing velocity of 1.2 mms^{-1}, frequency of 40 Hz, duty ratio of 2%, and drop spacing of 15 µm: a) Printed morphologies of the dots observed by the optical microscope, b) profiles of the deposited dots obtained by ImageJ. The scale bar is 50 µm.

Figure 6-13 shows the printed structures on the Z40 substrate (θ_a = 34.7°, θ_r = 0°), with drop spacing ranging from 1 to 7 µm at printing speeds of 0.4 and 2 mms^{-1}, respectively. There is a distinct transition in behaviour as the drop spacing is reduced from 7 to 6 µm. At the larger separation the drops remain distinct and irregular, with the surrounding region showing a spray of fine droplets as the result of local charging. In contrast at a spacing of 6 µm and lower, continuous liquid beads form on the surface and the spray deposition is absent. This is believed to be the result of charge neutralisation following the coalescence of oppositely charged adjacent droplets. At a drop spacing of 6 µm, continuous wavy line structures form at both printing speeds. As the drop spacing decreases, stable parallel sided lines form at both 5 and 4 µm drop spacing when printing at 2 mms^{-1}, and at 5 µm drop spacing at 0.4 mms^{-1}. Further decrease in drop spacing leads to unstable periodic bulging instabilities for both printing speeds, with the bulges in the structure growing larger with decreased drop spacing.

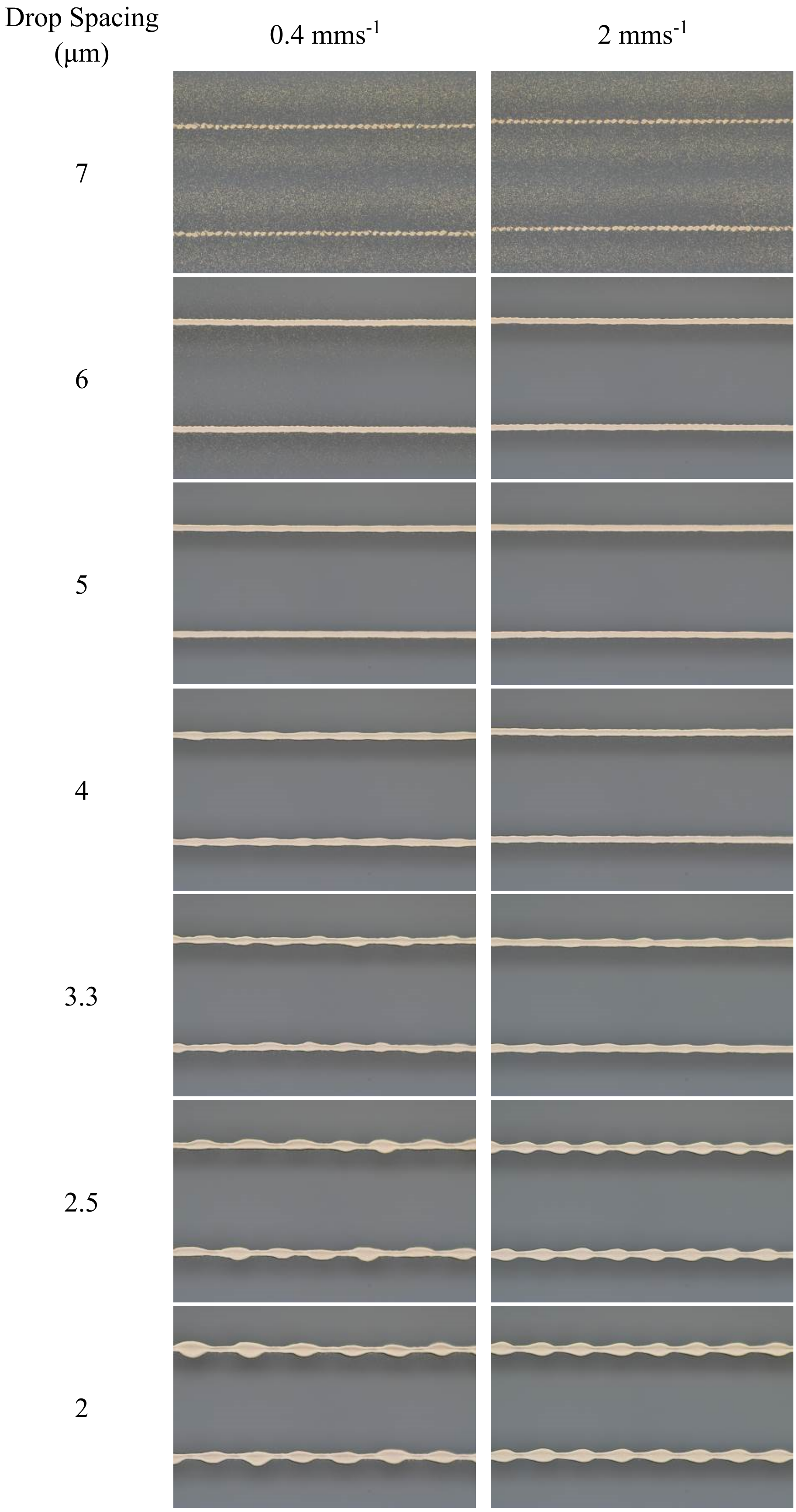
Drop Spacing (μm)
0.4 mms-1
2 mms-1
7
6
5
4
3.3
2.5
2

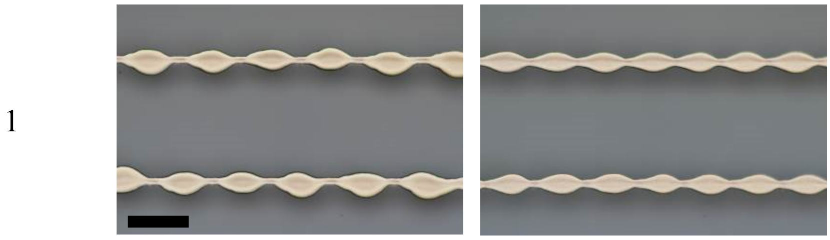

Figure 6-13 Lines printed on the Z40 substrate, with drop spacing ranged from 7 to 1 μm, and printing speed of 2 and 0.4 mms^{-1}. The scale bar is 50 μm.

The stability map showing our experimental results displayed using the normalisation as presented in Chapter 4 along with the predictions of Stringer's model [14] is plotted in Figure 6-14. See Appendix B for a full description of the method used to determine the drop spacing and printing velocity from EHD printing parameters. The model predictions show a similar form to the experiment results but are shifted to the left by about $0.5d_0$ compared with our experimental results. Meanwhile, compared with the predicted stability region on the Z10 (Si) substrate with a contact angle of 10.9° (red dashed line in the figure), it is clear that increasing the contact angle considerably reduces the range of drop spacing that leads to a stable line, even though the resulting lines are considerably thinner than attainable on low contact angle surfaces. The greater discrepancy between prediction and experiment as the contact angle increases may reflect an uncertainty as to the drop volume, which was determined from the irregular spread diameter and an assumption that this could be approximated by a spherical cap.

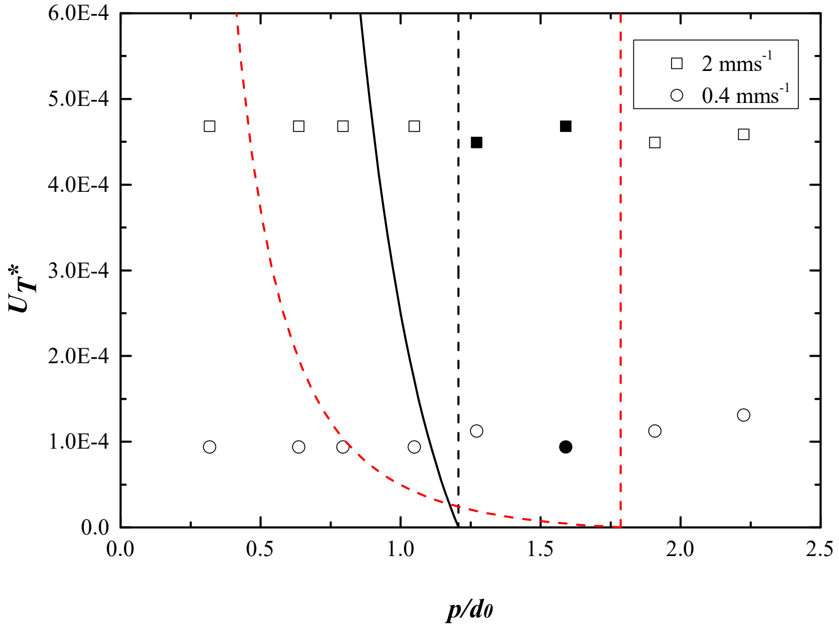

Figure 6-14 Stability map showing the condition for the maximum and minimum drop spacing limits for stable lines with data from the super inkjet printing experiments on the Z40 substrate (black lines), along with the bounds for the Z10 substrate (red dashed lines) as comparison. Open symbols indicate unstable morphology and filled symbols indicate stable morphology. The vertical lines show the maximum drop spacing bounds, and the curved lines are the bulging instability bounds.

The mean bulge and ridge width of the printed line structures on the Z40 substrate as a function of drop spacing, along with the line width prediction for a stable parallel sided liquid bead at the same conditions, at the printing velocity of 0.4 and 2 mms^{-1} are plotted in Figure 6-15 a and b, respectively. It can be seen that the ridge width maintains in a same level at decreased drop spacing for both printing speeds, while the bulge width at the two printing speeds both increase dramatically with decreased drop spacing. In addition, large deviations of bulge width were observed at the printing velocity of 0.4 mms^{-1} and drop spacing from 2.5 to 1 µm, while for the bulge width at 2 mms^{-1}, large deviation was only observed at the drop spacing of 1 µm.

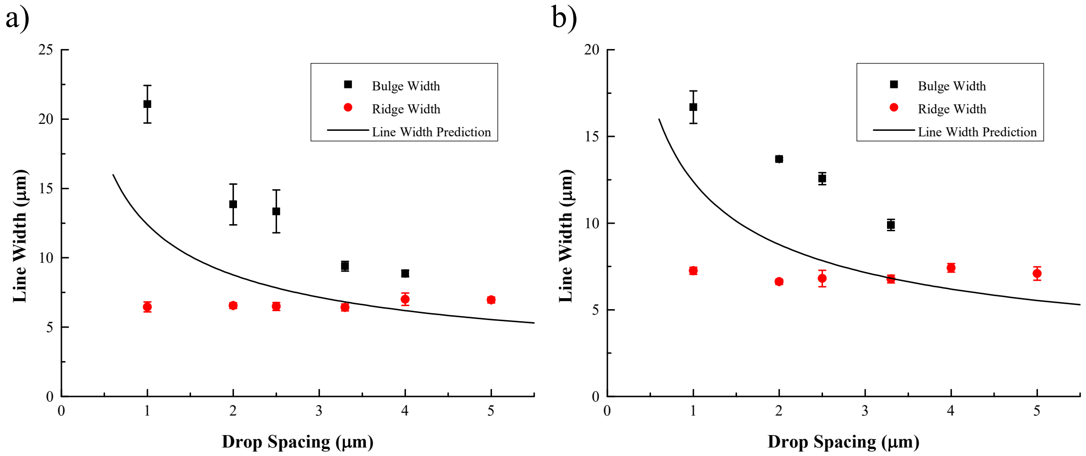

Figure 6-15 Mean bulge and ridge width results of the printed lines at the printing velocity of a) 0.4 mms^{-1}, and b) 2 mms^{-1}, along with the width prediction for a stable parallel sided liquid bead from Equation 4 – 2a in Chapter 4.

6.2.4 Discussion

To achieve stable drop-on-demand printing using the EHD printing system, the first step is to achieve identical ejected volume per pulse. From Equation 6 – 3, the ejected volume per pulse is determined by the jetting flow rate Q and the pulse width time T_p. As the applied voltage, nozzle to substrate distance, nozzle parameter and ink properties remain the same for the printing set up, the electric pressure $\varepsilon_0 E^2/2$, hydrostatic pressure ΔP, and capillary pressure $2\gamma/d_N$ also remain the same during printing. Thus, the jetting flow rate Q should maintain the same for the specific printing set up according to Equation 6 – 2, and our experiment results for the relationship between deposited droplet diameter and pulse width time validated this assumption.

However, the pulse width time for EHD printing is strongly influenced by the applied frequency. For the previous results in Chapter 4 and 5 carried out using Dimatix piezoelectric printheads, the jetting period (pulse width time) is around 12 μs for the ANP Jetting Waveform, and for the rest of the time in one total period the ANP Non-Jetting waveform with zero voltage was applied. Thus, the waveform set up makes the applied frequency having little effect on the jetting period and the ejected droplet size. For the Super Inkjet Printing System, however, there is no such Non-Jetting waveform to maintain the same pulse width at various frequencies, thus the pulse width time is linked with the applied frequency at fixed duty ratio, and the identical pulse width time can only be achieved by applying different frequency and duty ratio combinations at various printing conditions (see Appendix A). The single deposited droplets with the same diameter obtained at various applied frequencies on the Z10 substrate (Figure 6-5) verified the above analysis. The ejected volume per pulse can be calculated from the deposited droplet diameter and the advancing contact angle on the substrate by using volume conservation, assuming a spherical cap geometry (Equation 6 – 5). As the deposited single dots on the Z10 substrate all have uniform circular shapes, with same diameter size and small variance, we hypothesize that the calculated ejected volume per pulse from the equation is very close to the real value, and can be applied to the further calculations for the line stability and electrical properties.

The morphologies of the lines printed on the 10 min UV-Ozone treated silicon (Z10 substrate) have a similar trend compared with those printed on the 30 min UV-Ozone treated PDMS with Dimatix printheads in Chapter 4. Discrete line segments were obtained above a certain drop spacing, and the maximum drop spacing for stable overlapping is independent of the printing velocity, while bulging instabilities were obtained below a certain drop spacing, also as a function of printing velocity. However, for the lines printed on the Z10 substrate in this chapter, the predicted maximum drop spacing bound is slightly smaller than the observed stability limit, and continuous lines (although unstable) can still be obtained at a drop spacing larger than the maximum bound (Figure 6-7).

The maximum drop spacing bound predicts the maximum droplet overlapping for a stable parallel sided liquid bead, hence continuous lines can also be achieved at a drop spacing larger than the maximum limit, but with an unstable wavy shape due to insufficient droplet overlapping and surface tension minimization.[13] This wavy shape morphology can be observed from the continuous lines obtained at the drop spacing of 6 μm (Figure 6-7 a and b), and the line segments obtained at the drop spacing of 7 μm (Figure 6-7 c and d), on the Z10 substrate.

For the minimum drop spacing bound above bulging instability on the Z10 substrate, the predictions from the model generally agree well with our experimental results. As the silicon substrate is conductive, the charges from the deposited liquid could transfer from the substrate to the below metal platform, thus charging effect can be neglected. The good agreement shows that the stability model can still be applied to predict the minimum drop spacing bound with femtolitre drops at zero receding contact angle.

The line width model can accurately predict the line width at high printing speeds, while big deviations occur at low printing speeds and small drop spacings, where bulges were formed (Figure 6-9), absorbing the liquid of the adjacent ridge and limiting the spreading of the ridge bead to its equilibrium state.

From the printed grid results it can be seen that the printing resolution can be further increased by decreasing the pulse width time, due to decreased ejected volume per pulse. However, the pulse width time has a minimum value required to allow stable deformation of the meniscus during printing.[106] In our experiments, stable jetting was achieved with pulse width time of 0.25ms.

To investigate the stability of the printed line structures with ultra high resolution at elevated contact angle, printing was carried out on the 40 min UV-Ozone treated PDMS coated glass substrate (Z40 substrate). To reduce the charging effect on the nonconductive PDMS substrate, a bipolar waveform was applied during printing. Through the waveform design, the positive and negative charges from the adjacent deposited droplets were found to neutralize charging effects on the nonconductive substrate. Similar ac-pulse based waveforms have been applied to achieve stable EHD inkjet deposition in the previous literature.[172, 196, 197] This method minimized charging effects when printing continuous lines at a drop spacing < 6 μm, however, severe charging effect was still observed from the discrete dot structures at the drop spacing larger than 6 μm, as shown in Figure 6-12 and Figure 6-13. As the printed individual dot structures don't coalesce with each other, the positive and negative charges from the droplets are not neutralized, hence leading to the charging effect. Meanwhile, as no continuous lines were formed on the nonconductive substrate, the droplet ejection for the dot printing can also be unstable, with unwanted spraying of droplets out of the nozzle, thus exasperate the charging effect. A schematic diagram showing the deposition at different printing conditions is shown in Figure 6-16.

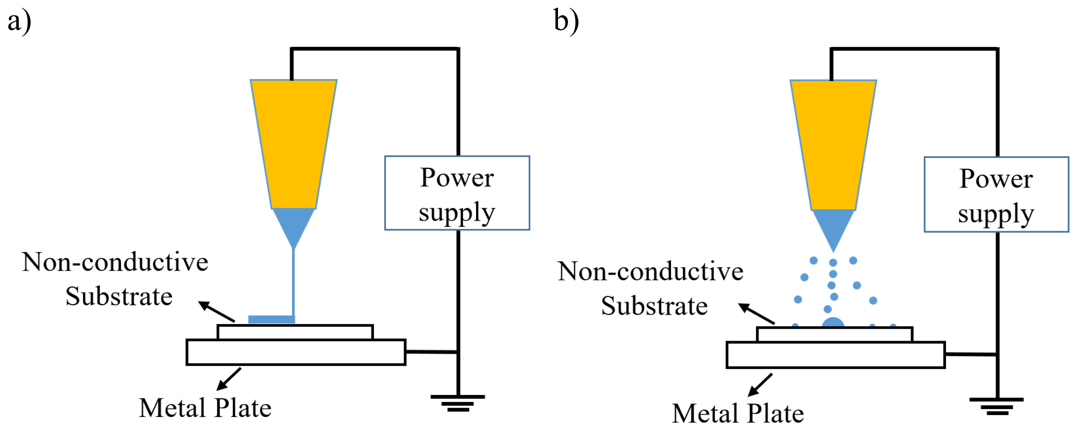

Figure 6-16 Schematic diagram showing the deposition on the nonconductive PDMS substrate for a) continuous line structures, and b) individual dots.

For the three cases where parallel sided lines were printed (Figure 6-15), the measured line width is always slightly larger than that predicted by Equation 4 – 2a. One possible explanation for this behaviour is that the ejected drop diameter is larger than that estimated from the shape and spread area of single printed droplets. A larger expected drop diameter could also explain the discrepancy between the predicted upper and lower bounds for drop stability predicted by Equations 4 – 3 and 4 – 7 and the results presented in Figure 6-14. If we use the data of the three stable cases presented in Figure 6-15 to determine the mean drop volume, this results in a larger value of around 25 fL and thus a larger droplet diameter in flight. Notice that the drop spacing in the stability map is in dimensionless form, the maximum and minimum drop spacing bounds remain constant with elevated drop diameter, while the experimental results shift left due to increased d_0, as shown in Figure 6-17. With increased droplet diameter, the model shows better predictions, although the maximum drop spacing bound is still smaller than the experimental results.

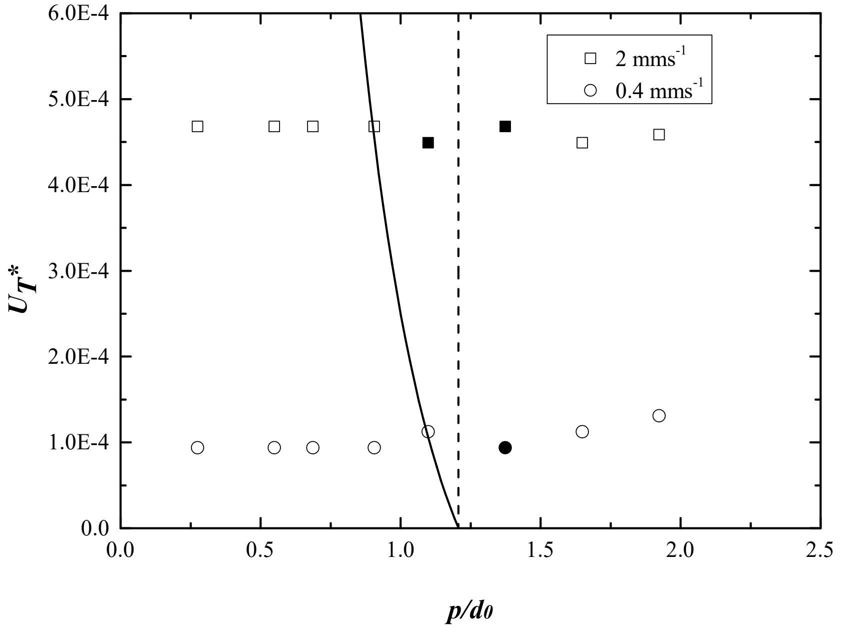

Figure 6-17 Stability map showing the condition for the maximum and minimum drop spacing limits for stable lines with data on the Z40 substrate with droplet volume of 25 fL. Open symbols indicate unstable morphology and filled symbols indicate stable morphology. The dashed line shows the maximum drop spacing bound, and the solid line is the bulging instability bound.

The increased contact angle condition leads to a narrower stability region compared with that obtained on the Z10 substrate, which is in consistent with our experimental results, with stable parallel sided lines only obtained at drop spacing of 5 or 4 μm. This indicates that the contact angle has a significant influence on the stability of the printed lines, especially at small feature size, and printing at a high contact angle in this circumstance may not be an appropriate option as the drop spacing range for stable line formation is relatively small.

The ridge width of the printed lines at both printing speeds on the Z40 substrate remains in a same level close to the single deposited droplet diameter d_{eqm} with decreased drop spacing, which is different from our previous results on the 30 min UV-Ozone treated PDMS in Chapter 4, with increased ridge width at elevated drop spacing. Duineveld [12] proposed that in the case of high advancing contact angle and zero receding contact angle, the axial transported flow back along the bead, generated by the Laplace pressure difference, is relatively large, resulting in the newly deposited liquid flowing towards the low pressure region to form periodic regular bulging instability if the bead contact angle is larger than the advancing contact angle. In this circumstance, the liquid in the ridge will be absorbed to the adjacent bulges, and the ridge width was shown to be equal to the d_{eqm}. For our experimental results at high advancing contact angle in Chapter 4, the spreading of the ridges was suppressed in the presence of bulges, however, due to the use of low volatile ink and large droplet size, the ridge could still spread after printing during the long drying process, hence leading to the ridge width larger than d_{eqm} at decreased drop spacing. For the printings on the Z40 substrate, the drying time of the printed line structures is reduced with femtolitre droplet size, thus the spreading of the ridge in the bulging lines after printing is limited, resulting in the ridge width similar to the d_{eqm}.

There is a substantial literature on the use of EHD printing to fabricate thin lines using a range of inks and substrates. We have used this data to subject Stringer's model to a further validation of its applicability at ultralow drop volume. Although it was not always possible to determine the full rheological data and printing parameters used in all these publications, we have been able to identify a number of studies using drops in the range 1 fL – 10 pL on substrates with contact angles in the range 12° – 50°.[111, 114, 121, 176, 198, 199] It is notable that at this small drop size other authors have reported an upper and lower bound for drop spacing in accordance with Stringer's model but there has been no overall quantitative analysis of this behaviour. In Figure 6-18 we use the plot of the $g(p^*, \theta)$ function to compare the minimum drop spacing (bulging instability) reported by a range of authors. It is clear that there is excellent agreement of the model with the data from a large number of independent studies.

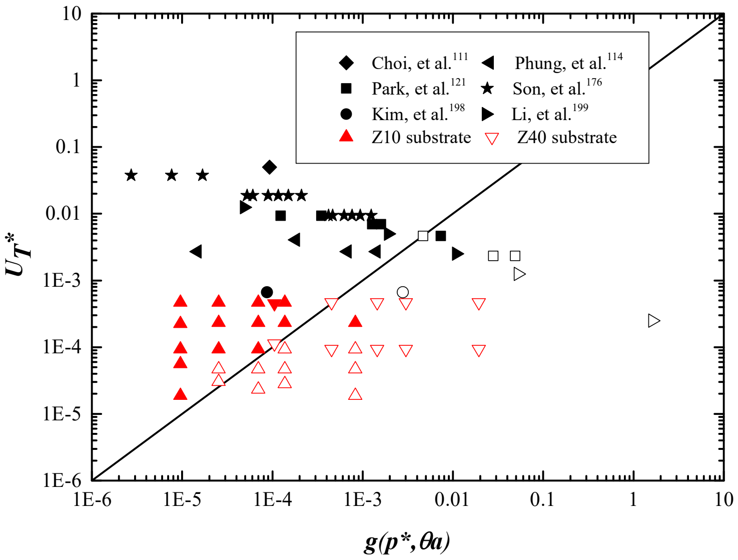

Figure 6-18 Combined data from the literature along with our experimental results showing the bulging instability. The results on the Z40 substrate are corrected using a droplet volume of 25 fL. Black symbols are results from the literature, and red symbols are our EHD printing results. The solid line is the bulging instability bound. Open symbols indicate unstable morphology and filled symbols indicate stable morphology.

In order to consider the predictions for both drop spacing stability bounds we plot the data as a function of dimensionless velocity and dimensionless drop spacing in Figure 6-19. It can be seen that the predictions for both stability bounds generally agree with the EHD printed line results over a range of contact angles. Thus, our analysis of data from the literature along with our experimental results together show that Stringer's line stability model can be applied to EHD printed lines with femtolitre drops, with the conditions of zero receding contact angle and minimised charging effect.

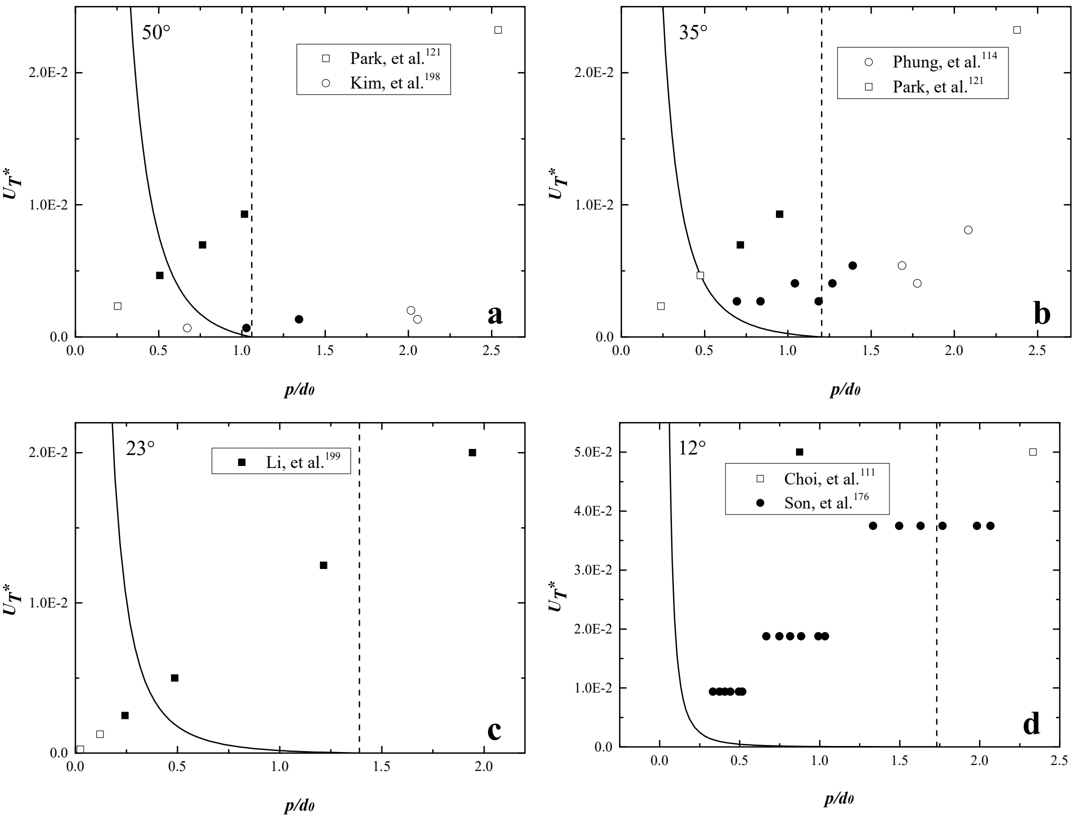

Figure 6-19 Stability map with the data from the EHD printing literature at various contact angle conditions. The dashed line shows the maximum drop spacing bound, and the solid line is the bulging instability bound. Open symbols indicate unstable morphology and filled symbols indicate stable morphology in all the plots.

6.3 Printed Line Electrodes

To investigate the electrical properties of the printed silver lines at ultra high resolution, line conductors, with a range of printing layers, were printed onto the UV-Ozone treated silicon (Z10), UV-Ozone treated PDMS (Z40), and polyimide (PI) substrates by using a Super-Fine printhead. The test conductors were composed of a 2 mm line between two 100 µm × 100 µm squares on both sides for electrical testing. One minute interval was set between each layer printing of the line, with the purpose of depositing on a partial solidified structure hence increasing the aspect ratio. Four samples were prepared for each printing layer. After printing the deposited structures were annealed at 150 °C for 1 h and the conductance of the electrodes was then measured by using a two-point probe.

6.3.1 Printed Electrodes on Silicon

The printing on the Z10 substrate was carried out using the single pulse waveform (Figure 6-1) with printing speed of 2 mms^{-1} and drop spacing of 4 µm. The applied voltage, pulse width time and nozzle to substrate distance parameters remained the same as that used to generate individual droplets previously, and an ejected volume per pulse of 11 fL was obtained from the printing set up.

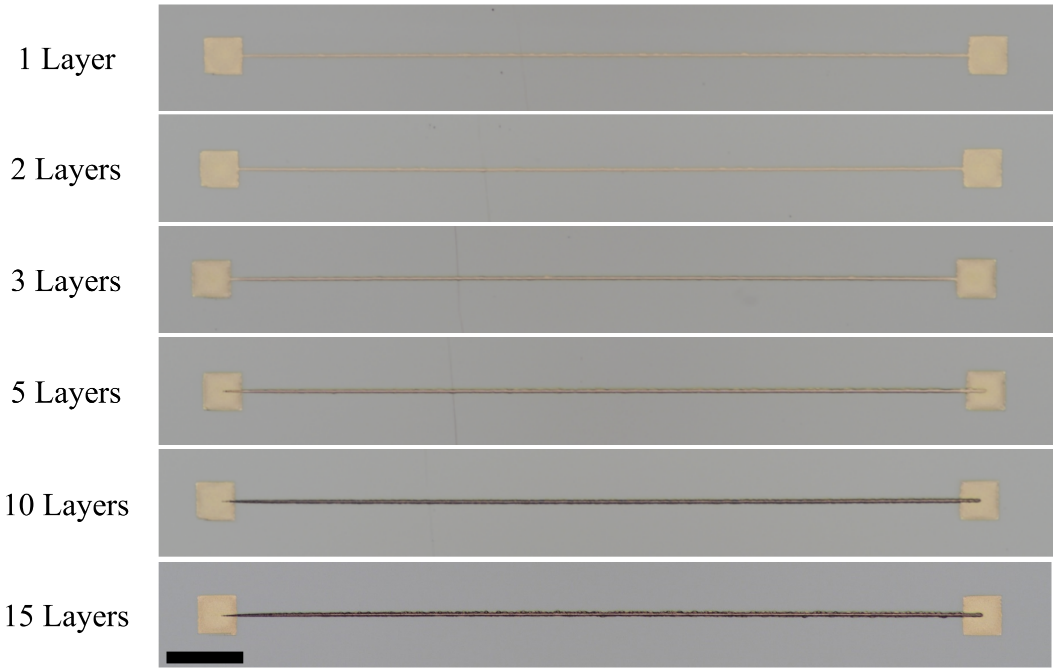

Figure 6-20 Printed line electrodes with various printing layers on the Z10 substrate at the drop spacing of 4 µm and printing velocity of 2 mms^{-1}. The scale bar is 200 µm.

Figure 6-20 shows the annealed morphologies of the printed electrodes at various printing layers. It can be seen that all the printed lines were stable parallel sided, with no unstable bulges or large ridge width deviations. For a better viewing, magnified pictures of the line electrodes at various printing layers are shown in Figure 6-21.

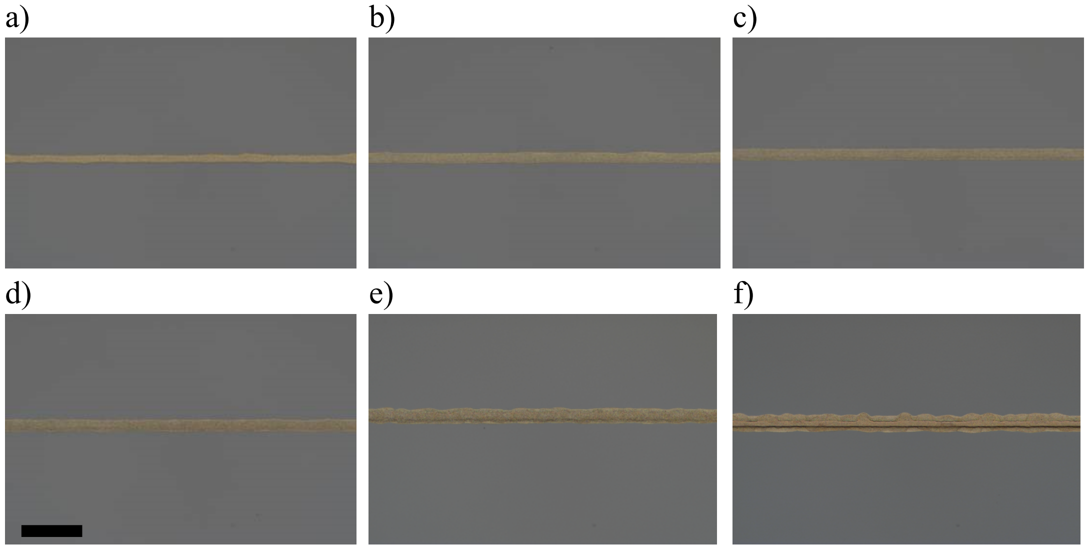

Figure 6-21 Magnified pictures showing the morphologies of the printed line electrodes at various printing layers: a) 1 layer, b) 2 layers, c) 3 layers, d) 5 layers, e) 10 layers and f) 15 layers. The scale bar is 50 µm.

Figure 6-22 shows the measured line width and conductance results of the printed line electrodes at various printing layers. Five measurements of line width were established from various positions for each sample, resulting in 20 results to obtain the mean line width for each printing layer. Both the mean line width and the conductance of the printed electrodes increase with increasing printing layers. Notice that after printing a single layer, no conductance was measured, which is possibly due to discontinuous deposition during printing or cracks forming during annealing.

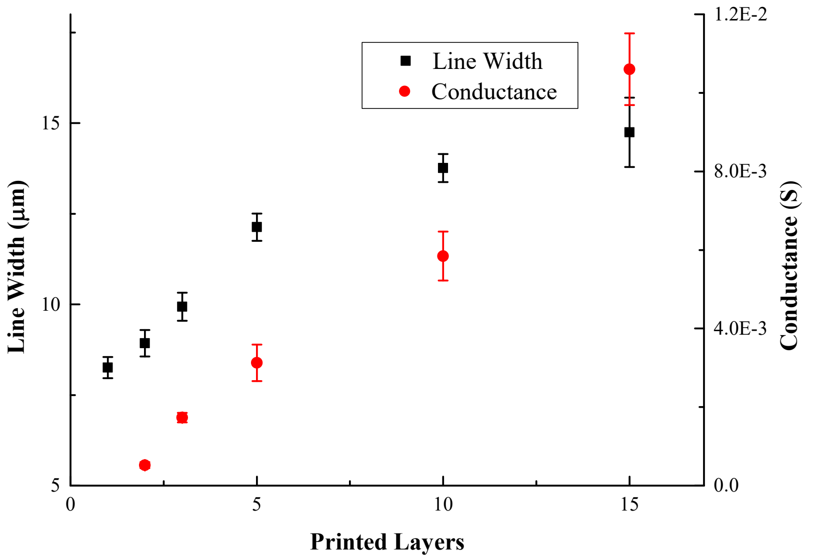

Figure 6-22 Measured mean line width and conductance results of the printed line electrodes on the Z10 substrate at various printing layers.

The conductivity of the printed electrodes can be estimated by calculating the total deposited silver on the substrate. Assuming the solvent is totally evaporated during annealing, the total deposited silver mass on the substrate can be estimated as:

$$m_{Ag} = N_{layer} N_{drop} V_0 \rho_{ink} A_{ratio} \qquad (6-6)$$

where N_{layer} is the number of printed layers on the substrate, N_{drop} is the number of deposited droplets per layer, which is 500, V_0 is the ejected volume per pulse, which is around 11 fL, ρ_{ink} is the silver ink density, which is 1.45 gml^{-1}, and A_{ratio} is the silver mass ratio in the ink, which is 29.7% according to the TGA test, as shown in Figure 6-23.

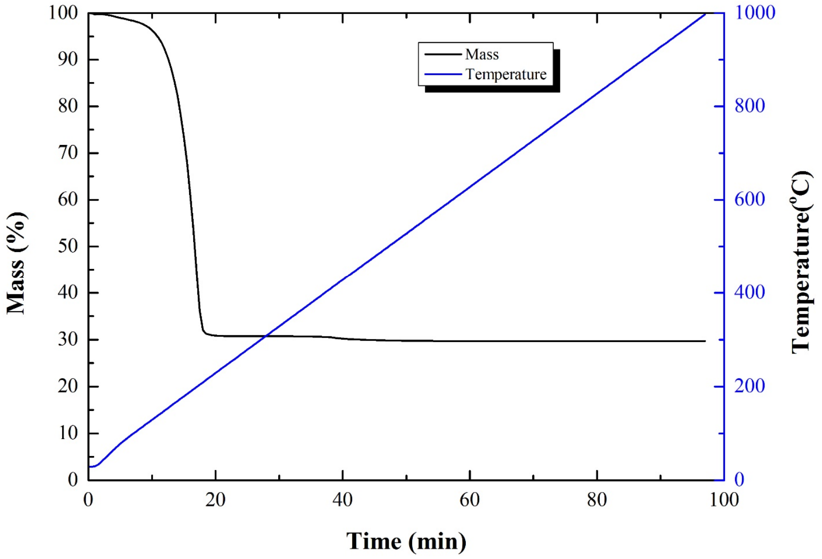

Figure 6-23 TGA test of the silver nanoparticle ink.

Assuming the deposited line electrodes have uniform cross sections and contain no porosity, the cross section area can be expressed as:

$$A_{Ag} = \frac{m_{Ag}}{\rho_{Ag} L} \qquad (6-7)$$

where ρ_{Ag} is the bulk silver density, L is the length of the printed electrode. Thus, the conductivity of the printed line electrodes can be calculated as:

$$\sigma = \frac{GL}{A_{Ag}} \qquad (6-8)$$

where G is the measured conductance of the printed electrodes. The calculated conductivity as a function of printed layers is shown in Figure 6-24. The conductivity has a significant increase from printing 2 layers to 3, and then retains approximately constant at about 1 × 10^7 Sm^{-1}, although the conductivity reaches its highest value of 1.2 × 10^7 Sm^{-1} after printing 15 layers. This is significantly lower than the value for the conductivity of bulk silver, 6.3 × 10^7 Sm^{-1}. However, it is well known that printed nanoparticle inks often show conductivities lower than bulk values. Reviews of the literature show that typical conductivity measurements for printed Ag to range from 10% - 50% of bulk silver and our value of 15 – 20% is within this range.

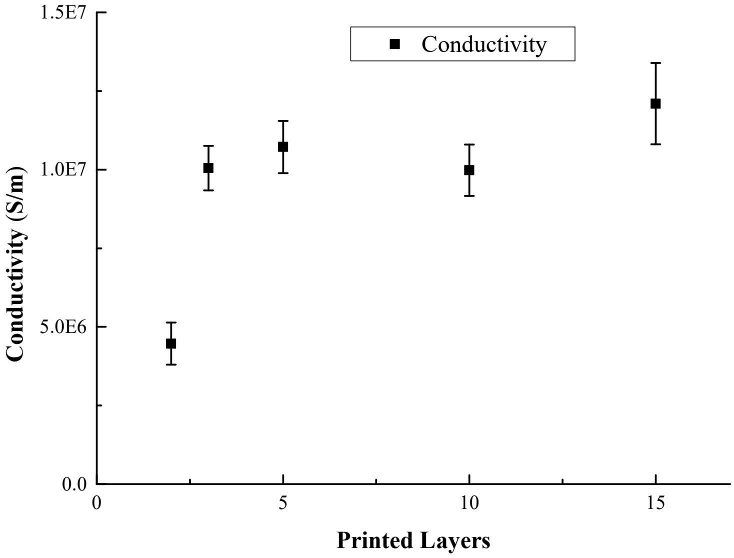

Figure 6-24 Calculated conductivity results of the printed line electrodes on the Z10 substrate at various printing layers.

6.3.2 Printed Electrodes on PDMS

The printing on the Z40 substrate was carried out using a bipolar waveform (Figure 6-11) with applied voltage of 500 V, at the printing speed of 1.6 mms^{-1} and drop spacing of 4 µm. The nozzle to substrate distance and pulse width time parameters remained the same as that used to generate lines on the Z40 substrate previously. Figure 6-25 shows the morphologies of the printed electrodes after annealing as a function of printing layers. Stable line electrodes were obtained at the printing layer of 1 and 2, while bulging instabilities were observed at increased printing layers, and severe line width deviation was observed at the printing layer of 10 (Figure 6-25 e).

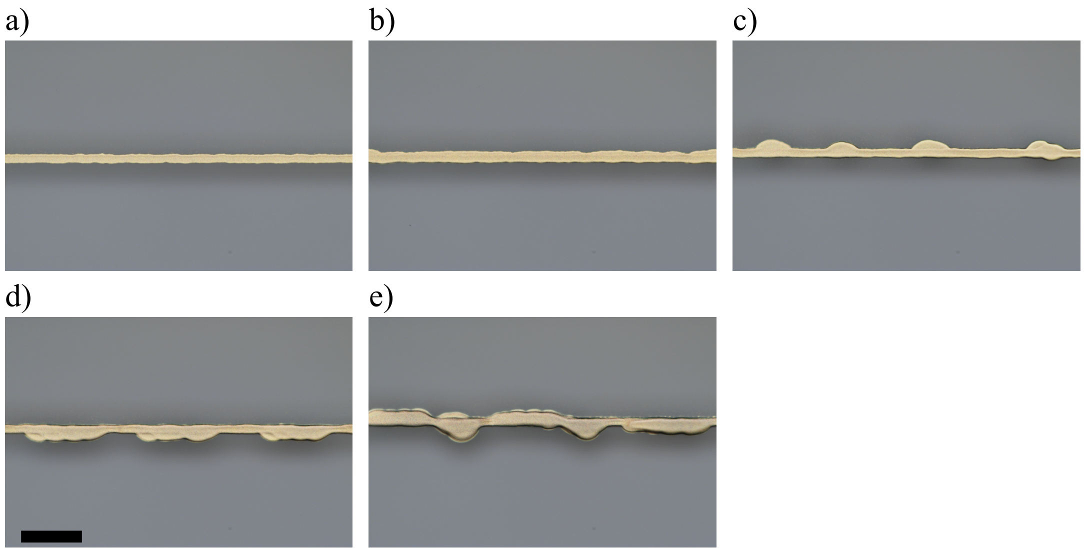

Figure 6-25 Printed line electrodes on the Z40 substrate at the printing velocity of 1.6 mms^{-1}, drop spacing of 4 µm, jetting frequency of 200 Hz and duty ratio of 10%, with various printing layers: a) 1 layer, b) 2 layers, c) 3 layers, d) 5 layers, and e) 10 layers. The scale bar is 50 µm.

Figure 6-26 shows the measured mean line width and conductance results of the printed line electrodes at various printing layers. The mean width of the printed lines increases with increasing printing layers, and the standard deviation of line width increases with number of printed layers due to the presence of bulges. The conductance of the line is low when a single line is printed, and increases with increasing number of layers.

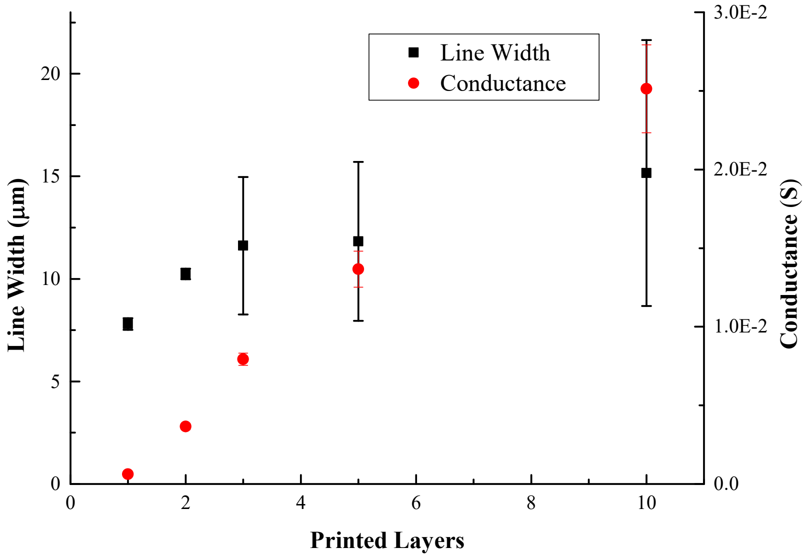

Figure 6-26 Measured mean line width and conductance results of the printed line electrodes on the Z40 substrate at various printing layers.

The calculated conductivity results as a function of printing layers using Equation 6 – 6 to 6 – 8 are plotted in Figure 6-27. The conductivity increases in an approximately linear manner from printing layers of 1 to 3, and maintains a constant level around 3 × 10^7 Sm^{-1}, or approximately 50% of the bulk value, as the number of layer increases.

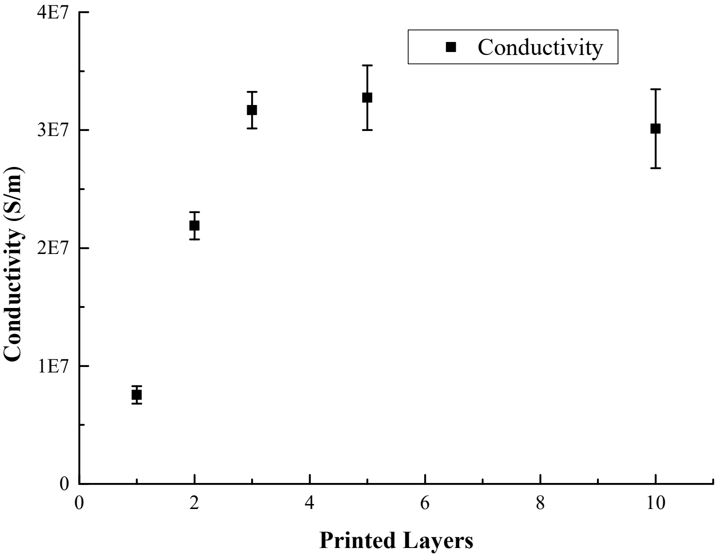

Figure 6-27 Calculated conductivity results of the printed line electrodes on the Z40 substrate at various printing layers.

6.3.3 Printed Electrodes on Polyimide

Flexible electronics have received increasing attention in the last couple of decades.[200] To achieve direct inkjet printing on flexible substrates with high-resolution feature size is also of great interest. From previous experiments stable line structures with small feature size and good conductivity were successfully achieved on the flexible PDMS substrate. In this section silver nanoparticle suspensions were printed onto another type of flexible substrate, polyimide. The polyimide substrate was stuck to a silicon wafer using tapes to better control its flatness. The nozzle to substrate distance was set to 20 μm. As the polyimide film is nonconductive, hence a bipolar waveform was applied (Figure 6-11), with an applied voltage of 600 V and the width time of 0.5 ms.

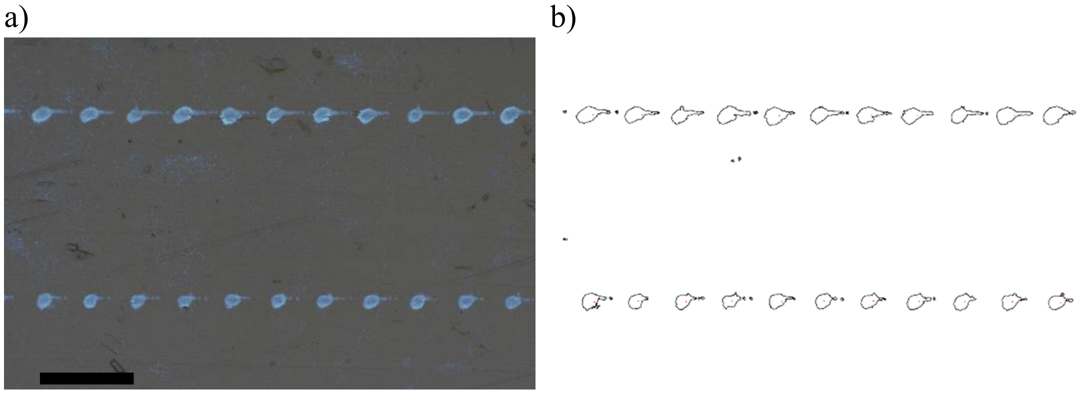

Figure 6-28 Printed dots at applied voltage 600 V, nozzle to substrate distance 20 μm, and pulse width time 0.5 ms, with printing velocity of 2 mms^{-1}, jetting frequency of 40 Hz and duty ratio of 2%: a) Printed morphologies of the dots observed by the optical microscope, b) profiles of the deposited dots obtained by ImageJ. The scar bar is 50 μm.

Figure 6-28 a shows the printed individual dots at a drop spacing larger than the droplet equilibrium diameter on the surface. It can be seen that a tail of subsidiary drops was deposited onto the surface following the deposition of the individual dots, and unwanted spraying of nanoparticles can also be observed on the surrounding area of the substrate. These defects indicate random spraying of the ink induced by the charging effect during printing on the substrate. The mean area of the deposited droplets was obtained by analysing the total area of 22 deposited dots by ImageJ, as shown in Figure 6-28 b. Assuming a stable deposition of the droplets on the substrate with the spherical cap shape, the mean deposited droplet diameter can be estimated from the mean area, which is 9.3 μm. The ejected volume per pulse can then be estimated from the mean deposited droplet diameter and the advancing contact angle (19.1°) on the substrate by using Equation 6 – 5, which is around 27 fL.

To investigate the electrical properties of the printed silver line structures, a series of line conductors was printed onto the polyimide substrate at the printing speed of 2 mms^{-1} and drop spacing of 5 μm. The applied voltage, pulse width time and nozzle to substrate distance parameters remained the same as those used to generate individual droplets previously. Figure 6-29 shows the annealed morphologies of the printed electrodes on the polyimide substrate at various printing layers. Although the printed line electrodes show no obvious bulging instabilities, the printed lines are not stable parallel sided structures as those printed on the Z10 substrate, and the width of electrodes show distinct deviations, possibly due to the roughness of the surface. The width deviation is most severe after printing 20 layers, and an obvious spreading of the ink to both sides of the line could also be observed (Figure 6-29 e).

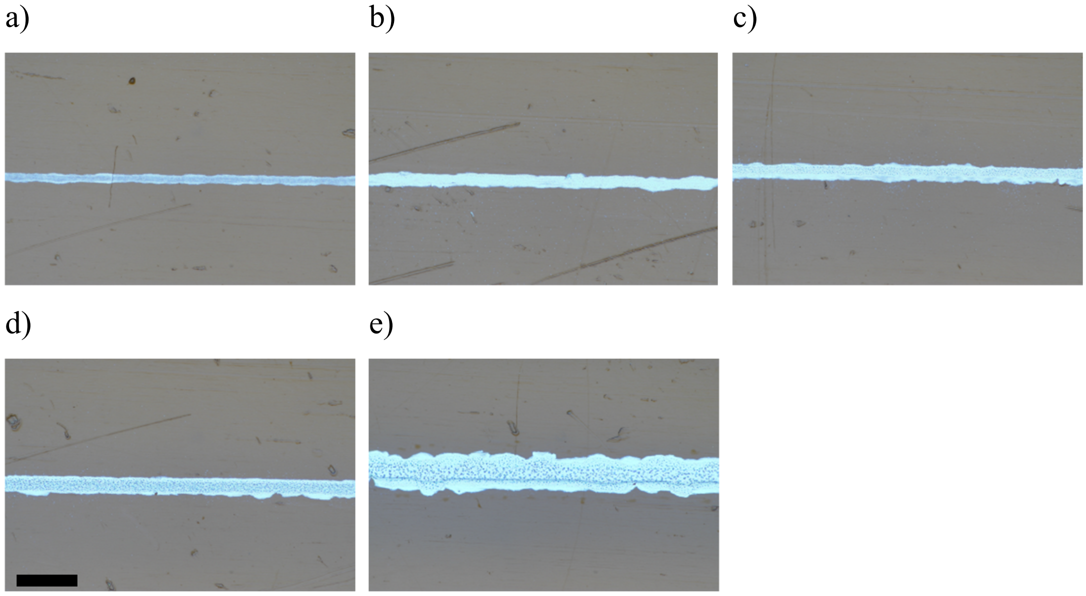

Figure 6-29 Printed line electrodes on the polyimide substrate at the drop spacing of 5 µm, printing velocity of 2 mms^{-1}, jetting frequency of 200 Hz and duty ratio of 10%, with various printing layers: a) 1 layer, b) 2 layers, c) 5 layers, d) 10 layers, and e) 20 layers. The scale bar is 50 µm.

Figure 6-30 shows the measured mean line width and conductance results of the printed line electrodes at various printing layers. The mean line width of the printed electrodes increases gradually with increasing the number of printed layers from 1 to 10, while a significant increase was observed from the printing layers of 10 to 20. The conductance of the electrode exhibited a relatively low value at the printing layer of 2, and increases gradually from printing layers of 2 to 10, and a dramatic increase was observed from printing layers of 10 to 20. No conductivity was obtained after printing a single layer.

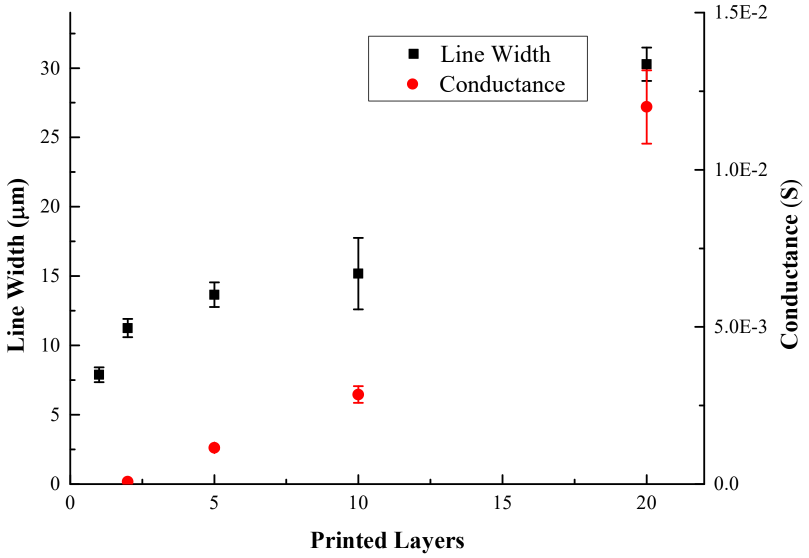

Figure 6-30 Mean line width and conductance results of the printed line electrodes on the polyimide substrate at various printing layers.

Figure 6-31 shows the calculated conductivity results as a function of printed layers using Equation 6 – 6 to 6 – 8. In this case the conductivity continues to increase with increasing number of printed layers. The highest conductivity value obtained is 5.4 × 10^6 Sm^{-1} at the printing layer of 20, which is below 10% of the conductivity of bulk silver, 6.3 × 10^7 Sm^{-1}. This is significantly lower than that found with printing on both the Si and PDMS substrates.

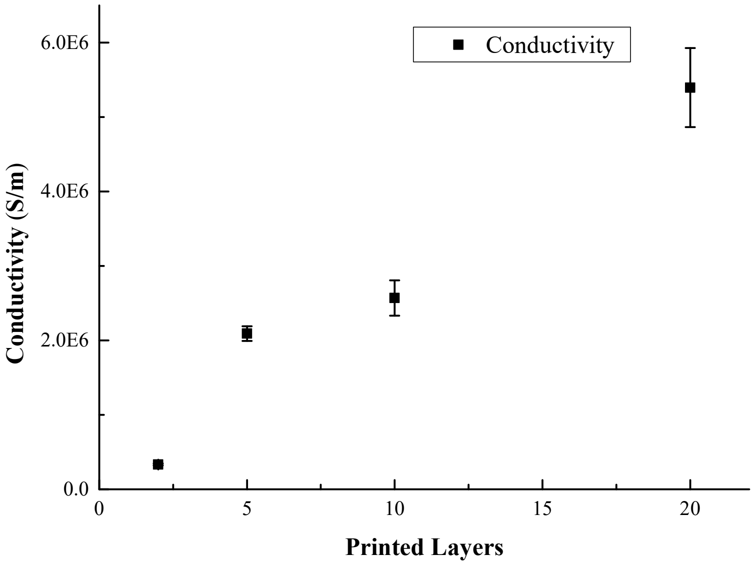

Figure 6-31 Calculated conductivity results of the printed line electrodes on the polyimide substrate as a function of printing layers.

6.3.4 Discussion

To investigate the electrical properties of the deposited silver lines at high resolution, printed test conductor lines with a range of numbers of printed layers were carried out on the Z10 substrate. As the resistance of the silicon substrate is around 0.73 MΩ of the same distance for an electrode, the influence of silicon conductance on the electrode resistance measurements can be neglected. Conductivity of the printed lines was < 50% of that expected for bulk silver, but such low printed conductor conductivity is also found after conventional inkjet printing Ag inks.

The conductance results for the electrodes printed on the Z40 substrate are shown to be larger than those obtained on the Z10 substrate for the same printing layers, due to the larger ejected volume per pulse for the printings on Z40 substrate and thus more silver deposited on the substrate. Meanwhile, the conductivity results for the electrodes on the two substrates both maintain in a similar level from the printing layers of 3. This indicates that the conductivity of the electrodes is influenced by the discontinuous deposition or connection problems at the printing layers of 1 and 2, while from the printing layers of 3 the conductivity reaches the limit value that the silver nanoparticle ink could provide. As we also notice, the conductivity results were calculated from the proportion of silver deposited on the substrate, assuming a stable uniform line. Thus, as the electrodes printed on the Z40 substrate generate unstable bulges from the printing layers of 3 leading to width deviations, and the ejected volume per pulse used in the calculation is smaller than the real value, the real conductivity values are possibly smaller than the calculated ones. The presence of bulges on the multilayer printing electrodes on the Z40 substrate rather than on the Z10 substrate is possibly due to the higher contact angle leading to a larger axial transported flow rate during multilayer printing.

As the deposited dots on the polyimide substrate show irregular shapes, the ejected volume per pulse based on the contact angle and the equivalent droplet diameter assuming a spherical cap geometry might generate deviations to the real value. The conductivity results were shown to be smaller than those obtained on the Z10 and Z40 substrates, which is possibly due to the width deviations of the printed lines and deviations from calculated droplet volume. Nevertheless, the conductivity results on the polyimide substrate show the prospect of EHD printing in the flexible electronics applications with ultra high resolution.

The conductivities of the printed line electrodes on the three substrates generally ranged from approximate 5% to 50% of bulk silver, which are within the range of the values reported in the literature.[170, 176, 177, 179] However, there are still some problems occurred in the printed line conductors. Some of the printed lines with single layer showed no conductance, possibly due to the discontinuous deposition during printing or cracks forming during annealing. On the other hand, the methodology of setting a time period between each printing layer to increase the aspect ratio of the lines is also not satisfactory, as the multilayer printed lines were not uniform. One strategy to solve these problems is the use of high viscosity silver ink for EHD printing. By applying a high viscosity silver ink, the printed lines are continuous with high aspect ratio and are less likely to break, showing better uniformity and electrical properties.[175]

6.4 Conclusions

1) Stable drop-on-demand EHD printing was achieved by maintaining the same flow rate and pulse width time.
2) The model proposed by Stringer to determine the range of stable printing conditions has been validated for drop volumes down to 11 fL on the UV-Ozone treated silicon substrate.
3) The predictions from the line stability model show discrepancies with the experimental results of the printed structures on the UV-Ozone treated PDMS coated silicon substrate. This is possibly due to the deviations from the calculated ejected volume per pulse leading to a larger p^* of the results.
4) Stable silver line electrodes with ultra high resolution were successfully achieved on the silicon, PDMS and polyimide substrates, with relatively good conductivities compared with bulk silver.

Chapter 7 Conclusions and Future Work

7.1 Conclusions

The thesis has explored the stability and electrical properties of inkjet printed line structures at small drop volume. Thus, to investigate the influence of droplet size and printing conditions on the printed line stability, silver nanoparticle ink was deposited onto a wide range of substrates, with two inkjet printing systems. First, we presented an experimental study of the maximum and minimum bounding drop spacing for a parallel sided liquid line on the substrate with zero receding contact angle produced by the Dimatix piezoelectric 10 and 1 pL printheads. The line stability results were compared with Stringer's line stability model. The model for the maximum drop spacing bound shows good agreement with our results. The minimum drop spacing bound is limited by a bulging instability and our results agree with the existing model, except for the printings with large drop volumes at low temperature. It is shown that in this circumstance there is a different mechanism for bulging that occurs after printing over a period of minutes, if the liquid bead is present on the surface for a significant period of time before drying.

Second, the stability of printed line structures on the substrates with finite receding contact angle was investigated also using the Dimatix 10 and 1 pL printheads. All the printed structures were shown to be unstable, and the instability changes from retracted individual big dots to a periodic bulging instability with decreased advancing and receding contact angle. Compared with the lines on the substrate with zero receding contact angle, the instability obtained for the printed lines with finite receding contact angles is due to a change in the local boundary conditions, with the ridges connecting the bulges displaying a pinned contact line, while the contact line in the bulges was free to move. A model based on Duineveld's analysis was established to predict the wavelength between the adjacent bulges. It was also shown that it is possible to stabilize line structures on substrates with a finite receding contact angle by pre-depositing droplets to generate small disturbances for the controlled generation of periodic bulges, thus making the ridges relatively stable due to loss of liquid to the adjacent bugles. This method was also shown to affect the bulges formed when printing at small drop spacing on substrates with zero receding contact angle.

Third, to investigate the stability and electrical properties of printed line structures at ultra high resolution, silver nanoparticle suspensions were deposited onto a range of substrates by using an electrohydrodynamic based Super Inkjet Printing System. By applying the electrostatic force, droplets with femtolitre volume could be achieved. Stable drop-on-demand EHD printing was achieved by maintaining the same flow rate and pulse width time. The model for line stability shows good agreement with our experimental results on the silicon substrate, however, when comparing with the results on the PDMS substrate, large discrepancies were observed. This is possibly due to the deviations from the calculated ejected volume per pulse leading to a larger p^* of the results. With corrected droplet volume, the bulging instability predictions for both piezoelectric DOD printing and EHD printing agree well with our experimental results, as shown in Figure 7-1. Finally, stable inkjet printed line electrodes with sub ten micrometre were successfully achieved, with conductivities within an order magnitude of bulk silver.

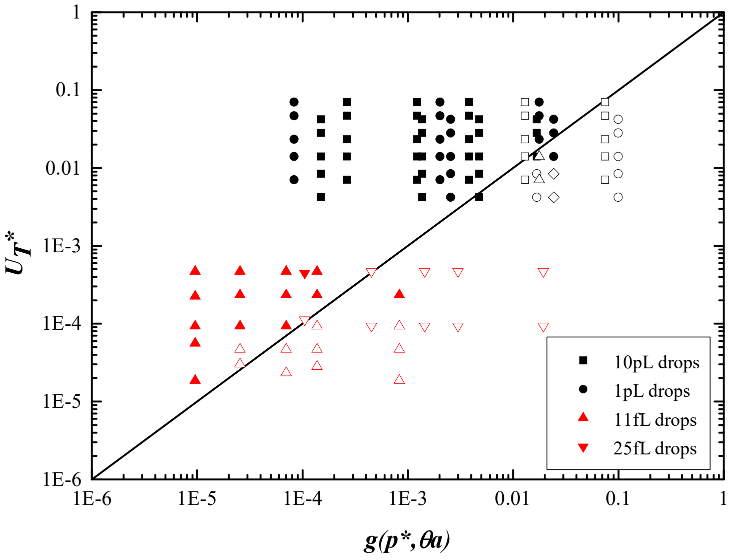

Figure 7-1 Stability map showing the onset of bulging instability along with our experimental data. Black symbols are results from piezoelectric DOD printing, and red symbols are results from EHD printing. The droplet volume of 25 fL is calculated and corrected from stable deposited lines on the Z40 substrate. The solid line is the bulging instability bound. Open symbols indicate a bulging morphology and filled symbols indicate stable morphology.

7.2 Future Work

This thesis presents a fundamental study of inkjet printed line stability at high and ultra high resolution with two printing systems. While we have validated the applicability of Stringer’s line stability model down to 10 fL drops to determine the drop spacing bounding for a stable parallel sided liquid bead, and have demonstrated stable silver lines with good conductivities of sub ten micrometre size by EHD printing, further investigations of the line stability with other ink and printing conditions, the EHD printing mechanism, as well as applications of EHD printing in electronic devices, are also of great interest. Thus, the following part will show the recommended future work based on the results and conclusions of this thesis.

In Chapter 4, it was shown that the model proposed by Stringer to determine the drop spacing bounding conditions for the inkjet printed straight parallel lines with zero receding contact angle has been validated for drop volumes down to 1.5 pL subject to the condition that the ink dries rapidly after deposition. As our experiments were carried out on the substrates with certain advancing contact angles, it’s worth establishing experiments on the substrates with other advancing contact angle conditions to further verify the model at small drop volume. The drying time after deposition will influence the morphology of the final structure. Thus, it’s worthwhile to carry out experiments with other inks of different volatilities to investigate the influence of evaporation rate on the final line stability. Meanwhile, there is an effect of printing speed resulting the line width being smaller at decreased printing speed, and we concluded that this is possibly due to droplet volume change due to change of printing frequency. Thus, a systematic study of the printing frequency influence on the ejected droplet size with small drop volume is required to further improve the model.

In Chapter 5, the instabilities of the printed lines changed from individual big dots to periodic bulging lines with decreased advancing and receding contact angle. Thus, it’s worthwhile to investigate the influence of contact angle and droplet size on the instability change to explore the fluid dynamics of the printed liquid beads on the substrate with finite receding contact angle. A model based on Duineveld’s analysis was established to predict the wavelength between the adjacent bulges of the printed lines. This wavelength model needs to be further verified on the other substrates with different contact angle conditions. The model also lacks a full predictive capability as it requires considerable measurements on printed tracks. A more complete and sophisticated investigation of fluid flows during drop coalescence to form lines is required.

We have successfully achieved stabilized line structures, and the maximum length of the stable line period reaches 2 mm. Our results provide an innovative method to print partial stable lines on the substrates with finite receding contact angle, and this method could be further used into electronic applications such as printed line electrodes, with the stabilized lines as conductive patterns and the bulges on either side as the electrodes.

In Chapter 6, a relationship between the flow rate Q and electric, hydrostatic and capillary pressures was used to analysis our experiment results, however, no quantitative relationship was obtained. Thus, the relationship between the flow rate and the driving forces needs to be investigated, which could further comprehend the fundamental mechanism of EHD printing as well as provide a better control of ejected feature size. Stable dot structures with identical small scale feature size were achieved by optimizing the printing parameters, which could be further applied to the applications such as inkjet printing quantum dots at ultra high resolution. In addition, as stable lines with sub ten micrometre were achieved through EHD printing, it’s also worthwhile to investigate EHD printed thin films with better uniformity and fidelity at a range of scales.

Appendix A Printing Parameter Design for Single Pulse Waveform

The printing parameters for the experiments with a single pulse waveform are listed in the tables below. To investigate the stability and electrical properties of the EHD printed lines, printing at fixed printing velocity with various drop spacings and at fixed drop spacing with various printing velocities are required. Thus, the printing velocity and drop spacing parameters need to be designed. The printing velocity can be easily adjusted through the printer's built-in function, and the drop spacing was adjusted by changing the printing velocity at specific jetting frequency by using $p=v/f$, where p is the drop spacing, v is the printing velocity and f is the jetting frequency. To maintain the same pulse width time, the jetting frequency and waveform duty ratio were designed through $T_p=x_p/f$, where T_p is the pulse width time and x_p is the duty ratio.

Table A-1 Printing parameters at the printing speed of 2 mms^{-1}.

V (mm/s)	**P (μm)**	**F (Hz)**	**Pulse Time (ms)**	**Waveform (%)**
1.96	7	280	0.5	14
1.92	6	320	0.5	16
2	5	400	0.5	20
2	4	500	0.5	25
2	3.3	600	0.5	30
2	2.5	800	0.5	40
2	2	1000	0.5	50

Table A-2 Printing parameters at the printing speed of 1 mms^{-1}.

V (mm/s)	**P (μm)**	**F (Hz)**	**Pulse Time (ms)**	**Waveform (%)**
0.98	7	140	0.5	7
0.96	6	160	0.5	8
1	5	200	0.5	10

0.96	4	240	0.5	12
1	3.3	300	0.5	15
1	2.5	400	0.5	20
1	2	500	0.5	25
1	1	1000	0.5	50

Table A-3 Printing parameters at the printing speed of 0.4 mms^{-1}.

V (mm/s)	**P (μm)**	**F (Hz)**	**Pulse Time (ms)**	**Waveform (%)**
0.42	7	60	0.5	3
0.36	6	60	0.5	3
0.4	5	80	0.5	4
0.4	4	100	0.5	5
0.4	3.3	120	0.5	6
0.4	2.5	160	0.5	8
0.4	2	200	0.5	10
0.4	1	400	0.5	20

Table A-4 Printing parameters at the printing speed of 0.2 mms^{-1}.

V (mm/s)	**P (μm)**	**F (Hz)**	**Pulse Time (ms)**	**Waveform (%)**
0.28	7	40	0.5	2
0.24	6	40	0.5	2
0.2	5	40	0.5	2
0.24	4	60	0.5	3
0.2	3.3	60	0.5	3
0.2	2.5	80	0.5	4
0.2	2	100	0.5	5
0.2	1	200	0.5	10

Table A-5 Printing parameters at the printing speed of 0.1 mms^{-1}.

V **(mm/s)**	**P** **(µm)**	**F** **(Hz)**	**Pulse Time** **(ms)**	**Waveform** **(%)**
0.14	7	20	0.5	1
0.12	6	20	0.5	1
0.1	5	20	0.5	1
0.08	4	20	0.5	1
0.132	3.3	40	0.5	2
0.1	2.5	40	0.5	2
0.12	2	60	0.5	3
0.08	1	80	0.5	4

Appendix B Printing Parameter Design for Bipolar Waveform

The printing parameters for the experiments with a bipolar waveform are listed in the tables below. The printing velocity can be easily adjusted through the printer's built-in function. As time period between adjacent positive and negative pulses was set to be the same to ensure deposition with identical drop spacing, the deposition frequency is twice the applied pulse frequency. Thus, the drop spacing was adjusted through $p=0.5v/f$. To maintain the same pulse width time, the jetting frequency and waveform duty ratio were designed through $T_p=x_p/f$.

Table B-1 Printing parameters at the printing speed of 2 mms^{-1}.

V (mm/s)	**P (μm)**	**F (Hz)**	**Pulse Time (ms)**	**Waveform (%)**
1.96	7	140	0.5	7
1.92	6	160	0.5	8
2	5	200	0.5	10
1.92	4	240	0.5	12
2	3.3	300	0.5	15
2	2.5	400	0.5	20
2	2	500	0.5	25
2	1	1000	0.5	50

Table B-2 Printing parameters at the printing speed of 0.4 mms^{-1}.

V (mm/s)	**P (μm)**	**F (Hz)**	**Pulse Time (ms)**	**Waveform (%)**
0.56	7	40	0.5	2
0.48	6	40	0.5	2
0.4	5	40	0.5	2
0.48	4	60	0.5	3
0.4	3.3	60	0.5	3

0.4	2.5	80	0.5	4
0.4	2	100	0.5	5
0.4	1	200	0.5	10

Reference

1. Derby, B., Inkjet Printing of Functional and Structural Materials: Fluid Property Requirements, Feature Stability, and Resolution. In *Annual Review of Materials Research, Vol 40*, Clarke, D. R.; Ruhle, M.; Zok, F., Eds. Annual Reviews: Palo Alto, 2010; Vol. 40, pp 395-414.

2. Derby, B., Additive Manufacture of Ceramics Components by Inkjet Printing. *Engineering* **2015,** 1, (1), 113-123.

3. Shimoda, T.; Morii, K.; Seki, S.; Kiguchi, H., Inkjet printing of light-emitting polymer displays. *MRS Bull.* **2003,** 28, (11), 821-827.

4. de Gans, B. J.; Duineveld, P. C.; Schubert, U. S., Inkjet printing of polymers: state of the art and future developments. *Adv. Mater.* **2004,** 16, (3), 203-213.

5. Nakamura, M.; Kobayashi, A.; Takagi, F.; Watanabe, A.; Hiruma, Y.; Ohuchi, K.; Iwasaki, Y.; Horie, M.; Morita, I.; Takatani, S., Biocompatible inkjet printing technique for designed seeding of individual living cells. *Tissue Eng.* **2005,** 11, (11-12), 1658-1666.

6. Derby, B., Bioprinting: inkjet printing proteins and hybrid cell-containing materials and structures. *J. Mater. Chem.* **2008,** 18, (47), 5717-5721.

7. Sirringhaus, H.; Kawase, T.; Friend, R. H.; Shimoda, T.; Inbasekaran, M.; Wu, W.; Woo, E. P., High-resolution inkjet printing of all-polymer transistor circuits. *Science* **2000,** 290, (5499), 2123-2126.

8. Kim, D.; Jeong, Y.; Song, K.; Park, S. K.; Cao, G.; Moon, J., Inkjet-printed zinc tin oxide thin-film transistor. *Langmuir* **2009,** 25, (18), 11149-54.

9. Jang, J.; Kang, H.; Chakravarthula, H. C. N.; Subramanian, V., Fully Inkjet-Printed Transparent Oxide Thin Film Transistors Using a Fugitive Wettability Switch. *Adv. Electron. Mater.* **2015,** 1, (7), 7.

10. Smith, P.; Shin, D.-Y.; Stringer, J.; Derby, B.; Reis, N., Direct ink-jet printing and low temperature conversion of conductive silver patterns. *J. Mater. Sci.* **2006,** 41, (13), 4153-4158.

11. Stringer, J.; Derby, B., Limits to feature size and resolution in ink jet printing. *J. Eur. Ceram. Soc.* **2009,** 29, (5), 913-918.

12. Duineveld, P. C., The stability of ink-jet printed lines of liquid with zero receding contact angle on a homogeneous substrate. *J. Fluid Mech.* **2003,** 477, 175-200.

13. Soltman, D.; Subramanian, V., Inkjet-printed line morphologies and temperature control of the coffee ring effect. *Langmuir* **2008,** 24, (5), 2224-2231.

14. Stringer, J.; Derby, B., Formation and Stability of Lines Produced by Inkjet Printing. *Langmuir* **2010,** 26, (12), 10365-10372.

15. Lee, S.; Shin, K.; Hwang, J.; Kang, K.; Kang, H., Silver inkjet printing with control of surface energy and substrate temperature. *J. Micromech. Microeng.* **2008,** 18, (7), 075014.

16. Soltman, D.; Smith, B.; Morris, S.; Subramanian, V., Inkjet printing of precisely defined features using contact-angle hysteresis. *J. Colloid Interface Sci.* **2013,** 400, 135-139.

17. Hsiao, W.-K.; Martin, G. D.; Hutchings, I. M., Printing stable liquid tracks on a surface with finite receding contact angle. *Langmuir* **2014,** 30, (41), 12447-12455.

18. Onses, M. S.; Sutanto, E.; Ferreira, P. M.; Alleyne, A. G.; Rogers, J. A., Mechanisms, capabilities, and applications of high‐resolution electrohydrodynamic jet printing. *Small* **2015,** 11, (34), 4237-4266.

19. Taylor, G. I., Disintegration of water drops in an electric field. *Proc. R. Soc. London, Ser. A* **1964,** 280, (1382), 383-397.

20. Savart, F., Mémoire sur le choc d'une veine liquide lancée contre un plan circulaire. *Ann. chim* **1833,** 54, (56), 1833.

21. Plateau, M., XXXVII. On the recent theories of the constitution of jets of liquid issuing from circular orifices. *The London, Edinburgh, and Dublin Philosophical Magazine and Journal of Science* **1856,** 12, (79), 286-297.

22. Rayleigh, L., On the instability of jets. *Proc. London Math. Soc.* **1878,** 1, (1), 4-13.

23. Rune, E., Measuring instrument of the recording type. In Google Patents: 1951.

24. Shen, W. F., Properties of SnO2 based gas-sensing thin films prepared by ink-jet printing. *Sens. Actuator B-Chem.* **2012,** 166, 110-116.

25. He, P.; Brent, J.; Ding, H.; Yang, J.; Lewis, D.; O'Brien, P.; Derby, B., Fully printed high performance humidity sensors based on two-dimensional materials. *Nanoscale* **2018,** 10, (12), 5599-5606.

26. Hoth, C. N.; Schilinsky, P.; Choulis, S. A.; Brabec, C. J., Printing highly efficient organic solar cells. *Nano Lett.* **2008,** 8, (9), 2806-2813.

27. Angmo, D.; Larsen‐Olsen, T. T.; Jørgensen, M.; Søndergaard, R. R.; Krebs, F. C., Roll‐to‐roll inkjet printing and photonic sintering of electrodes for ITO free polymer solar cell modules and facile product integration. *Adv. Energy Mater.* **2013,** 3, (2), 172-175.

28. Eggers, H.; Schackmar, F.; Abzieher, T.; Sun, Q.; Lemmer, U.; Vaynzof, Y.; Richards, B. S.; Hernandez‐Sosa, G.; Paetzold, U. W., Inkjet‐Printed

Micrometer‐Thick Perovskite Solar Cells with Large Columnar Grains. *Adv. Energy Mater.* **2020,** 10, (6), 1903184.

29. Lee, D. H.; Chang, Y. J.; Stickle, W.; Chang, C. H., Functional porous tin oxide thin films fabricated by inkjet printing process. *Electrochem. Solid State Lett.* **2007,** 10, (11), K51-K54.

30. Dou, R.; Wang, T.; Guo, Y.; Derby, B., Ink‐Jet Printing of Zirconia: Coffee Staining and Line Stability. *J. Am. Ceram. Soc.* **2011,** 94, (11), 3787-3792.

31. Liu, Y.; Derby, B., Experimental study of the parameters for stable drop-on-demand inkjet performance. *Phys. Fluids* **2019,** 31, (3), 032004.

32. Hoth, C. N.; Choulis, S. A.; Schilinsky, P.; Brabec, C. J., High photovoltaic performance of inkjet printed polymer: fullerene blends. *Adv. Mater.* **2007,** 19, (22), 3973-3978.

33. Villani, F.; Vacca, P.; Nenna, G.; Valentino, O.; Burrasca, G.; Fasolino, T.; Minarini, C.; della Sala, D., Inkjet printed polymer layer on flexible substrate for OLED applications. *J. Phys. Chem. C* **2009,** 113, (30), 13398-13402.

34. Van Osch, T. H.; Perelaer, J.; de Laat, A. W.; Schubert, U. S., Inkjet printing of narrow conductive tracks on untreated polymeric substrates. *Adv. Mater.* **2008,** 20, (2), 343-345.

35. Song, D.; Zare Bidoky, F.; Hyun, W. J.; Walker, S. B.; Lewis, J. A.; Frisbie, C. D., All-printed, self-aligned carbon nanotube thin-film transistors on imprinted plastic substrates. *ACS Appl. Mater. Interfaces* **2018,** 10, (18), 15926-15932.

36. Gao, A.; Yan, J.; Wang, Z.; Liu, P.; Wu, D.; Tang, X.; Fang, F.; Ding, S.; Li, X.; Sun, J., Printable CsPbBr 3 perovskite quantum dot ink for coffee ring-free fluorescent microarrays using inkjet printing. *Nanoscale* **2020,** 12, (4), 2569-2577.

37. Le, L. T.; Ervin, M. H.; Qiu, H.; Fuchs, B. E.; Lee, W. Y., Graphene supercapacitor electrodes fabricated by inkjet printing and thermal reduction of graphene oxide. *Electrochem. Commun.* **2011,** 13, (4), 355-358.

38. Torrisi, F.; Hasan, T.; Wu, W.; Sun, Z.; Lombardo, A.; Kulmala, T. S.; Hsieh, G.-W.; Jung, S.; Bonaccorso, F.; Paul, P. J., Inkjet-printed graphene electronics. *ACS nano* **2012,** 6, (4), 2992-3006.

39. He, P.; Derby, B., Inkjet printing ultra-large graphene oxide flakes. *2D Materials* **2017,** 4, (2), 021021.

40. Roth, E. A.; Xu, T.; Das, M.; Gregory, C.; Hickman, J. J.; Boland, T., Inkjet printing for high-throughput cell patterning. *Biomaterials* **2004,** 25, (17), 3707-3715.

41. Martin, G. D.; Hoath, S. D.; Hutchings, I. M. In *Inkjet printing-the physics of manipulating liquid jets and drops*, Journal of Physics: Conference Series, 2008; IOP Publishing: 2008; p 012001.

42. Sweet, R. G., High frequency recording with electrostatically deflected ink jets. *Rev. Sci. Instrum.* **1965,** 36, (2), 131-136.

43. Buehner, W.; Hill, J.; Williams, T.; Woods, J., Application of ink jet technology to a word processing output printer. *IBM J. Res. Dev.* **1977,** 21, (1), 2-9.

44. Driessen, T.; Jeurissen, R., Drop formation in inkjet printing. *Fundamentals of Inkjet Printing* **2016**, 93-115.

45. Cummins, G.; Desmulliez, M. P., Inkjet printing of conductive materials: a review. *Circuit world* **2012**.

46. Le, H. P., Progress and trends in ink-jet printing technology. *J. Imaging Sci. Technol.* **1998,** 42, (1), 49-62.

47. Xu, T.; Jin, J.; Gregory, C.; Hickman, J. J.; Boland, T., Inkjet printing of viable mammalian cells. *Biomaterials* **2005,** 26, (1), 93-99.

48. Setti, L.; Fraleoni-Morgera, A.; Mencarelli, I.; Filippini, A.; Ballarin, B.; Di Biase, M., An HRP-based amperometric biosensor fabricated by thermal inkjet printing. *Sensors Actuators B: Chem.* **2007,** 126, (1), 252-257.

49. Cui, X.; Boland, T., Human microvasculature fabrication using thermal inkjet printing technology. *Biomaterials* **2009,** 30, (31), 6221-6227.

50. Daly, R.; Harrington, T. S.; Martin, G. D.; Hutchings, I. M., Inkjet printing for pharmaceutics–a review of research and manufacturing. *Int. J. Pharm.* **2015,** 494, (2), 554-567.

51. Hansell, C. W., Jet sprayer actuated by supersonic waves. In Google Patents: 1950.

52. Dijksman, J., Hydrodynamics of small tubular pumps. *J. Fluid Mech.* **1984,** 139, 173-91.

53. Reis, N.; Ainsley, C.; Derby, B., Ink-jet delivery of particle suspensions by piezoelectric droplet ejectors. *J. Appl. Phys.* **2005,** 97, (9), 094903.

54. Li, E.; Xu, Q.; Sun, J.; Fuh, J.; Wong, Y.; Thoroddsen, S. T., Design and fabrication of a PET/PTFE-based piezoelectric squeeze mode drop-on-demand inkjet printhead with interchangeable nozzle. *Sens. Actuator A Phys.* **2010,** 163, (1), 315-322.

55. Saunders, R. E.; Gough, J. E.; Derby, B., Delivery of human fibroblast cells by piezoelectric drop-on-demand inkjet printing. *Biomaterials* **2008,** 29, (2), 193-203.

56. Shim, I.-K.; Lee, Y. I.; Lee, K. J.; Joung, J., An organometallic route to highly monodispersed silver nanoparticles and their application to ink-jet printing. *Mater. Chem. Phys.* **2008,** 110, (2-3), 316-321.

57. Dankoco, M.; Tesfay, G.; Bènevent, E.; Bendahan, M., Temperature sensor realized by inkjet printing process on flexible substrate. *Mater. Sci. Eng., B* **2016,** 205, 1-5.

58. Fan, K.-C.; Chen, J.-Y.; Wang, C.-H.; Pan, W.-C., Development of a drop-on-demand droplet generator for one-drop-fill technology. *Sens. Actuator A Phys.* **2008,** 147, (2), 649-655.

59. Brünahl, J. Physics of piezoelectric shear mode inkjet actuators. Mikroelektronik och informationsteknik, 2003.

60. Steirer, K. X.; Berry, J. J.; Reese, M. O.; van Hest, M. F.; Miedaner, A.; Liberatore, M. W.; Collins, R.; Ginley, D. S., Ultrasonically sprayed and inkjet printed thin film electrodes for organic solar cells. *Thin Solid Films* **2009,** 517, (8), 2781-2786.

61. Derby, B., Inkjet printing ceramics: From drops to solid. *J. Eur. Ceram. Soc.* **2011,** 31, (14), 2543-2550.

62. Zhao, N.; Chiesa, M.; Sirringhaus, H.; Li, Y.; Wu, Y.; Ong, B., Self-aligned inkjet printing of highly conducting gold electrodes with submicron resolution. *J. Appl. Phys.* **2007,** 101, (6), 064513.

63. Caironi, M.; Gili, E.; Sakanoue, T.; Cheng, X.; Sirringhaus, H., High yield, single droplet electrode arrays for nanoscale printed electronics. *ACS nano* **2010,** 4, (3), 1451-1456.

64. Sung, J.; Kang, B. J.; Oh, J. H., Fabrication of high-resolution conductive lines by combining inkjet printing with soft lithography. *Microelectron. Eng.* **2013,** 110, 219-223.

65. Gilbert, W.; Short, P., On the magnet and magnetic bodies, and on that great magnet the Earth. *Ser. Sci. Classicists (Akad. Nauk SSSR, Moscow, 1956)* **1956**.

66. Zeleny, J., The electrical discharge from liquid points, and a hydrostatic method of measuring the electric intensity at their surfaces. *Phys. Rev.* **1914,** 3, (2), 69.

67. Tucker, N.; Stanger, J. J.; Staiger, M. P.; Razzaq, H.; Hofman, K., The history of the science and technology of electrospinning from 1600 to 1995. *J. Eng. Fibers Fabr.* **2012,** 7, (2_suppl), 155892501200702S10.

68. Wilm, M. S.; Mann, M., Electrospray and Taylor-Cone theory, Dole's beam of macromolecules at last? *Int. J. Mass Spectrom. Ion Processes* **1994,** 136, (2-3), 167-180.

69. Morozov, V. N.; Morozova, T. Y., Electrospray deposition as a method for mass fabrication of mono-and multicomponent microarrays of biological and biologically active substances. *Anal. Chem.* **1999,** 71, (15), 3110-3117.

70. Jaworek, A., Electrospray droplet sources for thin film deposition. *J. Mater. Sci.* **2007,** 42, (1), 266-297.

71. Yarin, A. L.; Koombhongse, S.; Reneker, D. H., Taylor cone and jetting from liquid droplets in electrospinning of nanofibers. *J. Appl. Phys.* **2001,** 90, (9), 4836-4846.

72. Bognitzki, M.; Czado, W.; Frese, T.; Schaper, A.; Hellwig, M.; Steinhart, M.; Greiner, A.; Wendorff, J. H., Nanostructured fibers via electrospinning. *Adv. Mater.* **2001,** 13, (1), 70-72.

73. Demir, M. M.; Yilgor, I.; Yilgor, E.; Erman, B., Electrospinning of polyurethane fibers. *Polymer* **2002,** 43, (11), 3303-3309.

74. Park, J.-U.; Hardy, M.; Kang, S. J.; Barton, K.; Adair, K.; kishore Mukhopadhyay, D.; Lee, C. Y.; Strano, M. S.; Alleyne, A. G.; Georgiadis, J. G., High-resolution electrohydrodynamic jet printing. *Nat. Mater.* **2007,** 6, (10), 782.

75. Kang, J.; Jang, Y.; Kim, Y.; Cho, S.-H.; Suhr, J.; Hong, B. H.; Choi, J.-B.; Byun, D., An Ag-grid/graphene hybrid structure for large-scale, transparent, flexible heaters. *Nanoscale* **2015,** 7, (15), 6567-6573.

76. Chang, J.; He, J.; Lei, Q.; Li, D., Electrohydrodynamic printing of microscale PEDOT: PSS-PEO features with tunable conductive/thermal properties. *ACS Appl. Mater. Interfaces* **2018,** 10, (22), 19116-19122.

77. Jayasinghe, S.; Edirisinghe, M., Electric-field driven jetting from dielectric liquids. *Appl. Phys. Lett.* **2004,** 85, (18), 4243-4245.

78. Mishra, S.; Barton, K. L.; Alleyne, A. G.; Ferreira, P. M.; Rogers, J. A., High-speed and drop-on-demand printing with a pulsed electrohydrodynamic jet. *J. Micromech. Microeng.* **2010,** 20, (9), 095026.

79. Chen, C.-H.; Saville, D.; Aksay, I., Scaling laws for pulsed electrohydrodynamic drop formation. *Appl. Phys. Lett.* **2006,** 89, (12), 124103.

80. Singh, M.; Haverinen, H. M.; Dhagat, P.; Jabbour, G. E., Inkjet printing—process and its applications. *Adv. Mater.* **2010,** 22, (6), 673-685.

81. Jang, D.; Kim, D.; Moon, J., Influence of fluid physical properties on ink-jet printability. *Langmuir* **2009,** 25, (5), 2629-2635.

82. Liu, Y.-F.; Tsai, M.-H.; Pai, Y.-F.; Hwang, W.-S., Control of droplet formation by operating waveform for inks with various viscosities in piezoelectric inkjet printing. *Appl. Phys. A* **2013,** 111, (2), 509-516.

83. Kwon, K.-S., Waveform design methods for piezo inkjet dispensers based on measured meniscus motion. *J. Microelectromech. Syst.* **2009,** 18, (5), 1118-1125.

84. Duineveld, P. C.; De Kok, M. M.; Buechel, M.; Sempel, A.; Mutsaers, K. A.; Van de Weijer, P.; Camps, I. G.; Van de Biggelaar, T.; Rubingh, J.-E. J.; Haskal, E. I. In *Ink-jet printing of polymer light-emitting devices*, Organic Light-Emitting Materials and Devices V, 2002; International Society for Optics and Photonics: 2002; pp 59-67.

85. McKinley, G. H.; Renardy, M., Wolfgang von ohnesorge. *Phys. Fluids* **2011,** 23, (12), 127101.

86. Fromm, J., Numerical calculation of the fluid dynamics of drop-on-demand jets. *IBM J. Res. Dev.* **1984,** 28, (3), 322-333.

87. Reis, N.; Derby, B., Ink jet deposition of ceramic suspensions: Modeling and experiments of droplet formation. *MRS Online Proceedings Library Archive* **2000,** 625.

88. Stow, C. D.; Hadfield, M. G., An experimental investigation of fluid flow resulting from the impact of a water drop with an unyielding dry surface. *Proc. R. Soc. London, Ser. A* **1981,** 373, (1755), 419-441.

89. Bhola, R.; Chandra, S., Parameters controlling solidification of molten wax droplets falling on a solid surface. *J. Mater. Sci.* **1999,** 34, (19), 4883-4894.

90. Xu, D.; Sanchez-Romaguera, V.; Barbosa, S.; Travis, W.; de Wit, J.; Swan, P.; Yeates, S. G., Inkjet printing of polymer solutions and the role of chain entanglement. *J. Mater. Chem.* **2007,** 17, (46), 4902-4907.

91. Haskal, E.; Buechel, M.; Dijksman, J.; Duineveld, P.; Meulenkamp, E.; Mutsaers, C.; Sempel, A.; Snijder, P.; Vulto, S.; Van de Weijer, P. In *21.1: Ink Jet Printing of Passive ‐ Matrix Polymer Light Emitting Displays*, SID Symposium Digest of Technical Papers, 2002; Wiley Online Library: 2002; pp 776-779.

92. Bogy, D. B.; Talke, F., Experimental and theoretical study of wave propagation phenomena in drop-on-demand ink jet devices. *IBM J. Res. Dev.* **1984,** 28, (3), 314-321.

93. Liu, Y.-F.; Pai, Y.-F.; Tsai, M.-H.; Hwang, W.-S., Investigation of driving waveform and resonance pressure in piezoelectric inkjet printing. *Appl. Phys. A* **2012,** 109, (2), 323-329.

94. Wu, H.-C.; Lin, H.-J.; Hwang, W.-S., A numerical study of the effect of operating parameters on drop formation in a squeeze mode inkjet device. *Modell. Simul. Mater. Sci. Eng.* **2004,** 13, (1), 17.

95. Kwon, K.-S., Experimental analysis of waveform effects on satellite and ligament behavior via in situ measurement of the drop-on-demand drop

formation curve and the instantaneous jetting speed curve. *J. Micromech. Microeng.* **2010,** 20, (11), 115005.

96. Noguera, R.; Lejeune, M.; Chartier, T., 3D fine scale ceramic components formed by ink-jet prototyping process. *J. Eur. Ceram. Soc.* **2005,** 25, (12), 2055-2059.

97. Chen, A. U.; Basaran, O. A., A new method for significantly reducing drop radius without reducing nozzle radius in drop-on-demand drop production. *Phys. Fluids* **2002,** 14, (1), L1-L4.

98. Shin, P.; Sung, J.; Lee, M. H., Control of droplet formation for low viscosity fluid by double waveforms applied to a piezoelectric inkjet nozzle. *Microelectron. Reliab.* **2011,** 51, (4), 797-804.

99. Gan, H.; Shan, X.; Eriksson, T.; Lok, B.; Lam, Y., Reduction of droplet volume by controlling actuating waveforms in inkjet printing for micro-pattern formation. *J. Micromech. Microeng.* **2009,** 19, (5), 055010.

100. Lee, A.; Jin, H.; Dang, H.-W.; Choi, K.-H.; Ahn, K. H., Optimization of experimental parameters to determine the jetting regimes in electrohydrodynamic printing. *Langmuir* **2013,** 29, (44), 13630-13639.

101. Hayati, I.; Bailey, A.; Tadros, T. F., Mechanism of stable jet formation in electrohydrodynamic atomization. *Nature* **1986,** 319, (6048), 41-43.

102. Collins, R. T.; Harris, M. T.; Basaran, O. A., Breakup of electrified jets. *J. Fluid Mech.* **2007,** 588, 75-129.

103. Bober, D. B.; Chen, C.-H., Pulsating electrohydrodynamic cone-jets: from choked jet to oscillating cone. *J. Fluid Mech.* **2011,** 689, 552-563.

104. Hayati, I.; Bailey, A.; Tadros, T. F., Investigations into the mechanisms of electrohydrodynamic spraying of liquids: I. Effect of electric field and the environment on pendant drops and factors affecting the formation of stable jets and atomization. *J. Colloid Interface Sci.* **1987,** 117, (1), 205-221.

105. Ganan-Calvo, A. M., Cone-jet analytical extension of Taylor's electrostatic solution and the asymptotic universal scaling laws in electrospraying. *Phys. Rev. Lett.* **1997,** 79, (2), 217.

106. Li, J., On the meniscus deformation when the pulsed voltage is applied. *J. Electrostatics* **2006,** 64, (1), 44-52.

107. Yu, M.; Ahn, K. H.; Lee, S. J., Design optimization of ink in electrohydrodynamic jet printing: Effect of viscoelasticity on the formation of Taylor cone jet. *Materials & Design* **2016,** 89, 109-115.

108. Juraschek, R.; Röllgen, F., Pulsation phenomena during electrospray ionization. *Int. J. Mass spectrom.* **1998,** 177, (1), 1-15.

109. Marginean, I.; Nemes, P.; Vertes, A., Order-chaos-order transitions in electrosprays: The electrified dripping faucet. *Phys. Rev. Lett.* **2006,** 97, (6), 064502.

110. Choi, H. K.; Park, J.-U.; Park, O. O.; Ferreira, P. M.; Georgiadis, J. G.; Rogers, J. A., Scaling laws for jet pulsations associated with high-resolution electrohydrodynamic printing. *Appl. Phys. Lett.* **2008,** 92, (12), 123109.

111. Choi, J.; Kim, Y.-J.; Lee, S.; Son, S. U.; Ko, H. S.; Nguyen, V. D.; Byun, D., Drop-on-demand printing of conductive ink by electrostatic field induced inkjet head. *Appl. Phys. Lett.* **2008,** 93, (19), 193508.

112. Lee, M. W.; An, S.; Kim, N. Y.; Seo, J. H.; Huh, J.-Y.; Kim, H. Y.; Yoon, S. S., Effects of pulsing frequency on characteristics of electrohydrodynamic inkjet using micro-Al and nano-Ag particles. *Exp. Therm Fluid Sci.* **2013,** 46, 103-110.

113. An, S.; Lee, M. W.; Kim, N. Y.; Lee, C.; Al-Deyab, S. S.; James, S. C.; Yoon, S. S., Effect of viscosity, electrical conductivity, and surface tension on direct-current-pulsed drop-on-demand electrohydrodynamic printing frequency. *Appl. Phys. Lett.* **2014,** 105, (21), 214102.

114. Phung, T. H.; Kim, S.; Kwon, K.-S., A high speed electrohydrodynamic (EHD) jet printing method for line printing. *J. Micromech. Microeng.* **2017,** 27, (9), 095003.

115. Kim, J.; Oh, H.; Kim, S. S., Electrohydrodynamic drop-on-demand patterning in pulsed cone-jet mode at various frequencies. *J. Aerosol Sci* **2008,** 39, (9), 819-825.

116. Yarin, A. L., Drop impact dynamics: splashing, spreading, receding, bouncing…. *Annu. Rev. Fluid Mech.* **2006,** 38, 159-192.

117. Schiaffino, S.; Sonin, A. A., Molten droplet deposition and solidification at low Weber numbers. *Phys. Fluids* **1997,** 9, (11), 3172-3187.

118. Cassie, A., Contact angles. *Discuss. Faraday Soc.* **1948,** 3, 11-16.

119. Guo, L.; Duan, Y.; Huang, Y.; Yin, Z., Experimental Study of the Influence of Ink Properties and Process Parameters on Ejection Volume in Electrohydrodynamic Jet Printing. *Micromachines* **2018,** 9, (10), 522.

120. Laurila, M.; Khorramdel, B.; Dastpak, A.; Mäntysalo, M., Statistical analysis of E-jet print parameter effects on Ag-nanoparticle ink droplet size. *J. Micromech. Microeng.* **2017,** 27, (9), 095005.

121. Park, J.; Kim, B.; Kim, S.-Y.; Hwang, J., Prediction of drop-on-demand (DOD) pattern size in pulse voltage-applied electrohydrodynamic (EHD) jet printing of Ag colloid ink. *Appl. Phys. A* **2014,** 117, (4), 2225-2234.

122. Picknett, R.; Bexon, R., The evaporation of sessile or pendant drops in still air. *J. Colloid Interface Sci.* **1977,** 61, (2), 336-350.

123. Erbil, H. Y.; McHale, G.; Newton, M., Drop evaporation on solid surfaces: constant contact angle mode. *Langmuir* **2002,** 18, (7), 2636-2641.

124. Bourges-Monnier, C.; Shanahan, M., Influence of evaporation on contact angle. *Langmuir* **1995,** 11, (7), 2820-2829.

125. Schönfeld, F.; Graf, K.-H.; Hardt, S.; Butt, H.-J., Evaporation dynamics of sessile liquid drops in still air with constant contact radius. *Int. J. Heat Mass Transfer* **2008,** 51, (13-14), 3696-3699.

126. Lam, C. N. C.; Wu, R.; Li, D.; Hair, M. L.; Neumann, A. W., Study of the advancing and receding contact angles: liquid sorption as a cause of contact angle hysteresis. *Adv. Colloid Interface Sci.* **2002,** 96, (1), 169-191.

127. Dettre, R. H.; Johnson Jr, R. E., Contact angle hysteresis: II. Contact angle measurements on rough surfaces. In ACS Publications: 1964.

128. Eick, J.; Good, R.; Neumann, A., Thermodynamics of contact angles. II. Rough solid surfaces. *J. Colloid Interface Sci.* **1975,** 53, (2), 235-248.

129. Johnson Jr, R. E.; Dettre, R. H., Contact angle hysteresis. III. Study of an idealized heterogeneous surface. *The journal of physical chemistry* **1964,** 68, (7), 1744-1750.

130. Brandon, S.; Marmur, A., Simulation of contact angle hysteresis on chemically heterogeneous surfaces. *J. Colloid Interface Sci.* **1996,** 183, (2), 351-355.

131. Fadeev, A. Y.; McCarthy, T. J., Trialkylsilane monolayers covalently attached to silicon surfaces: wettability studies indicating that molecular topography contributes to contact angle hysteresis. *Langmuir* **1999,** 15, (11), 3759-3766.

132. Deegan, R. D., Pattern formation in drying drops. *Phys. Rev. E* **2000,** 61, (1), 475.

133. Deegan, R. D.; Bakajin, O.; Dupont, T. F.; Huber, G.; Nagel, S. R.; Witten, T. A., Capillary flow as the cause of ring stains from dried liquid drops. *Nature* **1997,** 389, (6653), 827-829.

134. Deegan, R. D.; Bakajin, O.; Dupont, T. F.; Huber, G.; Nagel, S. R.; Witten, T. A., Contact line deposits in an evaporating drop. *Phys. Rev. E* **2000,** 62, (1), 756.

135. He, P.; Derby, B., Controlling coffee ring formation during drying of inkjet printed 2D inks. *Adv. Mater. Interfaces* **2017,** 4, (22), 1700944.

136. Xu, X.; Luo, J., Marangoni flow in an evaporating water droplet. *Appl. Phys. Lett.* **2007,** 91, (12), 124102.

137. Kim, D.; Jeong, S.; Park, B. K.; Moon, J., Direct writing of silver conductive patterns: Improvement of film morphology and conductance by controlling solvent compositions. *Appl. Phys. Lett.* **2006,** 89, (26), 264101.

138. Yunker, P. J.; Still, T.; Lohr, M. A.; Yodh, A., Suppression of the coffee-ring effect by shape-dependent capillary interactions. *Nature* **2011,** 476, (7360), 308-311.

139. Park, J.; Moon, J., Control of colloidal particle deposit patterns within picoliter droplets ejected by ink-jet printing. *Langmuir* **2006,** 22, (8), 3506-3513.

140. Lim, J. A.; Lee, W. H.; Lee, H. S.; Lee, J. H.; Park, Y. D.; Cho, K., Self‐organization of ink‐jet‐printed triisopropylsilylethynyl pentacene via evaporation‐induced flows in a drying droplet. *Adv. Funct. Mater.* **2008,** 18, (2), 229-234.

141. Still, T.; Yunker, P. J.; Yodh, A. G., Surfactant-induced Marangoni eddies alter the coffee-rings of evaporating colloidal drops. *Langmuir* **2012,** 28, (11), 4984-4988.

142. Majumder, M.; Rendall, C. S.; Eukel, J. A.; Wang, J. Y.; Behabtu, N.; Pint, C. L.; Liu, T.-Y.; Orbaek, A. W.; Mirri, F.; Nam, J., Overcoming the “coffee-stain” effect by compositional Marangoni-flow-assisted drop-drying. *J. Phys. Chem. B* **2012,** 116, (22), 6536-6542.

143. Davis, S. H., Moving contact lines and rivulet instabilities. Part 1. The static rivulet. *J. Fluid Mech.* **1980,** 98, (2), 225-242.

144. Schiaffino, S.; Sonin, A. A., Formation and stability of liquid and molten beads on a solid surface. *J. Fluid Mech.* **1997,** 343, 95-110.

145. Abunahla, R.; Rahman, M. S.; Naderi, P.; Grau, G., Improved Inkjet-Printed Pattern Fidelity: Suppressing Bulges by Segmented and Symmetric Drop Placement. *Journal of Micro and Nano-Manufacturing* **2020,** 8, (3).

146. Wang, J.; Zheng, Z.; Li, H.; Huck, W.; Sirringhaus, H., Dewetting of conducting polymer inkjet droplets on patterned surfaces. *Nat. Mater.* **2004,** 3, (3), 171-176.

147. Kant, P.; Hazel, A. L.; Dowling, M.; Thompson, A. B.; Juel, A., Controlling droplet spreading with topography. *Physical Review Fluids* **2017,** 2, (9), 094002.

148. Li, W.; Wang, Y.; Li, M.; Garbarini, L. P.; Omenetto, F. G., Inkjet printing of patterned, multispectral, and biocompatible photonic crystals. *Adv. Mater.* **2019,** 31, (36), 1901036.

149. Nguyen, P. Q.; Yeo, L.-P.; Lok, B.-K.; Lam, Y.-C., Patterned surface with controllable wettability for inkjet printing of flexible printed electronics. *ACS Appl. Mater. Interfaces* **2014,** 6, (6), 4011-4016.

150. Kant, P.; Hazel, A. L.; Dowling, M.; Thompson, A. B.; Juel, A., Sequential deposition of microdroplets on patterned surfaces. *Soft Matter* **2018,** 14, (43), 8709-8716.

151. Lee, W.; Son, G., Numerical study of droplet impact and coalescence in a microline patterning process. *Computers & Fluids* **2011,** 42, (1), 26-36.

152. Fukai, J.; Ishizuka, H.; Sakai, Y.; Kaneda, M.; Morita, M.; Takahara, A., Effects of droplet size and solute concentration on drying process of polymer solution droplets deposited on homogeneous surfaces. *Int. J. Heat Mass Transfer* **2006,** 49, (19-20), 3561-3567.

153. Thompson, A. B.; Tipton, C. R.; Juel, A.; Hazel, A. L.; Dowling, M., Sequential deposition of overlapping droplets to form a liquid line. *J. Fluid Mech.* **2014,** 761, 261-281.

154. Du, Z.; Xing, R.; Cao, X.; Yu, X.; Han, Y., Symmetric and uniform coalescence of ink-jetting printed polyfluorene ink drops by controlling the droplet spacing distance and ink surface tension/viscosity ratio. *Polymer* **2017,** 115, 45-51.

155. Soltman, D.; Smith, B.; Morris, S.; Subramanian, V. In *Methodology for Inkjet Printing Partially Wetting Films*, NIP & Digital Fabrication Conference, 2010; Society for Imaging Science and Technology: 2010; pp 292-296.

156. Lee, H.-H.; Chou, K.-S.; Huang, K.-C., Inkjet printing of nanosized silver colloids. *Nanotechnology* **2005,** 16, (10), 2436.

157. Chen, S.-P.; Chiu, H.-L.; Wang, P.-H.; Liao, Y.-C., Inkjet printed conductive tracks for printed electronics. *ECS J. Solid State Sci. Technol.* **2015,** 4, (4), P3026-P3033.

158. Drury, C.; Mutsaers, C.; Hart, C.; Matters, M.; De Leeuw, D., Low-cost all-polymer integrated circuits. *Appl. Phys. Lett.* **1998,** 73, (1), 108-110.

159. Jeong, S.; Song, H. C.; Lee, W. W.; Choi, Y.; Ryu, B.-H., Preparation of aqueous Ag Ink with long-term dispersion stability and its inkjet printing for fabricating conductive tracks on a polyimide film. *J. Appl. Phys.* **2010,** 108, (10), 102805.

160. Wu, Y.; Li, Y.; Ong, B. S.; Liu, P.; Gardner, S.; Chiang, B., High‐performance organic thin‐film transistors with solution‐printed gold contacts. *Adv. Mater.* **2005,** 17, (2), 184-187.

161. Kang, J. S.; Kim, H. S.; Ryu, J.; Hahn, H. T.; Jang, S.; Joung, J. W., Inkjet printed electronics using copper nanoparticle ink. *J. Mater. Sci.: Mater. Electron.* **2010,** 21, (11), 1213-1220.

162. Reinhold, I.; Hendriks, C. E.; Eckardt, R.; Kranenburg, J. M.; Perelaer, J.; Baumann, R. R.; Schubert, U. S., Argon plasma sintering of inkjet printed silver tracks on polymer substrates. *J. Mater. Chem.* **2009,** 19, (21), 3384-3388.

163. Perelaer, J.; Klokkenburg, M.; Hendriks, C. E.; Schubert, U. S., Microwave flash sintering of inkjet‐printed silver tracks on polymer substrates. *Adv. Mater.* **2009,** 21, (47), 4830-4834.

164. Denneulin, A.; Blayo, A.; Neuman, C.; Bras, J., Infra-red assisted sintering of inkjet printed silver tracks on paper substrates. *J. Nanopart. Res.* **2011,** 13, (9), 3815-3823.

165. Polzinger, B.; Schoen, F.; Matic, V.; Keck, J.; Willeck, H.; Eberhardt, W.; Kueck, H. In *UV-sintering of inkjet-printed conductive silver tracks*, 2011 11th IEEE International Conference on Nanotechnology, 2011; IEEE: 2011; pp 201-204.

166. Huang, Q.; Shen, W.; Xu, Q.; Tan, R.; Song, W., Properties of polyacrylic acid-coated silver nanoparticle ink for inkjet printing conductive tracks on paper with high conductivity. *Mater. Chem. Phys.* **2014,** 147, (3), 550-556.

167. Kao, Z.-K.; Hung, Y.-H.; Liao, Y.-C., Formation of conductive silver films via inkjet reaction system. *J. Mater. Chem.* **2011,** 21, (46), 18799-18803.

168. Dearden, A. L.; Smith, P. J.; Shin, D. Y.; Reis, N.; Derby, B.; O'Brien, P., A Low Curing Temperature Silver Ink for Use in Ink‐Jet Printing and Subsequent Production of Conductive Tracks. *Macromol. Rapid Commun.* **2005,** 26, (4), 315-318.

169. Wu, J.-T.; Hsu, S. L.-C.; Tsai, M.-H.; Hwang, W.-S., Inkjet printing of low-temperature cured silver patterns by using AgNO3/1-dimethylamino-2-propanol inks on polymer substrates. *J. Phys. Chem. C* **2011,** 115, (22), 10940-10945.

170. Perelaer, J.; Hendriks, C. E.; de Laat, A. W.; Schubert, U. S., One-step inkjet printing of conductive silver tracks on polymer substrates. *Nanotechnology* **2009,** 20, (16), 165303.

171. Richner, P.; Kress, S. J.; Norris, D. J.; Poulikakos, D., Charge effects and nanoparticle pattern formation in electrohydrodynamic NanoDrip printing of colloids. *Nanoscale* **2016,** 8, (11), 6028-6034.

172. Wei, C.; Qin, H.; Ramirez-Iglesias, N. A.; Chiu, C.-P.; Lee, Y.-s.; Dong, J., High-resolution ac-pulse modulated electrohydrodynamic jet printing on highly insulating substrates. *J. Micromech. Microeng.* **2014,** 24, (4), 045010.

173. Lei, Q.; He, J.; Zhang, B.; Chang, J.; Li, D., Microscale electrohydrodynamic printing of conductive silver features based on in situ reactive inks. *J. Mater. Chem. C* **2018,** 6, (2), 213-218.

174. Wang, K.; Paine, M. D.; Stark, J. P., Fully voltage-controlled electrohydrodynamic jet printing of conductive silver tracks with a sub-100 μm linewidth. *J. Appl. Phys.* **2009,** 106, (2), 024907.

175. Rahman, M. K.; Kim, S.-j.; Phung, T. H.; Lee, J.-S.; Yu, J.; Kwon, K.-S., Three-dimensional surface printing method for interconnecting electrodes on opposite sides of substrates. *Scientific reports* **2020,** 10, (1), 1-14.

176. Son, S.; Lee, S.; Choi, J., Fine metal line patterning on hydrophilic non-conductive substrates based on electrohydrodynamic printing and laser sintering. *J. Electrostatics* **2014,** 72, (1), 70-75.

177. Qin, H.; Wei, C.; Dong, J.; Lee, Y.-S., Direct printing and electrical characterization of conductive micro-silver tracks by alternating current-pulse modulated electrohydrodynamic jet printing. *J. Manuf. Sci. Eng.* **2017,** 139, (2).

178. Wang, Z.; Zhang, G.; Huang, H.; Qian, L.; Liu, X.; Lan, H., The self-induced electric-field-driven jet printing for fabricating ultrafine silver grid transparent electrode. *Virtual and Physical Prototyping* **2021,** 16, (1), 113-123.

179. Wang, D.; Wang, Q.; Meng, Q.; Li, K.; Li, J.; Xiong, S.; Liu, C.; Yuan, X.; Ren, T.; Liang, J., High temperature-assisted electrohydrodynamic jet printing of sintered type nano silver ink on a heated substrate. *J. Micromech. Microeng.* **2019,** 29, (4), 045012.

180. Zhang, Z.; Zhang, X.; Xin, Z.; Deng, M.; Wen, Y.; Song, Y., Controlled inkjetting of a conductive pattern of silver nanoparticles based on the coffee‐ring effect. *Adv. Mater.* **2013,** 25, (46), 6714-6718.

181. Bridonneau, N.; Mattana, G.; Noël, V.; Zrig, S.; Carn, F., Morphological Control of Linear Particle Deposits from the Drying of Inkjet-Printed Rivulets. *The Journal of Physical Chemistry Letters* **2020,** 11, (12), 4559-4563.

182. Jiang, J.; Bao, B.; Li, M.; Sun, J.; Zhang, C.; Li, Y.; Li, F.; Yao, X.; Song, Y., Fabrication of transparent multilayer circuits by inkjet printing. *Adv. Mater.* **2016,** 28, (7), 1420-1426.

183. Zhang, R.; Qi, L.; Luo, J.; Lian, H., A novel method to improve the line resolution of stretchable graphene-based line by embedded uniform droplet printing. *J. Phys. D: Appl. Phys.* **2020,** 53, (38), 385301.

184. Qian, L.; Lan, H.; Zhang, G., A theoretical model for predicting the feature size printed by electrohydrodynamic jet printing. *Appl. Phys. Lett.* **2018,** 112, (20), 203505.

185. Dimatix, F., Dimatix Materials Printer DMP-2800 Series User Manual. In August: 2008.

186. Smith, P. J.; Shin, D. Y.; Stringer, J. E.; Derby, B.; Reis, N., Direct ink-jet printing and low temperature conversion of conductive silver patterns. *Journal of Materials Science* **2006,** 41, (13), 4153-4158.

187. Kang, B. J.; Oh, J. H., Geometrical characterization of inkjet-printed conductive lines of nanosilver suspensions on a polymer substrate. *Thin Solid Films* **2010,** 518, (10), 2890-2896.

188. Shanahan, M.; Bourges, C., Effects of evaporation on contact angles on polymer surfaces. *Int. J. Adhes. Adhes.* **1994,** 14, (3), 201-205.

189. Schneider, J.; Rohner, P.; Thureja, D.; Schmid, M.; Galliker, P.; Poulikakos, D., Electrohydrodynamic nanodrip printing of high aspect ratio metal grid transparent electrodes. *Adv. Funct. Mater.* **2016,** 26, (6), 833-840.

190. Can, T. T. T.; Nguyen, T. C.; Choi, W.-S., patterning of High-Viscosity silver paste by an electrohydrodynamic-Jet printer for Use in tFt Applications. *Scientific reports* **2019,** 9, (1), 1-8.

191. Cui, Z.; Han, Y.; Huang, Q.; Dong, J.; Zhu, Y., Electrohydrodynamic printing of silver nanowires for flexible and stretchable electronics. *Nanoscale* **2018,** 10, (15), 6806-6811.

192. Li, X.; Kim, K.; Oh, H.; Moon, H. C.; Nam, S.; Kim, S. H., Cone-jet printing of aligned silver nanowire/poly (ethylene oxide) composite electrodes for organic thin-film transistors. *Org. Electron.* **2019,** 69, 190-199.

193. Parry, A. V. S.; Straub, A. J.; Villar-Alvarez, E. M.; Phuengphol, T.; Nicoll, J. E. R.; Lim, W. K. X.; Jordan, L. M.; Moore, K. L.; Taboada, P.; Yeates, S. G.; Edmondson, S., Submicron Patterning of Polymer Brushes: An Unexpected Discovery from Inkjet Printing of Polyelectrolyte Macroinitiators. *J. Am. Chem. Soc.* **2016,** 138, (29), 9009-9012.

194. Ahn, S. H.; Lee, H. J.; Kim, G. H., Polycaprolactone scaffolds fabricated with an advanced electrohydrodynamic direct-printing method for bone tissue regeneration. *Biomacromolecules* **2011,** 12, (12), 4256-4263.

195. Shigeta, K.; He, Y.; Sutanto, E.; Kang, S.; Le, A.-P.; Nuzzo, R. G.; Alleyne, A. G.; Ferreira, P. M.; Lu, Y.; Rogers, J. A., Functional protein microarrays by electrohydrodynamic jet printing. *Anal. Chem.* **2012,** 84, (22), 10012-10018.

196. Park, J.; Hwang, J., Fabrication of a flexible Ag-grid transparent electrode using ac based electrohydrodynamic Jet printing. *J. Phys. D: Appl. Phys.* **2014,** 47, (40), 405102.

197. Qin, H.; Dong, J.; Lee, Y.-S., AC-pulse modulated electrohydrodynamic jet printing and electroless copper deposition for conductive microscale patterning on flexible insulating substrates. *Rob. Comput. Integr. Manuf.* **2017,** 43, 179-187.

198. Kim, Y.; Jang, S.; Oh, J. H., High-resolution electrohydrodynamic printing of silver nanoparticle ink via commercial hypodermic needles. *Appl. Phys. Lett.* **2015,** 106, (1), 014103.

199. Li, X.; Jung, E. M.; Kim, K. S.; Oh, J. H.; An, T. K.; Lee, S. W.; Kim, S. H., Printed water-based ITO nanoparticle via Electrohydrodynamic (EHD) jet printing and its application of ZnO transistors. *Electronic Materials Letters* **2019,** 15, (5), 595-604.

200. Sun, Y.; Rogers, J. A., Inorganic semiconductors for flexible electronics. *Adv. Mater.* **2007,** 19, (15), 1897-1916.